INVESTIGATIONS ON FRACTAL APERTURES IN WAVEGUIDES, CONDUCTING SCREENS AND CAVITIES

A THESIS

Submitted in partial fulfilment of the requirements for the award of the degree of

DOCTOR OF PHILOSOPHY

in

ELECTRONICS AND COMPUTER ENGINEERING

by

BASUDEB GHOSH

DEPARTMENT OF ELECTRONICS AND COMPUTER ENGINEERING
INDIAN INSTITUTE OF TECHNOLOGY ROORKEE
ROORKEE - 247 667 (INDIA)

APRIL, 2009

INDIAN INSTITUTE OF TECHNOLOGY ROORKEE
ROORKEE

CANDIDATE'S DECLARATION

I hereby certify that the work which is being presented in the thesis entitled INVESTIGATIONS ON FRACTAL APERTURES IN WAVEGUIDES, CONDUCTING SCREENS AND CAVITIES in partial fulfilment of the requirement for the award of the Degree of Doctor of Philosophy and submitted in the Department of **Electronics and Computer Engineering** of the Indian Institute of Technology Roorkee, Roorkee is an authentic record of my own work carried out during a period from July, 2004 to April, 2009 under the supervision of **Dr. Sachendra N. Sinha**, Professor and **Dr. M. V. Kartikeyan**, Associate Professor, **Department of Electronics and Computer Engineering** of Indian Institute of Technology Roorkee, Roorkee.

The matter presented in this thesis has not been submitted by me for the award of any other degree of this or any other Institute.

Basudeb Ghosh.

(BASUDEB GHOSH)

This is to certify that the above statement made by the candidate is correct to the best of our knowledge.

M V Kartikeyan

(M. V. Kartikeyan)
Supervisor

S N Sinha 6/4/09

(Sachendra N. Sinha)
Supervisor

Date: 06.04.2009

The Ph.D. Viva-Voce Examination of **Basudeb Ghosh**, Research Scholar, has been held on .....

Signature of Supervisors

Signature of External Examiners

To

my father

Late Nandadulal Ghosh

Abstract

Fractal geometries have widely been used in electromagnetics, specifically, in antennas and frequency selective surfaces (FSS). The self-similarity of fractal geometry gives rise to a multiband response, whereas the space-filling nature of the fractal geometries makes it an efficient element in antenna and FSS unit cell miniaturization. Till date, no effort has been made to study the behavior of these fractal geometries in the aperture coupling problems. Aperture coupling problem is an important boundary value problem in electromagnetics and has widely been used in waveguide filters and power dividers, slotted ground planes, frequency selective surfaces and metamaterials. The present work is primarily intended to initiate a study on the characteristics of fractal apertures in waveguides, conducting screens and cavities.

In order to carry out a unified analysis of these entirely dissimilar problems, the 'generalized network formulation for the aperture problems' proposed by Mautz and Harrington has been extended to multiple-aperture geometry. We have considered the problem of coupling between two arbitrary regions coupled together via multiple apertures of arbitrary shape. The two regions are decoupled by the application of equivalence principle and enforcement of boundary conditions over the aperture regions leads to an operator equation. The operator equation is then reduced to matrix form via the Method of Moments (MoM).

Abstract

The general problem of coupling through apertures is formulated in such a manner that only part of the problem needs to be reformulated for the solution of different problems like fractal diaphragms in a rectangular waveguide, radiation from waveguide-fed fractal apertures, coupling through fractal apertures in a conducting screen, and radiation from cavity-backed fractal apertures. A Galerkin procedure with rooftop and Rao-Wilton-Glisson (RWG) functions has been used for the first three problems, while a hybrid method using Finite Element Method (FEM) and MoM has been used for the cavity-backed fractal aperture problem. MATLAB codes have been developed for the problems and validated with the results available in the literature as well as through simulation on ANSOFT's HFSS.

The use of resonant apertures in the transverse cross-section of rectangular waveguide improves the out-of-band rejection ratio of waveguide filters and also results in more compact and light weight waveguide filters. The multiple aperture irises further improve the out-of-band rejection due to the formation of rejection band. Till now, some regular geometries have been analyzed in the literature. Due to requirement of multiple aperture iris and compact waveguide filters, we have studied the behavior of fractal apertures in the transverse cross-section of a waveguide. Two types of basis functions have been used in the analysis. In the first case, the roof-top functions are used to model rectangular aperture problem in which the aperture surface is discretized in small rectangular sub-areas. The integrals involving the Green's function are calculated analytically over the rectangular domain. In the second approach, the apertures are discretized in triangular sub-areas in order to model the arbitrary aperture surface and RWG functions are used as the basis functions. The integrals over triangular domain are calculated numerically using Gaussian quadrature. The frequency responses

of several fractal apertures are studied and some novel self-affine fractal geometries are proposed to obtain multiband response. A study has also been carried out to find a relation between the scale factor of the fractal geometry and the frequency response of the waveguide diaphragm. The study has further been extended to analyze the performance of finite periodic arrangement of these fractal apertures in the design of multiband waveguide filters and electromagnetic bandgap structures (EBG).

The problem of electromagnetic coupling between two regions via apertures in infinite screen has widely been used in the design of FSS, antenna arrays and slotted ground plane. An infinite screen perforated with multiple apertures has a bandpass response when illuminated by a plane wave of varying frequency. The coupling through fractal apertures in an infinite screen has been solved with RWG basis functions. In this case, the integrals involving the free space Green's function suffer from singularity problem. Singularity cancelation method has been used to calculate the integral which has the advantage of being accurate and, also, the calculation of these integrals over triangular domain can be done with a purely numerical technique. Several self-similar and space-filling fractal geometries are studied and, also, the effect of the variation of angle of incidence on the frequency response of fractal apertures has been investigated. It has been found that the variation of angle of incidence affects the performance of fractal apertures and some additional pass bands arise for inclined incidence. It is found that the fractal apertures support subwavelength transmission of electromagnetic waves and this property is more prominent in the space-filling fractal apertures. The coupling through the fractal apertures in infinite screen has been extended to the case of radiation through waveguide-fed fractal apertures. It has been found that the radiation from such fractal apertures improves the antenna input

matching and dual-band waveguide radiators can easily be realized.

Cavity-backed aperture antennas are very popular in aerospace applications due to their conformal nature. The cavity-backed aperture antenna satisfies the requirements of being flush mounted as well as light weight and small size. Also, the use of metallic cavity makes the radiation pattern unidirectional. Another most important advantage of the cavity backed apertures is that they offer very small mutual coupling between the elements and are very useful in the design of phased arrays. Cavity-backed fractal aperture is another field which could be explored in order to design small size multiband antennas. The problem has been formulated using combined FEM and MoM method. In the combined FEM/MoM method, the electric field inside the cavity is found using FEM and the surface magnetic current over the aperture surface is calculated using MoM. For FEM formulation, the cavity has been discretized into tetrahedral elements and the apertures into triangular elements. The simultaneous equations obtained over the sub domains are added to form the global matrix equation. This procedure gives a partly sparse and a partly dense matrix, which is then solved to find the unknown electric field over the apertures. The radiation characteristics and input characteristics of the antenna are then calculated from the electric field. The performance of cavity backed fractal apertures with a coaxial probe feeding has been investigated. The numerical results are again validated with simulation results on HFSS. A novel effort has been made to relate the electromagnetic behavior of the fractal aperture with the scale factor of the geometry. It has been found that the location of resonant frequency of the antenna can be changed by changing the scale factor of fractal apertures.

Acknowledgements

First and foremost, I wish to express my sincere gratitude and indebtedness to Prof. Sachendra N. Sinha whose constructive guidance, perceptive criticism, valuable suggestions and amiable treatment that have been indispensable in the completion of present work. I feel too short of dictum to thank him for providing encouragement and inspiring me throughout the tenure of this work. It has been an honor to work with him. I am also thankful to Prof. Sachendra. N. Sinha for providing necessary facilities in the Advanced Microwave Lab.

I sincerely thank Dr. M. V. Kartikeyan, my associate supervisor, for being a source of inspiration and enthusiasm. His advice and encouragement helped me to overcome many challenges and frustrations. I am also thankful to him for his support in writing the thesis.

My appreciation goes to my other research committee members as well: Prof. R. Mittra, Prof. R. C. Mittal and Dr. Dharmendra Singh for having accepted to examine this work and for providing valuable insights and advice. I am also thankful to all the faculty members of Microwave engineering, specially, Dr. Amalendu Patnaik, for his encouragement, advice and support.

I am also thankful to my colleagues, Anuradha and S. K. Jain and the technical staffs, Mr. Lakhan Giri and Mr. Rajaram, for their help and cooperation.

Thanks to my friends Ravi, Rohit, Rishi, Triloki, A. N. Gaikwad, Prashant,

Tapan, Debashis, Harish and Naveen for their motivation, encouragement and help. I am especially thankful to Ravi for his help and advice in developing the MATLAB code. Thanks to Rishi and Triloki for sharing lots of suggestions and light moments at tea time. They never let me feel alone.

It gives me a great pleasure in expressing my loving gratitude and affection to my wife Jayashree for her emotional and psychological support throughout this study. She knows more than anyone else about the sacrifices that had to be made. I would like to thank for her love, encouragement, patience and understanding throughout the tenure of my stay here. I am also thankful to my mother, brother and in-laws for their love and encouragement which made me to complete this work.

Finally, I thank Ministry of Human Resource Development (MHRD), Govt. of India for providing me financial support during my research work.

Basudeb Ghosh

Table of Contents

List of Figures

List of Tables

Chapter 1

INTRODUCTION

The rapid growth in the wireless systems during the past several years has set new demands on electromagnetic engineers. There is a trend to integrate the entire system, including antennas, on a single chip. This requires the design of miniaturized, power efficient, and low profile antennas. Further, multiband operation of wireless systems has been receiving considerable attention during the last decade. This requirement has initiated research in various directions, especially, in the design of compact multiband antennas and filters. One of the promising area of research for multiband operation is fractal electrodynamics, in which the fractal geometry is combined with electromagnetics for the purpose of investigating a new class of radiation and scattering problems. Fractals are complex shapes which contain an infinite number of scaled copies of the geometry and resonate at different frequencies. This property has been successfully used in the design of multiband antennas, frequency selective surfaces (FSS) and electromagnetic band gap (EBG) structures.

A survey of the large body of literature on fractal electromagnetics shows that no effort has been made so far, to exploit the multiband properties of fractals

in aperture problems. Apertures in conducting screens, waveguides, and cavities constitute an important class of boundary value problems and find many applications in electromagnetic systems. The aim of the present study is to initiate research in the investigation of the properties of fractal apertures.

To lay an understanding on the behavior of fractal geometries in the aperture coupling problems, a brief review of fractal geometries and their applications in the electromagnetic engineering is presented. This is followed by a brief review on the study and analysis of different aperture coupling problems in waveguides, conducting screens and cavities.

1.1 Fractal Electrodynamics

1.1.1 Fractal Geometries

Many patterns in the nature are so irregular and fragmented that they exhibit not only a higher degree, but also a higher level of complexity. The number of distinct scales required to describe the natural phenomenon are infinite. Hence, it was generally believed by scientists and mathematicians that these natural phenomenon were beyond rigorous explanations before Mandelbrot [1] proposed a new geometry and its use in various diverse fields. The geometry describes many of the irregular and fragmented patterns of nature around us. Mandelbrot coined the term 'fractal' from the Latin word '*frangere*' which means to break, to create irregular fragments. He used the term fractal to describe some complex and convoluted objects such as mountains, coastlines and many other natural phenomenon.

An iteration algorithm such as multiple reduction copy machine (MRCM) is applied in order to construct the ideal fractal geometries [2]. Basically, the

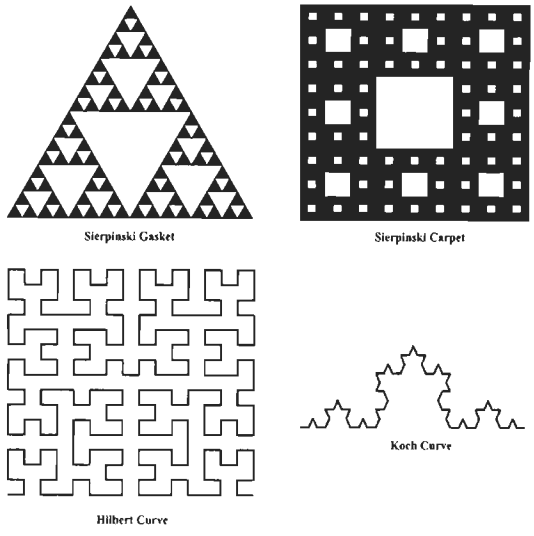

Figure 1.1: Some of the most commonly used fractal geometries.

process consists of an initiator and a generator. Based upon the nature of the iteration process, there may be deterministic and random fractals. Also, depending upon the mass ratio, the fractals may be homogeneous or heterogeneous [3]. Some of the most commonly used fractal geometries, such as Sierpinski gasket, Sierpinski carpet, Hilbert curve, Koch curve are shown in Fig 1.1. The generation procedure of all the geometries follows the same rule and starts with an initiator and a generator. For example, as shown in Fig. 1.2, an equilateral triangle is taken as the initial geometry for the generation of Sierpinski gasket fractal. The mid points of each sides are connected and the initial triangle is subdivided into four triangles. The center triangle is removed and this gives the generator of the Sierpinski gasket fractal. In the next iteration, the same process is repeated on the remaining three triangles and if this iteration process is continued for an infinite number of times, then one can obtain an ideal Sierpinski gasket geometry.

The important properties of the fractal geometries are self-similarity, space-filling ability, and lacunarity. When an object is composed of smaller copies

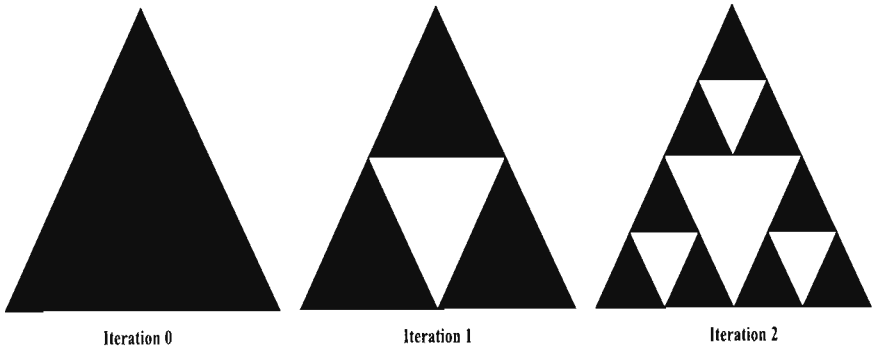

Figure 1.2: Generation steps of Sierpinski gasket fractal.

of the original geometry, it is said to be self-similar. A self-similar object can be described as a cluster, which is again made up of smaller clusters that are identical to the entire geometry. Thus, within the whole geometry, an infinite number of similar copies can be found. Hence, fractal geometries are said to have no characteristic size. The scaling factors in two orthogonal directions can be same or different. The former gives a self-similar geometry and the later produces a self-affine geometry. Geometries like Hilbert curve or Peano curve, when iterated for large number of times, fill a two dimensional area with the curve length tending to infinity which describes the space-filling property of the fractal geometries. Lacunarity is a term which describes the hollow space in a fractal geometry [1].

Another unique feature of the fractal geometries is the fractional dimension. There are different notations of the dimension of fractal geometries, such as topological dimension, *Hausdorf dimension*, Box counting dimension, and self-similarity dimension [2]. Among these, the self-similarity dimension is one of the most important parameters for the characterization of the fractal geometries.

Table 1.1: Self-similarity dimension of typical fractal geometries.

Fractal Geometry	Scale Factor (s)	No. of Self-similar copies	Dimension D_s
Sierpinski Gasket	$\frac{1}{3}$	3	1.5850
Sierpinski Carpet	$\frac{1}{3}$	8	1.8927
Koch Curve	$\frac{1}{3}$	4	1.2619
Hilbert Curve	$\frac{1}{2}$	4	2

The self-similarity dimension of the fractal geometry is defined as

$$D_s = \frac{\log(N)}{\log \frac{1}{s}} \tag{1.1}$$

where N is the number of self-similar copies and s is the scale factor. The dimensions of some typical fractals are tabulated in Table 1.1. It should be noted here that the self-similarity dimension of the fractal does not uniquely describe the fractal geometry [4].

Iterative function system (IFS) is an extremely versatile tool for convenient generation of fractal geometries. The iterative function system is a collection of self-affine transformations [2] given by,

$$w\begin{pmatrix} x \\ y \end{pmatrix} = \begin{pmatrix} a & b \\ c & d \end{pmatrix}\begin{pmatrix} x' \\ y' \end{pmatrix} + \begin{pmatrix} e \\ f \end{pmatrix} \tag{1.2}$$

where the parameters a, b, c and d are defined by scaling and rotation of initial geometry and e and f denote the translation.

Let $\{w_n,\ n = 1, 2, 3, ..., N\}$ be a set of affine transformations defined in (1.2) and let A denotes the initial image. The application of this set of transformations on the initial image produces a set of self-affine copies $\{w_n(A),\ n = 1, 2, 3, ..., N\}$.

Finally, a new image is obtained by collecting all these images as

$$W(A) = w_1(A) \cup w_2(A) \cup ... \cup w_N(A) \tag{1.3}$$

where W is called the Hutchinson operator. By repeated application of W to the previous geometry, an ideal fractal geometry can be obtained. That is,

$$A_1 = W(A_0), \;\; A_2 = W(A_1), ..., A_k = W(A_{k-1}) \tag{1.4}$$

The IFS has proved to be a very powerful design tool for fractals because this provides a general framework for the description, classification and manipulation of the fractal geometries.

In the following subsections, a brief review is provided on the applications of fractals in electromagnetics.

1.1.2 Fractal Antenna Elements

The scattering and reflection from fractal screens have been studied extensively and a good review on the radiation and scattering from fractal surfaces can be found in [4]. It has been shown that the diffracted field in Franhauffer zone is self-similar. The interesting feature of fractal screens is that the scattered patterns from these fractal geometries contain the fractal pattern imprinted on these. Several self-similar geometries are used in the design of multiband antennas like Sierpinski gasket, Koch curve, Hilbert curve etc. A comprehensive review on the fractal antenna and frequency selective surface elements can be found in [5]. Sierpinski gasket is the most popular in fractal antenna engineering. The behavior of Sierpinski gasket monopole and dipole antennas have been investigated in [6, 7]. It has been found that the antenna exhibits a log periodic behavior with a periodicity of 2. A downward shift of resonant frequencies has been observed as the order of iteration increases. Also, the radiation patterns at different resonant

frequencies of the antenna show a large degree of similarity, although some side lobes are generated at higher resonant frequencies. The behavior of the Sierpinski gasket antenna was explained in terms of an iterative network model in [8, 9], where the scattering matrices for the initiator and generator were used to predict the behavior of fractal antenna by cascading the scattering matrices. It was demonstrated in [10] that the location of different resonant frequencies of the antenna can be controlled by changing the scale factor of the fractal geometry. The flare angle of the initial triangle affects the antenna input characteristics [11]. The resonant frequencies shift downward as the flare angle of the initial triangle is increased. Also, too small a flare angle causes the multiband fractal antenna to operate as a simple monopole antenna. Several modifications of the Sierpinski gasket antenna and its effects on the radiation pattern of the antenna have been investigated [12, 13, 14]. Design equations for determining the resonant frequencies of Sierpinski modes and for the side length of the Sierpinski gasket antenna is proposed in [15].

An important property of fractal curves is that the length of the curve tends to infinity, although the overall height of the curve remains same. Hence, fractal curves are very useful in reducing the resonant frequencies of the wire antenna. One of the widely used fractal geometry in the design of wire antennas is the Koch curve. The behavior of Koch curve fractal antenna has been presented in [16, 17] where, a fifth iteration Koch monopole antenna has been investigated and it has been found that the Koch curve effectively reduces the resonant frequency of the wire antenna. Additionally, the resonant frequencies are more closely spaced for higher order iterations of the fractal. A rigorous comparison of Koch curve fractal antenna and their Euclidean counterpart has been reported in [18, 19]. The effect of indentation angle on the performance of the monopole and dipole

antenna has been investigated in [20]. It was found that the indentation angle plays an important role in locating the resonant frequency of the antenna. Also, the resonant frequencies decrease with the increase in the indentation angle and this decrement is much more dominant in higher order resonant frequencies than at the primary resonance.

Hilbert curve is widely used in the miniaturization of antenna element because of its space-filling property. The advantage of Hilbert curve antenna is that it offers a higher frequency compression factor as compared to the Koch curve fractal antenna, since the length of the Hilbert curve is much larger than that of the Koch curve for a given 2D area [21, 22]. Hilbert curve fractal is also widely used in the design of reconfigurable antennas [23].

Due to the low input resistance of the small loop antenna, fractal loops have proved to be very efficient in increasing the input resistance of the antenna. A fractal loop antenna based on the Koch snow flake geometry is reported in [24, 25]. The input resistance of the antenna was found to increase with increase in the order of iteration. However, the fractal loop antenna exhibits a multilobe pattern due to the increased length of the antenna. Another kind of fractal loop antenna based upon the Minkowski fractal has been investigated in [18, 26, 27]. Also, the performance of Minkowski fractal antenna has been compared with another fractal curve known as 3/2 curve fractal antenna in [26]. A fractal loop antenna based on modified Minkowski fractal geometry has been investigated in [28] which has a better space-filling characteristics as compared to the conventional Minkowski fractal geometry. Several combinations of regular and fractal elements are reported in [29, 30, 31] which exhibit a considerable degree of improvement in the antenna performance. A small size patch antenna combining the Koch and Sierpinski carpet fractals is analyzed in [32].

Fractal antennas are not limited to monopole and dipole antennas; they can also be implemented in the design of microstrip patch antennas. Several fractal geometries are used to obtain multiband fractal patch antennas and a stacked arrangement has been shown to have a broadband response [33, 34]. Microstrip antennas having fractal boundaries and mass distribution are illustrated as antennas supporting localized modes. These localized modes are very useful to obtain a broadside and very directive pattern [35, 36]. Recently, a reactively loaded stacked patch antenna with fractal radiating edge has been investigated in [37] which gives a considerable amount of bandwidth enhancement. Comprehensive analysis on the resonance and radiation behavior of the conformal antenna based on the Sierpinski gasket is reported in [38, 39]. A printed log-periodic Koch dipole antenna is investigated in [40] which offers 12% reduction of the antenna size with a minimal degradation in impedance and bandwidth. The characteristics of a CPW-fed planar antenna based on the Koch fractal loop are presented in [41, 42]. A radial stub has been used in [41], whereas a stub embedded with U-slot has been used in [42] to obtain the impedance match. Two other fractal antenna based on circular fractal and Sierpinski carpet are also reported in [43, 44].

1.1.3 Fractal Frequency Selective Surfaces and Filters

Space-filling and multiband properties of fractal geometries are also used in the design of size miniaturized and multiband FSS. A dual-band fractal FSS based upon the Sierpinski gasket geometry has been reported in [45, 46, 47]. It was shown that the fractal FSS offers two stopbands with an attenuation level of 30 dB. A tri-band FSS designed with cross bar fractal tree has been reported in [48, 49]. The characteristics of the FSS were shown to remain unchanged

for both TE and TM polarizations. Also, it was shown that the ratio between the successive resonant frequencies of the FSS can be changed by changing the scale factor of the geometry. Several fractal frequency selective surfaces based upon Sierpinski carpet, Minkowski island and inset crossed dipole elements are reported in [50], which present dual-band and dual-polarized characteristics. A novel fractal frequency selective surface based on the Sierpinski tripole elements is presented in [51]. The fractal geometry is optimized in order to obtain a dual-polarized and dual-band frequency selective surface.

Recently, several fractal geometries are used in the design of microstrip filters. A dual mode bandpass filter based on the Sierpinski carpet fractal geometry with a perturbation at the corner of fractal element is reported in [52]. In [53], a wideband microstrip bandpass filter using a triangular patch element is analyzed. It is shown that introducing fractal defection in the patch, a wider bandwidth can be achieved. A low pass filter using Koch fractal geometry is reported in [54].

1.1.4 Fractal Electromagnetic Band gap Structures and High Impedance Surfaces

Electromagnetic bandgap structures and high impedance surfaces have attracted considerable amount of attention due to the growing interest in improving the antenna gain, reducing the mutual coupling and restricting the propagation of higher order modes. Three different fractal geometries have been investigated in [55] which are capable of producing a wider stopband along with additional new stopband. A circularly polarized compact and dual band GPS patch antenna has been investigated in [56] which is placed over a fractal EBG surface. The antenna exhibits wider axial ratio bandwidth. A high impedance metamaterial surface

based on the Hilbert curve and Peano curve inclusions has been shown to offer a reflection coefficient $\Gamma \simeq +1$, when illuminated by a plane wave [57, 58]. Kern *et al.* [59] proposed several design methodologies for multiband artificial magnetic conductors using Minkowski fractal geometry. An electromagnetic bandgap structure based on a novel fractal similar to that of a crown square fractal has been analyzed in [60].

1.2 Aperture Problems in Electromagnetics

Coupling through apertures is a classical problem in electromagnetic field theory and finds wide applications in microwave technology ranging from waveguide passive components, slotted waveguide antenna arrays, slotted conducting screens, frequency selective surfaces (FSS) to cavity-backed slot antennas. Aperture coupling problems have been exhaustively investigated during the past 50 years and a large amount of literature exists on their analysis and applications. In the following subsections, we present a brief review of the various types of aperture coupling problems.

1.2.1 Apertures in Waveguide Transverse Cross-section

Aperture in the transverse cross-section is one of the most common type of discontinuity in waveguides. When waveguides are used in practice, it is necessary to introduce some discontinuities to produce waveguide filters, matching networks, and power dividers. The presence of discontinuities basically modifies the propagation characteristics of the waveguide but the end result depends upon the type and dimension of discontinuity. Various types of discontinuities are incorporated into the waveguide, among which aperture type discontinuities in the

transverse plane of the rectangular waveguide is an important problem. Inductive or capacitive discontinuities in the transverse cross-section of the waveguide are widely used in the design of matching networks due to the weak dependence of their parameters on frequency. Traditional waveguide filters use inductive or capacitive elements or a combination of these in order to produce the desired filter response [61]. Largely, these filter elements consist of aperture irises of rectangular or circular shapes [62, 63, 64, 65], and are located in the transverse cross-section of the waveguide. The filter response improves with the increase in number of waveguide sections which makes the waveguide filter very large and bulky. Instead of using a non-resonant aperture, a resonant aperture can be used as a classical element. A waveguide filter with such resonant elements has been shown to have better out–of–band characteristics in [66, 67]. The filter response can be further improved by using multi-slot iris due to the formation of rejection resonance. The formation of such rejection frequency was first mentioned in [68] with a five aperture iris. Later in [69], the existence of total rejection frequency using two slots was explained by simultaneous excitation of two natural oscillations of the iris. It was shown in [70], along with [69], that to form a rejection resonance, it is necessary to have at least a pair of natural oscillations with close real parts of eigen frequencies and essentially different Q factors, determined by the imaginary parts and the number of zeros and poles in the frequency response depend upon the number of slots with different electromagnetic properties. Also, the number of sections needed to obtain the desired out–of–band rejection decreases with multi-aperture iris as compared to the single aperture iris [71]. Recently, frequency selective surfaces have been used to realize elliptical function filter with multiple attenuation poles in the stop band [72]. A much compact and light weight waveguide filter using two closely spaced

array of rectangular resonant apertures is reported in [73].

Several numerical and analytical methods are used to analyze the transverse discontinuity in a waveguide. Among all these methods, the most popular and powerful technique is the formulation of the problem in terms of an integral equation which is then solved using MoM. In 1972, Vu Khac [74] described the waveguide coupling problems by an integral equation. He solved this integral equation by expanding the field in terms of pulse functions and using point matching technique. Auda and Harrington [63] presented a solution for multiple inductive posts and diaphragms of arbitrary shape in a rectangular waveguide using moment method. The obstacles were approximated by a finite number of constant current strips or filaments. Electric dyadic Green's function was used to represent the field. Point matching technique was used in this analysis. In 1983, Auda and Harrington [75] used the equivalence principle to solve the waveguide junction problems. The fields were expressed using waveguide modes and a generalized network representation of the problem was obtained by using moment method. Sinha [76], in 1986, adopted the same procedure to analyze the discontinuities formed by multiple strips and apertures. A MoM analysis of two thick apertures in rectangular waveguide has been reported in [77]. In [78], a nonconventional T junction with thick apertures has been investigated using MoM. Later, in 1993, Yang and Omar [71] used a TE^{x}_{mn} modal expansion approach along with MoM to solve the scattering from multiple rectangular apertures. Recently, multilayered planar structures in the transverse cross-section of waveguide have been analyzed using generalized scattering matrix (GSM) in conjunction with MoM [79, 80].

It has been observed that MoM and mode matching methods exhibit an inherent phenomenon known as 'relative convergence', when used to solve waveguide discontinuity problems. Lee *et al.* [81], Mittra *et al.* [82] and Aksun *et al.* [83]

have reported a detailed study of the phenomenon and have proposed some useful guidance to solve this problem.

1.2.2 Coupling Through Apertures in an Infinite Conducting Screen

A thin conducting screen perforated with multiple apertures has a bandpass characteristic when illuminated by a plane wave of varying frequency and makes it a useful candidate for the design of frequency selective surfaces, electromagnetic band gap structures, bandpass radoms, artificial dielectric and antenna reflector or ground planes [84]. In some applications, apertures may cause undesirable coupling such as a crack or slit in the door of microwave oven or any RF transmitting equipment leading to the problems of electromagnetic compatibility and electromagnetic interference. A rejection band in the frequency response can also be realized using multiple apertures of different electromagnetic properties [85].

Photonic band gap structures are capable of reflecting the electromagnetic waves at a selected frequency and are conveniently constructed by using a periodic arrangement of dielectric materials. The dimension of the photonic band gap structures has to be a few times the wavelength of the point of total reflection which makes it very large for larger wavelength applications. Frequency selective surfaces are also capable of totally reflecting the incident electromagnetic wave. However, the frequency of total reflection is determined by the lateral dimension of unit cell and hence, it requires a larger surface area. It was shown in [86, 87] that the planar metallic fractal based upon H shape fractal geometry can reflect electromagnetic wave at a wavelength much larger than the dimension of sample size. The fractal pattern shows a quasi log periodic behavior for lower order iterations of fractal geometry, and the response becomes log periodic for large number

of iterations. It was pointed out in [88] that the increase in number of iterations downshifts the passbands, as well as, the stop bands. A fractal slit based on the same fractal geometry was analyzed in [89], where, it was pointed out that the fractal slit supports the subwavelength transmission of electromagnetic waves.

The general and rigorous formulation of coupling through apertures in conducting screen was made through the use of equivalence principle and equivalent magnetic currents [90]. The coupling through rectangular apertures in infinite screen was reported in [91]. An integral equation was obtained by using equivalence principle and image theory. The equation obtained in terms of the equivalent magnetic surface currents was solved using MoM. The aperture characteristics were presented in terms of transmission coefficient and transmission cross-section. Harrington and Aukland [92] analyzed the electromagnetic transmission through an aperture in a thick conducting screen using equivalence principle and MoM. The problem was decoupled into three independent problems consisting two half space regions and a closed cavity region. It was found that the apertures offer an exceptionally large transmission of electromagnetic energy at the resonant condition. Later, in 1982, Li and Harrington [93] analyzed the problem of electromagnetic transmission through an arbitrary shaped aperture in a thin conducting screen using the RWG functions [94]. The problem was solved using MoM and transmission through various arbitrarily shaped apertures were investigated.

Several other methods have also been investigated to analyze these problems. Lin *et al.* [95] used Babinet's principle in order to find the electric field distribution on the surface of aperture, as well as, in the far field region. Gluckstern, Li and Cooper [96] obtained the potential distribution on the surface of aperture using variational technique, where the effect of aperture in conducting screen was

expressed in terms of electric polarizability and magnetic susceptibility, using small aperture approximations. An approximate expression for the field distribution on the surface of a circular aperture was obtained in terms of circular aperture dimensions in [97]. Savov [98] analyzed the coupling between two circular apertures in an infinite screen using Fourier transform method and the reaction theorem. The effect of different polarizations on the coupling was also investigated. In 1994, Hajj and Kabalan [99] presented a characteristic mode solution of coupling through a rectangular aperture in an infinite conducting screen. The solution was obtained in terms of eigenvalues and eigenvectors using MoM. Kim and Eom [100] used the Fourier transform method in conjunction with mode matching technique to obtain the field distribution on the aperture surface. A rigorous analysis of coupling through apertures in conducting screen was analyzed using finite difference time domain (FDTD) method in [101].

The reflection and transmission coefficient characteristics of an infinite conducting screen perforated with multiple apertures have been investigated by many authors in the past. Chen [84] used MoM in conjunction with the Floquet space harmonics in order to solve the integral equation. The treatment of finite structure is also of practical interest. Early in 1984, Sarkar *et al.* [102] analyzed the problem of electromagnetic transmission through wire mesh covered aperture arrays by using MoM. Truncated periodic structures have been analyzed in [103, 104]. Recursive schemes have been successfully applied to analyze finite and non-periodic structures [105, 106]. In 1999, Park and Eom [107] presented a Fourier transform and mode matching method to analyze the electromagnetic scattering from multiple apertures of rectangular shapes. The numerical results were obtained for different number of apertures and angles of incidence. A similar analysis for multiple circular apertures were investigated in [108] using integral

transform and superposition principle. Anderson [109] carried out a method of moment formulation of electromagnetic transmission through multiple apertures using singular basis functions which greatly improved the convergence rate of the solution.

1.2.3 Rectangular Waveguide-fed Aperture Antennas

Waveguide-fed aperture antennas are widely used in radars, satellites, and phased arrays and as primary feed to parabolic reflectors. For an open-ended waveguide, the input matching is very poor. The input matching can be improved by either using a dielectric plug at the open end of the waveguide [110] or by using a resonant aperture [111]. Here, also multiple apertures of different dimension can be used to realize multiband waveguide radiators.

Several methods are used for the analysis of the rectangular waveguide fed aperture antennas. In [112], variational principle was used to analyze the radiation from aperture fed by a rectangular waveguide. The method proposed in this article was complicated even with the assumption of a single TE_{10} mode field distribution and numerical results were given only for guide wavelength up to $1\lambda_0$. Das [113] computed the admittance of an open-ended rectangular waveguide without flange. Jamieson and Rozzi [114] have given an nth order Rayleigh-Ritz variational solution to the flanged waveguide problem using longitudinal modes, LSE^y and LSE^x. MacPhie and Zaghloul [115] investigated the radiation from a rectangular waveguide terminated by an infinite flange and radiating into half space. The correlation functions of the TE and TM mode electric fields on the aperture and the conservation of complex power were used to obtain a correlation matrix from which the scattering matrix of the problem was derived. Baudrand *et al.* [116] presented a method based on the transverse operator. The boundary

condition in spectral domain was used to relate the electric and magnetic fields and the expansion of fields in TE and TM modes were used to obtain the admittance matrix. Mongiardo and Rozzi [117] analyzed the problem of radiation from flanged waveguide using singular integral approach. They used a basis function which satisfies the edge condition and therefore, improves the convergence of solution. Shen and MacPhie [118] presented a simple and effective method based on the extrapolation method. The half-space was approximated by a large waveguide with homogeneous filling with lossy dielectric and convergence data was obtained for different loss tangents. Based on the data, an extrapolation method was used to calculate the solution of original problem.

Many authors have used the integral equation approach with MoM or mode matching method to solve the aperture radiation from a flanged rectangular waveguide. The generalized network formulation for the aperture problem [90] based upon the equivalence principle and MoM was applied to waveguide with a thin window [119], finite phased arrays [120, 121], and reactively loaded waveguide arrays [122, 123]. Formulation in [119] and [123] used rooftop basis function, whereas the piecewise sinusoidal basis functions were used in [121]. In [122, 120] waveguide modes with sinusoidal aperture function were used.

1.2.4 Cavity-Backed Aperture Antenna

In satellite communication, the antennas are generally designed to have the radiation pattern directed towards the geostationary satellite. The antennas must be suitable for installation on mobile, as well as, stationary stations. Therefore, the antenna should be flat and flush mounted. A typical antenna is a planar microstrip antenna which suffers from feeder loss [124]. Slot antennas are used for their high efficiency and flush mounting nature. However, the slot antennas

suffer from their inherent bidirectional radiation pattern. In many applications, the antenna needs to be located in close proximity to earth, or conductive bodies, or to be integrated with the rest of the transceiver in a multilayered structure. In order to alleviate the adverse effects of the interaction between a slot antenna and the structure behind it, traditionally, a shallow cavity is used due to the unidirectional nature of the cavity-backed aperture antennas. When cavity-backed slot antenna is used as an array element, it produces small mutual effects between the elements and this makes it a suitable element in the design of large antenna array system, such as phased antenna array [125]. Also, the metallic cavity can serve as a heat sink to improve the heat dissipation. Generally, due to the resonance of the cavity, the cavity-backed aperture antenna suffers from low bandwidth. In [126], it has been shown that using two parallel parasitic slots, the bandwidth of the antenna can be increased. Several modifications have incorporated in the slot geometry in order to widen the bandwidth, such as, an S-type slot [127], meandered slot [128], rectangularly bent slots [129], and cross-loop slot [130]. Also, it has been found that the miniaturized slot antennas have higher bandwidth and efficiency compared to the electrically small wire antennas [131]. So, by using a cavity backing, efficient slot antennas can be designed [132]. A dual band antenna with three slots backed by a cavity has been proposed in [133] which uses a single feed.

In the earlier works presented in [134, 135, 136], the input characteristics of the antenna were calculated assuming a sinusoidal variation of voltage across the slot and the cavity was assumed as a short circuited section of rectangular waveguide. In 1989, Hadidi and Hamid [125] first presented a full wave analysis of cavity-backed slot antenna using MoM with the aid of dyadic Green's function in spatial domain to obtain the electric field on the aperture. In [137], the electric

field and the current distribution on a wide slot antenna backed by a cavity were analyzed using MoM.

The antenna fed by a coaxial probe is of practical interest and a detailed study of a probe-fed cavity-backed aperture antenna has been presented in [138, 139]. The effects of various parameters, such as, slot length and width, offset, probe locations on the input characteristics of the antenna were also investigated. In [140], the radiation pattern of a finite plane cavity-backed slot antenna was computed using MoM in conjunction with uniform geometrical theory of diffraction. A comprehensive comparison between the radiation pattern of cavity-backed antenna with infinite and finite planes was presented.

Lee *et al.* [141] presented a MoM formulation of a cavity-backed aperture antenna with dielectric overlay using the spectral domain Green's function. The integral equation was solved using both the entire domain and subdomain basis functions. Later in [142], a similar analysis was presented for the case of a cavity-backed aperture antenna with dielectric and magnetic overlays. The problem was formulated using modified magnetic field integral equation. A dyadic Green's function in space domain was used for the cavity region, whereas, the Green's function for overlayed medium was obtained in spectral domain. An MoM approach based on generalized network formulation and equivalence principle for the analysis of single as well as multiple apertures backed by cavity was proposed in [143].

In 1995, Despande *et al.* [144] analyzed the electromagnetic scattering by cylindrical cavity recessed in 3D metallic object. The equivalence principle was applied to decouple the problem and the field outside the cavity was expressed in terms of free space Green's function and equivalent surface magnetic currents. The fields inside the cavity were expressed using waveguide modal expansion

function. MoM is used to solve the coupled integral equation.

An FDTD approach for the analysis of cavity-backed aperture antenna was presented in [145]. The paper also deals with the problems encountered in the formulation and design of antennas using the FDTD method. The spectral leakage was decreased by means of time windows. However, it does not reduce the computation time and number of steps required for an estimation of input characteristics. The problem was analyzed with accurate estimation of input characteristics in [146].

In 1998, Rao *et al.* [147] presented a finite integral technique for the analysis of scattering from cavity-backed antennas. The cavity was subdivided into a number of triangular cylinders and constitutive material property was assigned to each cylinder. Unknown electric and magnetic fields were approximated by a specially designed basis function.

Nowadays, hybrid techniques are widely used in the analysis of complex electromagnetic problems. FDTD methods are used to model complex cavity-backed aperture geometries and the field radiated at a distance of few wavelengths is calculated using near-to-near field transformation. This requires a large amount of storage and computation time. So, this method is only applicable to relatively smaller geometries. On the other hand, finite element method (FEM) is simple and is very popular in the analysis of complex penetrable structures. This method results in a sparse matrix that can be stored efficiently and solved. However, it does not incorporate the Sommerfield radiation condition and hence requires discretization outside the source region, which limits the application of FEM in large structures. As compared to this, MoM incorporates the Sommerfield radiation condition through the use of appropriate Green's function and as a result, domain discretization can be kept minimum. However, this method is too

complicated for penetrable structures. Also, the MoM produces a dense matrix which requires a large storage for large complex structures. The unique feature of MoM is the knowledge of Green's function which limits its application to some regular shaped geometries whose Green's function is known. Additionally, the computation of admittance matrix involves slowly converging mode sum, which reduces the efficiency and increases the computation time. So, in order to take the advantage of individual methods, hybrid techniques have become very popular for the analysis of cavity-backed antennas. A hybrid FDTD-MoM method of analysis electromagnetic radiation from cavity-backed aperture antenna was proposed in [148]. The external and internal region of the cavity was modeled using MoM and FDTD, respectively, and the external radiation was computed using the reaction theory. In [149], a combined FEM-FDTD method was used to analyze the coupling of cavity-backed slot antennas.

The hybrid FEM-MoM [150, 151, 152, 153] is a very useful method for the analysis of cavity backed antennas. The problem is decoupled into two equivalent problems and the field inside the cavity is formulated using the finite element method and the field outside the cavity is calculated using the boundary integral approach. A detailed formulation of feeding structures is presented in [154, 155]. These papers also deal with the effect of finite ground plane on the antenna characteristics using geometrical theory of diffraction.

Chang, Kuo and Chung [156] analyzed a coaxial fed cavity-backed slot antenna. The equivalence principle was applied to find out the scattered field inside and outside of the cavity. The half space Green's function was used to calculate the field outside and Green's function inside the cavity was calculated using a parameter like extrapolation method. Complex Poynting theorem was used to calculate the input impedance.

A circuital approach to predict the behavior of electromagnetic field backed by a cavity has been proposed in [157]. The aperture is modeled as a stripline ended by a short and the metallic cavity is modeled as short circuited waveguide. The voltage on the apertures was calculated using Thevenen's equivalent circuit approach.

1.3 Motivation for Present Research

From the discussion presented in the previous section, it is evident that aperture coupling problem is an extremely important class of boundary value problem with wide ranging applications in antennas, waveguide filters and power dividers, frequency selective surfaces, and metamaterials. Apertures of both regular and irregular shapes, resonant and non-resonant, narrow and wide have been investigated.

In the past decade, application of fractal geometries has been proposed in the design of antenna elements, frequency selective surfaces and metamaterials, and the special characteristics offered by the fractals are widely acclaimed. Antennas using some of these fractal geometries are already available commercially. It is found that the use of fractal geometries leads to miniaturized, low profile antennas with moderate gain as compared to their Euclidean counterparts and the self-similarity property results in multiband antennas and FSS elements. What is missing, however, is the study of fractal geometries in aperture coupling problems. The present research work is primarily intended to initiate a study of the characteristics of fractal apertures in waveguides, conducting screens, and cavities.

During the course of this research work, several questions about the properties of fractal geometries are addressed and an effort has been made to answer these

questions by comparing the conventional fractal antennas and FSS elements with the present observations. A number of fractal geometries have been investigated in order establish the universal nature of the properties of fractal apertures. The investigations have been further extended to correlate the response of fractal apertures with different geometrical parameters and modifications. Some observations have also been made from an application point of view to show the effectiveness of the fractal apertures as compared to the existing multi aperture geometries.

1.4 Research Problems

The aim of the present research work is to investigate the properties of fractal apertures in different types of aperture coupling problems. Based on the aforementioned discussion on the requirement of multiband and reduced sized waveguide components and aperture antennas, and the efficiency of fractal geometries in the design of low profile, multiband and miniaturized antennas and FSS, the following problems have been taken up in this research work:

- Analysis of fractal apertures in the transverse cross-section of rectangular waveguide.
- Electromagnetic transmission through fractal apertures in an infinite conducting screen.
- Radiation from fractal apertures in an infinite screen fed by a rectangular waveguide.
- Analysis of cavity-backed fractal aperture antennas.

A major part of the analysis of above problems is the formulation using a suitable numerical procedure. The first three problems have been formulated using MoM and a hybrid FEM/MoM method has been used to analyze the problem of cavity-backed aperture antenna. Based on the formulation, MATLAB codes have been developed to find out different near-field and far-field parameters. The final task is to validate the numerical results which has been done by simulation on HFSS [158].

1.5 Organization of the Thesis

The work embodied in this thesis has been arranged as follows:

Chapter 2 presents the general MoM formulation of coupling between two arbitrary regions via multiple apertures of arbitrary shape and size. The formulation of matrix equation, geometric discretization, and the types of basis functions used are described. A detailed derivation of various matrix elements for different regions such as rectangular waveguide and free space regions, are presented. The last section of the chapter deals with computation of different measurement parameters.

In Chapter 3, properties of fractal apertures in the transverse cross-section of a rectangular waveguide have been presented. Some self-affine fractal structures based on the Sierpinski gasket and plus shape fractals are proposed and the effect of scale factor on the response is investigated. Self-similar structures like Hilbert curve, Koch curve and Minkowski fractals are shown to be efficient in reducing the resonant frequency of the aperture.

Chapter 4 investigates the electromagnetic transmission through fractal apertures in a thin infinite conducting screen. A number of fractal apertures, like Sierpinski gasket, Koch curve, Hilbert curve, Sierpinski carpet and Minkowski

fractal have been investigated. Numerical results are presented in terms of transmission coefficient and transmission cross-section for both parallel and perpendicular polarizations of incident wave. The effects of variation of angle of incidence on the frequency response of these fractal apertures are also investigated.

Chapter 5 combines the problems of chapter 3 and chapter 4 to analyze the problem of radiation from waveguide-fed fractal apertures in an infinite screen. The self-similarity and space-filling properties of fractals have been exploited to achieve multi-band radiation. Some self-affine fractal geometries, suitable for waveguide-fed apertures, have been proposed and investigated. It is shown that the scale factor of the fractal geometry can be used as a design parameter for controlling the resonant frequencies.

Chapter 6 deals with the characteristics of probe-fed cavity-backed fractal aperture antenna. A general formulation of the problem using hybrid FEM/MoM method is presented. The numerical results for input reflection coefficients and the far-field radiation pattern of the antenna are presented.

Chapter 7 summarizes the work with concluding remarks and outlines the possible future research directions inspired by the work presented here.

Chapter 2

METHOD OF MOMENT FORMULATION OF COUPLING THROUGH APERTURES

2.1 Introduction

Coupling between two regions via apertures is a classical problem in electromagnetic theory and finds wide applications in modern microwave technology ranging from waveguide filters, directional couplers, power dividers, slotted antenna arrays, cavity-backed aperture antennas to electromagnetic interference and compatibility. In general, the regions on opposite sides of apertures may be of different geometrical shape and electrical properties and also, the apertures may be of any arbitrary shape. Thus, it is desirable to formulate the problem in a manner such that dissimilar and diverse problems can be analyzed with as

little extra effort as possible.

In this chapter, a general mathematical formulation of the problem of coupling between two arbitrary regions through multiple arbitrarily shaped apertures is developed, based upon "*Generalized network formulation for aperture problems*" proposed by Harrington and Mautz [90]. The problem is first decoupled into two equivalent problems, one for each region, using equivalence principle. Enforcement of the boundary condition on tangential component of magnetic field over the aperture surfaces results in an operator equation in terms of unknown surface magnetic currents. The operator equation is then transformed into matrix equation using MoM, which is solved for the unknown surface magnetic currents. In order to obtain the matrix equation, the aperture surfaces are discretized and suitable basis functions need to be defined on each subsection. In the present work, two types of basis functions are used, namely, rooftop functions [119] for rectangular apertures and Rao-Wilton-Glisson (RWG) functions [94] for arbitrarily shaped apertures. The scattered fields are expressed in terms of Green's function and equivalent surface magnetic currents. The surface integrals involved in the computation of matrix elements are evaluated analytically for rectangular domains and numerically for triangular domains. Special treatment has been given for the calculation of singular integrals arising in the computation of integrals involving free space Green's function. The excitation vector elements are calculated considering two types of input excitations: a TE_{mn} mode is assumed to be incident for the waveguide problems, whereas, a uniform plane wave of arbitrary angle of incidence and polarization is considered for the coupling problems involving two half-space regions.

Once the matrix equation is solved, various near-field parameters, such as, scattering coefficient, transmission coefficient, aperture admittance, as well as,

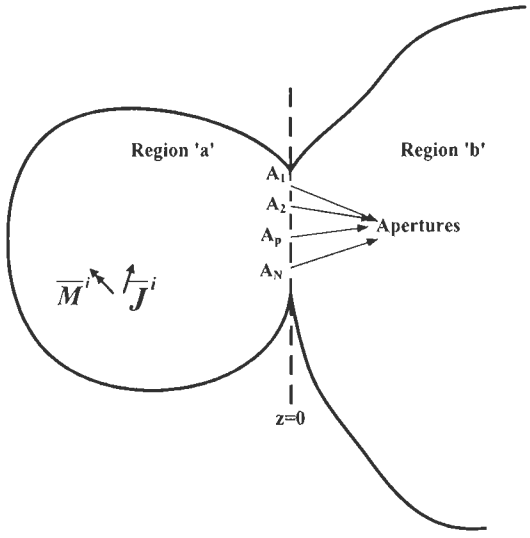

Figure 2.1: General problem geometry of coupling between two arbitrary regions.

far-field parameters, like, transmission cross-section, gain pattern can be computed.

2.2 General Formulation of Aperture Coupling Problem

Figure 2.1 shows the geometry of the general problem of coupling between two arbitrary regions through multiple apertures of arbitrary shape located in $z = 0$ plane. Impressed sources $\overrightarrow{J}^i$ and $\overrightarrow{M}^i$ are shown to be in region 'a', while region 'b' is assumed to be source free, although both the regions may contain impressed sources.

Equivalence principle is applied in order to decouple the original problem into two equivalent problems, one for each region, as shown in Fig. 2.2. The apertures are closed with perfect electric conductors (PEC) and equivalent surface magnetic

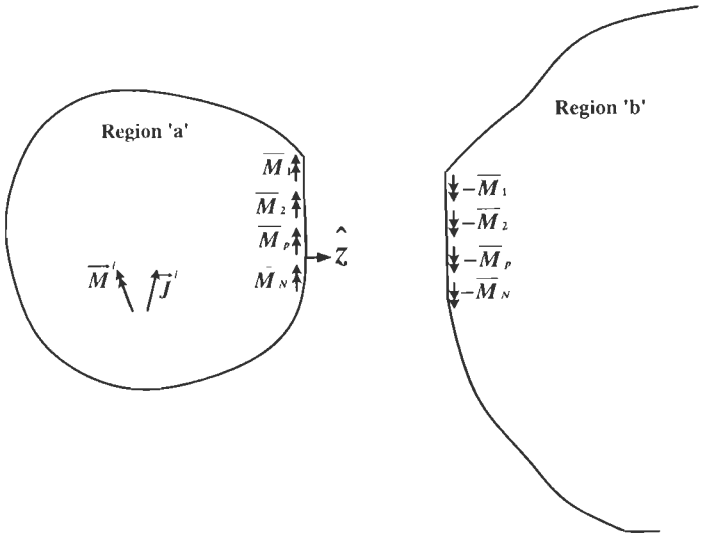

(a) model for region 'a' (b) model for region 'b'

Figure 2.2: Equivalent models.

currents $\overline{M}_1, \overline{M}_2, ..., \overline{M}_N$ are placed over the aperture surfaces in region 'a', where N is the total number of apertures. The equivalent surface magnetic current on the p^{th} aperture surface is defined as

$$\overline{M}_p = \hat{z} \times \overline{E}_p \tag{2.1}$$

where $\hat{z}$ is the unit outward normal to the p^{th} aperture and $\overline{E}_p$ is the electric field on the p^{th} aperture of original problem. Continuity of tangential component of electric field is ensured by placing $-\overline{M}_1, -\overline{M}_2, ..., -\overline{M}_N$ over the aperture surfaces in region 'b'. Hence, the original problem is decoupled into two equivalent problems, one for each region, which can be formulated independent of the other. The total field in region 'a' is due to the impressed sources $(\vec{J}^i, \vec{M}^i)$ and equivalent currents $\overline{M}_p$, $p = 1, 2, 3, ..., N$, whereas, the field in region 'b' is only due to the currents $-\overline{M}_p$ radiating in the presence of a complete conductor. Thus, the tangential component of magnetic field over the p^{th} aperture surface in region

'a' is given by

$$\overline{H}^a_{tp} = \overline{H}^i_{tp} + \overline{H}^a_{tp}(\overline{M}_1) + \overline{H}^a_{tp}(\overline{M}_2) + ... + \overline{H}^a_{tp}(\overline{M}_q) + ... + \overline{H}^a_{tp}(\overline{M}_N)$$

where $\overline{H}^i_{tp}$ is the tangential component of magnetic field over the p^{th} aperture surface due to the impressed sources and $\overline{H}^a_{tp}(\overline{M}_q)$ is the tangential component of magnetic field over the p^{th} aperture surface due to current $\overline{M}_q$ over the q^{th} aperture surface.

Similarly, tangential component of magnetic field over the p^{th} aperture in region 'b', denoted as $\overline{H}^b_{tp}$, is given by

$$\overline{H}^b_{tp} = \overline{H}^a_{tp}(-\overline{M}_1) + \overline{H}^a_{tp}(-\overline{M}_2) + ... + \overline{H}^a_{tp}(-\overline{M}_q) + ... + \overline{H}^a_{tp}(-\overline{M}_N)$$

Now, continuity of tangential component of magnetic field across the p^{th} aperture surface gives the basic operator equation

$$\overline{H}^a_{tp}(\overline{M}_1) + \overline{H}^a_{tp}(\overline{M}_2) + ... + \overline{H}^a_{tp}(\overline{M}_q) + ... + \overline{H}^a_{tp}(\overline{M}_N) + \overline{H}^b_{tp}(\overline{M}_1) + \overline{H}^b_{tp}(\overline{M}_2) + ... + \overline{H}^b_{tp}(\overline{M}_q) + ... + \overline{H}^b_{tp}(\overline{M}_N) = -\overline{H}^i_{tp} \quad (2.2)$$

The solution of (2.2) can be obtained by defining a set of basis functions $\{\overline{M}_{pn}, n = 1, 2, ..., N_p\}$ over the p^{th} aperture surface and expanding the magnetic current as

$$\overline{M}_p = \sum_{n=1}^{N_p} V_{pn}\overline{M}_{pn}, \quad p = 1, 2, 3, ..., N \quad (2.3)$$

where, V_{pn} are the unknown coefficients to be determined and N_p is the number of basis functions defined over the p^{th} aperture surface.

Substituting (2.3) in (2.2) and using the linearity of $\overline{H}_t$ operator, we obtain

$$\begin{aligned}
&\sum_{n=1}^{N_1} V_{1n}\overline{H}^a_{tp}(\overline{M}_{1n}) \;+\; \sum_{n=1}^{N_2} V_{2n}\overline{H}^a_{tp}(\overline{M}_{2n}) + \ldots + \\
&\qquad\qquad \sum_{n=1}^{N_q} V_{qn}\overline{H}^a_{tp}(\overline{M}_{qn}) + \ldots + \sum_{n=1}^{N_N} V_{Nn}\overline{H}^a_{tp}(\overline{M}_{Nn}) + \\
&\sum_{n=1}^{N_1} V_{1n}\overline{H}^b_{tp}(\overline{M}_{1n}) \;+\; \sum_{n=1}^{N_2} V_{2n}\overline{H}^b_{tp}(\overline{M}_{2n}) + \ldots + \\
&\qquad\qquad \sum_{n=1}^{N_q} V_{qn}\overline{H}^b_{tp}(\overline{M}_{qn}) + \ldots + \sum_{n=1}^{N_N} V_{Nn}\overline{H}^b_{tp}(\overline{M}_{Nn}) = -\overline{H}^i_{tp}
\end{aligned} \tag{2.4}$$

Now, we define the inner product as

$$\langle \overline{A}, \overline{B} \rangle = \iint_S \overline{A} \,.\, \overline{B}\; ds$$

and a set of testing functions $\{\overline{W}_{pm},\ p = 1, 2, 3, ..., N \text{ and } m = 1, 2, 3, ..., N_p\}$ over the p$^{\text{th}}$ aperture surface. Taking inner product of (2.4) with each of these testing functions, we obtain

$$\begin{aligned}
&\sum_{n=1}^{N_1} V_{1n}\left\langle \overline{W}_{pm}, \overline{H}^a_{tp}(\overline{M}_{1n})\right\rangle + \sum_{n=1}^{N_2} V_{2n}\left\langle \overline{W}_{pm}, \overline{H}^a_{tp}(\overline{M}_{2n})\right\rangle + \ldots + \\
&\sum_{n=1}^{N_q} V_{qn}\left\langle \overline{W}_{pm}, \overline{H}^a_{tp}(\overline{M}_{qn})\right\rangle + \ldots + \sum_{n=1}^{N_N} V_{Nn}\left\langle \overline{W}_{pm}, \overline{H}^a_{tp}(\overline{M}_{Nn})\right\rangle + \\
&\sum_{n=1}^{N_1} V_{1n}\left\langle \overline{W}_{pm}, \overline{H}^b_{tp}(\overline{M}_{1n})\right\rangle + \sum_{n=1}^{N_2} V_{2n}\left\langle \overline{W}_{pm}, \overline{H}^b_{tp}(\overline{M}_{2n})\right\rangle + \ldots + \\
&\sum_{n=1}^{N_q} V_{qn}\left\langle \overline{W}_{pm}, \overline{H}^b_{tp}(\overline{M}_{qn})\right\rangle + \ldots + \sum_{n=1}^{N_N} V_{Nn}\left\langle \overline{W}_{pm}, \overline{H}^b_{tp}(\overline{M}_{Nn})\right\rangle \\
&\qquad\qquad = \left\langle -\overline{W}_{pm}, \overline{H}^i_{tp}\right\rangle
\end{aligned} \tag{2.5}$$

Equation (2.5) is a set of algebraic equations which can be put in matrix form by defining the following matrices and vectors:

1. Admittance matrix for region 'a', denoted as $\mathbf{Y}^a$

$$[\mathbf{Y^a}] = \begin{bmatrix} \mathbf{Y}^a_{11} & \mathbf{Y}^a_{12} & \mathbf{Y}^a_{13} & \cdots & \mathbf{Y}^a_{1N} \\ \mathbf{Y}^a_{21} & \mathbf{Y}^a_{22} & \mathbf{Y}^a_{23} & \cdots & \mathbf{Y}^a_{2N} \\ \vdots & \vdots & \vdots & \ddots & \vdots \\ \mathbf{Y}^a_{N1} & \mathbf{Y}^a_{N2} & \mathbf{Y}^a_{N3} & \cdots & \mathbf{Y}^a_{NN} \end{bmatrix}_{(N_1+N_2+...+N_N)\times(N_1+N_2+...+N_N)} \tag{2.6}$$

where each sub-matrix $\mathbf{Y}^a_{pq}$ denotes the coupling matrix between p^{th} and q^{th} aperture and can be expressed as

$$\mathbf{Y}^a_{pq} = [- < \overline{W}_{pm}, \overline{H}^a_{tp}(\overline{M}_{qn}) >]_{N_p \times N_q} \tag{2.7}$$

The mn^{th} element of the sub-matrix $\mathbf{Y}^a_{pq}$ is given by

$$(Y^a_{pq})_{mn} = -\iint_{A_m} \overline{W}_{pm} \cdot \overline{H}^a_{tp}(\overline{M}_{qn})\, ds \tag{2.8}$$

It should be noted that, the matrix defined in (2.8) is obtained by assuming that the basis functions are numbered independently over each aperture region. Instead, if the functions are numbered continuously over the apertures, then an element of the matrix Y^a can be expressed as

$$\begin{aligned} Y^a_{mn} &= \left[-\langle \overline{W}_m, \overline{H}^a_t(\overline{M}_n)\rangle\right]_{N_T \times N_T} \\ &= -\iint_{A_m} \overline{W}_m \cdot \overline{H}^a_t(\overline{M}_n)\, ds \end{aligned} \tag{2.9}$$

where, A_m denotes the sub-sectional area over which the m^{th} testing function is non-zero and N_T denotes the total number of expansion functions.

2. Admittance matrix for region 'b', denoted as $\mathbf{Y}^b$, is also of the same form as (2.6). Similar to (2.8), an element of admittance matrix for region 'b' can be expressed as

$$(Y^b_{pq})_{mn} = -\iint_{A_m} \overline{W}_{pm} \cdot \overline{H}^b_{tp}(\overline{M}_{qn})\, ds \tag{2.10}$$

3. An excitation vector, $\overrightarrow{I}^i$ as

$$\overrightarrow{I}^i = \left[\mathbf{I}_1^i \quad \mathbf{I}_2^i \quad \cdots \quad \mathbf{I}_N^i\right]^T_{1\times(N_1+N_2+\ldots+N_N)} \tag{2.11}$$

where

$$\mathbf{I}_p^i = [< \overline{W}_{pm}, \overline{H}_{tp}^i >]_{N_p\times 1} \tag{2.12}$$

An element of the excitation vector can be expressed as

$$(I_p^i)_m = \iint_{A_m} \overline{W}_{pm} \cdot \overline{H}_{tp}^i \, ds \tag{2.13}$$

Again, if the expansion functions are numbered continuously over the aperture surfaces, then (2.13) can be written as

$$(I^i)_m = \iint_{A_m} \overline{W}_m \cdot \overline{H}_t^i \, ds \tag{2.14}$$

4. A coefficient vector $\overrightarrow{V}$ as

$$\overrightarrow{V} = \left[\mathbf{V}_1 \quad \mathbf{V}_2 \quad \cdots \mathbf{V}_N\right]^T_{1\times(N_1+N_2+\ldots+N_N)} \tag{2.15}$$

where

$$\mathbf{V}_p = [V_{pm}]_{N_p\times 1} \tag{2.16}$$

Therefore, (2.5) can be expressed as

$$[\mathbf{Y}^a + \mathbf{Y}^b]\overrightarrow{V} = \overrightarrow{I}^i \tag{2.17}$$

It can be seen from (2.8) and (2.10) that the aperture admittance matrix $[Y^a]$ depends only upon the parameters of region 'a' while $[Y^b]$ depends only upon the parameters of region 'b'. Thus, each of these matrices can be computed independent of the other and by suitably combining them, a host of altogether different problems can be analyzed.

The equivalent models for the geometries analyzed in this dissertation are presented in the following subsections.

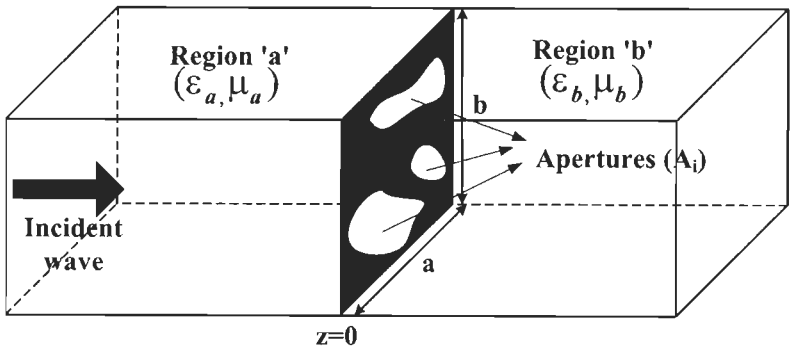

Figure 2.3: Multiple apertures in the transverse cross-section of a rectangular waveguide.

2.2.1 Fractal Diaphragm in Transverse Cross-section of Rectangular Waveguide

A perfectly conducting thin diaphragm perforated with multiple arbitrarily shaped apertures placed in the transverse cross-section of a rectangular waveguide is shown in Fig. 2.3. An electromagnetic field is assumed to be incident from left. Fig. 2.4 shows the equivalent models for region 'a' and region 'b'. Both the regions are semi-infinite rectangular waveguide sections short circuited at one end. Hence, the matrices $[Y^a]$ and $[Y^b]$ can be calculated by considering semi-infinite rectangular waveguides.

2.2.2 Coupling Between Two Half-spaces Via Fractal Apertures

Fig. 2.5 shows the problem of two half-spaces of arbitrary electrical parameters coupled through multiple apertures in an infinite conducting screen. A plane electromagnetic wave is assumed to incident on the apertures in region 'a'. Fig 2.6 shows the equivalent models for region 'a' and 'b'. Thus, the matrix $[Y^a]$ and

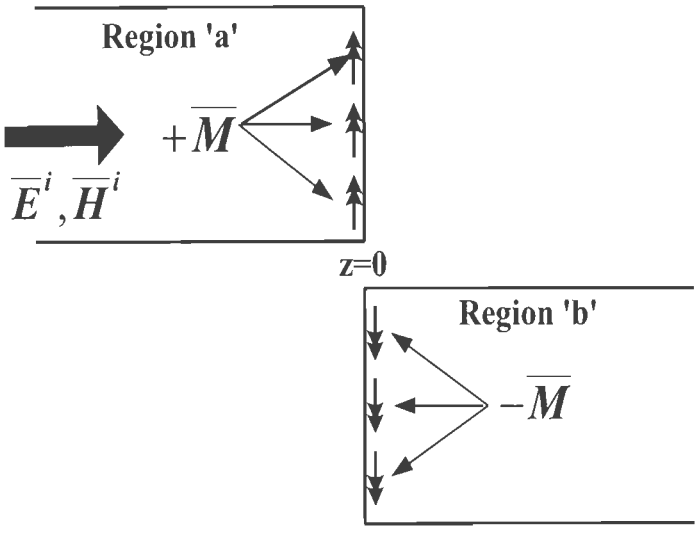

Figure 2.4: Equivalent models.

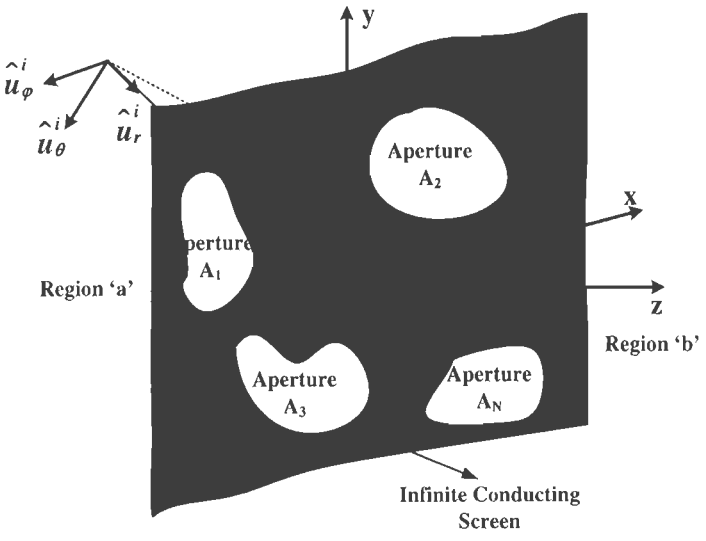

Figure 2.5: Coupling between two half-space regions through multiple apertures.

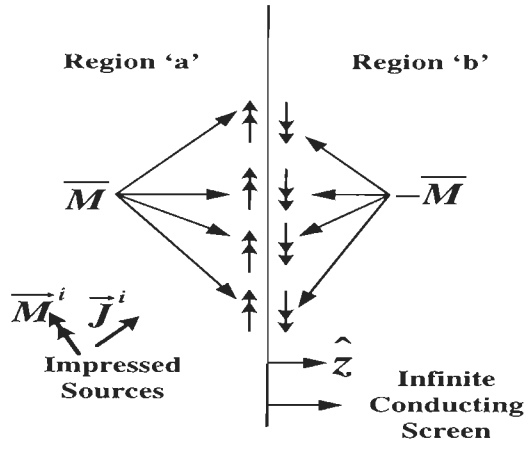

Figure 2.6: Equivalent model.

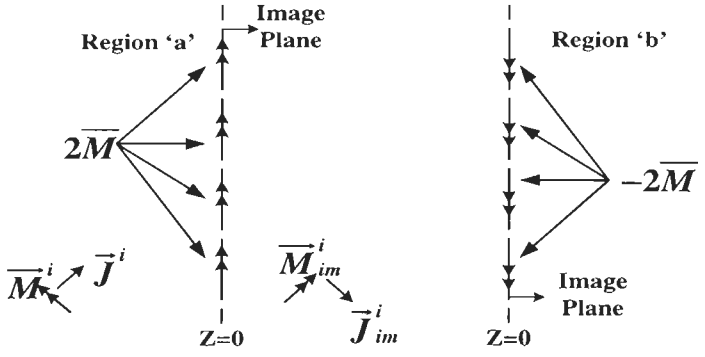

Figure 2.7: Equivalent models after the application of image theory.

$[Y^b]$ can be determined by considering a current $2\overline{M}$ radiating in free space as shown in Fig. 2.7.

2.2.3 Rectangular Waveguide-fed Multiple Apertures in Infinite Conducting Screen

The general problem geometry of rectangular waveguide-fed multiple apertures in an infinite conducting screen is shown in Fig. 2.8. The apertures are placed at

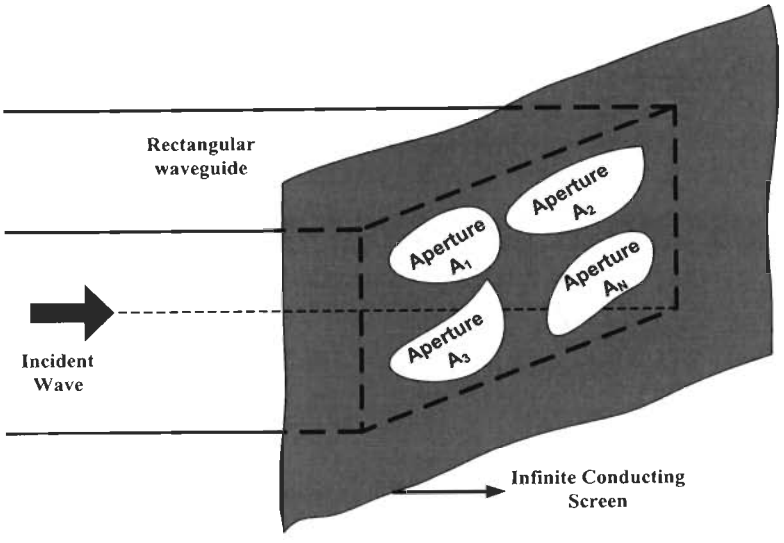

Figure 2.8: Waveguide-fed multiple apertures in an infinite screen.

$z = 0$ and a TE_{mn} mode is assumed to incident in the rectangular waveguide. Fig. 2.9 shows the equivalent problem geometries for region 'a' and region 'b', Thus, the elements of matrix $[Y^a]$ are computed by considering a semi-infinite rectangular waveguide short circuited at one end and the elements of matrix $[Y^b]$ are computed by considering a current $-2\overline{M}$ radiating into the free space. Here, the magnetic field $(\overline{H}_t^i)$ is twice than that of incident magnetic field due to the presence of complete conductor at $z = 0$.

2.2.4 Radiation From Multiple Apertures Backed by a Cavity

The general problem geometry of multiple apertures backed by a rectangular cavity is shown in Fig. 2.10. Impressed sources are assumed to be located inside the cavity. The apertures are located at $z = 0$ plane. Fig. 2.11 shows the equivalent model of the aperture antenna. The problem is analyzed using

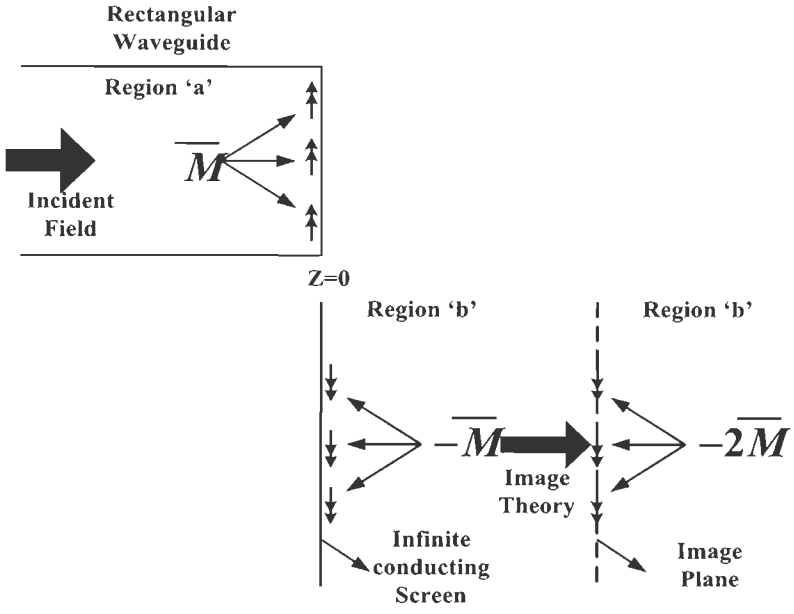

Figure 2.9: Equivalent models.

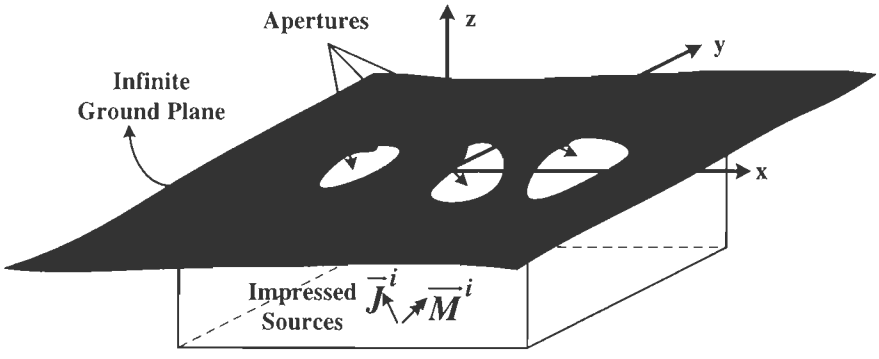

Figure 2.10: Cavity-backed aperture antenna.

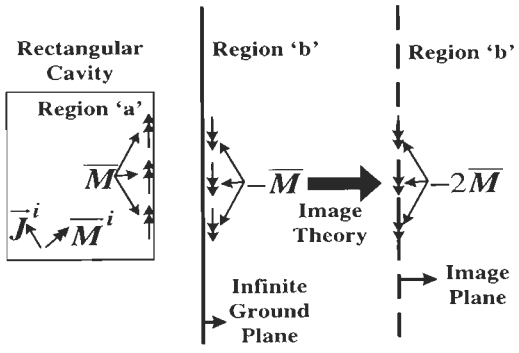

Figure 2.11: Equivalent models.

the finite element-boundary integral (FE-BI) method, in which the field inside the cavity is computed using the finite element method and the field above the ground plane is calculated using MoM by considering a current $-2\overline{M}$ radiating in free space.

2.3 Basis Functions

An important step in MoM solution is the choice of basis functions because it greatly affects the convergence and accuracy of the solution [83, 159]. Although, there can be an infinite number of possible sets of basis functions, only a few sets of basis functions are required practically to obtain accurate results. The basis functions are categorized as whole domain and subdomain basis functions. The whole domain basis functions exist over the entire surface and are applicable to the problems with regular geometries and where an approximate distribution of the unknown function is known *a priori*. On the other hand, subdomain basis functions offer greater flexibility to model arbitrary geometries and more complex problems. Piecewise sinusoidal functions, rooftop functions and Rao-Wilton-Glisson (RWG) functions are widely used in the MoM analysis. In the

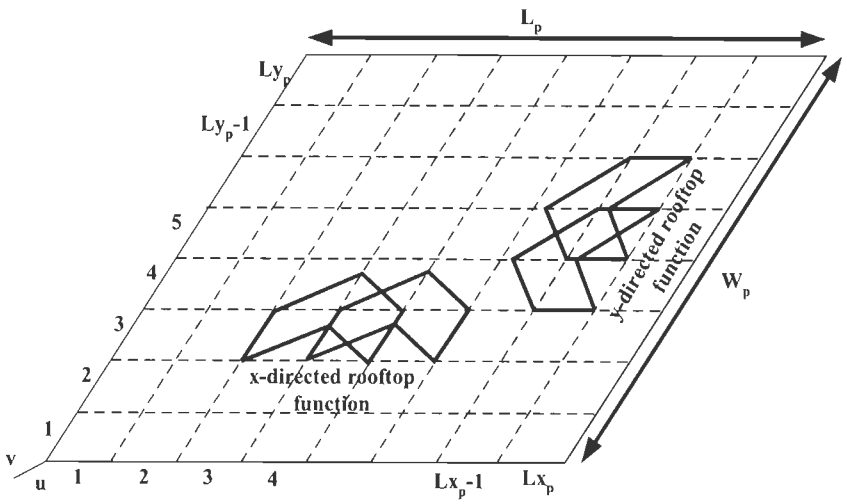

Figure 2.12: Geometry of x- and y-directed Rooftop functions.

present analysis, rooftop functions and RWG functions have been used. Brief introduction to these two basis functions are given in the following subsections.

2.3.1 Rooftop Functions

The rectangular apertures are divided into a number of rectangular subareas. Let us assume that pth aperture has a length L_p and width W_p and is subdivided into L_{xp} and L_{yp} number of subsections along x- and y-directions, respectively, as shown in Fig. 2.12. Let (x_{cp}, y_{cp}) is the center of pth aperture. Rooftop functions have a triangular variation in one direction and a pulse variation in other direction. The x- and y-directed components of rooftop functions $\overline{M}_{pm}$ are expressed as

$$\overline{M}^{x}_{p\ u+(v-1)(L_{xp}-1)} = \hat{x}T^{x}_{u}(x - x_{cp} + \frac{L_p}{2})\ P^{y}_{v}(y - y_{cp} + \frac{W_p}{2}) \tag{2.18}$$

$$u = 1, 2, 3, ..., (L_{xp} - 1)$$

$$v = 1, 2, 3, ..., L_{yp}$$

Similarly,

$$\overline{M}^{y}_{p\ u+(v-1)(L_{xp})} = \hat{y}T^{y}_{v}(y - y_{cp} + \frac{W_p}{2})\ P^{x}_{u}(x - x_{cp} + \frac{L_p}{2}) \tag{2.19}$$

$$\begin{aligned} u &= 1, 2, 3, ..., L_{xp} \\ v &= 1, 2, 3, ..., (L_{yp} - 1) \end{aligned}$$

where T and P denote the triangular and pulse functions, respectively. The triangular and pulse functions are defined as

$$T^{x}_{u}(x - x_p) = \begin{cases} \frac{x - x_p - (u-1)\triangle x_p}{\triangle x_p}, & x_p + (u-1)\triangle x_p \leq x \leq x_p + u\triangle x_p \\ \frac{(u+1)\triangle x_p - x + x_p}{\triangle x_p}, & x_p + u\triangle x_p \leq x \leq x_p + (u+1)\triangle x_p \\ 0, & \text{otherwise} \end{cases} \tag{2.20}$$

and

$$P^{x}_{u}(x - x_p) = \begin{cases} 1, & x_p + (u-1)\triangle x_p \leq x \leq x_p + u\triangle x_p \\ 0, & \text{otherwise} \end{cases} \tag{2.21}$$

where

$$\begin{aligned} x_p &= x_{cp} - \frac{L_p}{2} \\ y_p &= y_{cp} - \frac{W_p}{2} \end{aligned} \tag{2.22}$$

Similar, expressions may be written for T^{y}_{v} and P^{y}_{v}.

2.3.2 RWG Functions

The rooftop functions presented in the previous subsection are suitable for modeling rectangular regions. For modeling surfaces of arbitrary shape, however, RWG functions are more suitable. The aperture surfaces are discretized into triangular subareas and a pair of such triangles are shown in Fig. 2.13.

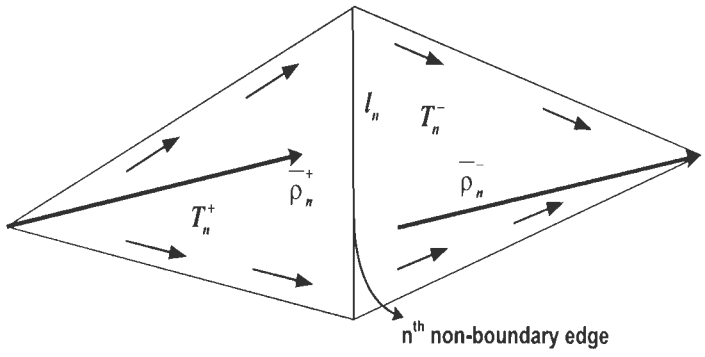

Figure 2.13: RWG basis function.

For any two triangles pair $T_n^{\pm}$, having areas $A_n^{\pm}$, the nth RWG function is defined as

$$\overline{M}_n = \begin{cases} \frac{l_n}{2A_n^+}\overline{\rho}_n^+, & \bar{r} \text{ in } A_n^+ \\ \frac{l_n}{2A_n^-}\overline{\rho}_n^-, & \bar{r} \text{ in } A_n^- \end{cases} \tag{2.23}$$

where l_n is the length of nth common edge shared by $T_n^{\pm}$, $\rho_n^+ = (\bar{r} - \bar{r}_n^+)$ is the vector drawn from free vertex of T_n^+ to the observation point, $\rho_n^- = (\bar{r}_n^- - \bar{r})$ is the vector drawn from observation point to the free vertex of T_n^- and $\bar{r}$ is the global position vector. The function is zero outside the triangle pair.

2.4 Evaluation of Admittance Matrix Elements

In this section, the evaluation of admittance matrix elements for different regions, such as, a semi-infinite rectangular waveguide and half-space region, has been presented.

2.4.1 Semi-infinite Rectangular Waveguide

The first region considered here is a semi-infinite rectangular waveguide short circuited at $z = 0$ with equivalent surface current density $\overline{M}$ over the aperture

region (Fig. 2.4). Following Galerkin's method, ijth element of admittance matrix, defined in (2.8), can be expressed as

$$(Y_{pq}^{wg})_{ij} = -\iint_{A_i} \overline{M}_{pi} \cdot \overline{H}_{tp}^{wg}(\overline{M}_{qj})\, ds \tag{2.24}$$

where the superscript 'wg' is used to denote the waveguide region. Here, $\overline{M}_{pi}$ denotes the ith testing function defined over the pth aperture surface, and $\overline{M}_{qj}$ defines the the jth expansion function defined over the qth aperture surface. The integration is performed over the sub-sectional area (A_i) of pth aperture surface over which the ith testing function is non-zero. $\overline{H}_{tp}(\overline{M}_{qj})$ is the tangential component of magnetic field over the pth aperture surface due to jth expansion function $\overline{M}_{qj}$ defined over the qth aperture surface. The magnetic field produced by a current element $\overline{M}_{qj}$ is expressed in terms of the magnetic dyadic Green's function ($\overline{\overline{G}}(\overline{r}|\overline{r}')$) for a semi-infinite rectangular waveguide as

$$\overline{H}_{tp}^{wg}(\overline{M}_{qj}) = -j\omega\varepsilon \iint_{A_j} \overline{\overline{G}}(\overline{r} \mid \overline{r}') \cdot \overline{M}_{qj}\, ds' \tag{2.25}$$

Here, A_j denotes the sub-sectional area of qth aperture surface over which jth basis function is non-zero. Primed and unprimed coordinates denote the source and observation points, respectively.

In general, the magnetic dyadic Green's function for a semi-infinite rectangular waveguide has nine components. Here, we are concerned only about the four transverse components which are expressed as [160]

$$G_{xx}(\overline{r}|\overline{r}') = \sum_{m=0}^{\infty}\sum_{n=0}^{\infty} \frac{\varepsilon_{0m}\varepsilon_{0n}}{\gamma_{mn}abk^2}\left[k^2 - \left(\frac{m\pi}{a}\right)^2\right]\varphi_x(x,y)\varphi_x(x',y') \tag{2.26}$$

$$G_{xy}(\overline{r}|\overline{r}') = -\sum_{m=0}^{\infty}\sum_{n=0}^{\infty} \frac{\varepsilon_{0m}\varepsilon_{0n}}{\gamma_{mn}abk^2}\left(\frac{m\pi}{a}\right)\left(\frac{n\pi}{b}\right)\varphi_x(x,y)\varphi_y(x',y') \tag{2.27}$$

$$G_{yx}(\overline{r}|\overline{r}') = -\sum_{m=0}^{\infty}\sum_{n=0}^{\infty}\frac{\varepsilon_{0m}\varepsilon_{0n}}{\gamma_{mn}abk^2}\left(\frac{m\pi}{a}\right)\left(\frac{n\pi}{b}\right)\varphi_y(x,y)\varphi_x(x',y') \tag{2.28}$$

$$G_{yy}(\overline{r}|\overline{r}') = \sum_{m=0}^{\infty}\sum_{n=0}^{\infty}\frac{\varepsilon_{0m}\varepsilon_{0n}}{\gamma_{mn}abk^2}\left[k^2-\left(\frac{n\pi}{b}\right)^2\right]\varphi_y(x,y)\varphi_y(x',y') \tag{2.29}$$

where

$$\gamma_{mn} = \sqrt{(m\pi/a)^2+(n\pi/b)^2-k^2}, \quad k=\omega\sqrt{\mu\epsilon}$$

and

$$\varepsilon_{0p} = \begin{cases} 1, & p=0 \\ 2, & p>0 \end{cases}$$

The functions $\varphi_x(x,y)$ and $\varphi_y(x,y)$ are defined as

$$\varphi_x(x,y) = \sin\left(\frac{m\pi x}{a}\right)\cos\left(\frac{n\pi y}{b}\right) \tag{2.30}$$

$$\varphi_y(x,y) = \cos\left(\frac{m\pi x}{a}\right)\sin\left(\frac{n\pi y}{b}\right) \tag{2.31}$$

Substituting (2.25) in (2.24), we obtain

$$(Y_{pq}^{wg})_{ij} = j\omega\varepsilon\iint_{A_i}\iint_{A_j}\overline{M}_{pi}(\overline{r})\ .\ \overline{\overline{G}}(\overline{r}\mid\overline{r}')\ .\ \overline{M}_{qj}(\overline{r}')\ ds'\ ds \tag{2.32}$$

Since, the functions $\overline{M}_{pj}$ and $\overline{M}_{qj}$ can be resolved into x and y components, the admittance matrix consists of four sub-matrices as

$$\left[Y_{pq}^{wg}\right] = \begin{bmatrix}\left[(Y_{pq}^{wg})^{xx}\right] & \left[(Y_{pq}^{wg})^{xy}\right] \\ \left[(Y_{pq}^{wg})^{yx}\right] & \left[(Y_{pq}^{wg})^{yy}\right]\end{bmatrix} \tag{2.33}$$

where each submatrix can be expressed as

$$(Y_{pq}^{wg})_{ij}^{xx} = j\omega\varepsilon\iint_{A_i}\iint_{A_j}M_{pi}^{x}(\overline{r})G_{xx}(\overline{r}\mid\overline{r}')M_{qj}^{x}(\overline{r}')\ ds'\ ds \tag{2.34}$$

$$(Y_{pq}^{wg})_{ij}^{xy} = j\omega\varepsilon \iint_{A_i} \iint_{A_j} M_{pi}^{x}(\bar{r}) G_{xy}(\bar{r} \mid \bar{r}') M_{qj}^{y}(\bar{r}')\, ds'\, ds \tag{2.35}$$

$$(Y_{pq}^{wg})_{ij}^{yx} = j\omega\varepsilon \iint_{A_i} \iint_{A_j} M_{pi}^{y}(\bar{r}) G_{yx}(\bar{r} \mid \bar{r}') M_{qj}^{x}(\bar{r}')\, ds'\, ds \tag{2.36}$$

$$(Y_{pq}^{wg})_{ij}^{yy} = j\omega\varepsilon \iint_{A_i} \iint_{A_j} M_{pi}^{y}(\bar{r}) G_{yy}(\bar{r} \mid \bar{r}') M_{qj}^{y}(\bar{r}')\, ds'\, ds \tag{2.37}$$

Substituting (2.26) in (2.34) and separating the integrals over primed and unprimed coordinates, an element of sub-matrix $[(Y_{pq}^{wg})^{xx}]$ can be expressed as

$$(Y_{pq}^{wg})_{ij}^{xx} = j\omega\varepsilon \sum_{m=0}^{\infty}\sum_{n=0}^{\infty} \frac{\varepsilon_{0m}\varepsilon_{0n}}{\gamma_{mn} abk^2} \left[k^2 - \left(\frac{m\pi}{a}\right)^2\right]$$
$$\iint_{A_i} M_{pi}^{x} \sin\left(\frac{m\pi x}{a}\right) \cos\left(\frac{n\pi y}{b}\right) dx\, dy \iint_{A_j} M_{qj}^{x} \sin\left(\frac{m\pi x'}{a}\right) \cos\left(\frac{n\pi y'}{b}\right) dx'\, dy' \tag{2.38}$$

Similarly, other three components can be expressed as

$$(Y_{pq}^{wg})_{ij}^{xy} = -j\omega\varepsilon \sum_{m=0}^{\infty}\sum_{n=0}^{\infty} \frac{\varepsilon_{0m}\varepsilon_{0n}}{\gamma_{mn} abk^2} \left(\frac{m\pi}{a}\right)\left(\frac{n\pi}{b}\right)$$
$$\iint_{A_i} M_{pi}^{x} \sin\left(\frac{m\pi x}{a}\right) \cos\left(\frac{n\pi y}{b}\right) dx\, dy \iint_{A_j} M_{qj}^{y} \cos\left(\frac{m\pi x'}{a}\right) \sin\left(\frac{n\pi y'}{b}\right) dx'\, dy' \tag{2.39}$$

$$(Y_{pq}^{wg})_{ij}^{yx} = -j\omega\varepsilon \sum_{m=0}^{\infty}\sum_{n=0}^{\infty} \frac{\varepsilon_{0m}\varepsilon_{0n}}{\gamma_{mn} abk^2} \left(\frac{m\pi}{a}\right)\left(\frac{n\pi}{b}\right)$$
$$\iint_{A_i} M_{pi}^{y} \cos\left(\frac{m\pi x}{a}\right) \sin\left(\frac{n\pi y}{b}\right) dx\, dy \iint_{A_j} M_{qj}^{y} \sin\left(\frac{m\pi x'}{a}\right) \cos\left(\frac{n\pi y'}{b}\right) dx'\, dy' \tag{2.40}$$

$$(Y_{pq}^{wg})_{ij}^{yy} = j\omega\varepsilon \sum_{m=0}^{\infty}\sum_{n=0}^{\infty} \frac{\varepsilon_{0m}\varepsilon_{0n}}{\gamma_{mn} abk^2} \left[k^2 - \left(\frac{n\pi}{b}\right)^2\right]$$
$$\iint_{A_i} M_{pi}^{y} \cos\left(\frac{m\pi x}{a}\right) \sin\left(\frac{n\pi y}{b}\right) dx\, dy \iint_{A_j} M_{qj}^{y} \cos\left(\frac{m\pi x'}{a}\right) \sin\left(\frac{n\pi y'}{b}\right) dx'\, dy' \tag{2.41}$$

These surface integrals are calculated either analytically or by numerical quadrature method depending upon the domain of integration. In the following subsections, the computation of such integrals for rectangular and triangular domains is presented.

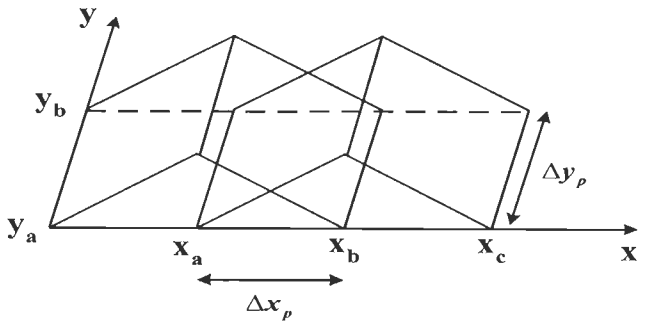

Figure 2.14: Geometry of ith x-directed rooftop function.

Computation of admittance matrix using Rooftop functions

Let us consider ith x-directed rooftop function as shown in Fig. 2.14. Here, the geometrical variables are defined as

$$\begin{aligned} x_a &= x_p + (u-1)\Delta x_p \\ x_b &= x_p + u\Delta x_p \\ x_c &= x_p + (u+1)\Delta x_p \\ y_a &= y_p + (v-1)\Delta y_p \\ y_b &= y_p + v\Delta y_p \end{aligned}$$

where

$$\begin{aligned} u &= 1, 2, 3, ..., (L_{xp} - 1) \\ v &= 1, 2, 3, ..., L_{yp} \end{aligned}$$

Substituting the expression of x-directed rooftop function from (2.18) and considering the origin at the center of waveguide cross-section, the integral in (2.38)

can be expressed as

$$\begin{aligned} I_p &= \iint_{A_i} M_{pi}^x \sin\left[\frac{m\pi}{a}(x+\frac{a}{2})\right] \cos\left[\frac{n\pi}{b}(y+\frac{b}{2})\right] \, dxdy \\ &= \frac{1}{\Delta x_p}\int_{y_a}^{y_b} \cos\left[\frac{n\pi}{b}(y+\frac{b}{2})\right] \, dy \times \\ &\quad \left\{\int_{x_a}^{x_b}(x-x_a)\sin\left[\frac{m\pi}{a}(x+\frac{a}{2})\right] \, dx + \int_{x_b}^{x_c}(x_c-x)\sin\left[\frac{m\pi}{a}(x+\frac{a}{2})\right] \, dx\right\} \end{aligned} \tag{2.42}$$

After computing the integrals, I_p is obtained as

$$\begin{aligned} I_p = (\Delta x_p)(\Delta y_p)\left[\frac{\sin(m\pi\Delta x_p/2a)}{(m\pi\Delta x_p/2a)}\right]^2 \left[\frac{\sin(n\pi\Delta y_p/2b)}{(n\pi\Delta y_p/2b)}\right] \\ \sin\left[\frac{m\pi}{a}(x_p+u\Delta x_p)\right]\cos\left[\frac{n\pi}{b}(y_p+(v-\frac{1}{2})\Delta y_p)\right] \end{aligned} \tag{2.43}$$

where x_p and y_p are redefined as

$$\begin{aligned} x_p &= x_{cp} - \frac{L_p}{2} + \frac{a}{2} \\ y_p &= y_{cp} - \frac{W_p}{2} + \frac{b}{2} \end{aligned} \tag{2.44}$$

Similarly, the integral over the q$^{\text{th}}$ aperture is obtained as

$$\begin{aligned} I_q = (\Delta x_q)(\Delta y_q)\left[\frac{\sin(m\pi\Delta x_q/2a)}{(m\pi\Delta x_q/2a)}\right]^2 \left[\frac{\sin(n\pi\Delta y_q/2b)}{(n\pi\Delta y_q/2b)}\right] \\ \sin\left[\frac{m\pi}{a}(x_q+s\Delta x_q)\right]\cos\left[\frac{n\pi}{b}(y_q+(t-\frac{1}{2})\Delta y_q)\right] \end{aligned} \tag{2.45}$$

Hence, an element of xx-component of admittance matrix is given by

$$\begin{aligned} (Y_{pq}^{wg})_{ij}^{xx} = j\omega\varepsilon \sum_{m=0}^{\infty}\sum_{n=0}^{\infty} \frac{\epsilon_{0m}\epsilon_{0n}}{\gamma_{mn}abk^2}[k^2-(\frac{m\pi}{a})^2] \, \Delta_{xy} \, S_{XP}^2 \, S_{YP} \, S_{XQ}^2 \, S_{YQ} \\ \sin\left[\frac{m\pi}{a}(x_p+u\Delta x_p)\right]\cos\left[\frac{n\pi}{b}(y_p+(v-\frac{1}{2})\Delta y_p)\right] \\ \sin\left[\frac{m\pi}{a}(x_q+s\Delta x_q)\right]\cos\left[\frac{n\pi}{b}(y_q+(t-\frac{1}{2})\Delta y_q)\right] \end{aligned} \tag{2.46}$$

where,

$$\begin{aligned} & & u &= 1, 2, 3, ..., (Lx_p - 1) \\ i &= u + (v-1)(Lx_p - 1) & & \\ & & v &= 1, 2, 3, ..., Ly_p \\ & & s &= 1, 2, 3, ..., (Lx_q - 1) \\ j &= s + (t-1)(Lx_q - 1) & & \\ & & t &= 1, 2, 3, ..., Ly_q \end{aligned} \tag{2.47}$$

Similarly, the other three components of the admittance matrix can be expressed as

$$\begin{aligned} (Y_{pq}^{wg})_{ij}^{xy} = -j\omega\varepsilon \sum_{m=0}^{\infty}\sum_{n=0}^{\infty} \frac{\epsilon_{0m}\epsilon_{0n}}{\gamma_{mn}abk^2}(\frac{m\pi}{a})(\frac{n\pi}{b})\ \Delta_{xy}\ S_{XP}^2\ S_{YP}\ S_{XQ}\ S_{YQ}^2 \\ \sin\left[\frac{m\pi}{a}(x_p + u\Delta x_p)\right] \cos\left[\frac{n\pi}{b}(y_p + (v-\frac{1}{2})\Delta y_p)\right] \\ \cos\left[\frac{m\pi}{a}(x_q + (s-\frac{1}{2})\Delta x_q)\right] \sin\left[\frac{n\pi}{b}(y_q + t\Delta y_q)\right] \end{aligned} \tag{2.48}$$

where,

$$\begin{aligned} & & u &= 1, 2, 3, ..., (Lx_p - 1) \\ i &= u + (v-1)(Lx_p - 1) & & \\ & & v &= 1, 2, 3, ..., Ly_p \\ & & s &= 1, 2, 3, ..., Lx_q \\ j &= s + (t-1)Lx_q & & \\ & & t &= 1, 2, 3, ..., (Ly_q - 1) \end{aligned} \tag{2.49}$$

$$(Y_{pq}^{wg})_{ij}^{yx} = -j\omega\varepsilon \sum_{m=0}^{\infty}\sum_{n=0}^{\infty} \frac{\epsilon_{0m}\epsilon_{0n}}{\gamma_{mn}abk^2}(\frac{m\pi}{a})(\frac{n\pi}{b})\ \Delta_{xy}\ S_{XP}\ S_{YP}^2\ S_{XQ}^2\ S_{YQ}$$
$$\cos\left[\frac{m\pi}{a}(x_p + (u-\frac{1}{2})\Delta x_p)\right] \sin\left[\frac{n\pi}{b}(y_p + v\Delta y_p)\right]$$
$$\sin\left[\frac{m\pi}{a}(x_q + s\Delta x_q)\right] \cos\left[\frac{n\pi}{b}(y_q + (t-\frac{1}{2})\Delta y_q)\right] \tag{2.50}$$

where,

$$u = 1, 2, 3, ..., Lx_p$$
$$i = u + (v-1)Lx_p$$
$$v = 1, 2, 3, ..., (Ly_p - 1)$$
$$s = 1, 2, 3, ..., (Lx_q - 1)$$
$$j = s + (t-1)(Lx_q - 1)$$
$$t = 1, 2, 3, ..., Ly_q \tag{2.51}$$

$$(Y_{pq}^{wg})_{ij}^{yy} = j\omega\varepsilon \sum_{m=0}^{\infty}\sum_{n=0}^{\infty} \frac{\epsilon_{0m}\epsilon_{0n}}{\gamma_{mn}abk^2}[k^2 - (\frac{n\pi}{b})^2]\ \Delta_{xy}\ S_{XP}\ S_{YP}^2\ S_{XQ}\ S_{YQ}^2$$
$$\cos\left[\frac{m\pi}{a}(x_p + (u-\frac{1}{2})\Delta x_p)\right] \sin\left[\frac{n\pi}{b}(y_p + v\Delta y_p)\right]$$
$$\cos\left[\frac{m\pi}{a}(x_q + (s-\frac{1}{2})\Delta x_q)\right] \sin\left[\frac{n\pi}{b}(y_q + t\Delta y_q)\right] \tag{2.52}$$

where,

$$\begin{aligned} & & u &= 1, 2, 3, ..., Lx_p \\ i &= u + (v-1)Lx_p & & \\ & & v &= 1, 2, 3, ..., (Ly_p - 1) \\ & & s &= 1, 2, 3, ..., Lx_q \\ j &= s + (t-1)Lx_q & & \\ & & t &= 1, 2, 3, ..., (Ly_q - 1) \end{aligned} \tag{2.53}$$

The variables Δ_{xy}, S_{XP}, S_{XQ}, S_{YP}, and S_{YQ} are defined as

$$\Delta_{xy} = \Delta x_p \Delta y_p \Delta x_q \Delta y_q$$

$$S_{XP} = \left[\frac{\sin(m\pi\Delta x_p/2a)}{(m\pi\Delta x_p/2a)}\right] \qquad S_{YP} = \left[\frac{\sin(n\pi\Delta y_p/2b)}{(n\pi\Delta y_p/2b)}\right]$$

$$S_{XQ} = \left[\frac{\sin(m\pi\Delta x_q/2a)}{(m\pi\Delta x_q/2a)}\right] \qquad S_{YQ} = \left[\frac{\sin(n\pi\Delta y_q/2b)}{(n\pi\Delta y_q/2b)}\right]$$

Computation of admittance matrix using RWG functions

In case of computation of matrix elements using RWG functions, the aperture surfaces are discretized into triangular areas and the RWG functions are defined for each non-boundary edge as given in (2.23). The RWG function can be resolved into x- and y-directed component as

$$M_p^{x\pm} = \pm\frac{l_p}{2A_p^{\pm}}(x - x_p^{\pm}) \tag{2.54}$$

$$M_p^{y\pm} = \pm\frac{l_p}{2A_p^{\pm}}(y - y_p^{\pm}) \tag{2.55}$$

where, $(x_p^{\pm}, y_p^{\pm})$ denotes the coordinates of free vertex of either plus or minus triangle.

In this case, instead of numbering the basis functions independently over each aperture, these are numbered continuously over all apertures. Hence, according to (2.9), the pqth element of the admittance matrix can be expressed as

$$(Y^{wg})_{pq} = -\iint\limits_{T_p^{\pm}} \overline{M}_p \,.\, \overline{H}_t^{wg}(\overline{M}_q)\, ds \tag{2.56}$$

Substituting (2.25) in (2.56), we get

$$(Y^{wg})_{pq} = j\omega\varepsilon \iint\limits_{T_p^{\pm}} \iint\limits_{T_q^{\pm}} \overline{M}_p(\bar{r}) \,.\, \overline{\overline{G}}(\bar{r}|\bar{r}') \,.\, \overline{M}_q(\bar{r}')\, ds'\, ds \tag{2.57}$$

Again, the decomposition of the functions $\overline{M}_p$ and $\overline{M}_q$ gives four submatrices as given in (2.33). Thus, according to (2.34), the pqth element of submatrix $[(Y^{wg})^{xx}]$ can be expressed as

$$\begin{aligned}(Y^{wg})^{xx}_{pq} &= j\omega\varepsilon \iint\limits_{T_P^{\pm}} \iint\limits_{T_q^{\pm}} M_p^{x\pm} G_{xx} M_q^{x\pm}\, ds'ds \\ &= j\omega\varepsilon \left\{ \iint\limits_{T_p^{+}} \iint\limits_{T_q^{+}} M_p^{x+} G_{xx} M_q^{x+} ds'ds + \iint\limits_{T_p^{+}} \iint\limits_{T_q^{-}} M_p^{x+} G_{xx} M_q^{x-} ds'ds \right. \\ &\qquad \left. \iint\limits_{T_p^{-}} \iint\limits_{T_q^{+}} M_p^{x-} G_{xx} M_q^{x+} ds'ds + \iint\limits_{T_p^{-}} \iint\limits_{T_q^{-}} M_p^{x-} G_{xx} M_q^{x-} ds'ds \right\}\end{aligned}$$

Substituting (2.54), the above equation becomes

$$\begin{aligned}(Y^{wg})^{xx}_{pq} = \frac{j\omega\varepsilon l_p l_q}{4} \Bigg\{ &\frac{1}{A_p^+ A_q^+} \iint\limits_{T_p^{+}} \iint\limits_{T_q^{+}} (x - x_p^+) G_{xx} (x' - x_q^+) ds'ds + \\ &\frac{1}{A_p^+ A_q^-} \iint\limits_{T_p^{+}} \iint\limits_{T_q^{-}} (x - x_p^+) G_{xx} (x_q^- - x') ds'ds + \\ &\frac{1}{A_p^- A_q^+} \iint\limits_{T_p^{-}} \iint\limits_{T_q^{+}} (x_p^- - x) G_{xx} (x' - x_q^+) ds'ds + \\ &\frac{1}{A_p^- A_q^-} \iint\limits_{T_p^{-}} \iint\limits_{T_q^{-}} (x_p^- - x) G_{xx} (x_q^- - x') ds'ds \Bigg\}\end{aligned} \tag{2.58}$$

where l_p and l_q are the lengths of p^{th} and q^{th} non-boundary edges, respectively, and $A_p^{\pm}$ and $A_q^{\pm}$ denote the area of either plus or minus triangles associated with p^{th} and q^{th} edges.

Now, each integral in the above equation is of the form

$$(L_{rs}^{ij})_{xx} = \iint_{T_r} \iint_{T_s} (x - x_i) G_{xx}(r|r')(x' - x_j)\, ds'ds$$
$$r, s = 1, 2, 3, ..., P$$
$$i, j = 1, 2, 3 \tag{2.59}$$

where T_r and T_s denote the r^{th} and s^{th} observation and source triangles, respectively and i and j denote the vertices of the r^{th} and s^{th} triangles. Similarly, xy, yx and yy components can be expressed as

$$(L_{rs}^{ij})_{xy} = \iint_{T_r} \iint_{T_s} (x - x_i) G_{xy}(r|r')(y' - y_j)\, ds'ds \tag{2.60}$$

$$(L_{rs}^{ij})_{yx} = \iint_{T_r} \iint_{T_s} (y - y_i) G_{yx}(r|r')(x' - x_j)\, ds'ds \tag{2.61}$$

$$(L_{rs}^{ij})_{yy} = \iint_{T_r} \iint_{T_s} (y - y_i) G_{yy}(r|r')(y' - y_j)\, ds'ds \tag{2.62}$$

Using (2.26) in (2.59), we obtain

$$(L_{rs}^{ij})_{xx} = \sum_{m=0}^{\infty} \sum_{n=0}^{\infty} \frac{\epsilon_{0m}\epsilon_{0n}}{\gamma_{mn} abk^2} [k^2 - (\frac{m\pi}{a})^2] \left\{ \iint_{T_r} (x - x_i) \sin(\frac{m\pi x}{a}) \cos(\frac{n\pi y}{b}) dxdy \right\}$$
$$\left\{ \iint_{T_s} (x' - x_j) \sin(\frac{m\pi x'}{a}) \cos(\frac{n\pi y'}{b}) dx'dy' \right\} \tag{2.63}$$

Similarly,

$$(L_{rs}^{ij})_{xy} = -\sum_{m=0}^{\infty} \sum_{n=0}^{\infty} \frac{\epsilon_{0m}\epsilon_{0n}}{\gamma_{mn} abk^2} (\frac{m\pi}{a})(\frac{n\pi}{b}) \left\{ \iint_{T_r} (x - x_i) \sin(\frac{m\pi x}{a}) \cos(\frac{n\pi y}{b}) dxdy \right\}$$
$$\left\{ \iint_{T_s} (y' - y_j) \cos(\frac{m\pi x'}{a}) \sin(\frac{n\pi y'}{b}) dx'dy' \right\} \tag{2.64}$$

$$(L_{rs}^{ij})_{yx} = -\sum_{m=0}^{\infty}\sum_{n=0}^{\infty}\frac{\epsilon_{0m}\epsilon_{0n}}{\gamma_{mn}abk^2}(\frac{m\pi}{a})(\frac{n\pi}{b})\left\{\iint_{T_r}(y-y_i)\cos(\frac{m\pi x}{a})\sin(\frac{n\pi y}{b})dxdy\right\}$$
$$\left\{\iint_{T_s}(x'-x_j)\sin(\frac{m\pi x'}{a})\cos(\frac{n\pi y'}{b})dx'dy'\right\} \tag{2.65}$$

$$(L_{rs}^{ij})_{yy} = \sum_{m=0}^{\infty}\sum_{n=0}^{\infty}\frac{\epsilon_{0m}\epsilon_{0n}}{\gamma_{mn}abk^2}[k^2-(\frac{n\pi}{b})^2]\left\{\iint_{T_r}(y-y_i)\cos(\frac{m\pi x}{a})\sin(\frac{n\pi y}{b})dxdy\right\}$$
$$\left\{\iint_{T_s}(y'-y_j)\cos(\frac{m\pi x'}{a})\sin(\frac{n\pi y'}{b})dx'dy'\right\} \tag{2.66}$$

From (2.63)-(2.66), it can be found that the computation of above components of L_{rs}^{ij} involves only two types of integrals, which are given as

$$I_1 = \iint_T (x-x_i)\sin(\frac{m\pi x}{a})\cos(\frac{n\pi y}{b})dxdy$$

and

$$I_2 = \iint_T (y-y_i)\cos(\frac{m\pi x}{a})\sin(\frac{n\pi y}{b})dxdy$$

These integrals are conveniently evaluated using the area coordinates $\mathcal{L}_1$, $\mathcal{L}_2$, $\mathcal{L}_3$ [161] as described in Appendix A. It may be noted that in the procedure presented here, the integration is carried out over the triangular regions and stored, since a particular integral will be required for the computation of more than one matrix element. This eliminates repeated calculations of integrals, which would occur if the integration is done over the edges of the triangles.

Once these integrals are calculated over all triangular areas, pqth element of

uv $(u, v \Rightarrow x, y)$ component of admittance matrix element can be expressed as

$$(Y^{wg})_{pq}^{uv} = \frac{j\omega\varepsilon l_p l_q}{4} \times \left\{ \frac{1}{A_p^+ A_q^+} \left(L_{r(p^+)s(q^+)}^{i(p^+)j(q^+)} \right)_{uv} - \frac{1}{A_p^+ A_q^-} \left(L_{r(p^+)s(q^-)}^{i(p^+)j(q^-)} \right)_{uv} - \frac{1}{A_p^- A_q^+} \left(L_{r(p^-)s(q^+)}^{i(p^-)j(q^+)} \right)_{uv} + \frac{1}{A_p^- A_q^-} \left(L_{r(p^-)s(q^-)}^{i(p^-)j(q^-)} \right)_{uv} \right\} \quad (2.67)$$

where, $r(p^{\pm})$ and $s(q^{\pm})$ are the numbers of plus or minus triangle associated with p^{th} and q^{th} edges and $i(p^{\pm})$ and $j(q^{\pm})$ are the number of free vertices of plus or minus triangle associated with p^{th} and q^{th} edges, respectively.

2.4.2 Half-Space Region

This section presents the computation of admittance matrix elements for the half-space region with a magnetic surface current source $\overline{M}$. Following Galerkin's method, an element of admittance of matrix given in (2.10), can be expressed as

$$Y_{mn}^{hs} = -\iint_{A_m} \overline{M}_m \cdot \overline{H}_t^{hs}(\overline{M}_n)\, ds \quad (2.68)$$

where the superscript 'hs' is used to denote half space region and $\overline{H}_t^{hs}(\overline{M}_n)$ denotes the magnetic field due to a surface magnetic current $\overline{M}_n$ radiating in the presence of a complete conductor. The computation of matrix elements can be simplified by using the image theory (Fig. 2.7) and hence, the field can be calculated by considering a current element $2\overline{M}_n$ radiating in free space. Hence, (2.68) can be written as

$$\begin{aligned} Y_{mn}^{hs} &= -\iint_{A_m} \overline{M}_m \cdot \overline{H}_t^{fs}(2\overline{M}_n)\, ds \\ &= -2\iint_{A_m} \overline{M}_m \cdot \overline{H}_t^{fs}(\overline{M}_n)\, ds \end{aligned} \quad (2.69)$$

where the superscript 'fs' denotes the free space region.

Now, the magnetic field produced by a magnetic current element $\overline{M}_n$ can be expressed in terms of electric vector potential $\overline{F}_n$ and magnetic scalar potential φ_n as

$$\overline{H_t}(\overline{M}_n) = -j\omega\overline{F}_n - \nabla\varphi_n \tag{2.70}$$

where the electric vector potential and magnetic scalar potential are defined as

$$\overline{F}_n = \frac{\varepsilon}{4\pi}\iint_{A_n} \overline{M}_n(\overline{r}')\ G(\overline{r}|\overline{r}')\ ds' \tag{2.71}$$

$$\varphi_n = \frac{-1}{4\pi j\omega\mu}\iint_{A_n} \nabla' \cdot \overline{M}_n(\overline{r}')G(\overline{r}|\overline{r}')\ ds' \tag{2.72}$$

Here, $G(r|r')$ is the free space Green's function, given by

$$G(\overline{r}|\overline{r}') = \frac{e^{-jk|\overline{r}-\overline{r}'|}}{|\overline{r}-\overline{r}'|} \tag{2.73}$$

Substituting (2.70) in (2.69) and using two-dimensional divergence theorem, Y_{mn} is obtained as

$$Y_{mn}^{hs} = j\omega\left[\frac{l_m}{A_m^+}\iint_{A_m^+} \bar{\rho}_m^+ \cdot \overline{F}_n(\bar{r})\ ds + \frac{l_m}{A_m^-}\iint_{A_m^-} \bar{\rho}_m^- \cdot \overline{F}_n(\bar{r})\ ds + \frac{-2l_m}{j\omega A_m^+}\iint_{A_m^+} \varphi_n\ ds + \frac{2l_m}{j\omega A_m^-}\iint_{A_m^-} \varphi_n\ ds\right]$$

The above equation contains quadruple integrals, a double integral over the observation triangle and a double integral over the source triangle. In order to simplify the computational complexity, the integrals over the observation triangle can be approximated by the value of integral at the centroid of the triangle to give

$$Y_{mn}^{hs} = j\omega l_m\left[\overline{F}_n(\bar{r}_m^{c+}) \cdot \bar{\rho}_m^{c+} + \overline{F}_n(\bar{r}_m^{c-}) \cdot \bar{\rho}_m^{c-}\right] - 2l_m\left[\varphi_n(\bar{r}_m^{c+}) - \varphi_n(\bar{r}_m^{c-})\right] \tag{2.74}$$

Now, according to (2.71), we can write

$$\overline{F}_n(\bar{r}_m^{c\pm}) = \frac{\epsilon}{4\pi} \iint\limits_{T_n^{\pm}} \overline{M}_n(\bar{r}') G(\bar{r}_m^{c\pm}|\bar{r}')\ ds'$$

$$= \frac{\epsilon l_n}{8\pi} \left\{ \frac{1}{A_n^+} \iint\limits_{T_n^+} \bar{\rho}_n^+(\bar{r}') G(\bar{r}_m^{c\pm}|\bar{r}')\ ds' + \frac{1}{A_n^-} \iint\limits_{T_n^-} \bar{\rho}_n^-(\bar{r}') G(\bar{r}_m^{c\pm}|\bar{r}')\ ds' \right\} \tag{2.75}$$

Similarly, the magnetic scalar potential can be expressed as

$$\varphi_n(\bar{r}_m^{c\pm}) = -\frac{1}{4\pi j\omega\mu} \iint\limits_{T_n^{\pm}} \nabla' \cdot \overline{M}_n(\bar{r}') G(\bar{r}_m^{c\pm}|\bar{r}')\ ds'$$

$$= -\frac{l_n}{4\pi j\omega\mu} \left[\frac{1}{A_n^+} \iint\limits_{T_n^+} G(\bar{r}_m^{c\pm}|\bar{r}')\ ds' - \frac{1}{A_n^-} \iint\limits_{T_n^-} G(\bar{r}_m^{c\pm}|\bar{r}')\ ds' \right] \tag{2.76}$$

Hence, using (2.75) and (2.76), the mn$^{\text{th}}$ element of admittance matrix is obtained as

$$Y_{mn}^{hs} = \frac{j\omega\epsilon l_m l_n}{8\pi}$$

$$\left\{ \begin{array}{l} \bar{\rho}_m^{c+}(\bar{r}) \cdot \dfrac{1}{A_n^+} \iint\limits_{T_n^+} \bar{\rho}_n^+(\bar{r}') G(\bar{r}_m^{c+}|\bar{r}')\ ds' + \bar{\rho}_m^{c+}(\bar{r}) \cdot \dfrac{1}{A_n^-} \iint\limits_{T_n^-} \bar{\rho}_n^-(\bar{r}') G(\bar{r}_m^{c+}|\bar{r}')\ ds' + \\ \bar{\rho}_m^{c-}(\bar{r}) \cdot \dfrac{1}{A_n^+} \iint\limits_{T_n^+} \bar{\rho}_n^+(\bar{r}') G(\bar{r}_m^{c-}|\bar{r}')\ ds' + \bar{\rho}_m^{c-}(\bar{r}) \cdot \dfrac{1}{A_n^-} \iint\limits_{T_n^-} \bar{\rho}_n^-(\bar{r}') G(\bar{r}_m^{c-}|\bar{r}')\ ds' \end{array} \right\}$$

$$+ \frac{l_m l_n}{2\pi j\omega\mu} \left\{ \begin{array}{l} \dfrac{1}{A_n^+} \iint\limits_{T_n^+} G(\bar{r}_m^{c+}|\bar{r}')\ ds' - \dfrac{1}{A_n^-} \iint\limits_{T_n^-} G(\bar{r}_m^{c+}|\bar{r}')\ ds' \\ -\dfrac{1}{A_n^-} \iint\limits_{T_n^+} G(\bar{r}_m^{c-}|\bar{r}')\ ds' + \dfrac{1}{A_n^-} \iint\limits_{T_n^-} G(\bar{r}_m^{c-}|\bar{r}')\ ds' \end{array} \right\} \tag{2.77}$$

The integrals in (2.77) are of following forms

$$\overline{F}_{pq}^{j} = \iint\limits_{T_q} \bar{\rho}_j(\bar{r}') G(\bar{r}_p|\bar{r}')\ ds' \tag{2.78}$$

$$p, q = 1, 2, 3, ..., P$$

$$j = 1, 2, 3$$

and

$$\varphi_{pq} = \iint_{T_q} G(\bar{r}_p|\bar{r})\, ds' \qquad (2.79)$$

$$p, q \;=\; 1, 2, 3, ..., P$$

where $\bar{\rho}_j(r') = \bar{r} - \bar{r}'$ for any vertex j of q^{th} triangle and r_p is the centroid of p^{th} triangle, and P denotes the total number of triangular subsections.

The Green's function becomes singular as the source and observation points coincide and the calculation of these singular integrals needs some special treatment. The procedure used for the calculation of the singular integrals is given in Appendix B.

Using this approach, the mn^{th} element of admittance matrix can be expressed as

$$Y^{hs}_{mn} = \frac{j\omega\varepsilon l_m l_n}{8\pi} \left\{ \begin{array}{l} \frac{1}{A_n^+}\overline{\rho}_m^{c+} \cdot \overline{F}^{j(n^+)}_{p(m^+)q(n^+)} - \frac{1}{A_n^-}\overline{\rho}_m^{c+} \cdot \overline{F}^{j(n^-)}_{p(m^+)q(n^-)} \\ +\frac{1}{A_n^+}\overline{\rho}_m^{c-} \cdot \overline{F}^{j(n^+)}_{p(m^-)q(n^+)} - \frac{1}{A_n^-}\overline{\rho}_m^{c-} \cdot \overline{F}^{j(n^-)}_{p(m^-)q(n^-)} \end{array} \right\}$$

$$+\frac{l_m l_n}{2\pi j\omega\mu} \left\{ \begin{array}{l} \frac{1}{A_n^+}\varphi_{p(m^+)q(n^+)} - \frac{1}{A_n^-}\varphi_{p(m^+)q(n^-)} \\ -\frac{1}{A_n^+}\varphi_{p(m^-)q(n^+)} + \frac{1}{A_n^-}\varphi_{p(m^-)q(n^-)} \end{array} \right\} \qquad (2.80)$$

Here, the subscript $p(m^{\pm})$ denotes the triangle number of either plus or minus triangle associated with m^{th} RWG function. The subscript $q(n^{\pm})$ has a similar meaning. Superscript $j(n^{\pm})$ is the free vertex number of either plus or minus triangle associated with the n^{th} RWG function.

2.5 Evaluation of Excitation Vector

In the present work, we have considered two types of input excitations: an incident TE_{mn} mode for waveguide problems and plane wave incidence for the

conducting screen problem. In the following subsections, the computation of excitation vector for these two cases is presented.

2.5.1 TE_{mn} Incident Mode in the Rectangular Waveguide

According to (2.13), an element of excitation vector is given by

$$(I_p^i)_q = \iint_{A_p} \overline{M}_{pq} \cdot \overline{H}_{tp}^i \, ds \tag{2.81}$$

For a TE_{mn} incident mode, the transverse component of incident magnetic field can be expressed as

$$\overline{H}_{tp}^i = Y_{mn} e^{-\gamma_{mn} z} \hat{z} \times \bar{e}_{mn}^{TE} \tag{2.82}$$

where Y_{mn} is the modal admittance of the mn^{th} incident mode and is given by

$$Y_{mn} = -j\frac{\gamma_{mn}}{Z_0 k}, \qquad Z_0 = 377\ \Omega \tag{2.83}$$

and $\bar{e}_{mn}^{TE}$ is the normalized transverse modal vector for the incident TE_{mn} mode which is given by

$$\bar{e}_{mn}^{TE} = \sqrt{\frac{ab\varepsilon_{0m}\varepsilon_{0n}}{(mb)^2+(na)^2}} \left\{ \hat{x}(\frac{n}{b}) \cos\left[\frac{m\pi}{a}(x+\frac{a}{2})\right] \sin\left[\frac{n\pi}{b}(y+\frac{b}{2})\right] \right.$$
$$\left. - \hat{y}(\frac{m}{a}) \sin\left[\frac{m\pi}{a}(x+\frac{a}{2})\right] \cos\left[\frac{n\pi}{b}(y+\frac{b}{2})\right] \right\} \tag{2.84}$$

with

$$\begin{aligned} m &= 0,1,2,3,... \\ n &= 0,1,2,3,... \qquad\qquad m+n \neq 0 \end{aligned}$$

Considering the discontinuities at $z = 0$ plane, substitution of (2.82) in (2.81) gives

$$(I_p^i)_q = Y_l \iint_{A_i} \overline{M}_{pq} \cdot \hat{z} \times \bar{e}_l^{TE} \, ds \tag{2.85}$$

where the subscript 'mn'has been replaced by 'l'. The integral in (2.85) can be evaluated using numerical or analytical methods as discussed in the following subsections.

Computation of Excitation integral using Rooftop functions

The integral in (2.85) can be resolved into two components as

$$(I_p^i)_q^x = Y_l(A_{pl})_q^x \tag{2.86}$$

and

$$(I_p^i)_q^y = Y_l(A_{pl})_q^y \tag{2.87}$$

where,

$$(A_{pl})_q^x = \iint_{A_p} M_{pq}^x \hat{x} \; . \; \hat{z} \times \bar{e}_l^{TE} \; ds \tag{2.88}$$

$$(A_{pl})_q^y = \iint_{A_p} M_{pq}^y \hat{y} \; . \; \hat{z} \times \bar{e}_l^{TE} \; ds \tag{2.89}$$

These integrals can be evaluated in a straightforward manner to give

$$(A_{pl})_q^x = \sqrt{\frac{ab\epsilon_{0m}\epsilon_{0n}}{(mb)^2+(na)^2}} \left(\frac{m}{a}\right) (\Delta x_p \Delta y_p) \left[\frac{\sin m\pi\Delta x_p/2a}{m\pi\Delta x_p/2a}\right]^2 \left[\frac{\sin n\pi\Delta y_p/2b}{n\pi\Delta y_p/2b}\right] \sin\left[\frac{m\pi}{a}(x_p + u\Delta x_p)\right] \cos\left[\frac{n\pi}{b}(y_p + (v-\frac{1}{2})\Delta y_p)\right] \tag{2.90}$$

where,

$$\begin{aligned} u &= 1, 2, 3, ..., (Lx_p - 1) \\ q &= u + (v-1)(Lx_p - 1) \\ v &= 1, 2, 3, ..., Ly_p \end{aligned} \tag{2.91}$$

and

$$(A_{mn})_q^y = \sqrt{\frac{ab\epsilon_{0m}\epsilon_{0n}}{(mb)^2+(na)^2}}\left(\frac{n}{b}\right)(\Delta x_p \Delta y_p)\left[\frac{\sin m\pi\Delta x_p/2a}{m\pi\Delta x_p/2a}\right]\left[\frac{\sin n\pi\Delta y_p/2b}{n\pi\Delta y_p/2b}\right]^2 \cos\left[\frac{m\pi}{a}(x_p+(u-\frac{1}{2})\Delta x_p)\right]\sin\left[\frac{n\pi}{b}(y_p+v\Delta y_p)\right] \tag{2.92}$$

where,

$$\begin{aligned} & u = 1,2,3,...,Lx_p \\ q = u + (v-1)Lx_p & \\ & v = 1,2,3,...,(Ly_p-1) \end{aligned} \tag{2.93}$$

Computation of Excitation integral using RWG functions

According to (2.14) and using centroid approximation q$^{\text{th}}$ element of the excitation vector can be expressed as,

$$\begin{aligned} (I^i)_q &= Y_l \iint_{T_q^{\pm}} \overline{M}_q \,.\, \hat{z}\times\bar{e}_l^{TE}\, ds \\ &= Y_l (A_l)_q \end{aligned} \tag{2.94}$$

where,

$$\begin{aligned} (A_l)_q &= \iint_{T_q^{\pm}} \overline{M}_q \,.\, \hat{z}\times e_l^{TE}\, ds \\ &= \frac{l_q}{2}\left\{\bar{\rho}_q^{c+} \,.\, \hat{z}\times\bar{e}_l^{TE}(\bar{r}_q^{c+}) + \bar{\rho}_q^{c-} \,.\, \hat{z}\times\bar{e}_l^{TE}(\bar{r}_q^{c-})\right\} \end{aligned} \tag{2.95}$$

where l_q is the length of q$^{\text{th}}$ non-boundary edge and $\bar{r}_q^{c\pm}$ denotes the centroid of the triangles associated with the q$^{\text{th}}$ non-boundary edge.

2.5.2 Plane Wave Incidence

For uniform plane wave travelling in free space, the magnetic field can be expressed as

$$\overline{H}^{io}(\bar{r}) = (\hat{u}_\theta H_\theta^i + \hat{u}_\varphi H_\varphi^i)e^{-j\bar{k}_i.\bar{r}} \tag{2.96}$$

where the unit vectors $\hat{u}_\theta$ and $\hat{u}_\varphi$ are defined in Fig. 2.5 and the wave vector $\bar{k}_i$ is defined as

$$\bar{k}_i = -\hat{u}_r k_i = -k_i(\hat{x}\sin\theta_i\cos\varphi_i + \hat{y}\sin\theta_i\sin\varphi_i + \hat{z}\cos\theta_i) \tag{2.97}$$

The magnetic field $\overline{H}^{io}$ can be resolved into three components as

$$\begin{aligned} H_x^{io} &= (H_\theta^{io}\cos\theta_i\cos\varphi_i - H_\varphi^{io}\sin\varphi_i)e^{-j\bar{k}_i.\bar{r}} \\ H_y^{io} &= (H_\theta^{io}\cos\theta_i\sin\varphi_i + H_\varphi^{io}\cos\varphi_i)e^{-j\bar{k}_i.\bar{r}} \\ H_z^{io} &= -H_\theta^{io}\sin\theta_i e^{-j\bar{k}_i.\bar{r}} \end{aligned} \tag{2.98}$$

Using (2.14), an element of excitation vector for a plane wave incidence can be expressed as

$$(I^i)_m = \iint\limits_{T_m^\pm} \overline{M}_m \,.\, \overline{H}_t^i \, ds \tag{2.99}$$

When the aperture is closed with a perfect conductor, $\overline{H}_t^i = 2\overline{H}_t^{i0}$. Hence, (2.99) can be expressed as

$$(I^i)_m = 2\iint\limits_{T_m^\pm} \overline{M}_m \,.\, \overline{H}_t^{i0} \, ds \tag{2.100}$$

Using centroid approximation, the above integral can be evaluated as

$$I_m^i = l_m\left[\bar{\rho}_m^{c+} \,.\, \overline{H}_t^{i0}(\bar{r}_m^{c+}) + \bar{\rho}_m^{c-} \,.\, \overline{H}_t^{i0}(\bar{r}_m^{c-})\right] \tag{2.101}$$

2.6 Far-Field Computation

A component of magnetic field H_m at a point $\bar{r}_m$ in region 'b' can be obtained by placing a magnetic dipole $\overline{K}\delta(\bar{r} - \bar{r}_m)$ at $\bar{r}_m$ and using the reciprocity theorem

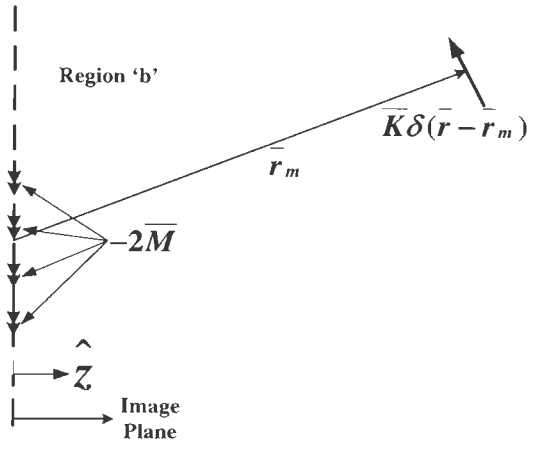

Figure 2.15: Measurement of magnetic field in region 'b'.

to its field and to the original field. The geometry of the problem is shown in Fig. 2.15.

Let, $\overline{E}^m(r)$ and $\overline{H}^m(r)$ be the fields produced by the dipole in free space and H_m is the component of magnetic field at r_m in the direction of the dipole due to the equivalent surface magnetic current $-2\overline{M}$ over the apertures radiating in free space. The application of reciprocity theorem gives

$$KH_m(\bar{r}_m) = -\iint 2\overline{M} \,.\, \overline{H}^m \, ds \tag{2.102}$$

Equation (2.102) is evaluated by substituting $\overline{M}$ as

$$KH_m(\bar{r}_m) = -\sum_n V_n \iint 2\overline{M}_n \,.\, \overline{H}^m \, ds \tag{2.103}$$

which can be expressed in matrix form as

$$KH_m(r_m) = \widetilde{P}^m \overrightarrow{V} \tag{2.104}$$

where $\widetilde{P}^m$ is the transpose of the measurement vector $\overrightarrow{P}^m$. An element of the measurement vector is given by

$$P_n^m = \iint_{T_n} -2\overline{M}_n \,.\, \overline{H}^m \, ds \tag{2.105}$$

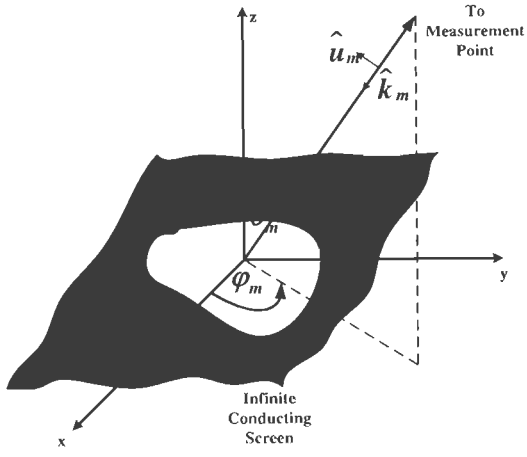

Figure 2.16: Measurement vector in region 'b'.

For the determination of far-field, the dipole $\overline{K}$ is oriented perpendicular to $\bar{r}_m$ and the dipole moment K is chosen such that it produces a uniform plane wave in the vicinity of origin. That is

$$\frac{1}{K} = -\frac{j\omega\varepsilon}{4\pi r_m} e^{-j\bar{k}_0.\bar{r}_m} \tag{2.106}$$

The plane wave is then given by

$$\overline{H}_m = \hat{u}_m e^{-j\bar{k}_m.\bar{r}} \tag{2.107}$$

where, $\hat{u}_m$ is the unit vector representing the polarization of the measurement and $\bar{k}_m$ is the wave vector pointing in the direction of wave travel as shown in Fig. 2.16

Substituting (2.106) into (2.104), we get

$$H_m = -\frac{j\omega\varepsilon}{4\pi r_m} e^{-j\bar{k}_0.\bar{r}_m} \widetilde{P}^m \overrightarrow{V} \tag{2.108}$$

Using (2.23), an element of the measurement vector is given by

$$\begin{aligned} P_n^m &= -\iint_{T_n^+} 2\overline{M}_n \cdot \overline{H}_t^m \, ds - \iint_{T_n^-} 2\overline{M}_n \cdot \overline{H}_t^m \, ds \\ &= -\frac{l_n}{A_n^+} \iint_{T_n^+} \bar{\rho}_n^+ \cdot \overline{H}_t^m \, ds - \frac{l_n}{A_n^-} \iint_{T_n^-} \bar{\rho}_n^- \cdot \overline{H}_t^m \, ds \end{aligned}$$

Using the centroid approximation, it can be written as

$$P_n^m = -l_n \left[\bar{\rho}_n^{c+} \cdot \overline{H}_t^m(\bar{r}_m^{c+}) + \bar{\rho}_n^{c-} \cdot \overline{H}_t^m(\bar{r}_m^{c-}) \right] \tag{2.109}$$

where

$$\overline{H}_t^m(\bar{r}_m^{c\pm}) = (\hat{u}_\theta H_\theta^m + \hat{u}_\varphi H_\varphi^m) e^{-j\bar{k}_m \cdot \bar{r}_m^{c\pm}}$$

2.7 Conclusion

This chapter presents a general MoM formulation of the problem of coupling between two dissimilar regions through multiple apertures in a thin conducting screen. Expressions for various matrices and vectors involved in the moment method solution have been derived and simplified as much as possible such that they can be conveniently implemented into a software code. The expressions for the far-field magnetic field has also been evaluated.

Chapter 3

FRACTAL FREQUENCY SELECTIVE DIAPHRAGMS IN RECTANGULAR WAVEGUIDE

Requirement of multiband and miniaturized waveguide filters with high out-of-band rejection has directed the focus on the use of frequency selective diaphragms in rectangular waveguides. Waveguide based periodic structures are also very important in suppressing the propagation of higher order modes in the rectangular waveguide without increasing the dimensions of the filter. Several electromagnetic band gap (EBG) structures based on conducting strips are presented in [162, 163].

This chapter deals with the investigations on several fractal frequency selective diaphragms. The self-similarity and space-filling property of fractal geometries are exploited to realize frequency selective diaphragms in rectangular waveguide which can find applications in the design of compact, light weight and multiband waveguide filters and waveguide based electromagnetic band gap

structures. Several self-affine structures based upon Sierpinski gasket, Sierpinski carpet, Devil's staircase fractal and plus shape fractals are proposed and the effects of different scale factors on their performance are also investigated. Self-similar structures like Hilbert curve, Koch curve and Minkowski curves are shown to be efficient in reducing the resonant frequency of the diaphragms. Some typical applications of fractal frequency selective diaphragms in the design of waveguide filters and electromagnetic band gap structures are also presented.

The general MoM formulation of coupling through multiple apertures presented in chapter 2 is specialized to the case of diaphragms in the transverse cross-section of a rectangular waveguide. In section 2, expressions for the determination of scattering parameters of the diaphragm are derived. Numerical results for different fractal frequency selective diaphragms are presented and discussed in section 3. The numerical results obtained from MoM code have been validated by simulations on ANSOFT HFSS. A dual-band waveguide filter based upon the modified Devil's staircase fractal geometry and an electromagnetic band gap structure based on self-affine Sierpinski gasket geometry are presented in section 4. Lastly, a brief summary of the results is presented in section 5.

3.1 Formulation of the Problem

A perfectly conducting thin diaphragm perforated with multiple arbitrarily shaped apertures placed in the transverse cross-section of a rectangular waveguide is shown in Fig. 3.1. An electromagnetic wave is assumed to be incident in the waveguide from left. Fig. 3.2 shows the equivalent models for region 'a' and region 'b'. Both the regions are semi-infinite rectangular waveguide sections short circuited at one end.

According to (2.2), the operator equation for the problem can be expressed

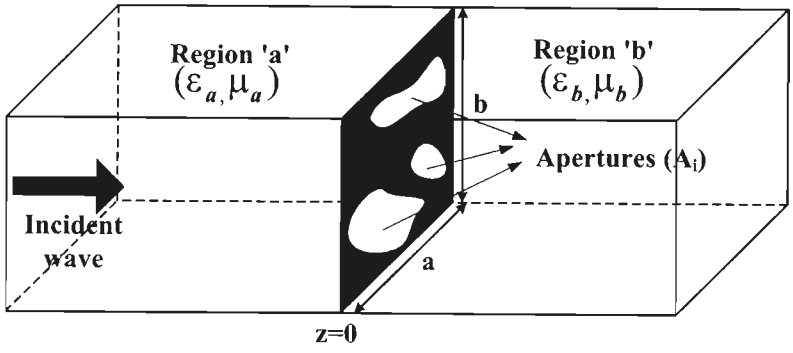

Figure 3.1: Multiple apertures in the transverse cross-section of a rectangular waveguide.

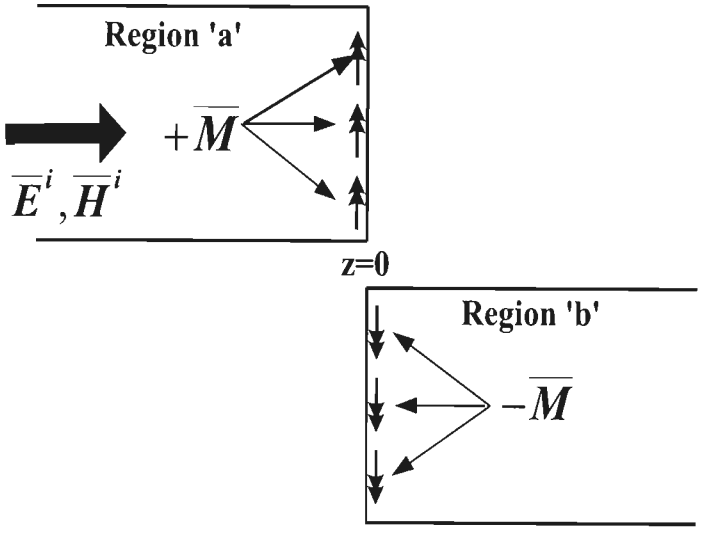

Figure 3.2: Equivalent models.

as

$$\overline{H}_t^a(\overline{M}) + \overline{H}_t^b(\overline{M}) = -(\overline{H}_t^i + \overline{H}_t^{ref}), \text{ over A} \tag{3.1}$$

where $A = \bigcup_{i=1}^{N_{ap}} A_i$, N_{ap} is the number of apertures, $\overline{H}_t^q(\overline{M})$ denotes the tangential component of magnetic field over A in the region 'q' due to equivalent surface magnetic current $\overline{M}$, and $\overline{H}_t^{inc}$, $\overline{H}_t^{ref}$ are the tangential components of magnetic field in the incident and reflected waves. Considering identical regions on both sides of the diaphragm and the presence of perfect conductor over $z = 0$, (3.1) becomes

$$\overline{H}_t^{wg}(\overline{M}) = -\overline{H}_t^i \tag{3.2}$$

Following the Galerkin's solution, the corresponding matrix equation for the problem is

$$[Y^{wg}]\overrightarrow{V} = \overrightarrow{I}^i \tag{3.3}$$

The elements of admittance matrix elements and the excitation vector can be calculated using (2.46-2.53) and (2.90-2.93) for rooftop functions and using (2.67) and (2.94) for RWG functions, respectively. Once the matrix equation is solved for the unknown surface currents, scattering parameters of the diaphragm can be calculated as described in the next section.

3.2 Computation of Scattering Coefficients

The transverse discontinuities in the rectangular waveguide are characterized by the scattering matrix,

$$[S] = \begin{bmatrix} [S_{11}] & [S_{12}] \\ [S_{21}] & [S_{22}] \end{bmatrix} \tag{3.4}$$

where, the pqth element of $[S_{ij}]$ is defined as the amplitude of pth scattered mode at the terminal plane T_i due to a qth incident mode of unit amplitude at terminal

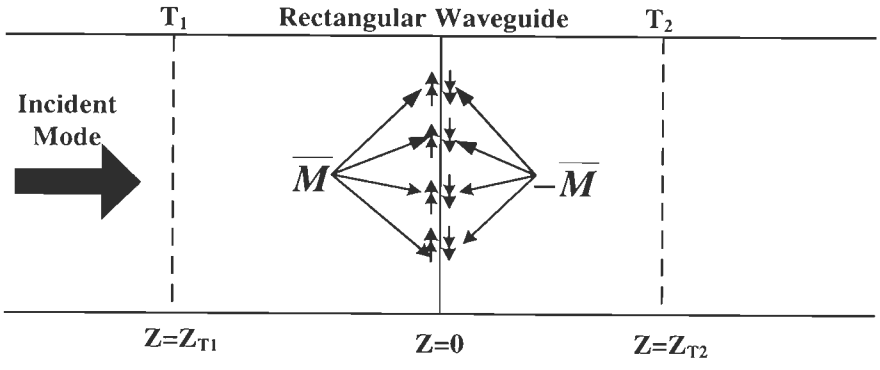

Figure 3.3: Geometry for calculation of scattering parameters of waveguide diaphragm.

plane T_j. The terminal planes are assumed to be located at the integral multiples of guide wavelength which ensure that the scattering coefficients calculated at the terminal planes are same as those calculated at the reference plane $z = 0$. The geometry for the calculation of scattering matrix is shown in Fig. 3.3.

Considering a multimode incident field at T_1 from region $z < Z_{T_1}$, the transverse component of electric field in the waveguide region can be expressed as

$$\overline{E}_t^a = \sum_s B_s^a \bar{e}_s^a e^{-\gamma_s^a z} + \sum_s C_s^a \bar{e}_s^a e^{+\gamma_s^a z} \tag{3.5}$$

where B_s^a and C_s^a represent the amplitudes of s^{th} incident and reflected modes, respectively, γ_s^a is the propagation constant and $\bar{e}_s^a$ denotes the normalized modal vector. The modal vectors are normalized such that

$$\iint_A \bar{e}_r^a \cdot \bar{e}_s^a \, ds = \delta_{rs} \tag{3.6}$$

where δ_{rs} is the Kronecker delta.

The submatrices $[S11]$ and $[S21]$ are computed by considering the input excitation from region 'a'. Assuming a single s^{th} incident mode of unit amplitude, the transverse component of incident and reflected electric fields at T_1 can be

expressed as

$$\overline{E}^a_{t,inc} = \bar{e}^a_s \tag{3.7}$$

$$\overline{E}^a_{t,sca} = -\bar{e}^a_s + \sum_{n=1}^{N_1} V_{1n}\overline{E}^a_t(\overline{M}_{1n}) + ... + \sum_{n=1}^{N_p} V_{pn}\overline{E}^a_t(\overline{M}_{pn}) + ... + \sum_{n=1}^{N_N} V_{Nn}\overline{E}^a_t(\overline{M}_{Nn}) \tag{3.8}$$

where $\overline{E}^a_t(\overline{M}_{pn})$ is the tangential component of electric field at T_1 due to the n^{th} basis function $\overline{M}_{pn}$ defined over the p^{th} aperture surface and is given by

$$\overline{E}^a_t(\overline{M}_{pn}) = \sum_{l=1}^{L_1} A^a_{pnl}\bar{e}^a_l \tag{3.9}$$

where L_1 is the number of waveguide modes necessary to approximate the field. The constant A^a_{pnl} denotes the amplitude of l^{th} mode due to current $\overline{M}_{pn}$, which can be expressed as

$$A^a_{pnl} = \iint_{A_p} \overline{M}_{pn} \,.\, \hat{z} \times \bar{e}^a_l \; ds \tag{3.10}$$

Thus, using (3.7), (3.8) and (3.10), the rs^{th} element of $[S_{11}]$ can be expressed as

$$(S_{11})_{rs} = \begin{cases} -1 + \sum_{n=1}^{N_1} V_{1n}A^a_{1nr} + ... + \sum_{n=1}^{N_p} V_{pn}A^a_{pnr} + ... + \sum_{n=1}^{N_N} V_{Nn}A^a_{Nnr}, & r = s \\ \sum_{n=1}^{N_1} V_{1n}A^a_{1nr} + ... + \sum_{n=1}^{N_p} V_{pn}A^a_{pnr} + ... + \sum_{n=1}^{N_N} V_{Nn}A^a_{Nnr}, & r \neq s \end{cases} \tag{3.11}$$

Now, the scattered field in the region 'b' is given by

$$\overline{E}^b_{t,sca} = \sum_{n=1}^{N_1} V_{1n}\overline{E}^b_t(-\overline{M}_{1n}) + ... + \sum_{n=1}^{N_p} V_{pn}\overline{E}^b_t(-\overline{M}_{pn}) + ... + \sum_{n=1}^{N_N} V_{Nn}\overline{E}^b_t(-\overline{M}_{Nn}) \tag{3.12}$$

with

$$\overline{E}^b_t(\overline{M}_{pn}) = \sum_{l=1}^{K_2} A^b_{pnl}\bar{e}^b_l \tag{3.13}$$

and

$$\begin{aligned} A^b_{pnl} &= \iint_{A_p} \overline{M}_{pn}.\bar{e}^b_l \times \hat{z} \; ds \\ &= -\iint_{A_p} \overline{M}_{pn}.\hat{z} \times \bar{e}^b_l \; ds \end{aligned} \tag{3.14}$$

Thus, comparing (3.14) with (3.10), it can be seen that $A^a_{pml} = -A^b_{pml}$, and hence an element of matrix $[S_{21}]$ can be expressed as

$$(S_{21})_{rs} = \sum_{n=1}^{N_1} V_{1n} A^a_{1nr} + ... + \sum_{n=1}^{N_p} V_{pn} A^a_{pnr} + ... + \sum_{n=1}^{N_N} V_{Nn} A^a_{Nnr} \tag{3.15}$$

Using the symmetry property, the elements of other submatrices can be obtained as

$$[S_{12}] = [S_{21}] \qquad [S_{22}] = [S_{11}] \tag{3.16}$$

3.3 Numerical Results

Based on the developed code, the scattering parameters of different fractal diaphragms are obtained. In all the cases considered here, a WR90 waveguide with cross-sectional dimension of 22.86 mm×10.16 mm is used. Further, a dominant TE_{10} mode of unit amplitude is assumed to be incident.

3.3.1 Modified Devil's Staircase Fractal Diaphragm

The generation steps of Devil's staircase fractal [2] are shown in Fig. 3.4. Taking a unit square as initial geometry, the base of the square is divided into three equal parts, from which the middle third part is removed and replaced by a rectangle of height $\frac{1}{2}$ and width $\frac{1}{3}$. This gives the generator of the fractal. In the second iteration, two rectangles of heights $\frac{1}{4}$ and $\frac{3}{4}$ with widths equal to $\frac{1}{9}$ are placed in the intervals $[\frac{1}{9}, \frac{2}{9}]$ and $[\frac{7}{9}, \frac{8}{9}]$, respectively. In the next iteration, four columns with heights $\frac{1}{8}$, $\frac{3}{8}$, $\frac{5}{8}$ and $\frac{7}{8}$ are placed in the intervals $[\frac{1}{27}, \frac{2}{27}]$, $[\frac{7}{27}, \frac{8}{27}]$, $[\frac{19}{27}, \frac{20}{27}]$ and $[\frac{25}{27}, \frac{26}{27}]$, respectively. After an infinite number of iterations, one can obtain an ideal fractal geometry. It is well known that the resonant frequency of a narrow rectangular aperture lies within the operating frequency of

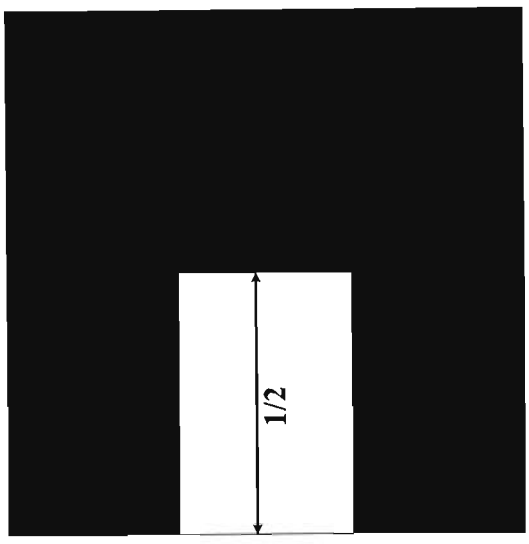

(a) 1st Iteration

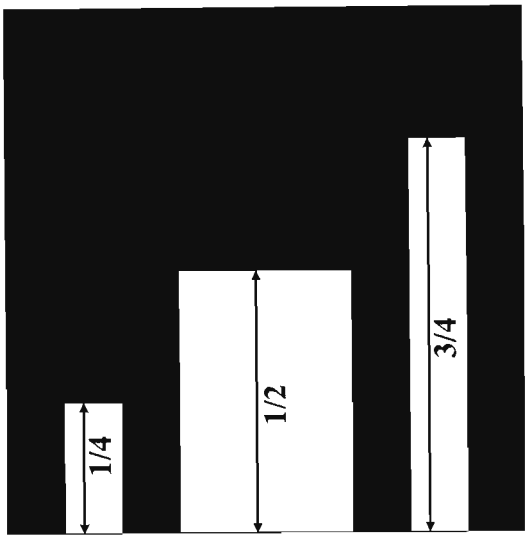

(b) 2nd Iteration

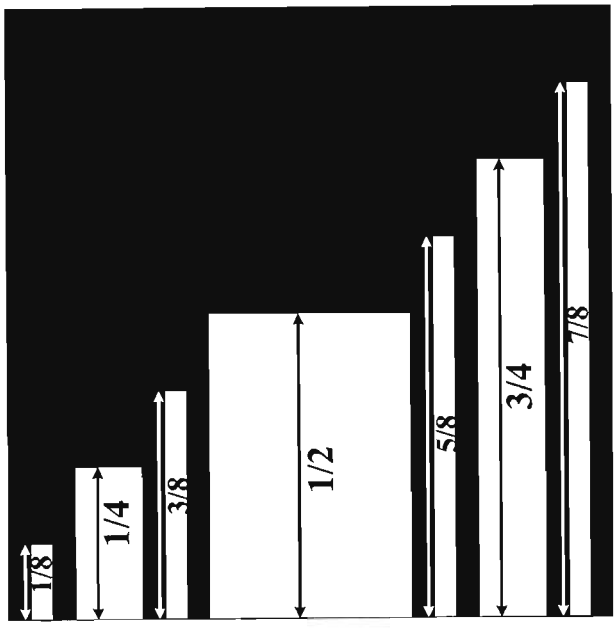

(c) 3rd Iteration

Figure 3.4: Generation steps of Devil's staircase fractal geometry.

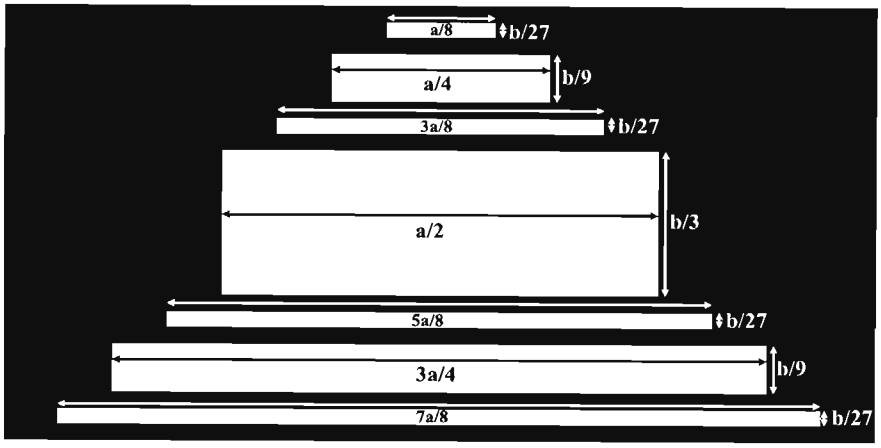

Figure 3.5: A 3rd iteration modified Devil's staircase fractal diaphragm (a=22.86 mm, b=10.16 mm).

the rectangular waveguide if the aperture length parallel to the larger dimension of the waveguide is sufficiently large [71]. With this consideration, an image of the original geometry is taken along the base of the fractal geometry and the resulting structure is rotated by 90° to fit into the waveguide cross-section. The geometry of the modified Devil's staircase fractal diaphragm after 3rd iteration is shown in Fig.3.5.

Due to the rectangular shape of the apertures, the problem is formulated with rooftop functions. Firstly, a convergence test is performed for the number of sections along x-direction (N_x) and y-direction (N_y), as well as, the number of modal indices for each iteration. The convergence analysis for the first iteration is given in Table 3.1. It can be seen from the table that 14 sections along the x-direction and 4 sections along y-direction, resulting in 94 rooftop functions, are sufficient to yield a converged result. Similar, analysis is also performed for the next two iterations. The number of rooftop functions required to obtain converged result are 123 and 191 for 2nd and 3rd iterations, respectively.

Table 3.1: Convergence analysis of single rectangular aperture.

S. No.	N_x	N_y	Modal Indices		$\|S_{11}\|$	% change
			M	N		
1	6	2	25	10	0.5068	
2	8	2	25	10	0.4899	3.34
3	10	2	30	10	0.4800	2.02
4	12	2	35	10	0.4734	1.38
5	14	2	40	10	0.4684	1.06
6	14	3	40	15	0.4766	1.75
7	14	4	40	15	0.4795	0.61

The variations of return loss for an incident TE_{10} mode is shown in Fig. 3.6 for three iterations. The results obtained from simulation on HFSS are also shown which are in a good agreement with the present MoM code. Table 3.2 summarizes the resonant frequencies of modified Devil's fractal diaphragm. For the first iteration, the single rectangular aperture of length $a/2$ (11.43 mm) resonates at 14.55 GHz. The corresponding length to wavelength ratio is 0.56. Due to smaller length of the aperture compared to the larger dimension of the waveguide, the resonant frequency is far beyond the normal operating band of the guide. In the second iteration, two apertures of lengths $3a/4$ (17.145 mm) and $a/4$ (5.715 mm) are introduced. It is found that an additional resonant frequency appears at 8.54 GHz due to the aperture of length 17.145 mm. The corresponding length to wavelength ratio is 0.49. So, the aperture resonates at a frequency at a wavelength equal to twice the length of the aperture. According to this observation, the resonant frequency of the aperture of length 5.715 mm will be around 26.25 GHz, which is well outside the frequency band considered

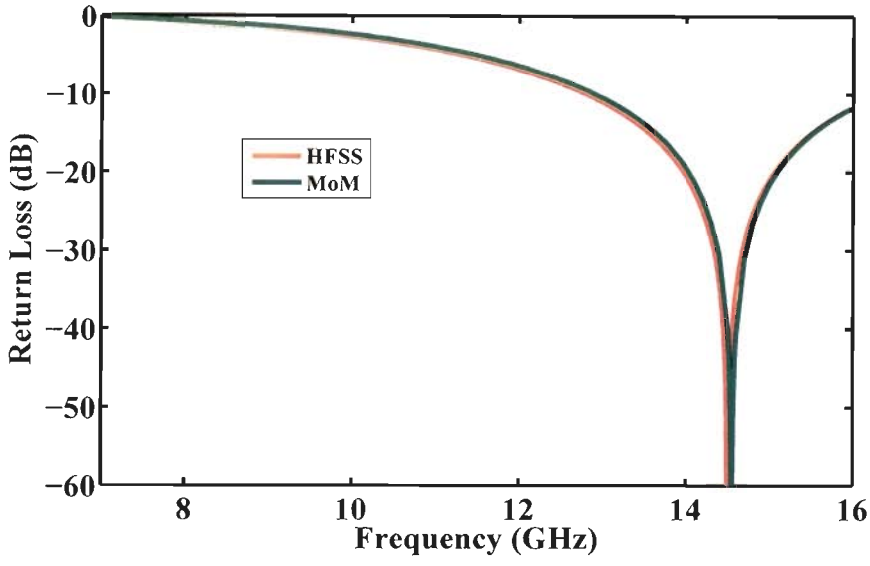

(a) 1st Iteration

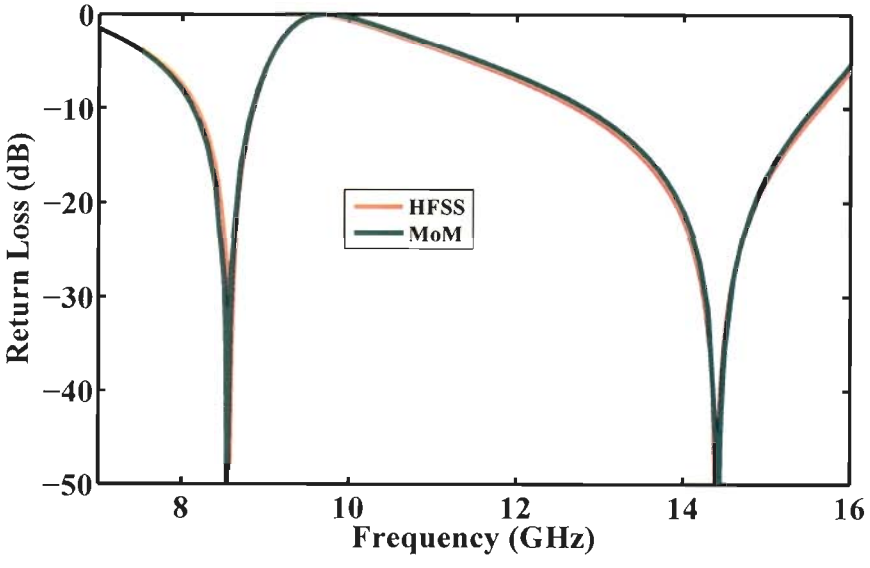

(b) 2nd Iteration

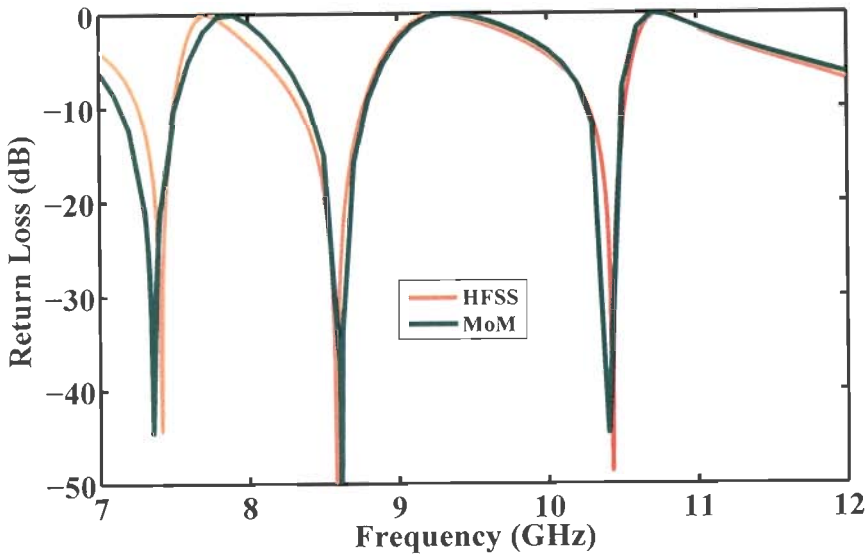

(c) 3rd Iteration

Figure 3.6: Return loss of modified Devil's staircase fractal diaphragm for different iterations.

Table 3.2: Resonant frequencies of modified Devil's staircase fractal diaphragm.

Iteration	Method	Resonant Frequencies (GHz)			Ratio	
		f_1	f_2	f_3	f_2/f_1	f_3/f_2
1	MoM	14.55				
	HFSS	14.50				
	Difference(%)	0.34				
2	MoM	8.54	14.42		1.69	
	HFSS	8.58	14.41		1.68	
	Difference(%)	0.47	0.07		0.60	
3	MoM	7.35	8.61	10.40	1.17	1.21
	HFSS	7.41	8.58	10.48	1.16	1.22
	Difference(%)	0.81	0.35	0.76	0.85	0.82

here. The ratio between the two resonant frequencies is 1.68, which is slightly greater than the theoretical value of 1.5. In the third iteration, two resonances occur at 7.35 GHz and 10.40 GHz. These resonances are due to the apertures of lengths $7a/8$ (20.002 mm) and $5a/8$ (14.2875 mm). Again, the resonances occur at wavelengths twice the lengths of the apertures. The ratios between the successive resonant frequencies are equal to 1.17 and 1.21, as compared to the theoretical values 1.17 and 1.2, respectively. Although the frequency response is shown up to 12 GHz, the resonance due to the first iteration aperture remains around 14.00 GHz. The resonance frequencies for other apertures lie outside the band considered here. Thus, a third iteration modified Devils fractal diaphragm is suitable for generating three resonances within the dominant mode operating band of the waveguide which can be effective in the design of multiband waveguide filters.

A further modification of the fractal has been investigated in order to obtain a symmetric arrangement of apertures. The apertures in the upper section of the waveguide introduced in the second and third iterations are removed and an image of the remaining apertures is taken. The resulting geometry of the diaphragm at third iteration is shown in Fig. 3.7 and the variation of return loss of the symmetric fractal diaphragm is shown in Fig. 3.8. The results are obtained with 288 rooftop functions. Again the present method shows a good agreement with the HFSS results. A comparison of frequency response between the the modified and symmetric Devil's staircase fractals diaphragms are tabulated in Table 3.3. From the table, it is evident that the resonant frequencies for the symmetric Devil's fractal diaphragm shows an upward shift. This is in line with the observation presented in [71] for the dual aperture array. However, the ratio between the resonant frequencies remains almost same as was in case of

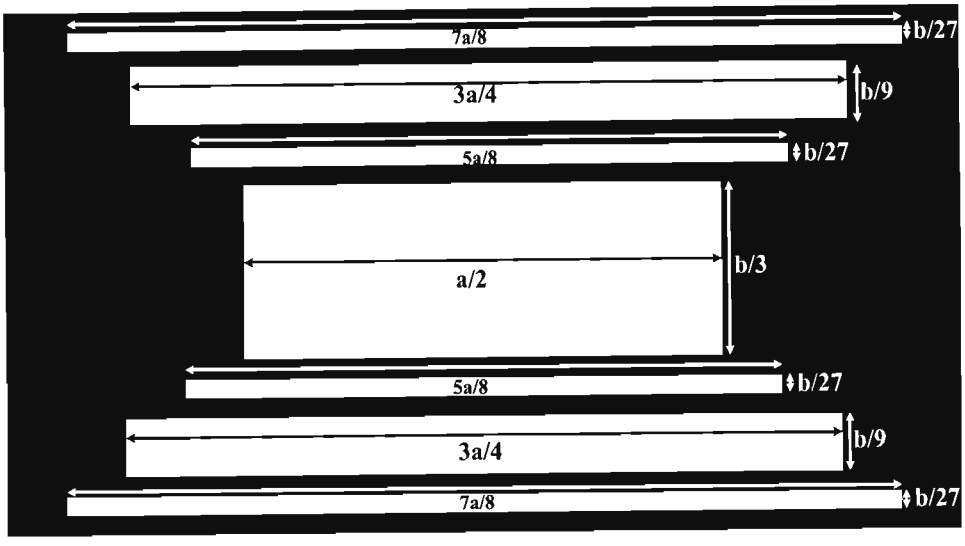

Figure 3.7: A 3rd iteration symmetric modified Devil's staircase fractal diaphragm(a=22.86 mm, b=10.16 mm).

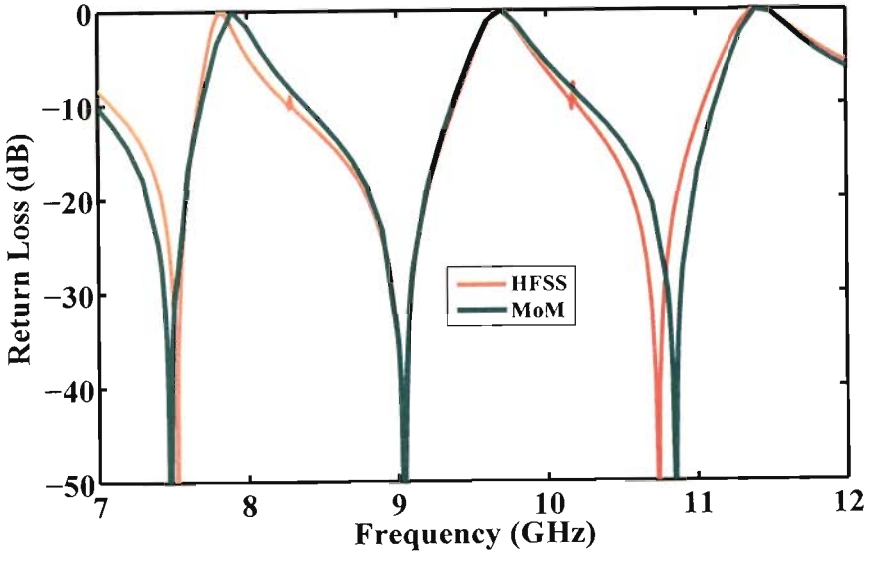

Figure 3.8: Return loss of 3rd iteration Symmetric modified Devil's staircase fractal diaphragm.

Table 3.3: Comparison of resonant frequencies between the modified and symmetric Devil's staircase fractal at 3rd iteration.

Geometry	Resonant Frequencies (GHz)			Ratio	
	f_1	f_2	f_3	f_2/f_1	f_3/f_2
Modified fractal	7.35	8.61	10.40	1.17	1.21
Symmetric fractal	7.47	9.03	10.85	1.21	1.20

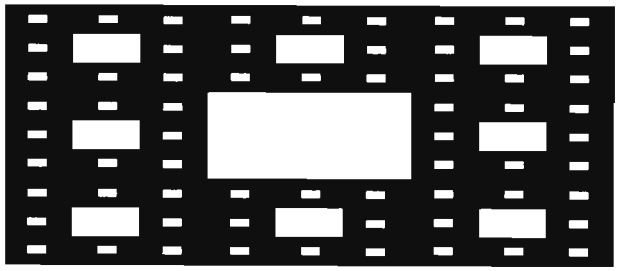

Figure 3.9: A 3rd iteration self-similar Sierpinski carpet fractal.

asymmetric Devil's staircase fractal diaphragm.

3.3.2 Self-affine Sierpinski Carpet Diaphragm

A square or a rectangle can be taken as the initial structure for the generation of original self similar Sierpinski carpet [2] fractal geometry. The rectangle is subdivided into nine equal subrectangles from which the center one is removed. The same process is iterated on the remaining subrectangles in the next iteration. The geometry of a 3rd iteration self-similar Sierpinski carpet fractal is shown in Fig. 3.9. For the self-similar fractal geometry, the scale factor in both x- and y-directions are same and equal to 1/3. Hence, as evident from Fig. 3.9, the aperture in 1st iteration will have a length a/3 (7.62 mm). The resonant frequency

of the aperture will be around 19.68 GHz and the ratio between the successive resonant frequency will be equal to 3 which will generate the resonance far outside the normal operating band of the waveguide. Taking this into consideration, a self-affine fractal geometry is proposed and the generation steps are shown in Fig. 3.10. The initial rectangle is subdivided into nine subrectangles such that the length of the three rectangles along the vertical axis are $s.L$ where s and L, respectively, denote scale factor and the length of the initial rectangle. The lengths of the other rectangles are $\frac{(1-s).L}{2}$. The initial rectangle is divided into three sections along y-axis. Thus, the widths of the rectangles are $W/3$, where W denotes the width of the initial rectangle. In the first iteration, the center rectangle is removed. In the next iteration, the same process is repeated on the remaining subrectangles. The dimensions of the removed rectangles along the vertical axis are $(s^2.L, w/9)$ and those along the sides of initial rectangle are $\left(\frac{(1-s)s.L}{2}, w/27\right)$. Now, the apertures with lengths much smaller than the larger dimension of the waveguide will have resonant frequency far away from the normal operating band of the guide and also, the apertures closer to the side wall of the waveguide will not affect the frequency response due to the weak electric field of TE_{10} mode close to the side wall. Hence, the apertures close to the sides of initial rectangle can be removed without affecting the final result. The resulting self-affine modified Sierpinski carpet fractal diaphragm is shown in Fig 3.11 for different iterations. The initial dimensions of the rectangle are (20.7 mm×5.10 mm) with s=0.87.

Similar to the analysis of Devil's fractal, first, a convergence analysis is carried out for the number of sections and the required number of waveguide modes. It is found that 28, 96 and 256 rooftop functions are required in the 1^{st}, 2^{nd} and 3^{rd} iterations, respectively. The frequency response of the modified self-affine

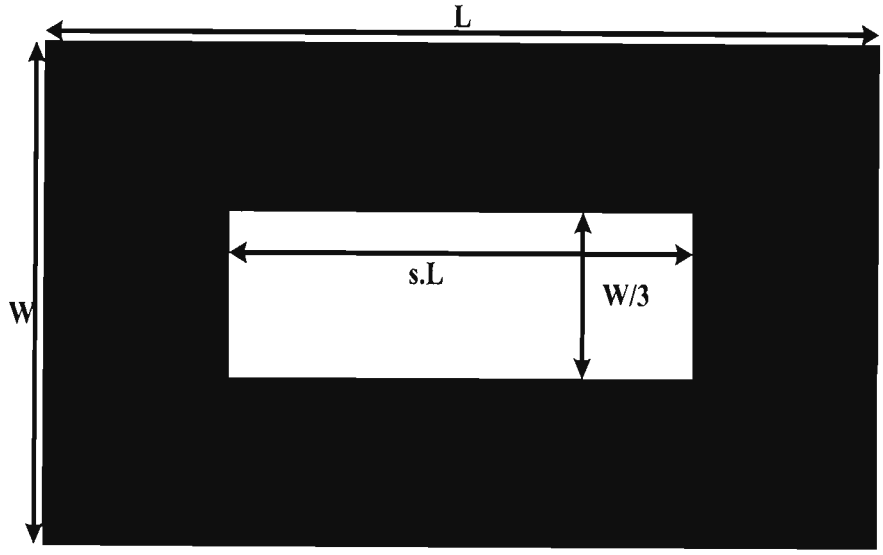

(a) 1st Iteration

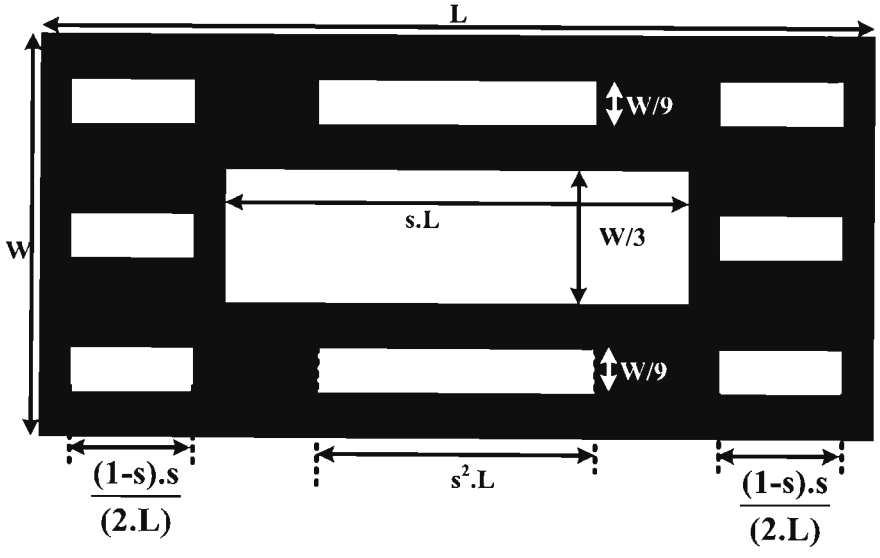

(b) 2nd Iteration

Figure 3.10: Generation steps of self-affine Sierpinski carpet fractal geometry.

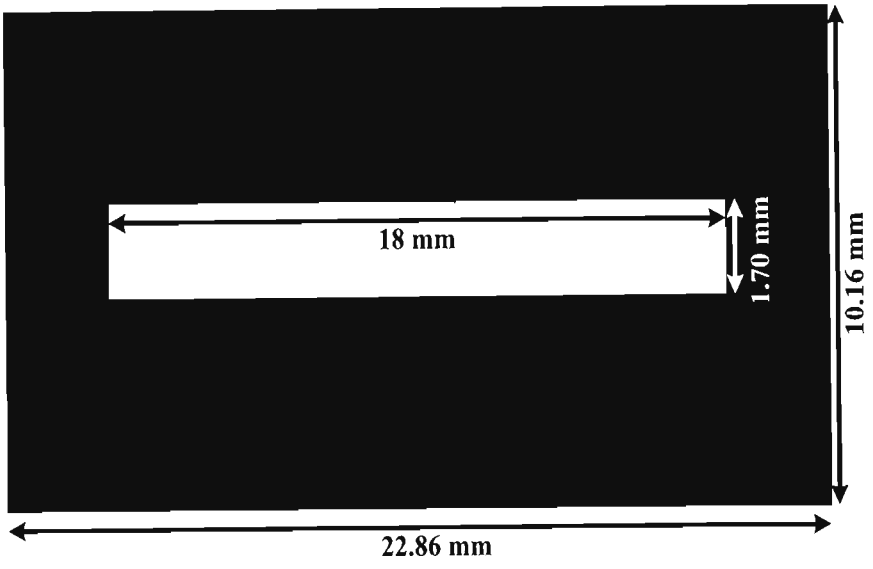

(a) 1st Iteration

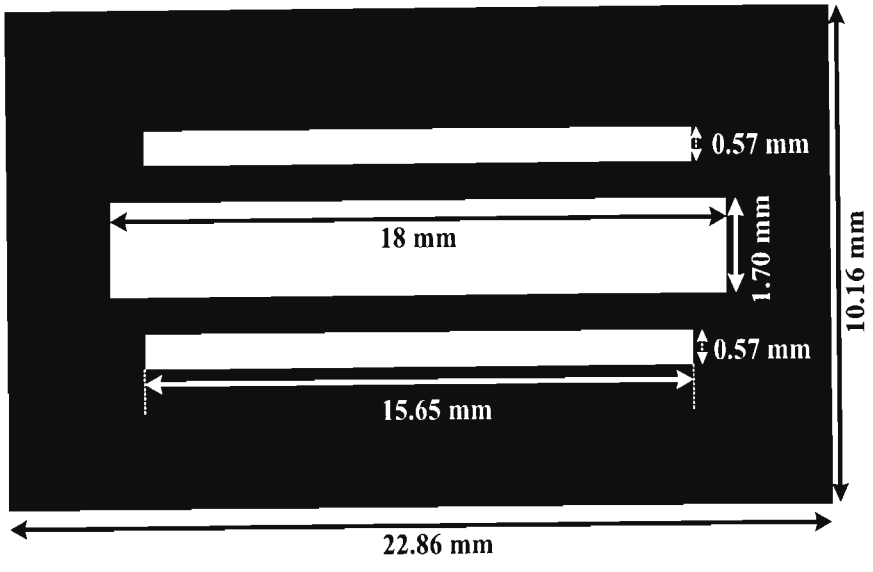

(b) 2nd Iteration

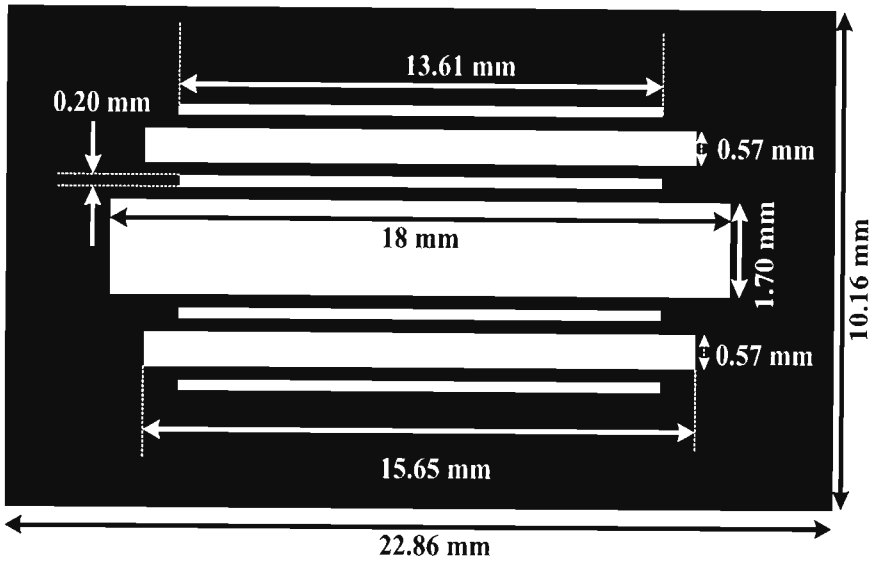

(c) 3rd Iteration

Figure 3.11: A self-affine modified Sierpinski carpet fractal diaphragm for different iterations.

Sierpinski carpet fractal aperture is shown in Fig. 3.12 and different parameters are tabulated in Table 3.4. At the first iteration, the aperture of length 18 mm resonates at 8.42 GHz, the corresponding wavelength is approximately twice the length of the aperture. In the second iteration, the second resonance at 10.5 GHz is generated due to the aperture length of 15.65 mm. The aperture length to resonant wavelength is 0.55. The ratio between the two resonant frequencies is 1.27 which is larger than the theoretical value 1.15. Also, first resonant frequency of the fractal diaphragm shifts downward. In the 3rd iteration, the resonant frequencies are 8.27 GHz, 9.91 GHz and 12.04 GHz with ratios between the successive resonant frequencies 1.20 and 1.21. Thus, the ratio approaches the theoretical value of 1.15 as the order of iteration increases. The second resonant frequency decreases sharply as compared to the first resonant frequency. Thus, using the

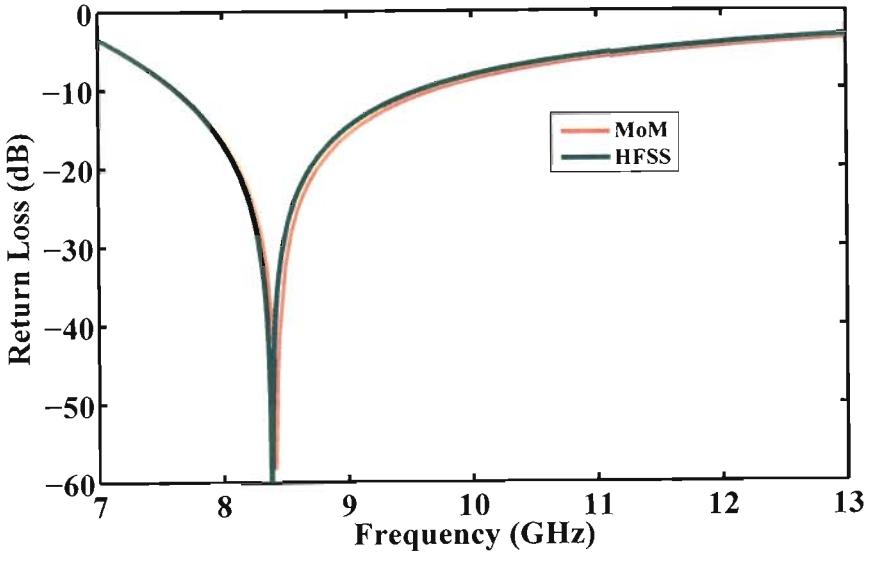

(a) 1st Iteration

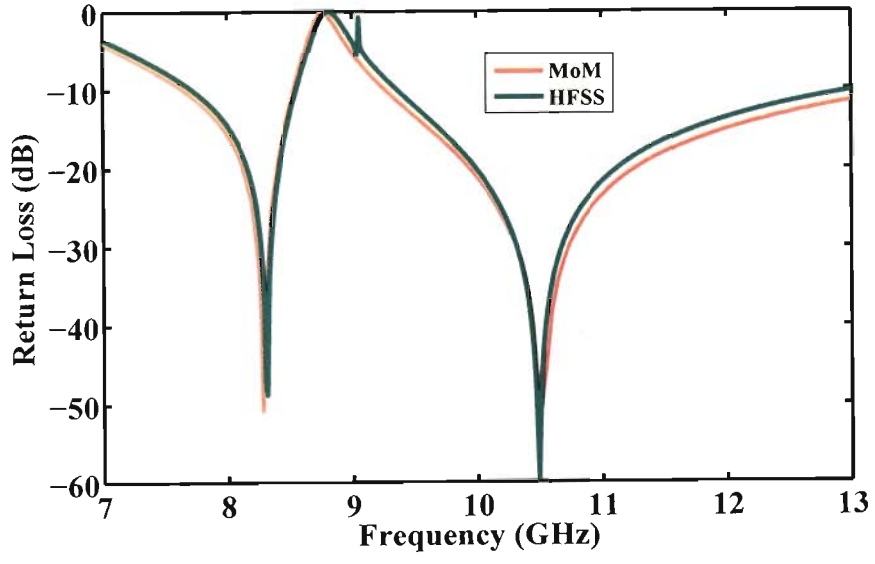

(b) 2nd Iteration

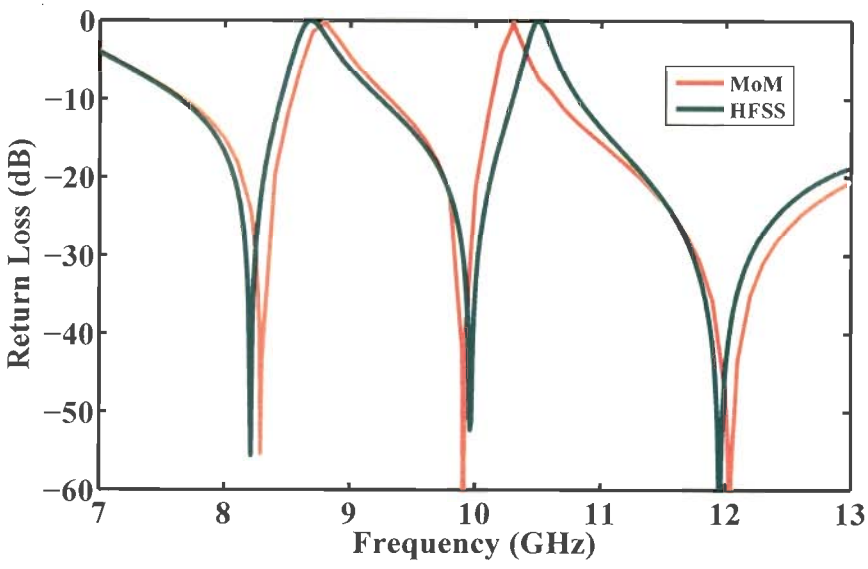

(c) 3rd Iteration

Figure 3.12: Return loss of modified self-affine Sierpinski carpet fractal diaphragm for different iterations.

Table 3.4: Resonant frequencies of self-affine Sierpinski carpet diaphragm.

Iteration	Method	Resonant Frequencies (GHz)			Ratio	
		f_1	f_2	f_3	f_2/f_1	f_3/f_2
1	MoM	8.42				
	HFSS	8.38				
	Difference(%)	0.48				
2	MoM	8.28	10.50		1.27	
	HFSS	8.30	10.49		1.26	
	Difference(%)	0.24	0.09		0.79	
3	MoM	8.27	9.91	12.04	1.20	1.21
	HFSS	8.21	9.96	11.96	1.21	1.20
	Difference(%)	0.73	0.50	0.66	0.83	0.83

self-affine fractal geometry three transmission bands are obtained. Since, the resonant frequencies are controlled by the lengths parallel to the larger dimension of the waveguide, the location of the resonant frequencies can also be changed by properly selecting the length of the initial rectangle. Also, by using different scale factor, one can control the location of resonant bands.

In the remaining subsections, the geometries considered are of arbitrary shape and Rao-Wilton-Glisson (RWG) functions are used to model the geometries.

3.3.3 Sierpinski Gasket Diaphragm

An ideal Sierpinski gasket [2] geometry is obtained by applying a geometric transformation on a generating triangle. An inverted triangle defined by the mid points of the sides of initial triangle is subtracted from the generating triangle. Successive repetition of this subtracting procedure results in an ideal Sierpinski gasket geometry. Due to practical limitations, only a few iterations are used in practice. The geometry of a 2^{nd} iteration Sierpinski gasket aperture in the transverse cross-section of a rectangular waveguide with cross-sectional dimensions $(a \times b)$ is shown in Fig. 3.13, with a scale factor $s = 0.5$. The vertices of generating triangle are chosen as $(0, 0)$, $(a, b/2)$ and $(0, b)$. Thus, the generating triangle has a base length b and height H equal to a. The resonant frequencies of this self-similar structure are spaced by a factor of 2. However, this factor can be chosen arbitrarily to allocate the resonant frequencies at a desired location [6]. In order to reduce the ratio of successive resonant frequencies of gasket aperture, we have developed a self-affine gasket geometry with a scale factor $s = 0.8$ as shown in Fig. 3.14. In the first iteration, the diaphragm consists of a single triangular aperture of length 18.29 mm $(0.8a)$ parallel to larger dimension of the waveguide. In the second iteration, three triangular apertures of lengths 14.63 mm $(0.64a)$

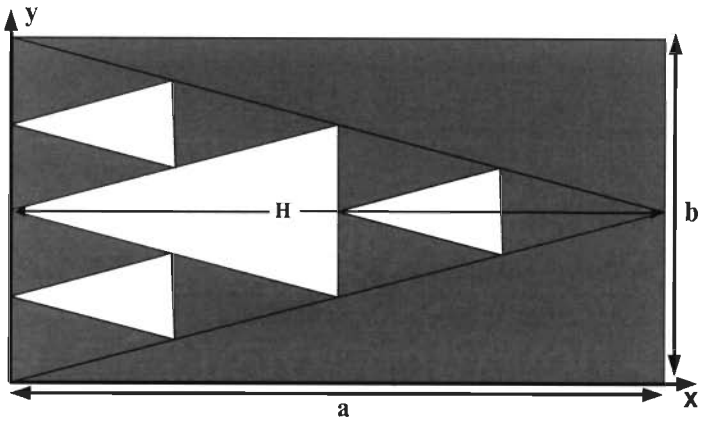

Figure 3.13: A 2^{nd} iteration self-similar Sierpinski gasket diaphragm with $s = 0.5$.

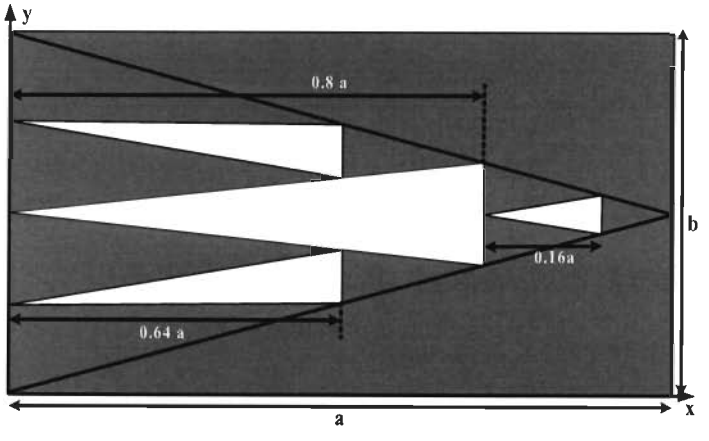

Figure 3.14: A 2^{nd} iteration self-affine Sierpinski gasket diaphragm with $s = 0.8$.

Table 3.5: Convergence analysis of single triangular aperture.

S. No.	No. of RWG functions	Modal Indices		$\|S_{11}\|$	% change
		M	N		
1	6	20	25	0.6728	
2	10	20	35	0.6981	3.76
3	14	25	45	0.7021	0.57
4	18	30	45	0.7085	0.91

and 3.66 mm ($0.16a$) are introduced.

Firstly, the convergence analysis for number of RWG functions and the required number of modal indices is performed for 1st iteration which is summarized in Table 3.5. It is found that 14 RWG functions are sufficient to obtain converged result with variation of magnitude of reflection coefficient less than 1%. Hence, the final output for the 1st iteration of Sierpinski gasket aperture is taken with 14 RWG functions. Similar convergence analysis is also performed for the 2nd iteration and it is found that 44 RWG functions are required to obtain a converged result. The variation of return loss of this gasket aperture placed inside an X-band rectangular waveguide is shown in Fig. 3.15 for two iterations. The single triangular aperture resonates at 9.04 GHz. It can be seen from the plots that for second iteration, the 1st resonant frequency shifts to 8.92 GHz and a second resonance appears at 11.72 GHz with a ratio between these two frequencies equal to 1.31. This 2nd resonance appears due to triangular apertures of lengths 14.63 mm, introduced in the second iteration. In general, the length parallel to the larger dimension of waveguide determines the resonant frequency of the aper-

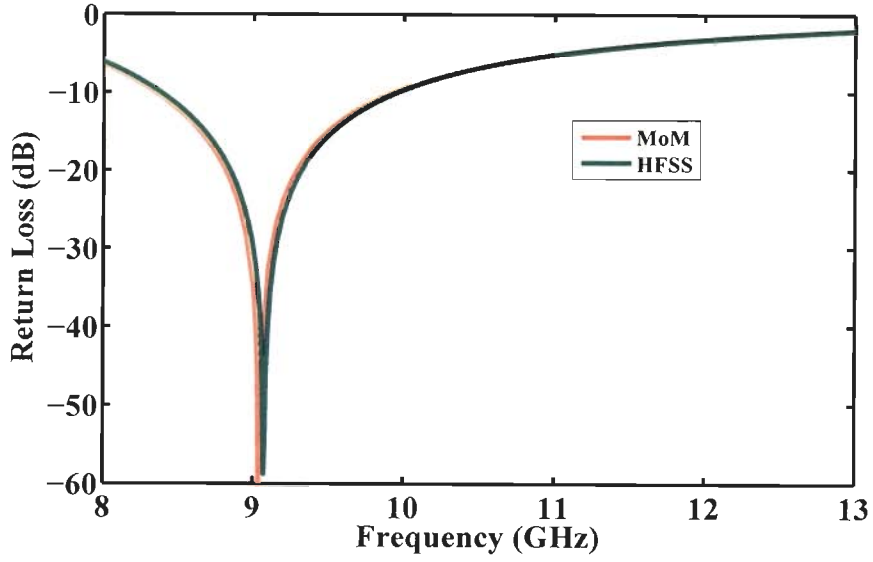

(a) 1st Iteration

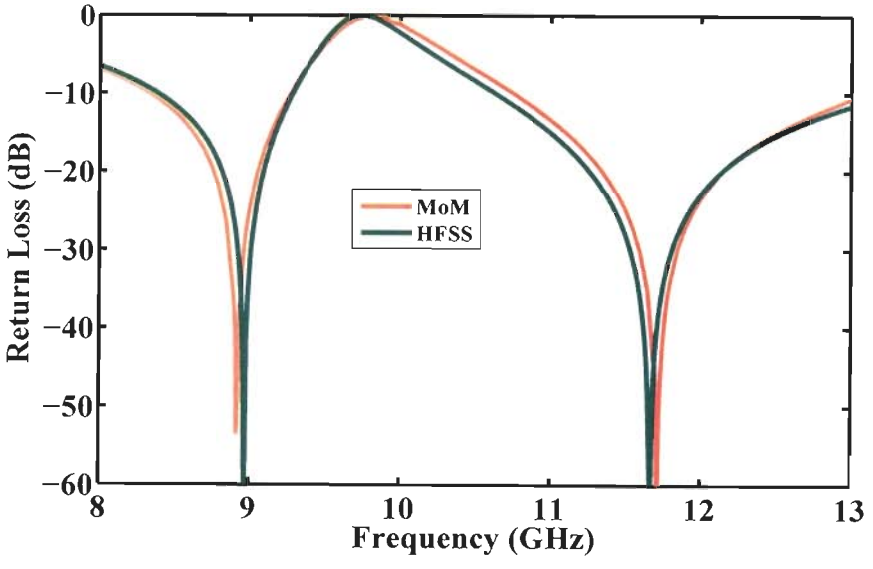

(b) 2nd Iteration

Figure 3.15: Return loss of self-affine Sierpinski gasket diaphragm with $s = 0.8$ for two iterations.

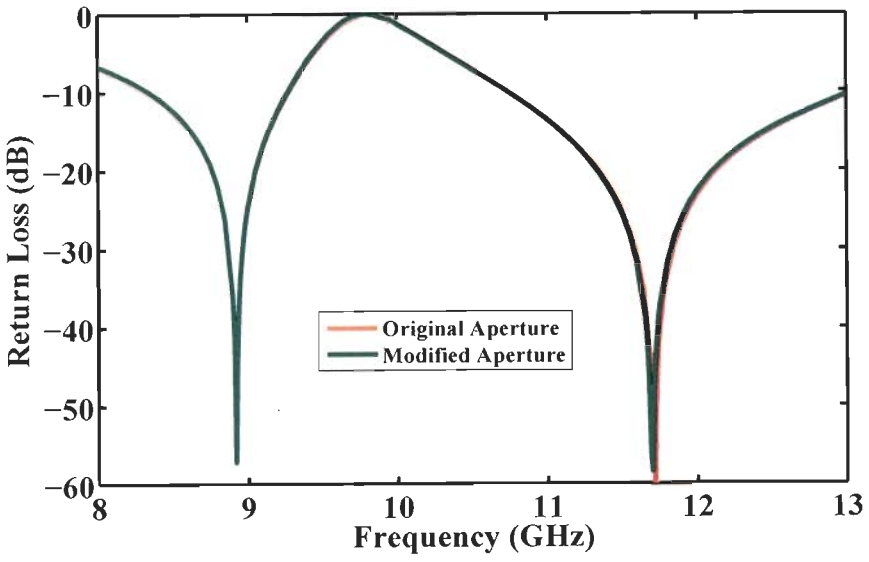

Figure 3.16: Return loss of 2nd iteration modified Sierpinski gasket diaphragm.

ture. Hence, it may be concluded that the smaller aperture of length 3.66 mm will have a resonant frequency far outside the frequency band under consideration and also, it will not affect the frequency response due to its position near to the side wall of the waveguide where the electric field of TE_{10} mode is weak. This is confirmed by Fig. 3.16, which shows the response with the 3.66 mm aperture removed. As can be seen from the plots, a rejection frequency is formed at 9.80 GHz for the 2nd iteration. The resonant frequencies of the Sierpinski gasket aperture are summarized in Table 3.6.

In order to study the effect of scale factor on the frequency response, two more gaskets with scale factors $s = 0.7$ and $s = 0.9$ were analyzed. However, if the same generating triangle of base length b and height a is used, the 1st iteration apertures will have lengths $0.7a$ and $0.9a$, respectively. In such a case, one of the resonant frequencies will fall well outside the normal operating band of the waveguide. Therefore, the length of first iteration triangle was kept constant and

Table 3.6: Resonant frequencies of Sierpinski gasket fractal diaphragm.

Method	1st Iteration	2nd Iteration		Ratio
	f_1 (GHz)	f_1 (GHz)	f_2 (GHz)	f_2/f_1
MoM	9.04	8.92	11.72	1.31
HFSS	9.07	8.97	11.67	1.30
Difference (%)	0.33	0.56	0.43	0.76

Table 3.7: Effect of scale factor on the frequency response of Sierpinski gasket diaphragm.

Scale Factor (s)	f_1 (GHz)	f_2 (GHz)	f_2/f_1	Theoretical Ratio
0.7	9.2	13.1	1.42	1.43
0.8	8.92	11.72	1.31	1.25
0.9	8.45	10.2	1.21	1.11

the height H of the generating triangles was changed such that $H = \frac{18.29}{s}$. The variations of return loss for 2^{nd} iteration gasket apertures is shown in Fig. 3.17 for three different scale factors. It can be seen from the plots that, for a fixed length of the 1^{st} iteration aperture, the first resonant frequency decreases with higher scale factor and the successive frequency ratios are 1.42, 1.31 and 1.21 for $s = 0.7$, $s = 0.8$ and $s = 0.9$, respectively. The effects of scale factors are shown in Table 3.7. Thus, the resonant frequencies can be controlled by changing the length of the primary triangle in conjunction with the scale factor.

Another modification of Sierpinski gasket structure is obtained by dipole arrangement of the original apertures. The generation steps of the modified dipole structure are same as that of an ideal gasket geometry except that an

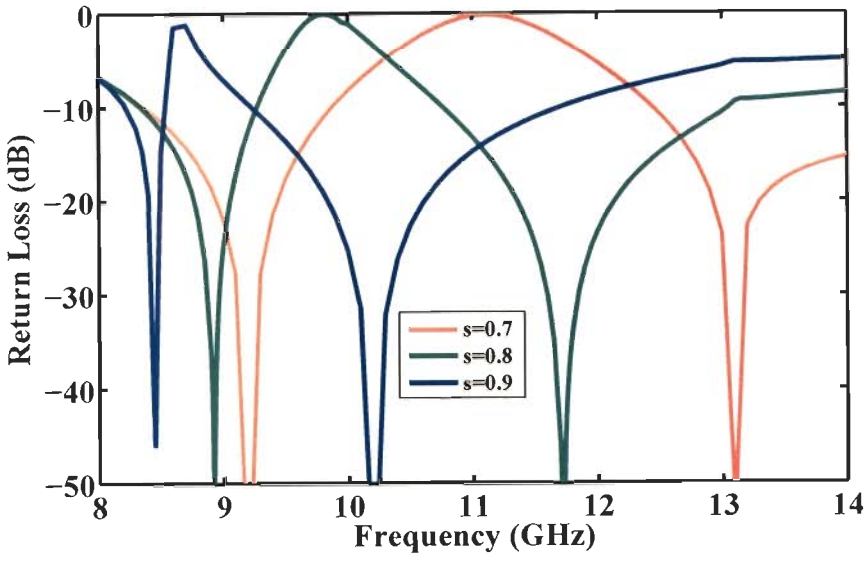

Figure 3.17: Return loss of 2nd iteration gasket diaphragm with different scale factors.

image of the original structure is taken about the base line of the initial triangle. The first two iterations of gasket dipole aperture are shown in Fig. 3.18. In order to ensure the continuity of apertures of original and image triangles, a certain amount of overlapping is incorporated. For scale factors greater than 0.5, the vertex of the subtracted triangle is kept at the mid point of the base of subtracted triangle instead of keeping it at the base of initial triangle, as illustrated in Fig. 3.19 for an arbitrary triangle with vertices (x_1, y_1), (x_2, y_2) and (x_3, y_3). The geometry of a 2nd iteration modified gasket dipole diaphragm is shown in Fig. 3.20 and the variation of return loss for different iterations is shown in Fig. 3.21. In this case, 17 and 51 RWG functions were used to obtain a converged result for 1st and 2nd iteration, respectively. It can be seen that the first resonant frequency decreases with the order of iteration. The resonant frequencies for the 2nd iteration gasket dipole geometry are at 8.70 GHz and

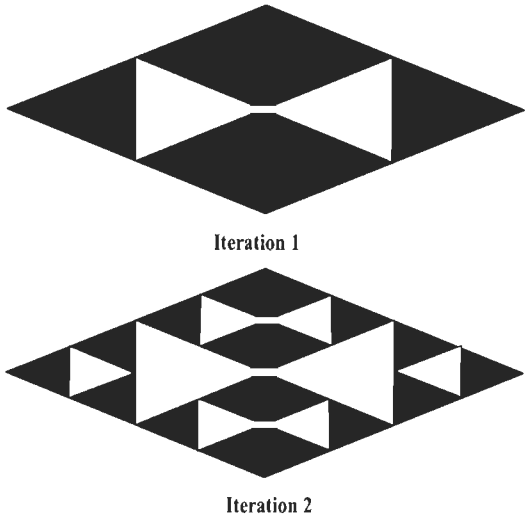

Figure 3.18: Generation steps of Sierpinski gasket dipole geometry.

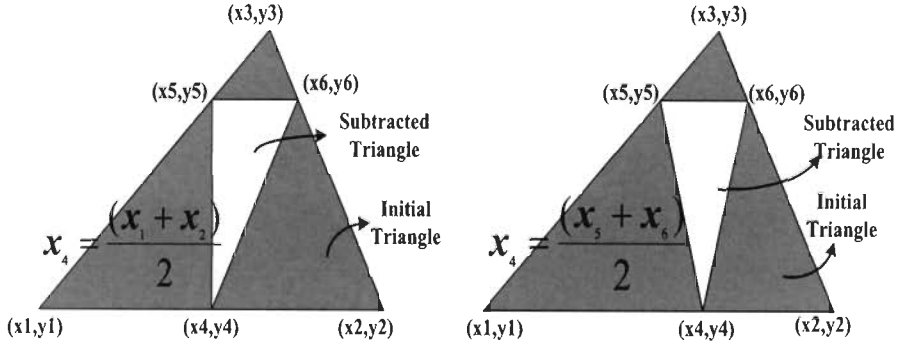

(a) Original Geometry (b) Modified Geometry

Figure 3.19: Geometric modification for dipole arrangement of 1st iteration gasket aperture with scale factor greater than 0.5.

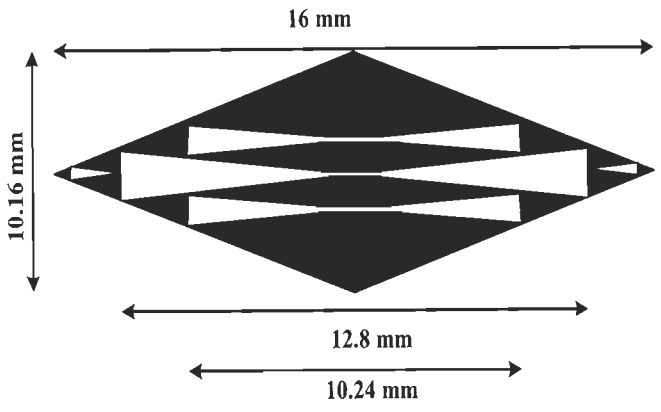

Figure 3.20: A 2nd iteration modified self-affine gasket dipole diaphragm.

13.05 GHz with a ratio of 1.5. This ratio is much higher than the ideal ratio 1.25 which is due to the incorporated geometrical modifications. Also, a comparison of the dimensions and resonant frequencies of the original gasket and the dipole aperture shows that the dipole aperture can resonate at a smaller frequency as compared to the original gasket aperture of same length.

3.3.4 Hilbert Curve Diaphragm

Hilbert curve fractal geometries are widely used in antenna miniaturization due to their space-filling properties. An important characteristic of space-filling curve is that, a relatively longer slot can be compacted into a smaller area and such slots resonate at a wavelength much larger than the wavelength corresponding to the initial area which it fills. The generation steps of Hilbert curve fractal can be found in [2]. Each successive stage consists of four copies of previous stage, connected with additional line segments. The geometry is not strictly self-similar due to these additional line segments. The dimension of the Hilbert curve approaches 2 as the number of iterations increase and for large number of

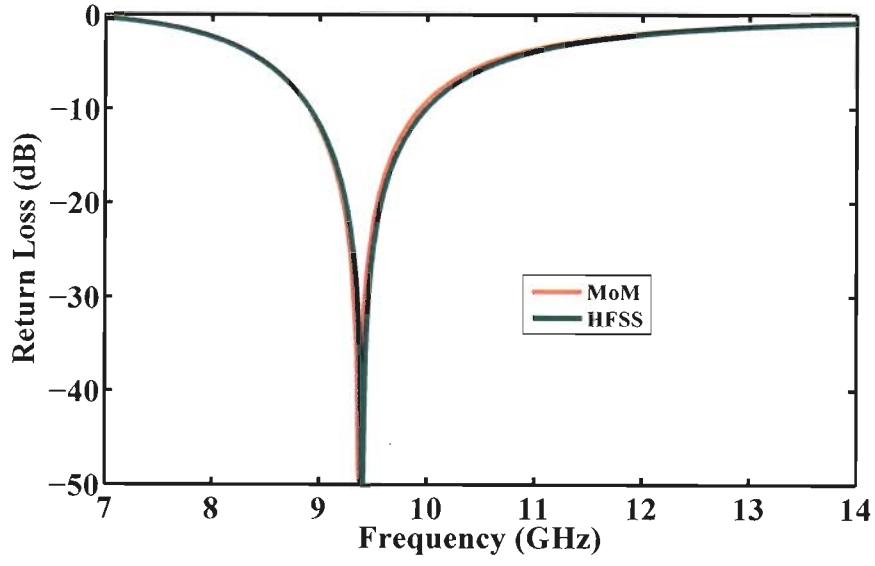

(a) 1st Iteration

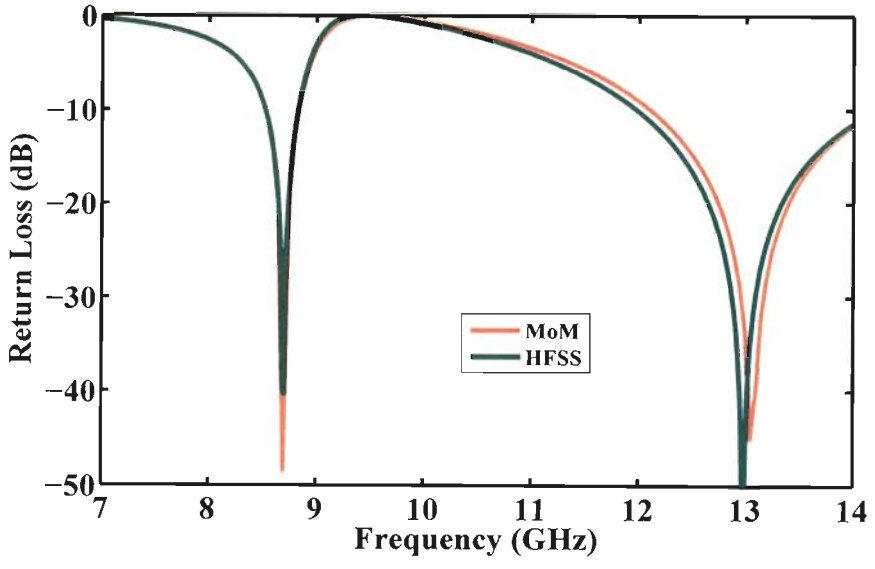

(b) 2nd Iteration

Figure 3.21: Return loss of Sierpinski gasket dipole diaphragm for two iterations.

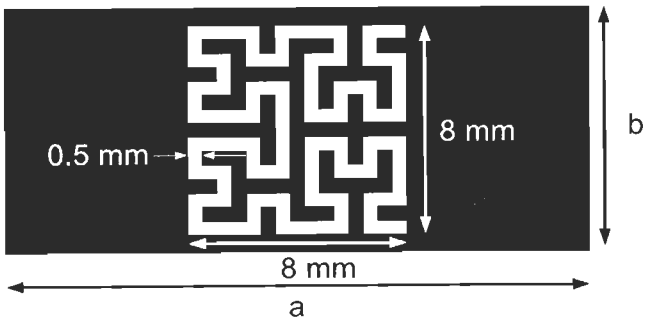

Figure 3.22: A 3rd iteration Hilbert curve fractal diaphragm.

iterations, the length of the additional line segments are negligible as compared to the total length of the curve which makes the geometry self-similar. Here, we have considered a Hilbert curve frequency selective diaphragm with an initial square of dimensions 8 mm × 8 mm. The geometry of a third iteration Hilbert curve diaphragm in the transverse cross-section of a rectangular waveguide is shown in Fig. 3.22.

The number of RWG functions required to obtain converged result for 1st, 2nd and 3rd iterations are 23, 51, and 103, respectively. The frequency response of Hilbert curve aperture for three iterations is shown in Fig. 3.23 and the results are summarized in Table 3.8. It can be seen from the plots that the first resonant frequency of Hilbert aperture decreases significantly as the order of iteration increases, despite the outer dimension of initial square being constant. The primary resonant frequency for the first iteration is 15.66 GHz. The value for the next two higher order iterations are 10.46 GHz and 7.55 GHz, respectively. Hence, there is a 51.78% decrease in the first resonant frequency. The ratios between the successive resonant frequencies for 3rd iteration Hilbert aperture are 1.59 and 1.63, whereas for 2nd iteration, the corresponding value is 1.80. Hence, by using higher order iterations, the fractal frequency selective diaphragm can

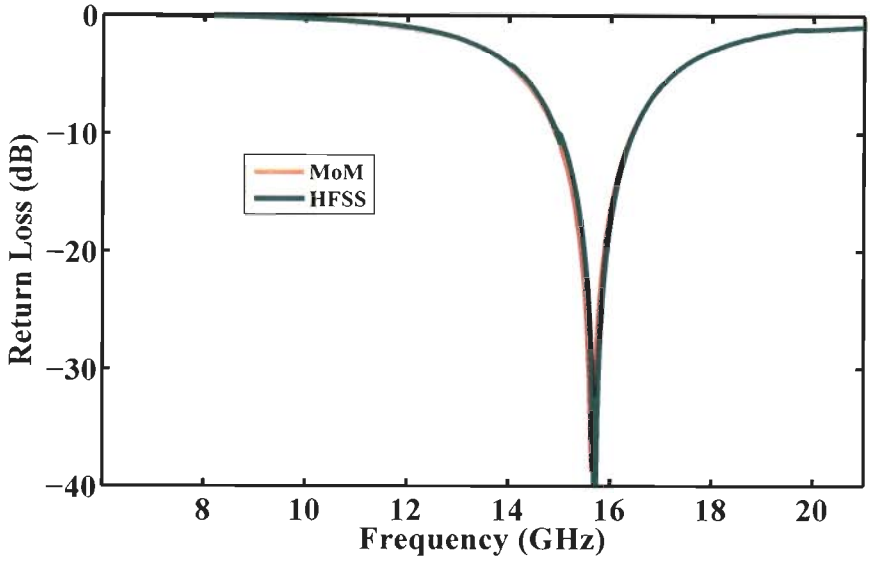

(a) 1st Iteration

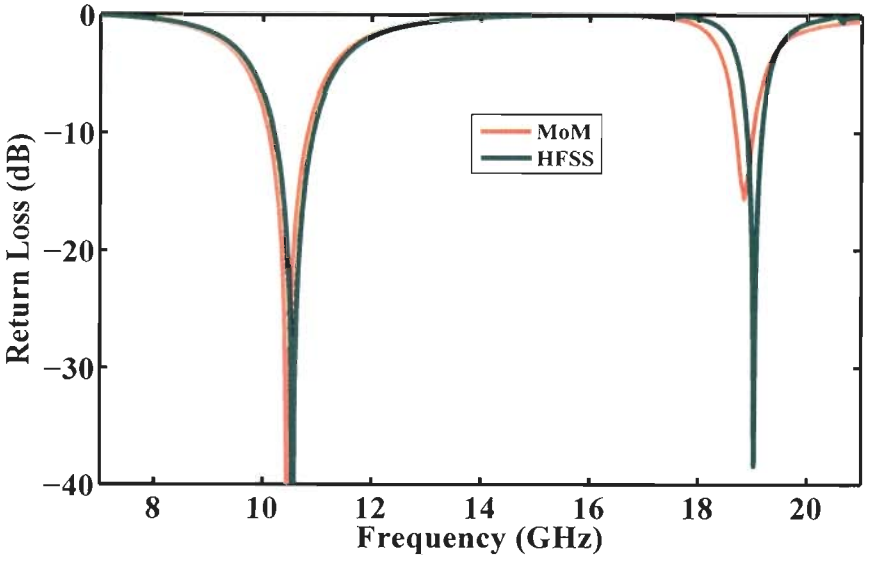

(b) 2nd Iteration

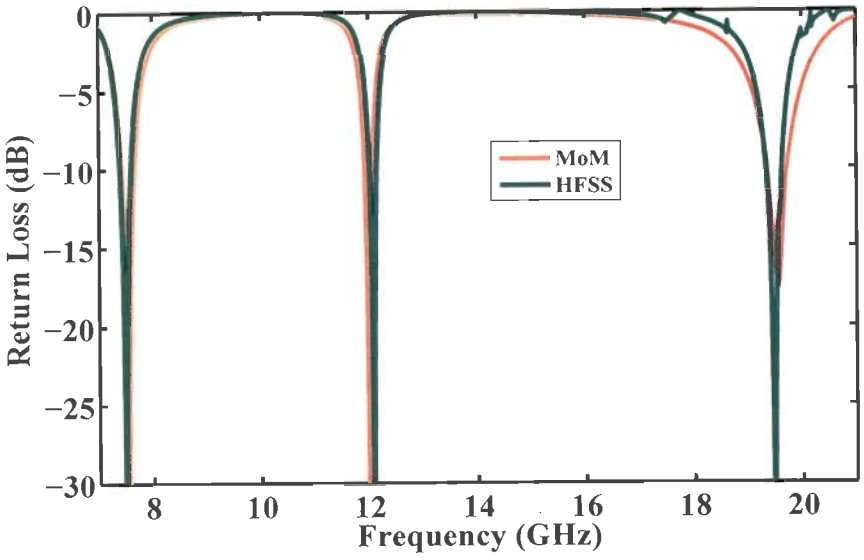

(c) 3rd Iteration

Figure 3.23: Return loss of Hilbert curve fractal diaphragm for different iterations.

Table 3.8: Resonant frequencies of Hilbert curve fractal diaphragm.

Iteration	Method	Resonant Frequencies (GHz)			Ratio	
		f_1	f_2	f_3	f_2/f_1	f_3/f_2
1	MoM	15.66				
	HFSS	15.71				
	Difference(%)	0.32				
2	MoM	10.46	18.85		1.80	
	HFSS	10.55	19.02		1.80	
	Difference(%)	0.86	0.90		0	
3	MoM	7.55	11.99	19.56	1.59	1.63
	HFSS	7.49	12.07	19.48	1.61	1.61
	Difference(%)	0.79	0.67	0.41	1.25	1.23

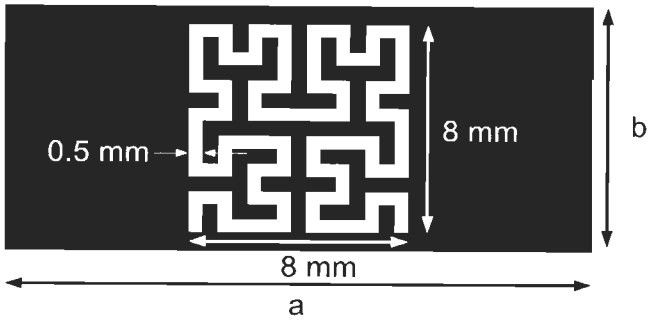

Figure 3.24: A 3rd iteration rotated Hilbert curve fractal diaphragm.

be made to resonate at smaller intervals. By changing the initial dimension of the square, the resonant bands can be placed at desired location.

The location of these resonant frequencies can also be changed by rotating the Hilbert aperture by 90° as shown in Fig. 3.24, since now the dominant mode electric field encounters a different orientation of the aperture geometry. The frequency response of the rotated Hilbert curve diaphragm of 3rd iteration is shown in Fig. 3.25. Here, the resonances occur at 10.35 GHz, 13.95 GHz, 20.35 GHz with ratios 1.35 and 1.46. It can be seen from the plots that the frequency response consists of wide stopbands separated by very sharp transmission bands. Also, by using higher iterations, we can locate the resonant frequencies within the operating band of X-band rectangular waveguide. It may be noted that the resonant frequencies are relatively closely spaced for the rotated Hilbert structure.

3.3.5 Plus Shape Fractal Diaphragm

Plus shape fractal apertures [50] are widely used in the design of frequency selective layers. An ideal plus shape fractal is generated by placing four copies of

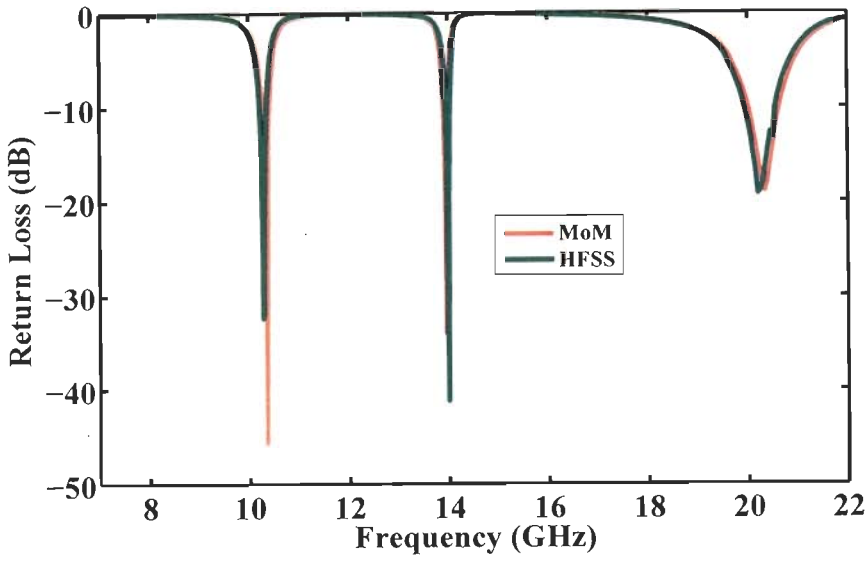

Figure 3.25: Return loss of 3rd iteration rotated Hilbert curve frequency selective diaphragm.

the initial geometry, each of which is scaled by a factor 0.5. The basic limitation of this geometry is that only a few iterations are possible, because the spacing between the elements decreases as the order of iteration increases. Here, we have designed a self-affine plus shape fractal aperture as shown in Fig. 3.26. The initial plus shape has a length 14 mm along x-direction and 8 mm along y-direction. In the 2nd iteration, the initial structure is scaled by 0.7 in x-direction and by 0.5 in y-direction and four such copies are placed at points defined as $(a/4, b/4)$, $(3a/4, b/4)$, $(3a/4, 3b/4)$ and $(a/4, 3b/4)$.

The numbers of RWG functions required to obtain converged result are 25 and 109 for 1st and 2nd iteration, respectively. The variation of return loss for TE_{10} mode incidence is shown in Fig. 3.27 for two iterations. As seen from the plot, the initial plus shape aperture resonates at 10.85 GHz. The ratio between horizontal length of the plus aperture and corresponding resonant wavelength is

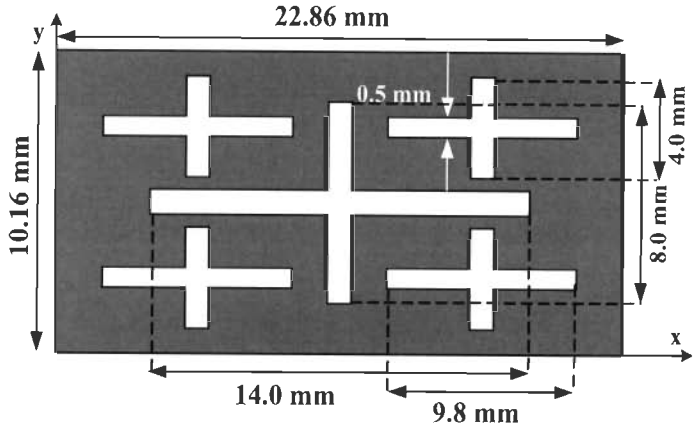

Figure 3.26: A 2nd iteration plus shape fractal diaphragm.

around 0.48. For the second iteration, the resonant frequencies are 10.34 GHz and 16.86 GHz with a ratio of 1.63. Evidently, the first resonant frequency of the fractal geometry decreases with the order of iteration. The wavelength corresponding to the second resonant frequency is around 1.82 times the horizontal length of the second iteration plus shape fractal. Since, the aperture length perpendicular to the incident electric field primarily determines the resonant frequency, the effect of vertical arm is expected to be small. Therefore, a modification of the above fractal structure was considered by removing the vertical arms of the plus shape resulting in five rectangular apertures of dimensions (14.0 mm $\times$ 0.5 mm) and (9.8 mm $\times$ 0.5 mm). The frequency response of the modified structure is shown in Fig. 3.28. It can be seen from the plot that the first resonant frequency is at 10.85 GHz which corresponds to that of the first iteration single rectangular aperture. The response remains the same for higher frequency region. Hence, it may be concluded that the length of vertical arm can be used as a parameter to fine tune the lower resonant frequency.

In order to see the effect of scale factor on the response, we have analyzed a

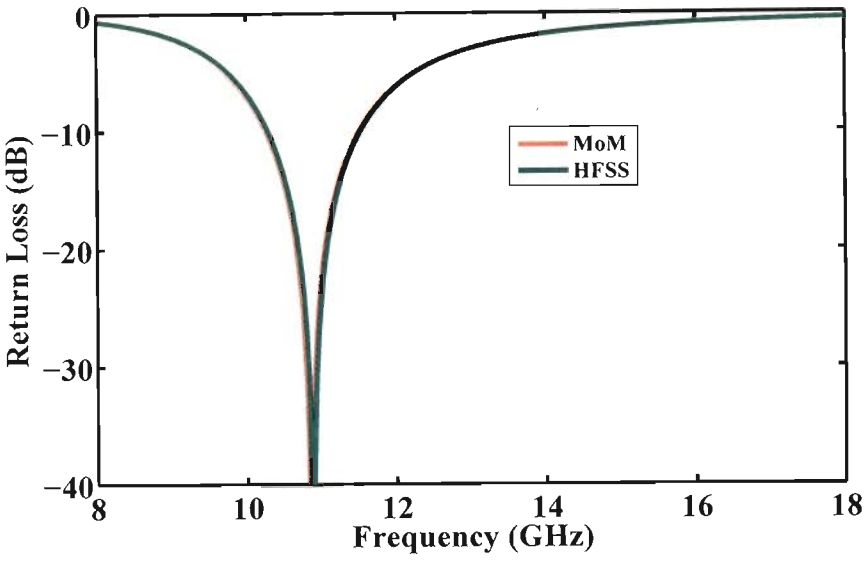

(a) 1st Iteration

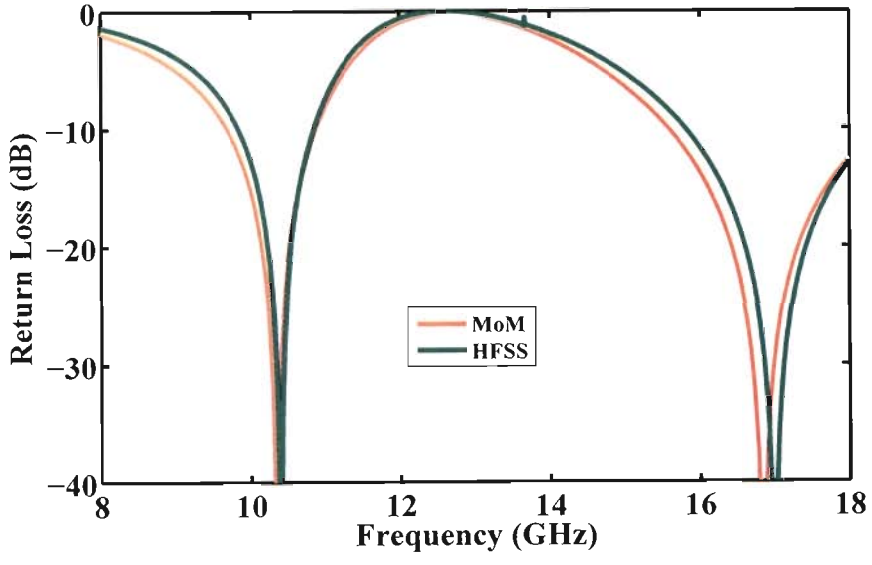

(b) 2nd Iteration

Figure 3.27: Return loss of plus shape fractal diaphragm for two iterations.

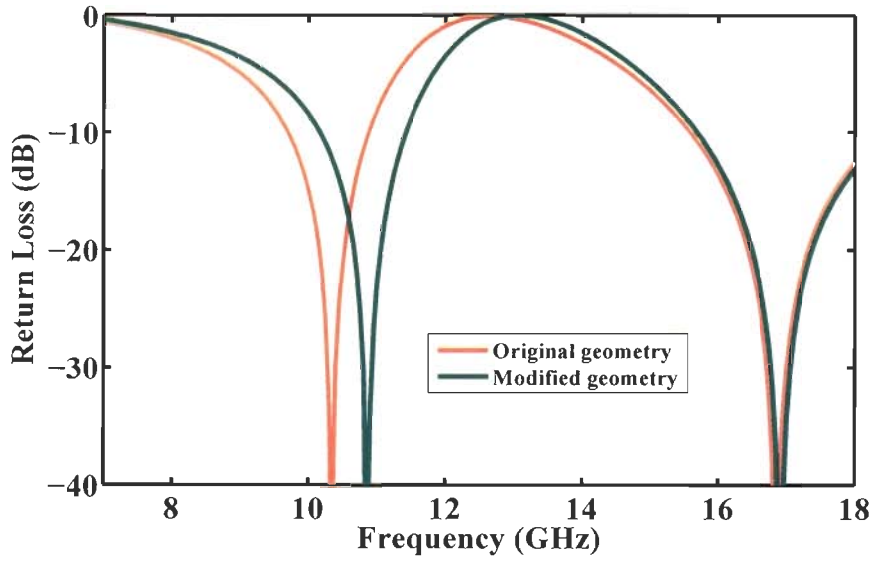

Figure 3.28: Return loss of 2nd iteration modified plus shape fractal diaphragm.

plus shape fractal with a scale factor of $s = 0.6$. The initial length of horizontal arm of plus shape has been taken to be 18 mm with vertical arm length equal to 8 mm. The size of the initial plus shape is chosen such that the second iteration plus apertures can be fitted within the cross sectional dimension of the waveguide. The initial geometry is scaled by 0.6 in x-direction and by 0.5 in y-direction resulting in four plus structures of horizontal length 10.8 mm and vertical length 4 mm. The variation of return loss of 2nd iteration plus fractal diaphragm with different scale factors is shown in Fig. 3.29. It can be seen from the plot that with $s = 0.6$, the resonant frequencies are at 8.05 GHz and 15.8 GHz with a ratio of 1.96. Again, the resonant wavelengths are approximately twice the horizontal length of the plus aperture. Hence, the scale factor along with the initial length of the plus shape can be used as a design parameter in order to locate the resonant band at a desired location.

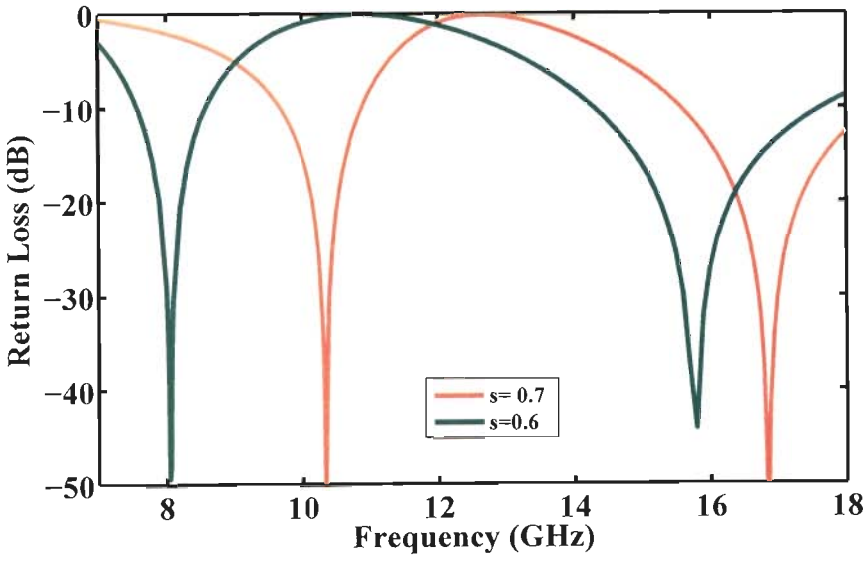

Figure 3.29: Return loss of 2nd iteration plus shape fractal diaphragm with different scale factors.

3.3.6 Minkowski Fractal Diaphragm

Minkowski fractal elements are also widely used in the design of antenna and frequency selective surface elements [50]. The fractal is generated by using an iterative process involving scaling and translation of the starting geometry. The initial geometry is a square and the prefractal consists of five transformations. The IFS of the Minkowski fractal can be expressed as [50]

$$W_1 \begin{pmatrix} x \\ y \end{pmatrix} = \begin{pmatrix} \frac{2}{5} & 0 \\ 0 & \frac{2}{5} \end{pmatrix} \begin{pmatrix} x' \\ y' \end{pmatrix} + \begin{pmatrix} \frac{3}{10} \\ \frac{3}{10} \end{pmatrix} \tag{3.17}$$

$$W_2 \begin{pmatrix} x \\ y \end{pmatrix} = \begin{pmatrix} \frac{1}{3} & 0 \\ 0 & \frac{1}{3} \end{pmatrix} \begin{pmatrix} x' \\ y' \end{pmatrix} + \begin{pmatrix} 0 \\ 0 \end{pmatrix} \tag{3.18}$$

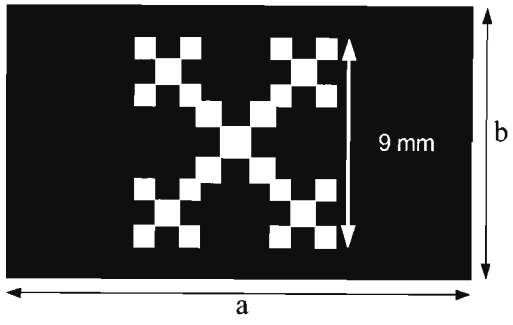

Figure 3.30: A 2nd iteration Minkowski fractal diaphragm.

$$W_3 \begin{pmatrix} x \\ y \end{pmatrix} = \begin{pmatrix} \frac{1}{3} & 0 \\ 0 & \frac{1}{3} \end{pmatrix} \begin{pmatrix} x' \\ y' \end{pmatrix} + \begin{pmatrix} \frac{2}{3} \\ 0 \end{pmatrix} \tag{3.19}$$

$$W_4 \begin{pmatrix} x \\ y \end{pmatrix} = \begin{pmatrix} \frac{1}{3} & 0 \\ 0 & \frac{1}{3} \end{pmatrix} \begin{pmatrix} x' \\ y' \end{pmatrix} + \begin{pmatrix} \frac{2}{3} \\ \frac{2}{3} \end{pmatrix} \tag{3.20}$$

$$W_5 \begin{pmatrix} x \\ y \end{pmatrix} = \begin{pmatrix} \frac{1}{3} & 0 \\ 0 & \frac{1}{3} \end{pmatrix} \begin{pmatrix} x' \\ y' \end{pmatrix} + \begin{pmatrix} 0 \\ \frac{2}{3} \end{pmatrix} \tag{3.21}$$

The geometry of 2nd iteration Minkowski fractal diaphragm is shown in Fig. 3.30, where the starting geometry is a square of dimensions 9 mm × 9 mm.

The frequency response of Minkowski diaphragm for different iterations are shown in Fig. 3.31. The numbers of RWG functions required to obtain a converged result are 40, 64, and 403 for 1st, 2nd and 3rd iteration, respectively. The resonant frequency of the square aperture is well beyond the dominant mode operating frequency range of the waveguide. As, the order of iteration increases,

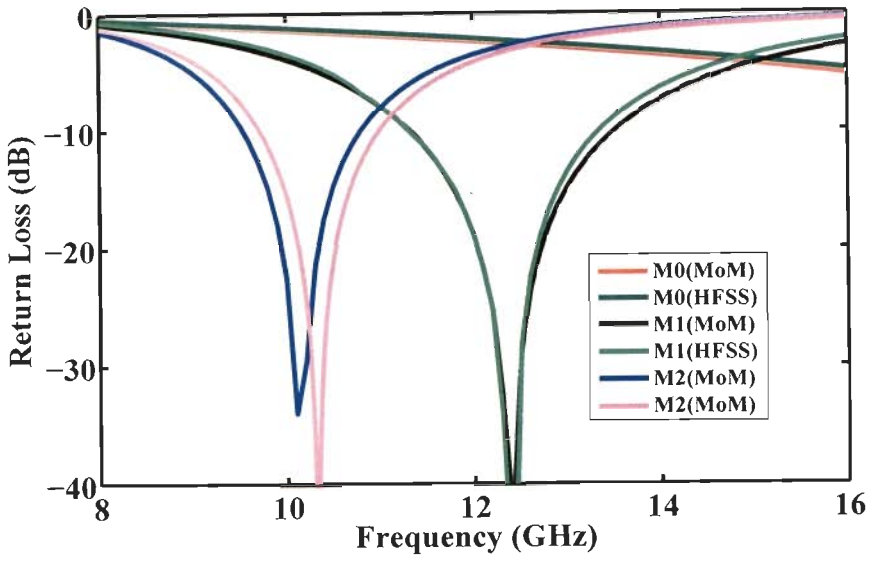

Figure 3.31: Return loss of Minkowski fractal diaphragm with different iterations.

the resonant frequency decreases significantly from 12.4 GHz to 10.1 GHz. Hence, there is a 19% reduction of resonant frequency from the 1st to 2nd iteration. Thus, the frequency selective diaphragm resonates at much larger wavelength than the corresponding wavelength for initial geometry. The scaling factor of the geometry is $\frac{1}{3}$ which causes the higher order resonant bands spaced by a factor around 3 and this frequency will fall well outside the considered frequency band.

3.3.7 Koch Fractal Diaphragm

Another fractal geometry which is extensively used in antenna miniaturization is Koch curve. The key feature of this fractal geometry is that the end-to-end length remains the same, although the total length of the curve increases by a factor 4/3 after each iteration. In this analysis, we have considered a 10 mm × 0.5 mm slot oriented along the larger dimension of the waveguide. A third iteration Koch fractal slot with 60° indentation angle is shown in Fig. 3.32.

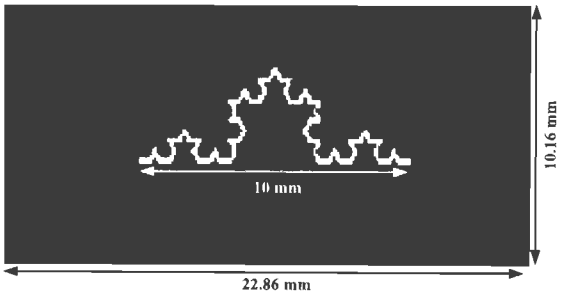

Figure 3.32: A 3rd iteration Koch fractal aperture.

Table 3.9: Resonant frequencies of a Koch fractal diaphragm.

Iteration	Resonant Frequencies (GHz)		Difference
	MoM	HFSS	(%)
0	14.80	14.85	0.34
1	12.10	12.06	0.33
2	10.29	10.18	0.1.07
3	9.45	9.43	0.21

The variation of return loss of the Koch fractal aperture is shown in Fig. 3.33, where K0 to K3 denote the 0^{th} to 3^{rd} iteration. The performance of Koch aperture is summarized in Table 3.9. The convergence analysis shows that 7, 48, 191 and 257 RWG functions are required to obtain converged result for K_0, K_1, K_2 and K_3, respectively. As expected, the increase in the order of iteration shifts the resonant frequency of the aperture downwards. The resonant frequency of the rectangular slot of length 10 mm is 14.85 GHz. As the order of iteration increases, the corresponding resonant frequencies are at 12.1 GHz, 10.3 GHz and 9.45 GHz for 1^{st}, 2^{nd} and 3^{rd} iterations, respectively. Hence, there is a significant amount of decrease in the resonant frequency of Koch aperture and by using such fractal diaphragm, the slot may be made to resonate within the single-mode frequency

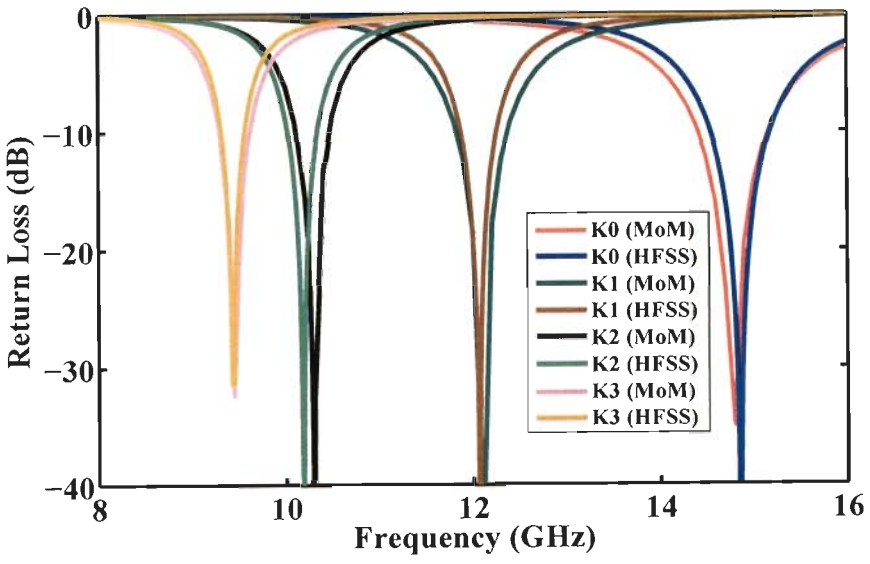

Figure 3.33: Return loss of Koch fractal diaphragm for different iterations.

region of the waveguide. It may also be mentioned here that the parameters like initial slot length and the indentation angle provide additional flexibility for locating the resonant frequency.

3.4 Finite Periodic Structures Based on Fractal Diaphragms

This section presents some typical applications of fractal frequency selective diaphragms in the design of filters and electromagnetic band gap structures. First, a waveguide dual-bandpass filter is investigated using the modified Devil's staircase fractal geometry. In the next subsection, electromagnetic band gap structure based on a 2^{nd} iteration self-affine Sierpinski gasket is described. The finite periodic structure is analyzed by obtaining the transfer matrix of the unit cell which is then cascaded in order to obtain the final response.

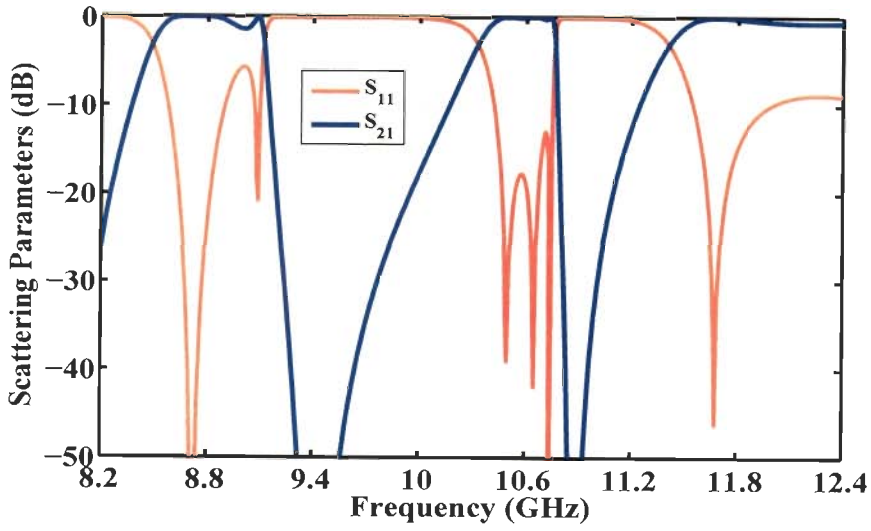

Figure 3.34: Frequency response of a dual-band waveguide filter based on modified Devil's staircase fractal diaphragm.

3.4.1 Dual-band Waveguide Filter

A 3rd iteration modified Devil's staircase fractal geometry of Fig. 3.5 is used to design a dual-band waveguide filter. From the numerical results shown in Fig. 3.6 it is found that the fractal diaphragm resonates at 7.35 GHz, 8.61 GHz, and 10.40 GHz. A periodic arrangement of three such diaphragms was considered with a separation of 8.5 mm between the diaphragms. Thus, the overall size of the filter is 25.5 mm. The frequency response of the filter is shown in Fig. 3.34. It can be seen that the filter offers three passbands with center frequencies at 8.45 GHz, 10.20 GHz, and 12 GHz. The first two passbands are separated by two stopbands which offers a good out-of-band rejection. So, it is desirable to operate the filter at the first two passbands. The bandwidth of the filter is around 3.65% and 4.00% at the first two passbands. The value of insertion loss is around 200 dB at the stopband between the two passbands.

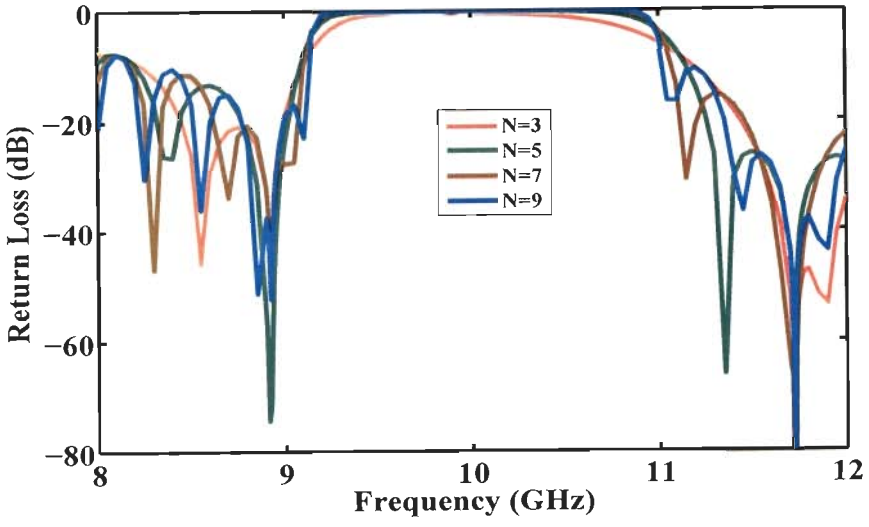

Figure 3.35: Return loss of EBG for different number of sections with p=20 mm.

3.4.2 Waveguide Based Electromagnetic Band Gap Structures

In this subsection, a rectangular waveguide based electromagnetic band gap structures based upon the self-affine Sierpinski gasket (Fig. 3.14) is presented. The structure consists of N number of fractal diaphragms with a periodicity p. It was found from Fig. 3.15 that the fractal diaphragm offers a stop band at 9.80 GHz. Fig. 3.35 shows the effect of number of sections (N) for a periodicity (p) equal to 20 mm. It is seen that the insertion loss goes into deep rejection and also, the rate of fall outside the bandgap is steeper for larger number of sections. The variation of periodicity on the behavior of fractal electromagnetic bandgap structure is shown in Fig. 3.36. It is seen that the bandgap is maximum when the periodicity is close to $\lambda_g/2$. The final electromagnetic bandgap structure response of the Sierpinski gasket diaphragm is shown in Fig. 3.37 with 7 sections and periodicity equal to 20 mm. It can be seen that the fractal diaphragm offers

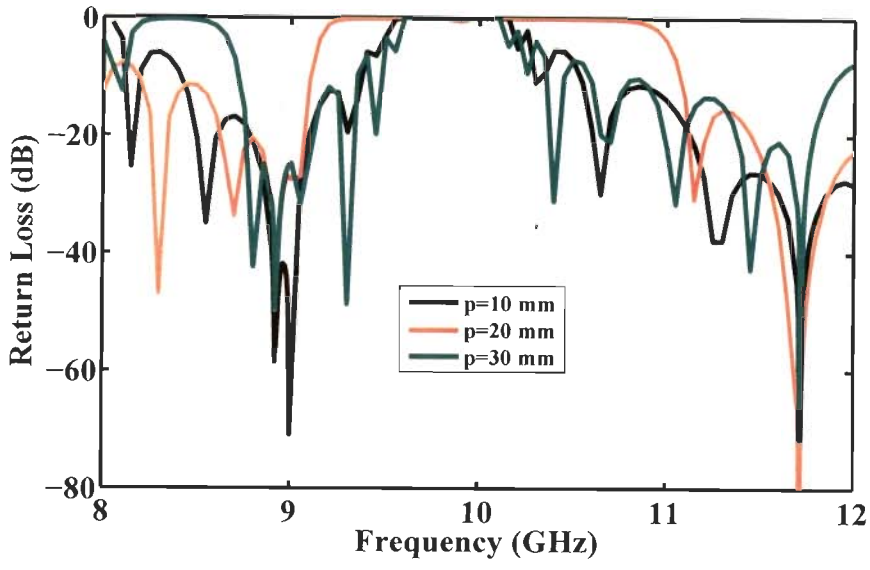

Figure 3.36: Return loss of EBG for different periodicity with N=7.

a bandgap of 20% with center of the band at 10 GHz.

3.5 Summary

The fundamental properties such as, self-similarity, self-affinity and space-filling properties, have been studied numerically for fractal apertures in the transverse cross section of a rectangular waveguide. The results presented in this chapter are aimed at establishing a relation between the self-affinity of fractal based frequency selective diaphragm and its frequency response. From the results, it can be concluded that, the location of the resonant bands can be controlled by selecting an appropriate scale factor. The important advantage of fractal frequency selective diaphragms based on Koch curve, Minkowski curve and Hilbert curve is the realization of resonant apertures with reduced overall physical size. Since, these fractal based frequency selective geometries offer transmission bands sep-

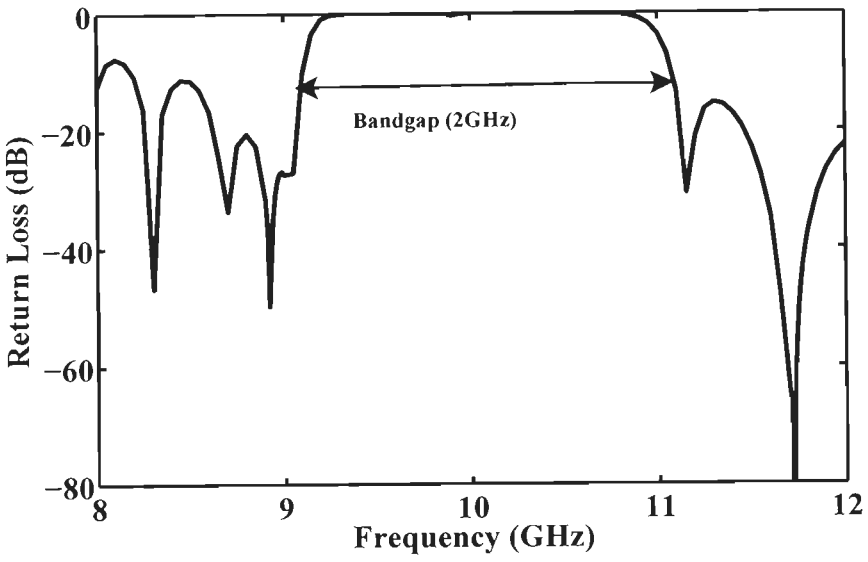

Figure 3.37: Return loss of EBG based on 2nd iteration Sierpinski gasket aperture.

arated by rejection band, they may offer good out-of-band rejection ratio in the design of waveguide filters. The ratio between the successive resonant frequencies are slightly greater than the ideal ratios which is a characteristics of fractal geometries of lower order iterations. Also, it is found that the resonant frequencies shifts upwards as the aperture location moves away from the center of the waveguide cross-section, which is another reason of obtaining larger frequency ratios. Two typical applications of fractal diaphragms are presented. It is found that the the dual-band waveguide filter offers good out-of-band rejection, since the transmission bands are separated by stopbands. However, the bandwidth of the filter at these bands is small, which can be increased by proper optimization of the fractal geometry. The fractal electromagnetic bandgap structure shows a wide bandwidth with a good roll-off outside the stopband. Such electromagnetic bandgap structures can be used in the design of band-rejection filter and harmonic suppression of waveguide resonators.

Chapter 4

ELECTROMAGNETIC TRANSMISSION THROUGH FRACTAL APERTURES IN CONDUCTING SCREEN

In this chapter, the problem of coupling through various fractal apertures in an infinite conducting screen is investigated. Based on MoM formulation described in chapter 2, a MATLAB code has been developed to determine the field distribution on the aperture surfaces. The triangulation of the aperture surfaces has been done using the MATLAB PDE toolbox. Although the formulation presented in chapter 2 is completely general, for simplicity, the regions on both sides of the infinite conducting screen are considered to be identical. The coupling characteristics of fractal apertures are expressed in terms of its transmission coefficient and the transmission cross-section which describe their behavior in near-field and far-field regions, respectively. In section 1, a MoM formulation of the problem of

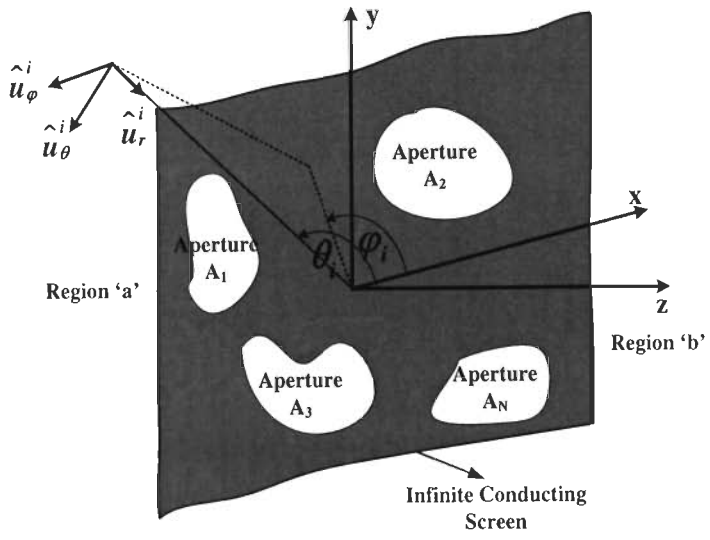

Figure 4.1: Coupling between two half-space regions through multiple apertures.

coupling through multiple apertures in an infinite conducting screen is presented. The computation of transmission coefficient and the transmission cross-section is presented in section 2. The present MoM code has been validated with some results on multiple rectangular apertures reported in earlier literature [109]. This is presented in section 3. In section 4, numerical results for some typical fractal apertures are presented and discussed. Finally, the main results are summarized in section 5.

4.1 General Formulation of the Problem

The general problem of coupling through multiple arbitrarily shaped apertures in an infinite conducting screen is shown in Fig. 4.1. As discussed in chapter 2, the equivalence principle and image theory are applied to decouple the original problem into two equivalent problems, one for each region (Fig. 4.2). Considering identical regions on opposite sides of the apertures, the operator equation for the

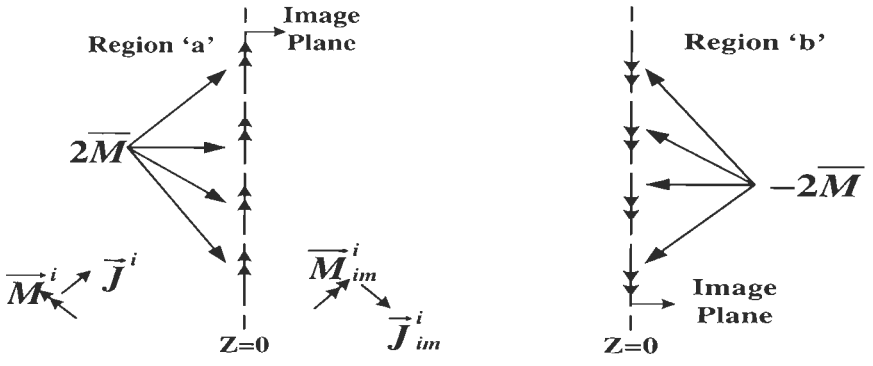

(a) Valid for region $z < 0$ (b) Valid for region $z > 0$

Figure 4.2: Equivalent models.

problem can be expressed as

$$2\overline{H}_t^{fs}(2\overline{M}) = -\overline{H}_t^i \tag{4.1}$$

where $\overline{H}_t^{fs}(2\overline{M})$ denotes the tangential component of the magnetic field due to a surface magnetic current $2\overline{M}$ radiating in free space. Application of MoM results in the following matrix equation

$$2[Y^{hs}]\overrightarrow{V} = \overrightarrow{I}^i \tag{4.2}$$

where an element of the admittance matrix $[Y^{hs}]$ can be expressed as given in (2.69) and can be computed according to (2.80). The excitation vector elements are computed using (2.101) assuming plane wave incidence.

4.2 Computation of Transmission Coefficient and Transmission Cross-Section

Once the matrix equation (4.2) is solved for the unknown magnetic surface currents, different near-field and far-field parameters can be computed.

4.2.1 Transmission Coefficient

The coupling through apertures in an infinite conducting screen illuminated by a uniform plane wave is characterized by the transmission coefficient which is defined as the ratio of time averaged power, P_{trans}, transmitted into region 'b' to the time averaged incident power, P_{inc}, intercepted by the apertures in region 'a'.

The power transmitted into region 'b' can be expressed as

$$P_{trans} = \frac{1}{2} Re \left(\iint_{apert} \overline{E} \times \overline{H}^{b*}(-2\overline{M}) \cdot \hat{n} \, ds \right) \tag{4.3}$$

where $\hat{n}$ is the unit outward normal to the aperture surface and $\overline{H}^{b*}(-2\overline{M})$ denotes complex conjugate of tangential component of magnetic field due to current $-2\overline{M}$ radiating in free space. Using $\overline{M} = \hat{z} \times \overline{E}$, (4.3) can be expressed as

$$P_{trans} = \frac{1}{2} Re \left(\iint_{apert} \overline{M} \cdot \overline{H}^{b*}(-2\overline{M}) \, ds \right) \tag{4.4}$$

Expanding $\overline{M}$ in terms of basis functions, we get

$$\overline{H}_t^b(-2\overline{M}) = -\sum_{n=1}^{N} V_n \overline{H}_t^b(2\overline{M}_n) \tag{4.5}$$

Thus, (4.4) is written as

$$\begin{aligned} P_{trans} = &= -\frac{1}{2} Re \left(\sum_n V_n^* \iint_{apert} \overline{M} \cdot \overline{H}_t^{b*}(2\overline{M}_n) \cdot ds \right) \\ &= \frac{1}{2} Re \left(-\sum_m \sum_n V_m V_n^* \iint_{apert} \overline{M}_m \cdot \overline{H}_t^{b*}(2\overline{M}_n) \, ds \right) \end{aligned}$$

If $\overline{M}_m$ are real, then the conjugate operator can be taken outside the integral and hence, the negative of integral term represents the admittance matrix elements for half space region as given in (2.69). Hence

$$P_{trans} = \frac{1}{2} Re \left(V_m V_n^* Y_{mn}^{hs*} \right) \tag{4.6}$$

which can be expressed in matrix form as

$$P_{trans} = \frac{1}{2} Re\left(\widetilde{V}[Y^{hs}]^* \overrightarrow{V}^*\right) \tag{4.7}$$

where $\widetilde{V}$ denotes the transpose of coefficient vector $\overrightarrow{V}$ and the asterisk denotes complex conjugate.

The time averaged incident power is given by

$$\begin{aligned} P_{inc} &= \frac{1}{2} Re\left(\iint_{Apert} \overline{E}^i \times \overline{H}^{i*} . \hat{n}\, ds\right) \\ &= \frac{1}{2}\eta |H_{i0}|^2 A \cos\theta_i \end{aligned} \tag{4.8}$$

where A denotes the aperture area and θ_i is the angle of incidence.

Hence, the transmission coefficient can be expressed as

$$T = \frac{Re\left(\widetilde{V}[Y^{hs}]^* \overrightarrow{V}^*\right)}{(\eta |H_{i0}|^2 A \cos\theta_i)} \tag{4.9}$$

4.2.2 Computation of Transmission Cross-section

Transmission cross-section is defined as the area which contains power to produce the radiation field $\overline{H}_m$ by omnidirectional radiation over half space. The computation of $\overline{H}_m$ is described in chapter 2 and can be obtained from (2.108). Mathematically, it can be expressed as

$$\begin{aligned} \tau &= 2\pi r_m^2 \frac{\eta_b |\overline{H}_m|^2}{\eta_a |\overline{H}^{i0}|^2} \\ &= 2\pi r_m^2 \frac{\omega^2 \varepsilon^2}{16\pi^2 r_m^2} \left|\widetilde{P}^m \overrightarrow{V}\right|^2 / \left|\overline{H}^{i0}\right|^2 \\ &= \frac{\omega^2 \varepsilon^2}{8\pi} \left|\widetilde{P}^m \overrightarrow{V}\right|^2 / \left|\overline{H}^{i0}\right|^2 \end{aligned} \tag{4.10}$$

where $\widetilde{P}_m$ denotes the transpose of measurement vector $\overrightarrow{P}_m$.

Now, depending on the polarization of measurement vector $\overrightarrow{P}^m$, transmission cross-section can be measured in four principal planes (see Fig. 4.3) as

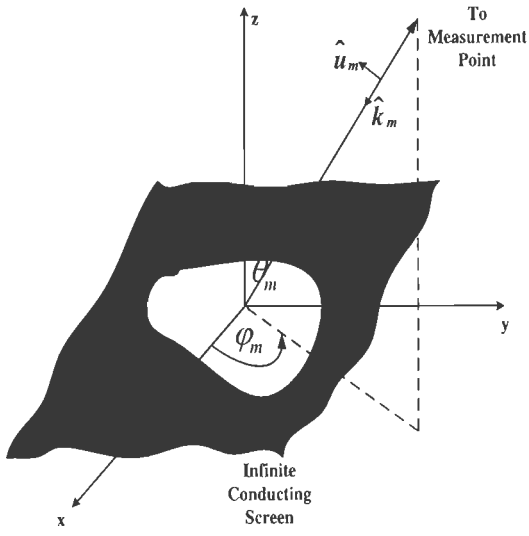

Figure 4.3: Measurement vector

1. τ_{yy}, for y-polarized measurement in $y = 0$ plane.

$$\varphi_m = 0^\circ, \qquad \hat{u}_m = \hat{y}$$

2. $\tau_{\theta y}$, for θ-polarized measurement in $y = 0$ plane.

$$\varphi_m = 0^\circ, \qquad \hat{u}_m = \hat{\theta}$$

3. $\tau_{\theta x}$, for θ-polarized measurement in $x = 0$ plane.

$$\varphi_m = 90^\circ, \qquad \hat{u}_m = \hat{\theta}$$

4. τ_{xx}, for x-polarized measurement in $x = 0$ plane.

$$\varphi_m = 90^\circ, \qquad \hat{u}_m = \hat{x}$$

where φ_m is defined in Fig 1.14. It is to be mentioned here that the transmission cross-section defined in (4.10) is normalized with respect to the square of the

Table 4.1: Convergence of transmission coefficient for an array of 4 square apertures.

No. of RWG Functions	Transmission Coefficient		Percentage Change	
	Parallel	Perpendicular	Parallel	Perpendicular
84	1.7633	1.2953	-	-
160	1.8271	1.3765	3.62	6.27
260	1.8583	1.4202	1.71	3.17
384	1.8767	1.4470	0.99	1.89
532	1.8888	1.4648	0.64	1.23
704	1.8973	1.4774	0.45	0.86

first resonant wavelength, λ_1, of fractal geometry and is expressed as

$$\tau(dB) = 10 \log \left(\frac{\tau}{(\lambda_1)^2} \right) \tag{4.11}$$

4.3 Validation of Computer Code

Based upon the formulation presented earlier, a computer code has been developed in MATLAB 7. The code has been validated by considering the problem of multiple rectangular apertures in an infinite conducting screen. This problem has been analyzed in [109] using rooftop basis functions with the correct edge singularity incorporated into them.

The first problem considered is an array of four square apertures in an infinite screen illuminated by a plane wave, shown in the inset of Fig. 4.4. In all the cases considered in the present work, the incidence plane is taken to be xz-plane. Before calculating the transmission coefficient, a convergence analysis was carried out and Table 4.1 shows the results of the convergence study for

Table 4.2: Convergence of transmission cross-section for six rectangular apertures.

No. of RWG functions	τ/λ^2		Percentage Change	
	Parallel	Perpendicular	Parallel	Perpendicular
108	0.6795	0.3503	-	-
270	0.5877	0.3901	13.51	11.36
504	0.5475	0.4280	6.84	9.72
810	0.5282	0.4522	3.53	5.61
1188	0.5177	0.4679	1.99	3.47
1638	0.5113	0.4787	1.24	2.31
2160	0.5071	0.4864	0.82	1.61

both parallel and perpendicular polarizations with normal incidence. The length of the side of each aperture is 0.5λ and the spacing between adjacent apertures is $d = 0.5a$. From the table, it can be seen that the transmission coefficients converge to within 2% for 384 RWG basis functions. From this study, it is found that the result converges when the maximum edge length is less than 0.1λ where λ is the operating wavelength. Also, it can be seen that the rate of convergence for parallel polarization is much faster than that for perpendicular polarization. Fig. 4.4 compares the results obtained from the present analysis with those reported in [109], where an excellent agreement can be seen. Next, in order to verify the far-field calculation, the transmission cross-section patterns of a configuration of six rectangular apertures (shown in the inset of Fig. 4.5) were computed. The convergence of transmission cross section normalized with respect to the square of operating wavelength for different polarizations of incident wave with 45° angle of incidence is given in Table 4.2. From the table, it is noted

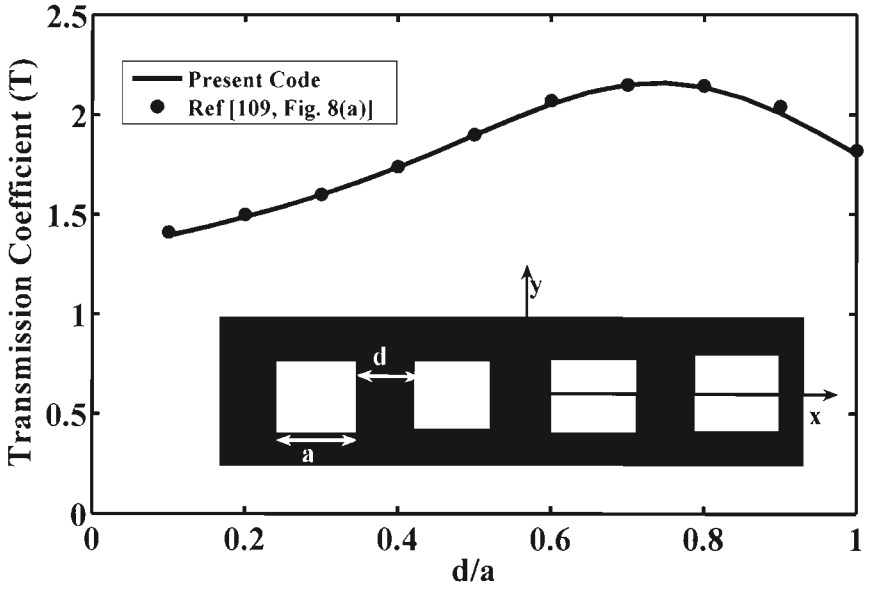

(a) Parallel Polarization

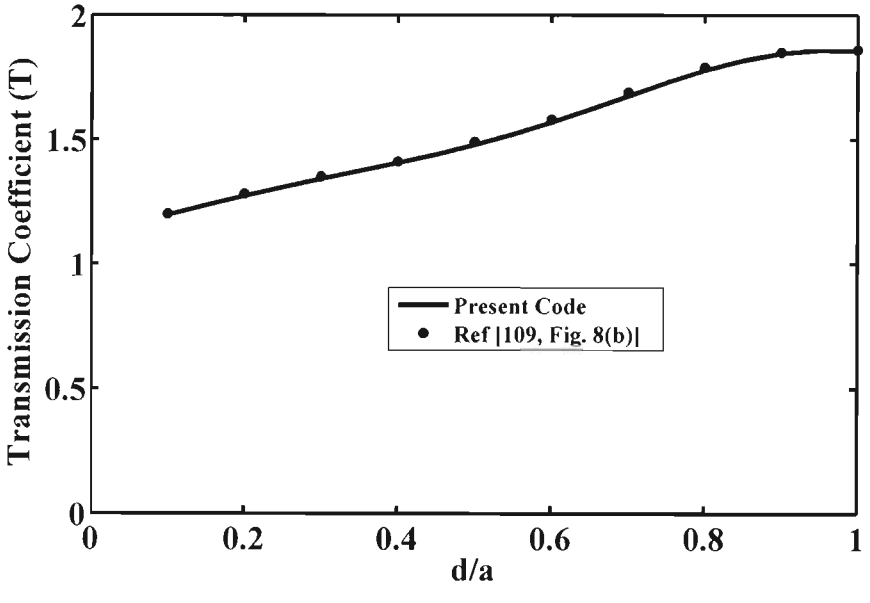

(b) Perpendicular Polarization

Figure 4.4: Transmission coefficient for an array of 4 square apertures versus inter-aperture distance at normal incidence. The length of the sides of each aperture is 0.5λ.

that 2160 expansion function are sufficient to yield converged result. Again the maximum edge length was around 0.1λ. Fig. 4.5 and Fig. 4.6 show the transmission cross-section patterns of six rectangular apertures for both parallel and perpendicular polarizations with 45° angle of incidence. The dimension of each aperture is $1\lambda \times 0.5\lambda$ and the inter-aperture distance is 0.25λ. Again, an excellent agreement with the results given in [109] can be noticed.

4.4 Transmission Through Fractal Apertures

4.4.1 Sierpinski Gasket Aperture

Sierpinski gasket fractal is the most popular fractal in antenna and frequency selective surface design. Here, the coupling through the Sierpinski gasket aperture in an infinite conducting screen is investigated. Before analyzing the properties of fractal geometry, the behavior of a single triangular aperture in an infinite conducting screen illuminated by a plane wave is investigated. The variation of transmission coefficient for different base width (b) with a fixed height (h) of 120 mm is shown in Fig. 4.7, for both parallel and perpendicular polarizations at normal incidence. The results are also tabulated in Table 4.3. It can be seen that the resonant frequency remains almost same for parallel polarization of incident wave, whereas, it decreases with the increase in base width for perpendicularly polarized incident wave. This is due to the fact that the electric field is perpendicular to height of the triangular aperture for parallel polarization of incident wave and hence, the resonant frequency remains constant with resonant wavelength approximately equal to $2h$. On the contrary, the electric field is perpendicular to the base of the triangle for perpendicular polarization of incident wave and the increase in base width results in a decrease in resonant

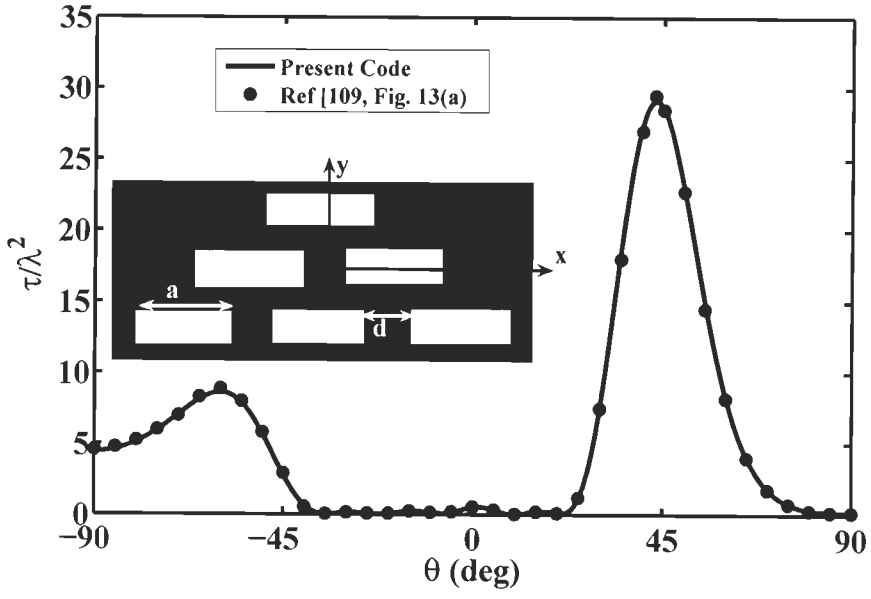

(a) $\varphi = 0°$

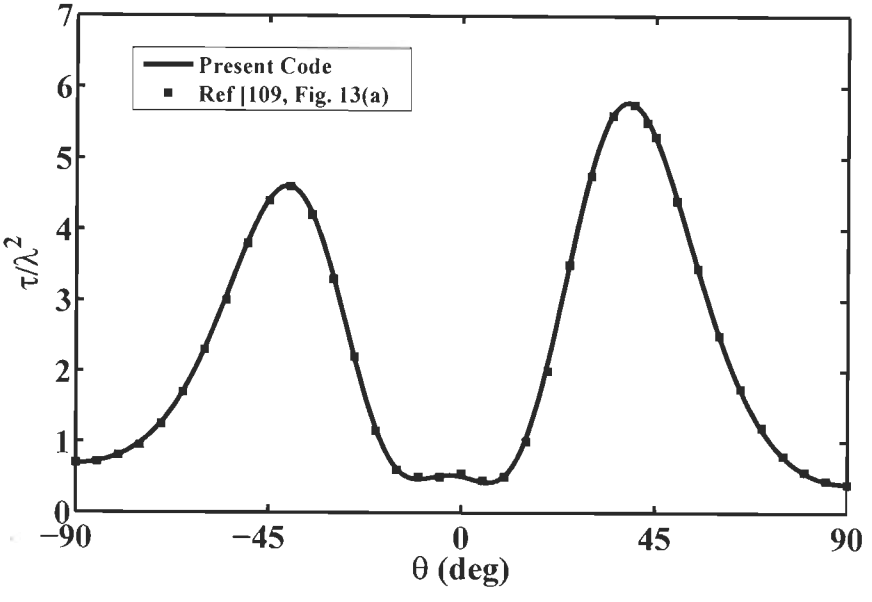

(b) $\varphi = 90°$

Figure 4.5: Transmission cross-section of six rectangular apertures for parallel polarization with 45° incidence. The dimension of each aperture is $1\lambda \times 0.5\lambda$ and the spacing between each aperture is 0.25λ.

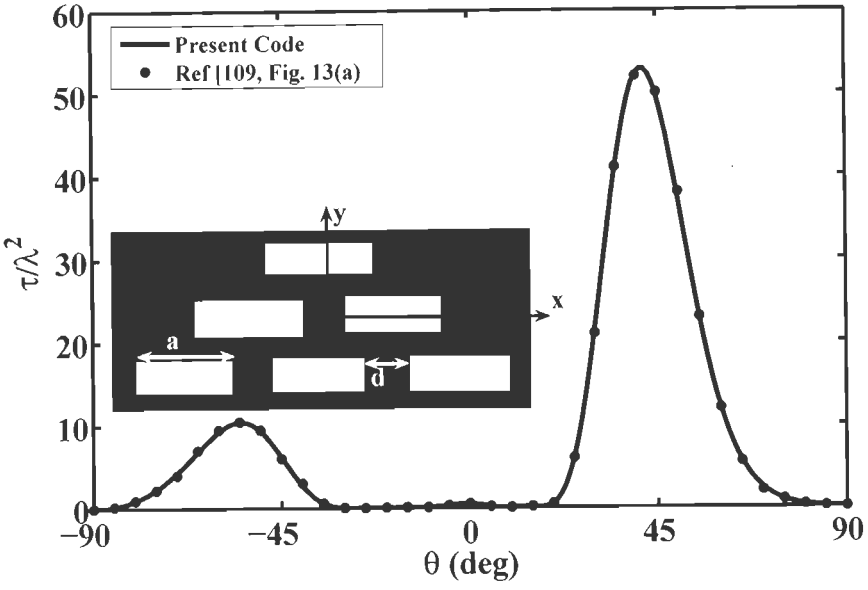

(a) $\varphi = 0°$

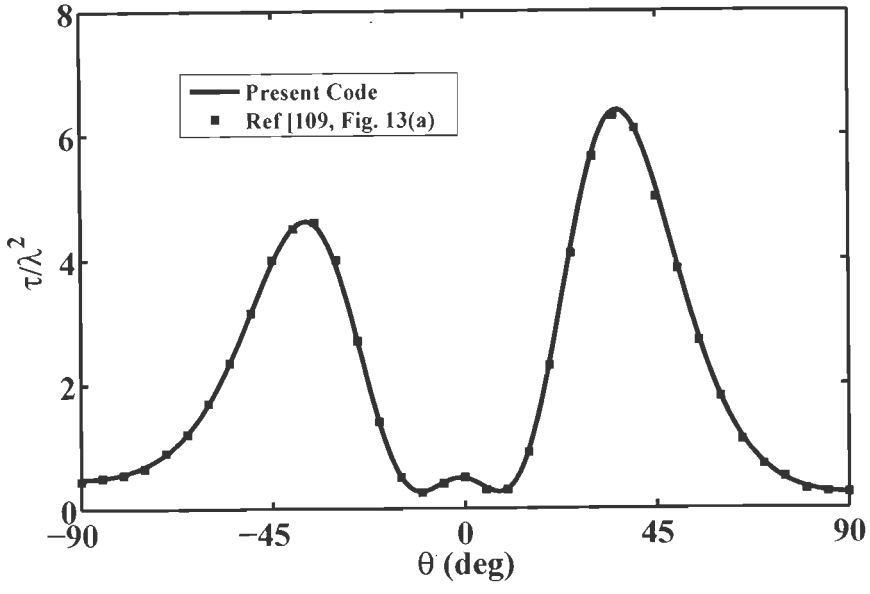

(b) $\varphi = 90^0$

Figure 4.6: Transmission cross section of six rectangular apertures for perpendicular polarization with 45° incidence. The dimension of each aperture is $1\lambda \times 0.5\lambda$ and the spacing between each aperture is 0.25λ.

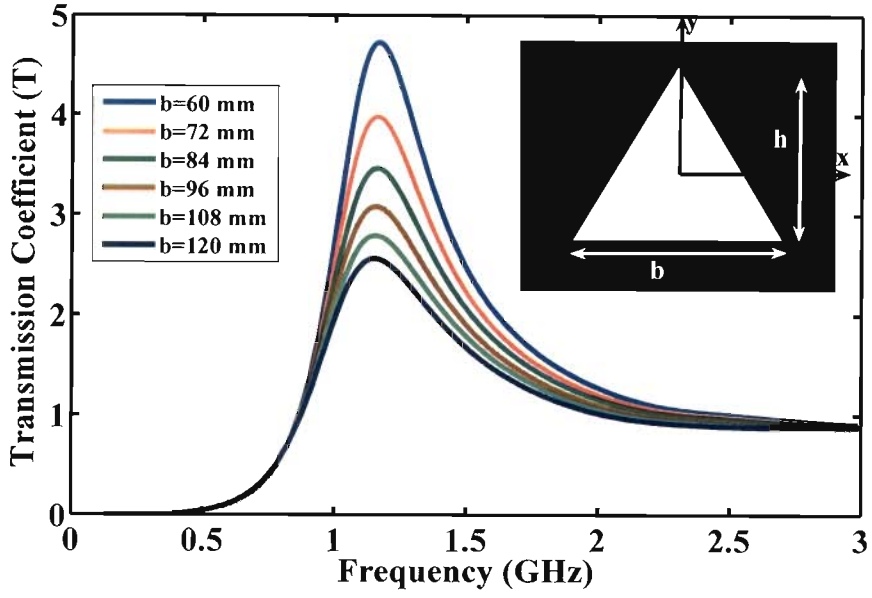

(a) Parallel Polarization

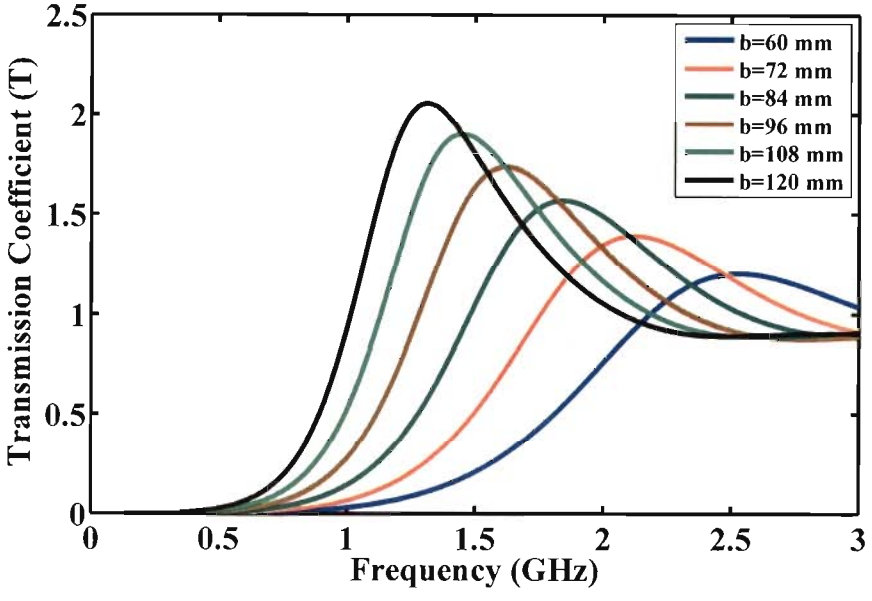

(b) Perpendicular Polarization

Figure 4.7: Transmission coefficient of a triangular aperture for different base width (b) with height (h) =120 mm.

Table 4.3: Resonant frequency of a triangular aperture for different base width (b) with height (h)=120 mm.

Base width (b) mm	Parallel Polarization		Perpendicular Polarization	
	Resonant Freq. (GHz)	h/λ	Resonant Freq.(GHz)	b/λ
60	1.17	0.47	2.53	0.51
72	1.16	0.46	2.12	0.51
84	1.16	0.46	1.84	0.51
96	1.16	0.46	1.62	0.52
108	1.15	0.46	1.45	0.52
120	1.15	0.46	1.31	0.52

frequency. The resonant wavelength is approximately equal to $2b$, as is evident from the Table 4.3. Similar behavior can be observed in Fig. 4.8, which shows the variation of transmission coefficient for different height (h) with fixed base width (b). The variation of resonant frequency and wavelength is summarized in Table 4.4. Here, the resonant frequency decreases with increase in height for parallel polarization and remains almost constant for perpendicular polarization. Thus, it can be concluded that the dimension perpendicular to the electric field vector of the incident wave determines the resonant frequency of the aperture, a behavior similar to that exhibited by a rectangular aperture.

The behavior of a triangular aperture of dimension b=120 mm and h=120 mm for different angles of incidence was also analyzed for both parallel and perpendicular polarizations. It is to be mentioned here that the transmission coefficient is normalized with respect to the incident power density at normal incidence rather than the actual power density at the oblique incidence. The variation of trans-

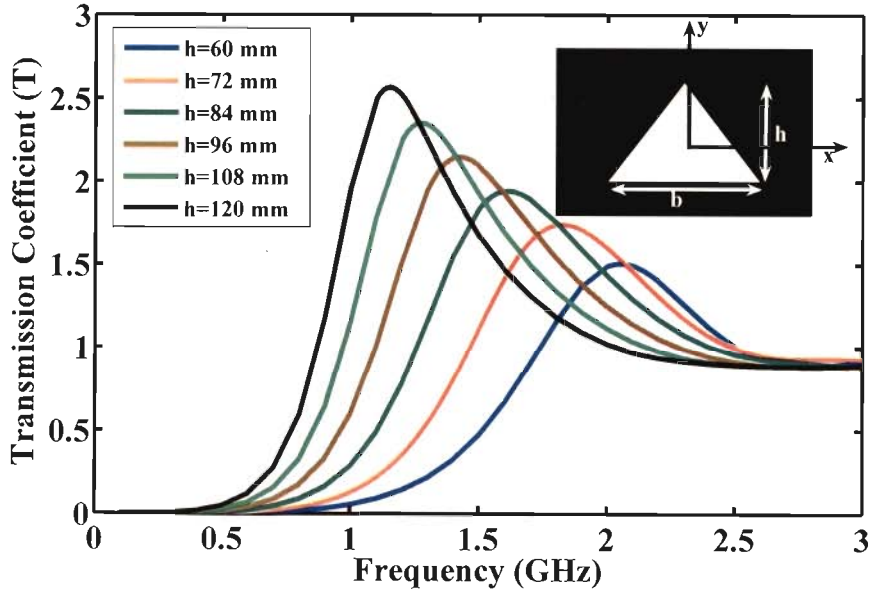

(a) Parallel Polarization

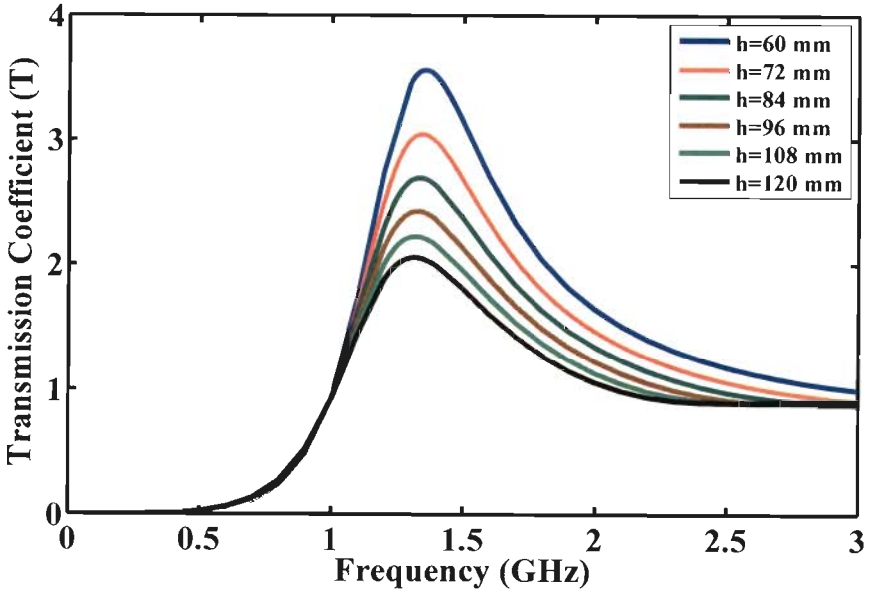

(b) Perpendicular Polarization

Figure 4.8: Transmission coefficient of a triangular aperture for different height (h) with base width (b) =120 mm.

Table 4.4: Resonant frequency of a triangular aperture for different height (h) with base width (b)=120 mm.

Height (h) mm	Parallel Polarization		Perpendicular Polarization	
	Resonant Freq. (GHz)	h/λ	Resonant Freq.(GHz)	b/λ
60	2.05	0.41	1.36	0.54
72	1.83	0.44	1.34	0.54
84	1.61	0.45	1.33	0.53
96	1.43	0.46	1.33	0.53
108	1.27	0.46	1.32	0.53
120	1.15	0.46	1.31	0.52

mission coefficient for different angles of incidence is shown in Fig. 4.9. As the angle of incidence is increased, for parallel polarization, a weak second resonance is generated around 2.4 GHz corresponding to $\frac{h}{\lambda} = 0.96$. On the other hand, the second resonance appears around 2.8 GHz for perpendicularly polarized incident wave which gives $\frac{b}{\lambda} = 1.12$. Also, the value of transmission coefficient decreases as the angle of incidence is increased and this decrement is sharper in case of perpendicular polarization. In order to get an insight into this phenomenon, the magnetic surface current distribution on the triangular aperture was studied. The plots of magnitude and phase of y-component of current along $y = -31.25$ cut for parallel polarization at 1.15 GHz and 2.4 GHz are shown in Fig. 4.10. It can be seen from the current distribution that, at the primary resonant frequency of the triangular aperture, the magnitude and phase of M_y are almost uniform over the entire aperture width of the triangle. Also, it is evident that the magnitude of current changes very little with the change in angle of incidence

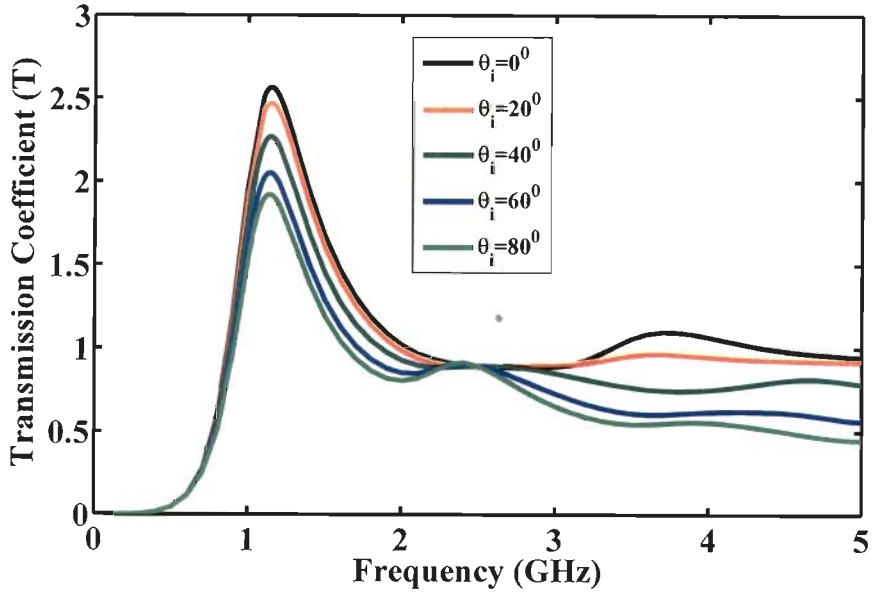

(a) Parallel Polarization

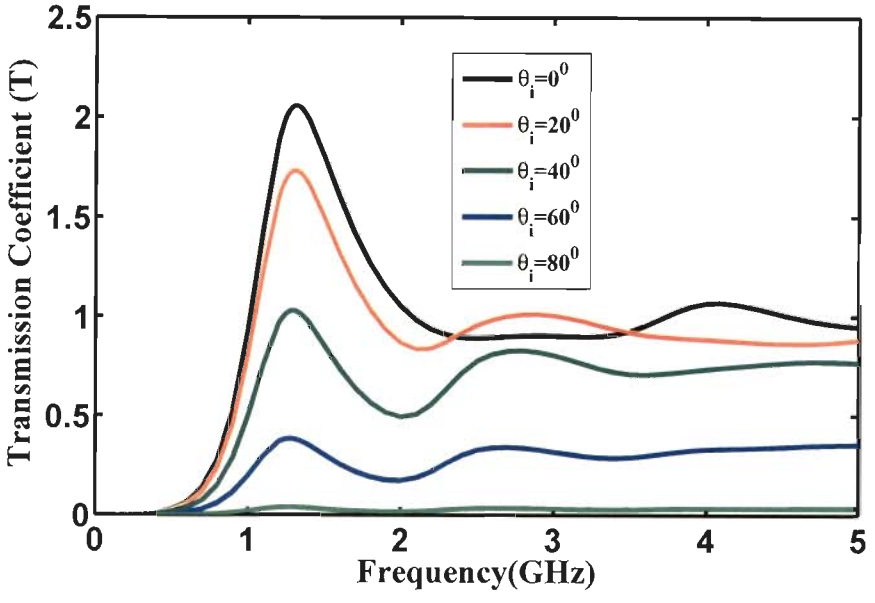

(b) Perpendicular Polarization

Figure 4.9: Transmission coefficient of a triangular aperture for different angles of incidence.

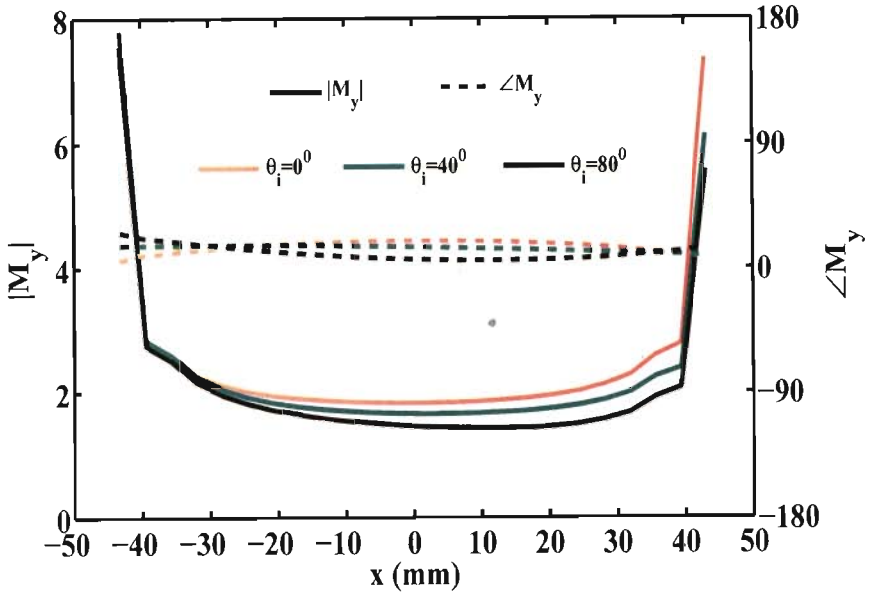

(a) Primary resonance at f = 1.15 GHz

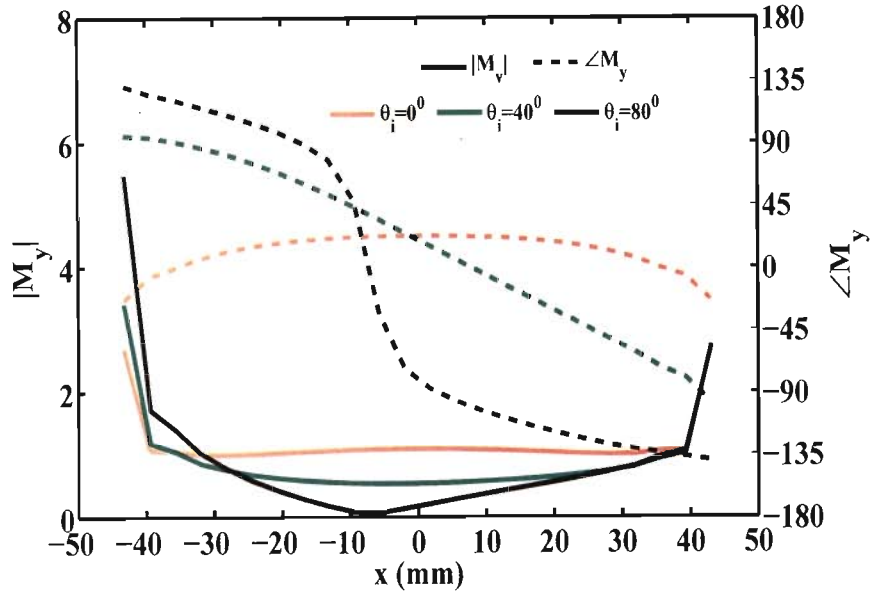

(b) Secondary resonance at f = 2.4 GHz

Figure 4.10: Current distribution of a triangular aperture with different angles of incidence at primary and secondary resonances for parallel polarization.

at primary resonance. At the second resonance, the current distribution shows a nearly uniform phase distribution for normal incidence. However, as the angle of incidence is varied, the phase of M_y changes around the center line of the triangle which causes a resonance. The magnitude of this current is far less than the magnitude at primary resonant frequency which causes a weak resonance. Similar behavior is obtained for perpendicular polarization as seen from Fig. 4.11. As the angle of incidence is increased, the magnitude of current decreases sharply for perpendicular polarization as compared to the case of parallel polarization, which causes a sharp decrease in the value of transmission coefficient at oblique incidence for perpendicular polarization. The behavior of phase is same as that of parallel polarization, which undergoes a phase reversal around the center line.

After having an insight in the behavior of a triangular aperture, the electromagnetic transmission through Sierpinski gasket aperture is investigated. Here, we consider a 2^{nd} iteration self-similar Sierpinski gasket aperture with h = 88.9 mm as shown in Fig. 4.12. The transmission coefficients for three different iterations are shown in Fig. 4.13 for a range of frequencies from 0.1 to 12 GHz for both parallel and perpendicular polarizations at normal incidence. Tables 4.5 and 4.6 summarize the main performance parameters of the Sierpinski gasket aperture. It can be seen from the table that, as the order of iteration increases, the resonant frequency shifts downward. Also, the transmission coefficients at a particular resonant frequency increase with the increase in order of iteration with a low transmission between two passbands. Hence, the fractal aperture exhibits good bandpass characteristics. From the study of magnetic current distribution, it was found that, as the order of iteration increases, the magnitude of equivalent magnetic surface current increases, which causes the increase in transmission coefficient. In [47], a dual band FSS based on Sierpinski gasket dipole was reported

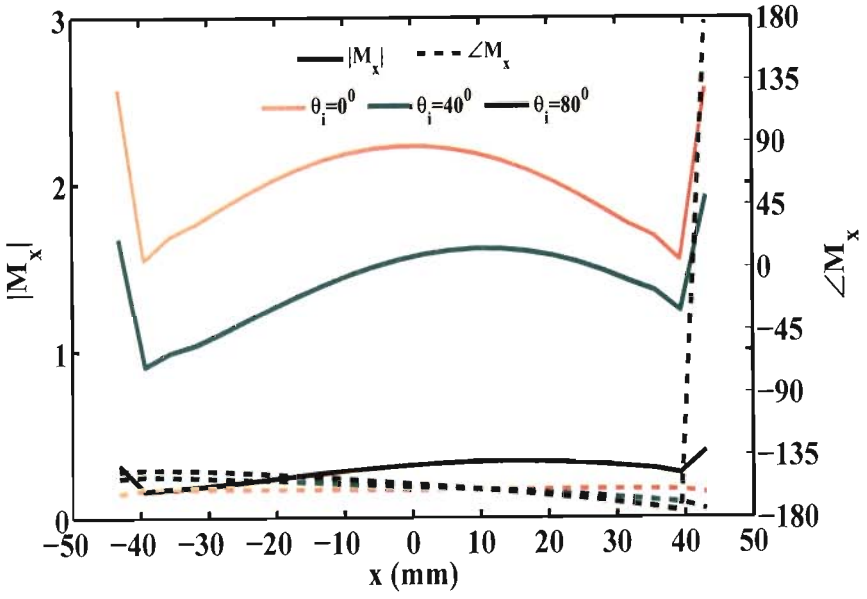

(a) Primary resonance at f = 1.30 GHz

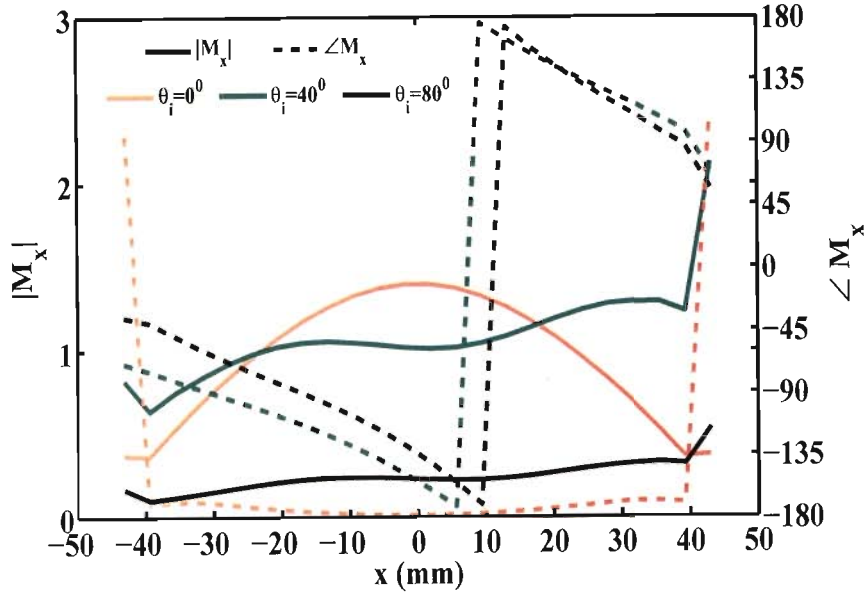

(b) Secondary resonance at f = 2.8 GHz

Figure 4.11: Current distribution of a triangular aperture with different angles of incidence at primary and secondary resonances for perpendicular polarization.

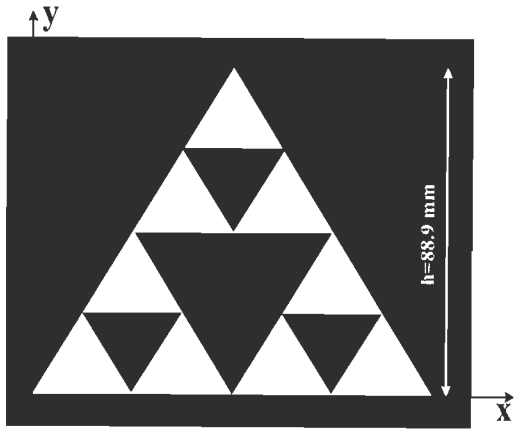

Figure 4.12: Sierpinski gasket aperture of 2^{nd} iteration in infinite screen. The white portions denote the aperture regions.

Table 4.5: Transmission parameters of Sierpinski gasket aperture for parallel polarization.

Iteration	Parallel Polarization		
	Resonant Frequency (GHz)	Transmission coefficient	Ratio (f_{n+1}/f_n)
0	1.54	2.31	-
1	1.40	4.05	-
	4.60	1.49	3.29
2	1.32	7.80	-
	3.90	3.61	2.95
	8.90	2.09	2.28

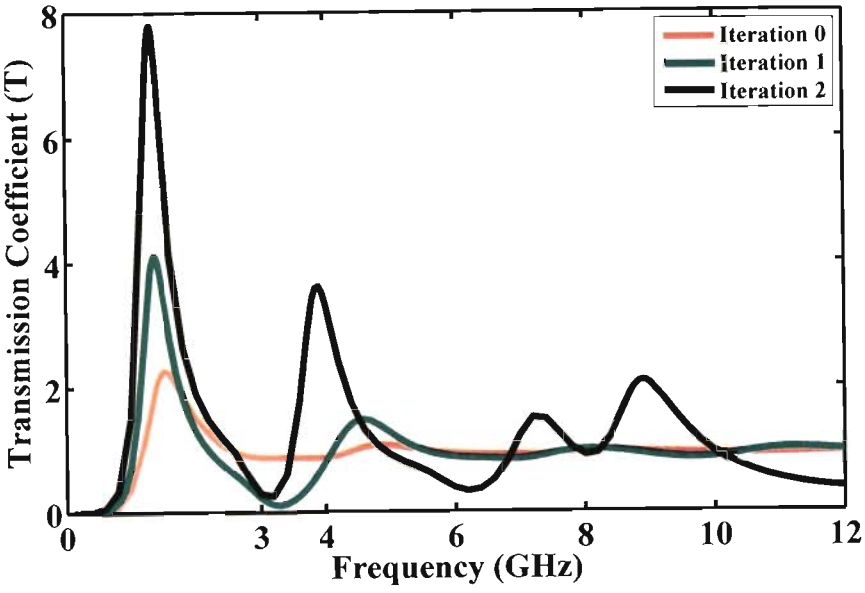

(a) Parallel Polarization

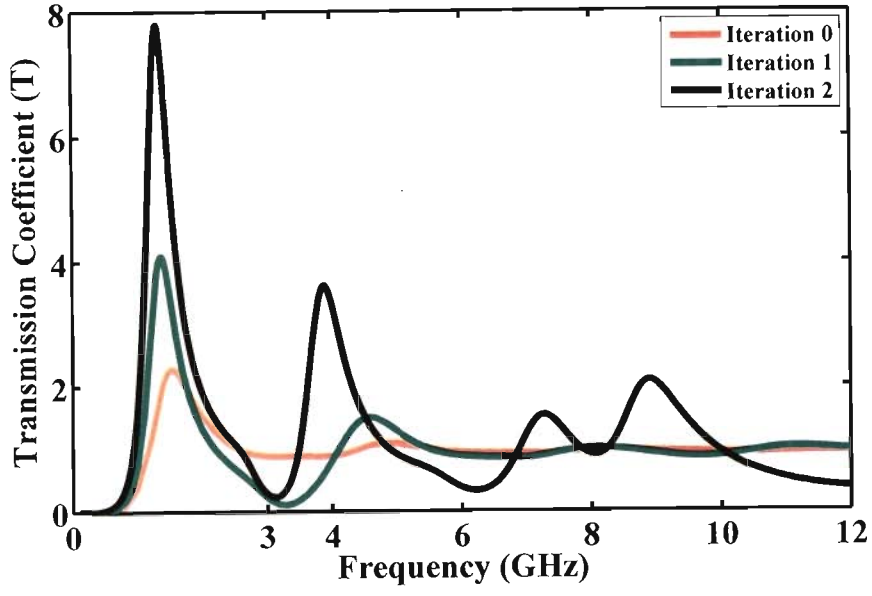

(b) Perpendicular Polarization

Figure 4.13: Transmission coefficient of Sierpinski gasket aperture for different iterations at normal incidence.

Table 4.6: Transmission parameters of Sierpinski gasket aperture for perpendicular polarization.

Iteration	Perpendicular Polarization		
	Resonant Frequency (GHz)	Transmission coefficient	Ratio (f_{n+1}/f_n)
0	1.54	2.31	-
1	1.37	4.09	-
	4.58	1.49	3.34
2	1.31	7.78	-
	3.92	3.59	2.99
	8.95	2.08	2.28

and it was stated that the first two resonant frequencies occur at

$$\frac{2h}{\lambda_1} = 0.4 \qquad \frac{2h}{\lambda_2} = 1.13 \tag{4.12}$$

where λ_1 and λ_2 are free space wavelengths for first two resonant frequencies. According to (4.12), the first two resonant frequencies for the present geometry should be at 1.35 GHz and 3.81 GHz, respectively.. From Table 4.5, it can be seen that the first two resonant frequencies occur at 1.32 GHz and 3.90 GHz which are within 2% of those predicted by (4.12). Also, the frequency ratios between successive resonant frequencies tend to approach the theoretical value 2 for higher order bands as the order of iterations increase. Since the initial geometry was an equilateral triangle, the response of the aperture for parallel and perpendicular polarizations of incident wave is almost similar.

Next, the flare angle of the triangle was varied. The transmission characteristics of the Sierpinski gasket aperture for three different flare angles, $\alpha = 30°$, $\alpha = 45°$ and $\alpha = 60°$ for both parallel and perpendicular polarizations of incident

wave at normal incidence have been studied and are shown in Fig. 4.14. It is evident from Fig. 4.14(a) that, as the flare angle of gasket aperture decreases, the transmission coefficient at the first resonant frequency increases. This is in line with our expectations, since a similar behavior was exhibited by a single aperture (Fig. 4.7(a)). It may be mentioned here that a similar variation of the resonant frequencies has been seen for a Sierpinski monopole antenna [11]. The transmission coefficient at the second and third resonant frequency decreases with the decrease in flare angle and the response for a flare angle of 30° becomes almost flat for frequencies greater than 6 GHz. However, as shown in Fig. 4.14(b), for perpendicularly incident wave, the fractal property remains unchanged, with a upward shift of resonant frequency with the decrease in flare angle. It is because, for perpendicularly polarized incident wave, the electric field is perpendicular to the base length and a decrease in flare angle means a smaller base length which corresponds to higher resonant frequencies.

The far-field characteristics of the gasket aperture have been expressed in terms of the transmission cross-section. The transmission cross-section patterns of gasket aperture in two principal planes $\phi = 0°$ and $\phi = 90°$ for parallel and perpendicular polarizations of incident wave are shown in Fig. 4.15. It is found that at higher resonant frequencies, the patterns become more directive and also, side lobes are generated.

Next, the angle of incidence was varied for a 2^{nd} iteration Sierpinski gasket aperture. The variation of transmission coefficient for different incidence angles for parallel and perpendicular polarizations are shown in Fig. 4.16. It is found that, in addition to the three resonant frequencies given in Tables 4.5 and 4.6, two more resonant frequencies appear around 2.80 GHz and 5.95 GHz for parallel polarization and around 2.75 GHz and 6.00 GHz for perpendicular polarization

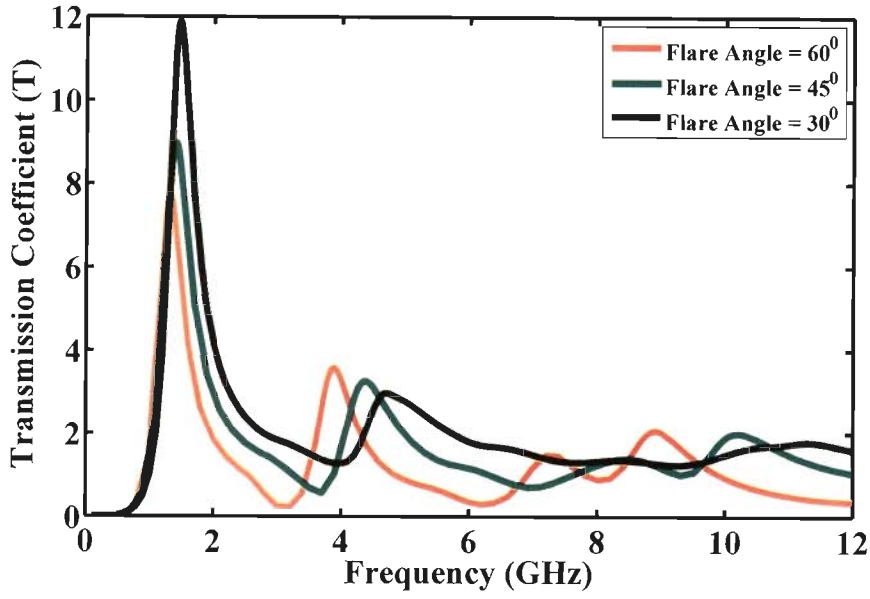

(a) Parallel Polarization

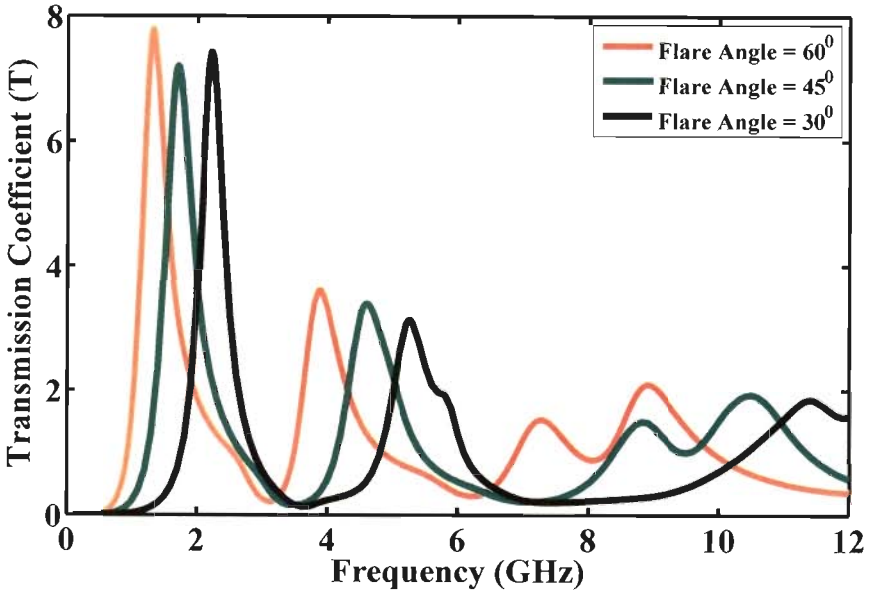

(b) Perpendicular Polarization

Figure 4.14: Transmission coefficient of 2nd iteration Sierpinski gasket aperture for different flare angles at normal incidence.

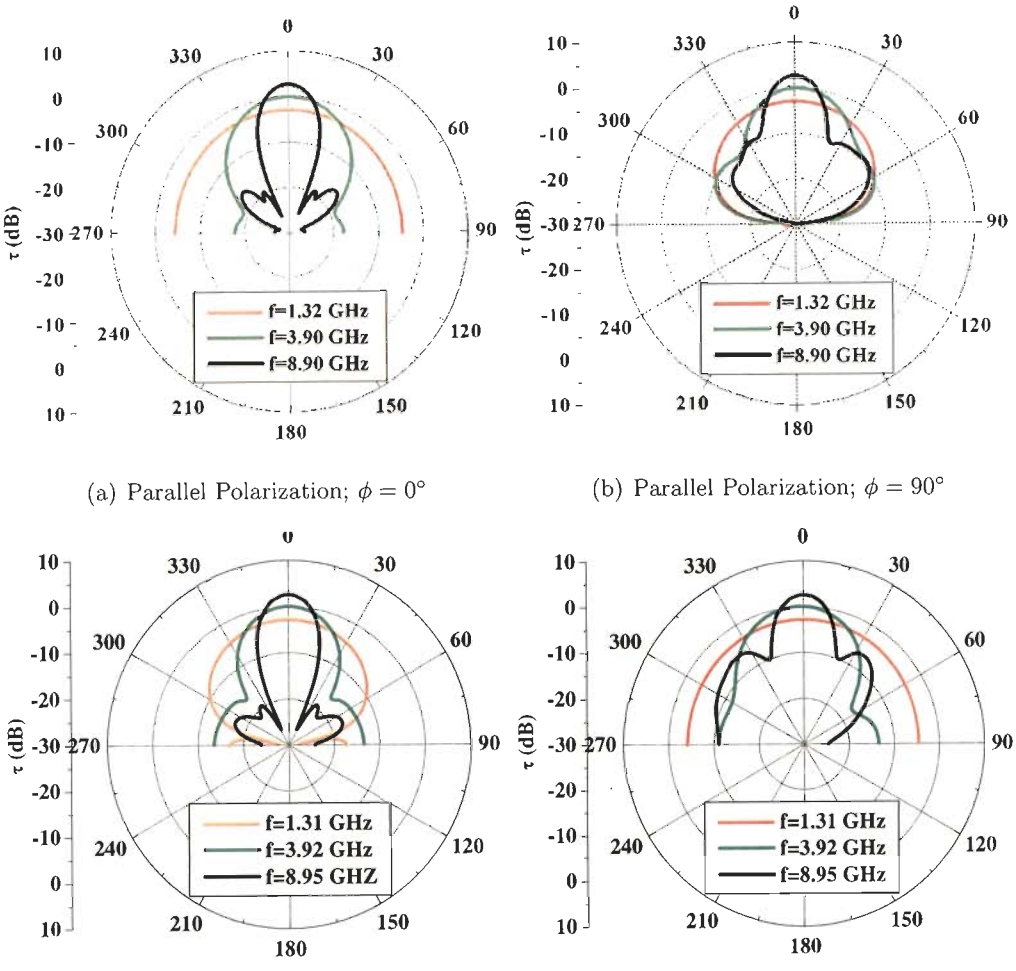

(a) Parallel Polarization; $\phi = 0°$

(b) Parallel Polarization; $\phi = 90°$

(c) Perpendicular Polarization; $\phi = 0°$

(d) Perpendicular Polarization; $\phi = 90°$

Figure 4.15: Transmission cross-section patterns of 2nd iteration Sierpinski gasket aperture at three resonant frequencies at normal incidence.

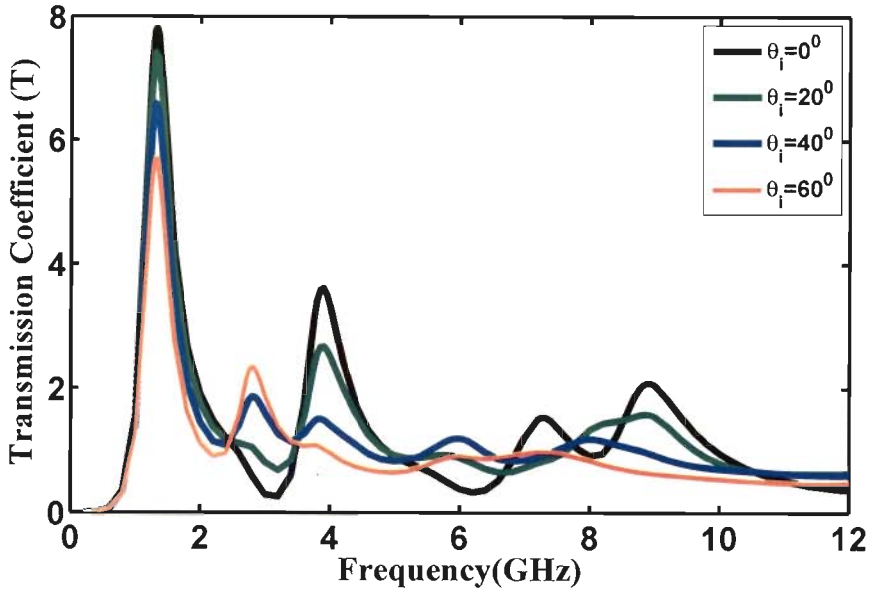

(a) Parallel Polarization

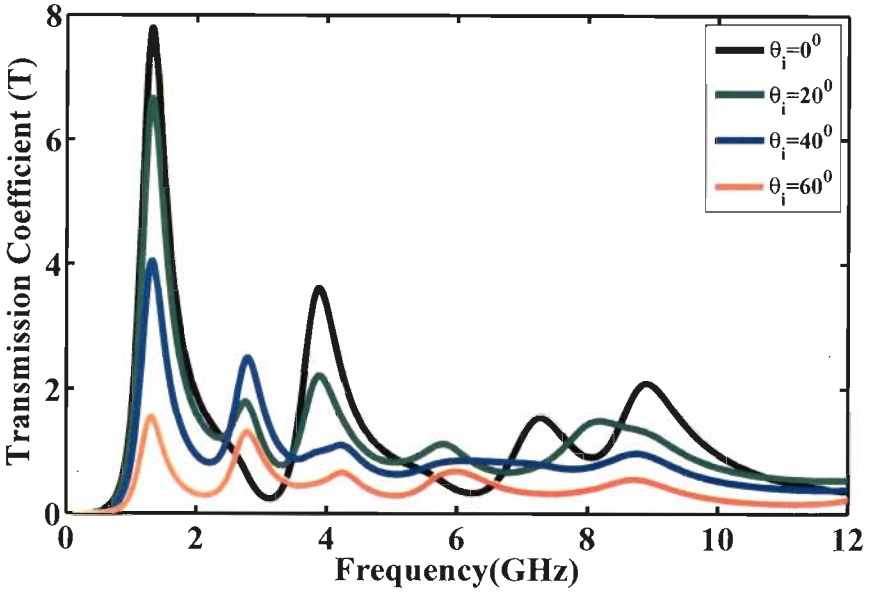

(b) Perpendicular Polarization

Figure 4.16: Transmission coefficient of 2nd iteration Sierpinski gasket aperture for different angles of incidence.

Table 4.7: Transmission parameters of Sierpinski gasket aperture for different angles of incidence with parallel polarization.

θ_i	f_1	f_2	f_3	f_4	f_5	h_1/λ_2	h_2/λ_4
0	1.32	-	3.88	-	8.90	-	-
20	1.32	-	3.88	-	8.90	-	-
40	1.31	2.81	3.84	5.98	8.01	0.83	0.89
60	1.31	2.80	3.76	5.97	7.29	0.83	0.88

Table 4.8: Transmission parameters of Sierpinski gasket aperture for different angles of incidence with perpendicular polarization.

θ_i	f_1	f_2	f_3	f_4	f_5	h_1/λ_2	h_2/λ_4
0	1.32	-	3.88	-	8.95	-	-
20	1.32	2.75	3.88	5.78	8.18	0.94	0.99
40	1.31	2.78	3.92	5.80	8.81	0.95	0.99
60	1.31	2.78	4.24	5.99	8.71	0.95	1.03

as shown in Table 4.7 and Table 4.8. These additional resonant wavelengths are around 1λ as was the case from single aperture. The behavior of current at those additional resonant frequencies are expected to be same as that of a single triangular aperture. Also, it is found that the response of gasket aperture for perpendicular polarization becomes almost flat for incidence angles greater than 60°.

4.4.2 Koch Fractal Slot

Koch curve monopole and dipole antennas have multiband property and are widely used in antenna miniaturization. In [20], a multi-resonant dipole antenna

based on Koch curve has been studied. It has been shown that by changing the indentation angle of the curve, which in turn changes the fractal dimension, the input characteristics of the Koch antennas can be changed. Iterated Function System (IFS) for a generalized Koch curve with a scale factor s and indentation angle θ can be expressed as [20],

$$W_1 \begin{pmatrix} x \\ y \end{pmatrix} = \begin{pmatrix} \frac{1}{s} & 0 \\ 0 & \frac{1}{s} \end{pmatrix} \begin{pmatrix} x' \\ y' \end{pmatrix} \tag{4.13}$$

$$W_2 \begin{pmatrix} x \\ y \end{pmatrix} = \begin{pmatrix} \frac{1}{s}\cos\theta & -\frac{1}{s}\sin\theta \\ \frac{1}{s}\sin\theta & \frac{1}{s}\cos\theta \end{pmatrix} \begin{pmatrix} x' \\ y' \end{pmatrix} + \begin{pmatrix} \frac{1}{s} \\ 0 \end{pmatrix} \tag{4.14}$$

$$W_3 \begin{pmatrix} x \\ y \end{pmatrix} = \begin{pmatrix} \frac{1}{s}\cos\theta & \frac{1}{s}\sin\theta \\ -\frac{1}{s}\sin\theta & \frac{1}{s}\cos\theta \end{pmatrix} \begin{pmatrix} x' \\ y' \end{pmatrix} + \begin{pmatrix} \frac{1}{2} \\ \frac{1}{s}\sin\theta \end{pmatrix} \tag{4.15}$$

$$W_4 \begin{pmatrix} x \\ y \end{pmatrix} = \begin{pmatrix} \frac{1}{s} & 0 \\ 0 & \frac{1}{s} \end{pmatrix} \begin{pmatrix} x' \\ y' \end{pmatrix} + \begin{pmatrix} \frac{s-1}{s} \\ 0 \end{pmatrix} \tag{4.16}$$

where,

$$s = 2(1 + cos(\theta)) \tag{4.17}$$

The self-similarity dimension of the curve is given by

$$D = \frac{\log 4}{\log s} \tag{4.18}$$

Hence, by changing the indentation angle, we can change the fractal dimension. Generalized Koch curve geometries for two indentation angles are shown in Fig. 4.17.

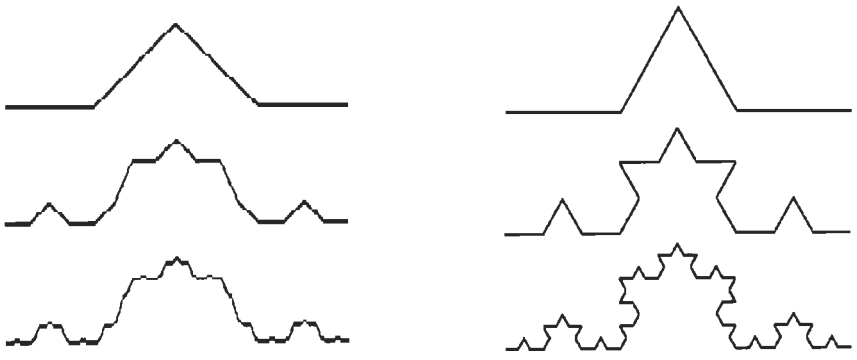

(a) Indentation angle=20° (b) Indentation angle=60°

Figure 4.17: Koch curve with different indentation angles.

Here, we have investigated the transmission properties of the Koch fractal slot of varying fractal dimension in an infinite conducting screen illuminated by a plane wave. For the present analysis, we have considered a rectangular slot of length 20 cm along the x-axis and width 5 mm along the y-axis as the initiator. An electromagnetic wave with perpendicular polarization is assumed to incident normally on the aperture. Fig. 4.18 shows the transmission coefficients of a Koch slot of 60° indentation angle for three different iterations. It can be seen that the resonant frequencies reduce as the order of iteration is increased. This is expected, since the total length of the slot increases with the order of iteration although the end-to-end length remains constant at 20 cm. Another factor that has a strong influence on the value of resonant frequencies and the magnitude of transmission coefficient at resonance, is the indentation angle. The variation of the primary resonant frequency (f_{r1}) for the first three iterations is given in Table 4.9 and the variation of magnitude of transmission coefficient at f_{r1} for different indentation angles is shown in Fig. 4.19, for a 3^{rd} iteration Koch slot. From a study of surface current distribution of Koch slot at the primary resonance, it is found that the current is maximum at the center of the slot and

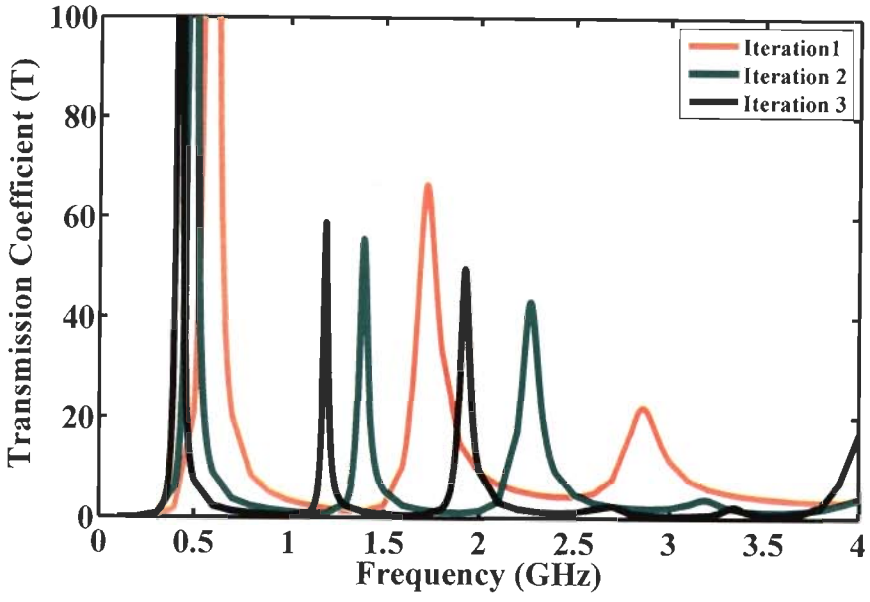

Figure 4.18: Transmission coefficient of Koch fractal slot for different iterations with 60° indentation angle.

Table 4.9: Variation of f_{r1} for Koch aperture with indentation angle.

Indentation Angle (deg.)	Primary Resonant frequency for various iterations of Koch slot (GHz)		
	Iteration 1	Iteration 2	Iteration 3
10	0.710	0.707	0.706
20	0.698	0.686	0.678
30	0.678	0.651	0.633
40	0.651	0.604	0.573
50	0.618	0.547	0.500
60	0.577	0.482	0.420
70	0.529	0.410	0.335
80	0.484	0.342	0.258

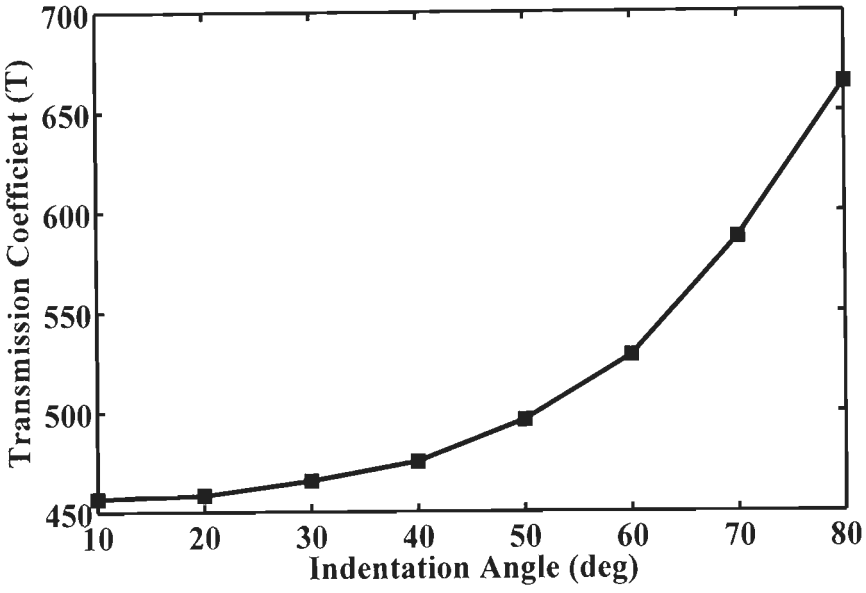

Figure 4.19: Transmission coefficient at primary resonant frequency of a 3rd iteration Koch fractal slot versus different indentation angles.

the magnitude of the maxima increases with the increase in indentation angle, which causes the increase in transmission coefficient. Thus, the indentation angle can be made a design parameter in order to achieve good transmission property at a particular frequency. The variation of resonant frequencies for three iterations with different indentation angles are shown in Fig. 4.20. It may be noted that the higher order resonant frequencies shift by larger amount than the lower order resonant frequencies. The ratio between successive resonant frequencies also changes with the change in indentation angle. The ratios of successive resonant frequencies with the indentation angle are tabulated in Table 4.10 from which it is evident that the indentation angle can be varied in order to place the transmission bands at desired locations. It is also found that the ratios are different for each interval, but they remain nearly constant for different iterations of the same

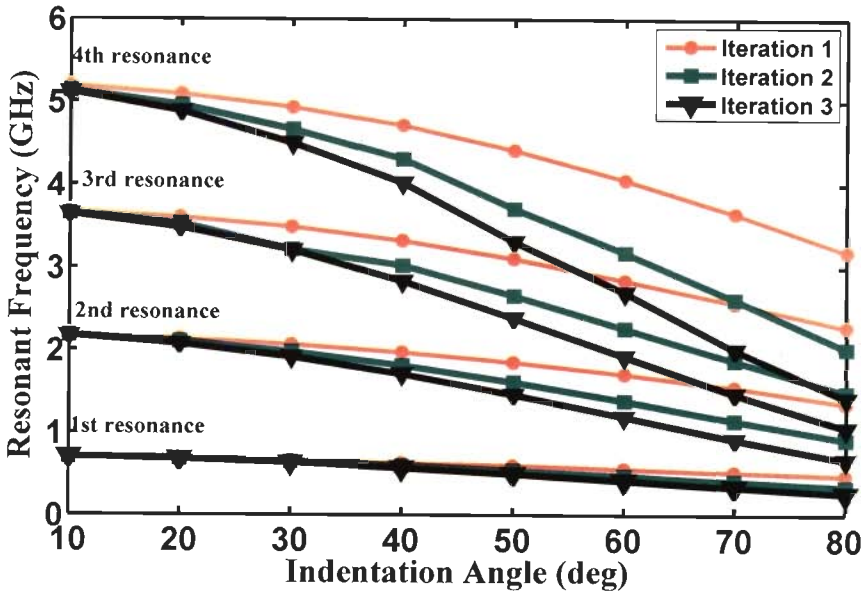

Figure 4.20: Resonant frequencies with different indentation angles for Koch fractal slot.

dimension. It may be mentioned here that a Koch fractal slot is expected to have characteristics similar to those of Koch monopole. The results presented here agree very well with those presented in [20] for a Koch dipole antenna. The transmission cross-section of a third iteration standard Koch slot for two orthogonal planes is shown in Fig. 4.21. It should be noted that the transmission cross-section at the resonant frequencies are similar to that of a linear slot. As the frequency is increased, some ripples are found in the transmission cross-section pattern. Also, it may be noticed that the transmission cross-section patterns remain almost symmetric for both the planes.

Next, the angle of incidence was varied for a Koch curve of 3^{rd} iteration with 60° indentation angle. The normalized transmission coefficient for different angles of incidence is shown in Fig. 4.22 for an incident wave with perpendicular

Table 4.10: Ratio between successive resonant frequencies of generalized Koch slot.

Indentation Angle (deg.)	Fractal Dimension	Fractal Iteration	f_2/f_1	f_3/f_2	f_4/f_3
10	1.006	1	3.09	1.68	1.41
		2	3.08	1.68	1.40
		3	3.08	1.68	1.40
20	1.023	1	3.08	1.68	1.41
		2	3.06	1.68	1.40
		3	3.06	1.68	1.40
30	1.053	1	3.07	1.68	1.41
		2	3.04	1.63	1.44
		3	3.03	1.67	1.40
40	1.099	1	3.05	1.68	1.42
		2	3.00	1.67	1.42
		3	2.98	1.65	1.42
50	1.165	1	3.02	1.67	1.42
		2	2.95	1.65	1.40
		3	2.92	1.63	1.39
60	1.262	1	2.98	1.66	1.42
		2	2.88	1.63	1.41
		3	2.83	1.62	1.40
70	1.404	1	2.94	1.66	1.42
		2	2.79	1.63	1.40
		3	2.73	1.60	1.36
80	1.625	1	2.81	1.68	1.40
		2	2.67	1.62	1.36
		3	2.59	1.58	1.34

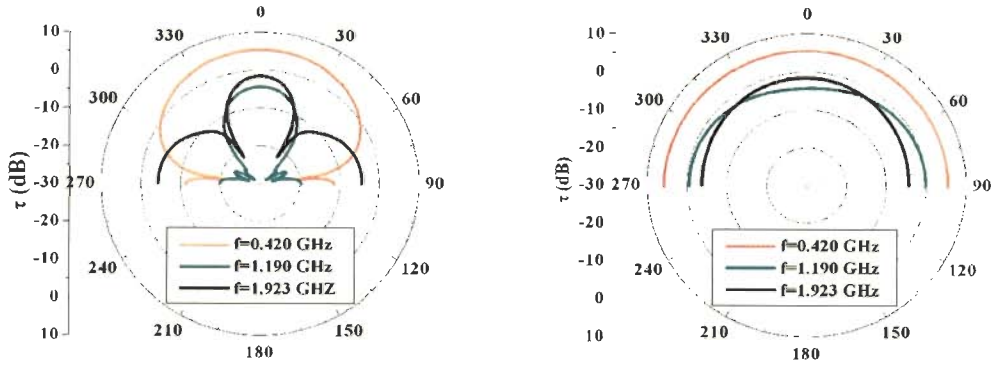

(a) $\phi = 0°$ (b) $\phi = 90°$

Figure 4.21: Transmission cross-section patterns of 3rd iteration Koch fractal slot with indentation angle equal to 60°.

polarization. It can be seen that, similar to gasket apertures, the variation of incidence angle introduces additional resonant frequencies around 0.814 GHz and 1.580 GHz. As the angle of incidence is increased, the transmission coefficient at the resonant frequencies for normal incidence decreases and for $\theta_i = 60°$, the response becomes almost flat for frequencies greater than 1 GHz. Although the transmission coefficient at the new resonant frequencies increases with increase in angle of incidence up to around 40°, it again decreases with increase in θ_i beyond 40°. To understand this phenomena, we studied the magnetic current distribution of a rectangular slot. It was found that, similar to the behavior obtained for a triangular aperture, an additional weak secondary resonance appears around $L = \lambda$ for inclined incidence, where L is the length of the slot. Also, the phase of the dominant component of current undergoes a phase reversal at the secondary resonant frequency, a behavior similar to that of the triangular aperture. The magnitude of current shows two maxima which are $L/2$ distance apart. The same behavior was seen in case of Koch curve for oblique incidence.

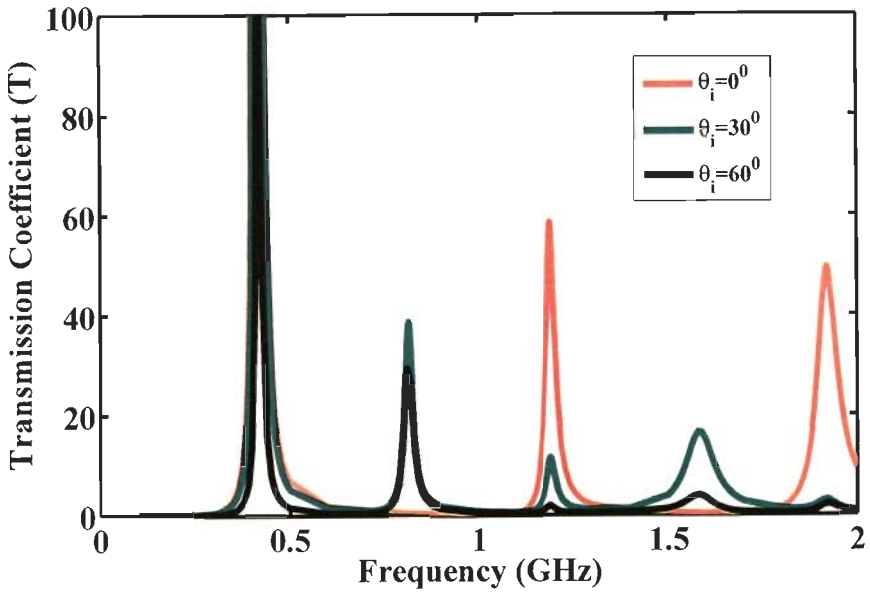

Figure 4.22: Transmission coefficient with different angles of incidence for 3rd iteration Koch fractal slot with indentation angle is 60°.

4.4.3 Hilbert Curve Aperture

Due to its space-filling property, the Hilbert curve can occupy a larger length in a given area than the Koch curve; hence it has been used for further miniaturization of monopole and dipole antennas [22]. The self-similarity of this geometry leads to a multi-band operation. The topological dimension of Hilbert curve is 1, since it is a simple curve. However, for a large number of iterations, the fractal dimension of the curve approaches 2. Considering the length and number of line segments in first and second iterations, the fractal dimension is 1.465. The corresponding fractal dimensions for next two iterations are 1.694 and 1.834, respectively. A fourth iteration Hilbert curve is shown in Fig. 4.23. In our analysis, the Hilbert geometry is assumed to occupy an area of 7.5 cm × 7.5 cm with the width of the slot taken to be 1 mm. The transmission characteristics of different

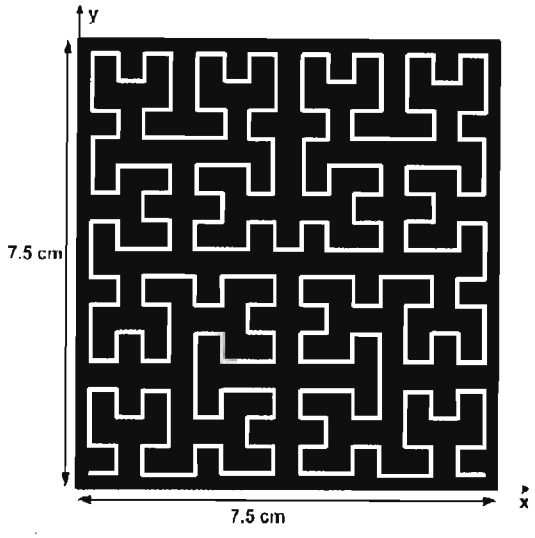

Figure 4.23: Hilbert fractal slot of 4^{th} iteration.

iterations of Hilbert curve fractal aperture illuminated by a plane wave of parallel and perpendicular polarizations with normal incidence are shown in Fig. 4.24. The difference in the transmission coefficient plots for different polarization is due to the fact that the curve is symmetric with respect to y-axis but asymmetric with respect to x-axis. It can be seen from the plot that the Hilbert aperture offers a multi-band behavior and the resonant frequencies decrease as the order of iteration increases due to the increase in the length of the slot. The variation of primary resonant frequency for different iterations of Hilbert curve aperture is summarized in Table 4.11. The transmission bandwidth increases for higher order resonances. Since the transmission coefficient plots show sharp transmission bands with very low transmission between two resonant peaks, it offers excellent band stop characteristics. Again from the current distribution plots, it was found that the current is distributed over the entire aperture region and at the higher resonances, the current is concentrated in the scaled copies of the geometry as shown in Fig. 4.25. Also, the magnitude of surface current decreases with in-

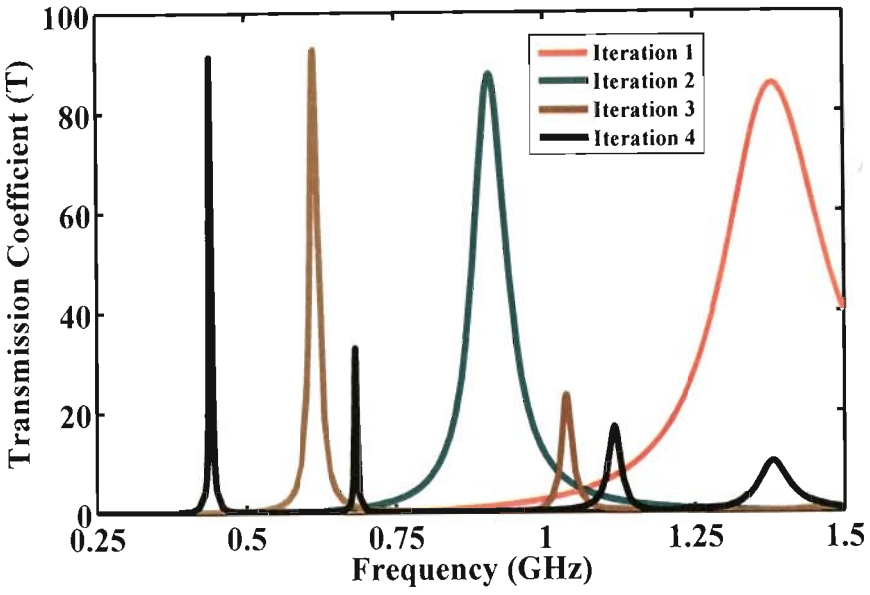

(a) Parallel Polarization

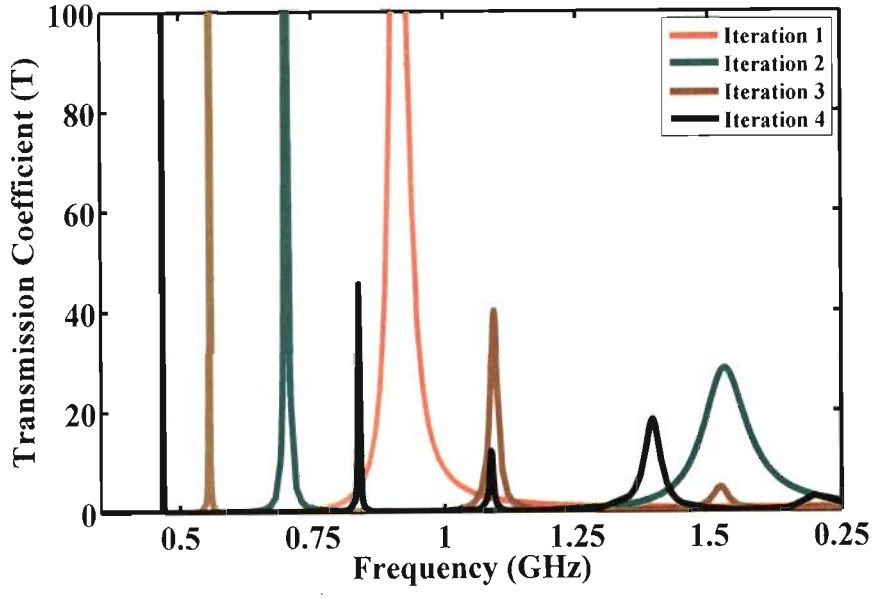

(b) Perpendicular Polarization

Figure 4.24: Transmission coefficient of Hilbert curve aperture for different iterations at normal incidence.

Table 4.11: Primary resonant frequency of Hilbert curve aperture of different iterations.

Iteration	Primary resonant frequency (GHz)	
	Parallel Polarization	Perpendicular Polarization
1	1.383	0.666
2	0.908	0.452
3	0.614	0.306
4	0.4404	0.2172

crease in order of resonance which causes the decrease in transmission coefficient.

The transmission cross-section patterns for a 4^{th} iteration Hilbert aperture at its first four resonant frequencies are shown in Fig. 4.26. From the transmission cross-section plots for both parallel and perpendicular polarizations, it may be stated that the pattern are symmetric at all resonant frequencies, although, the patterns become directive for higher order resonant frequencies.

The variation of transmission coefficient of a 4^{th} iteration Hilbert aperture with different angles of incidence is shown in Fig. 4.27. Again, some additional resonances occur as the angle of incidence is increased. The transmission coefficients at these additional resonant frequencies increase with the increase in angle of incidence. The occurrence of these resonances can be explained in a similar manner as for the case of Koch slot from the current distribution which shows additional maxima at inclined incidence. For perpendicular polarization, some additional resonant frequencies appear but the transmission coefficients at these frequencies are very small as compared to those at the resonant frequencies for normal incidence. Also, the transmission coefficient at a particular resonant

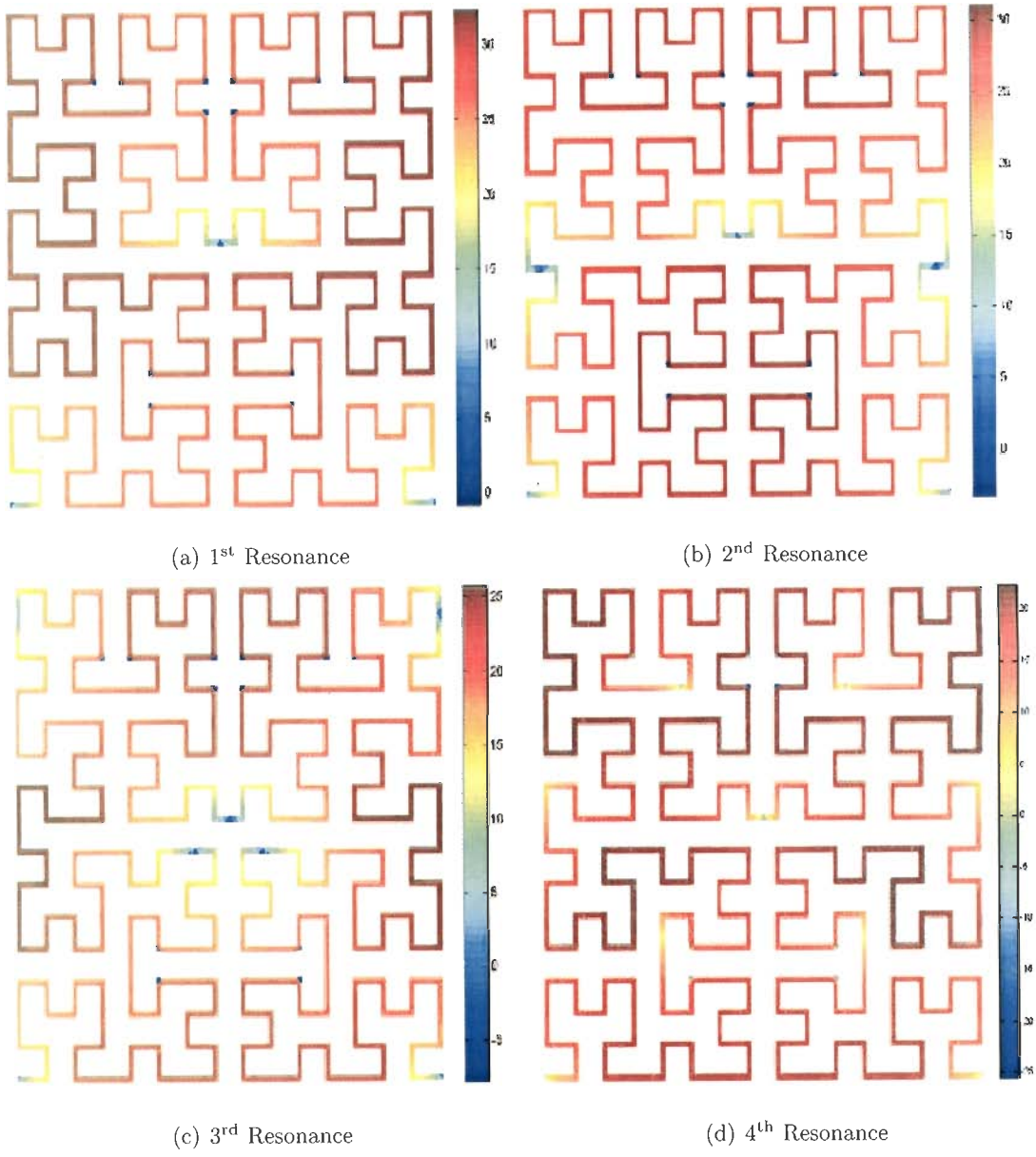

(a) 1st Resonance

(b) 2nd Resonance

(c) 3rd Resonance

(d) 4th Resonance

Figure 4.25: Current distribution on a 4th iteration Hilbert curve aperture at different resonant frequencies.

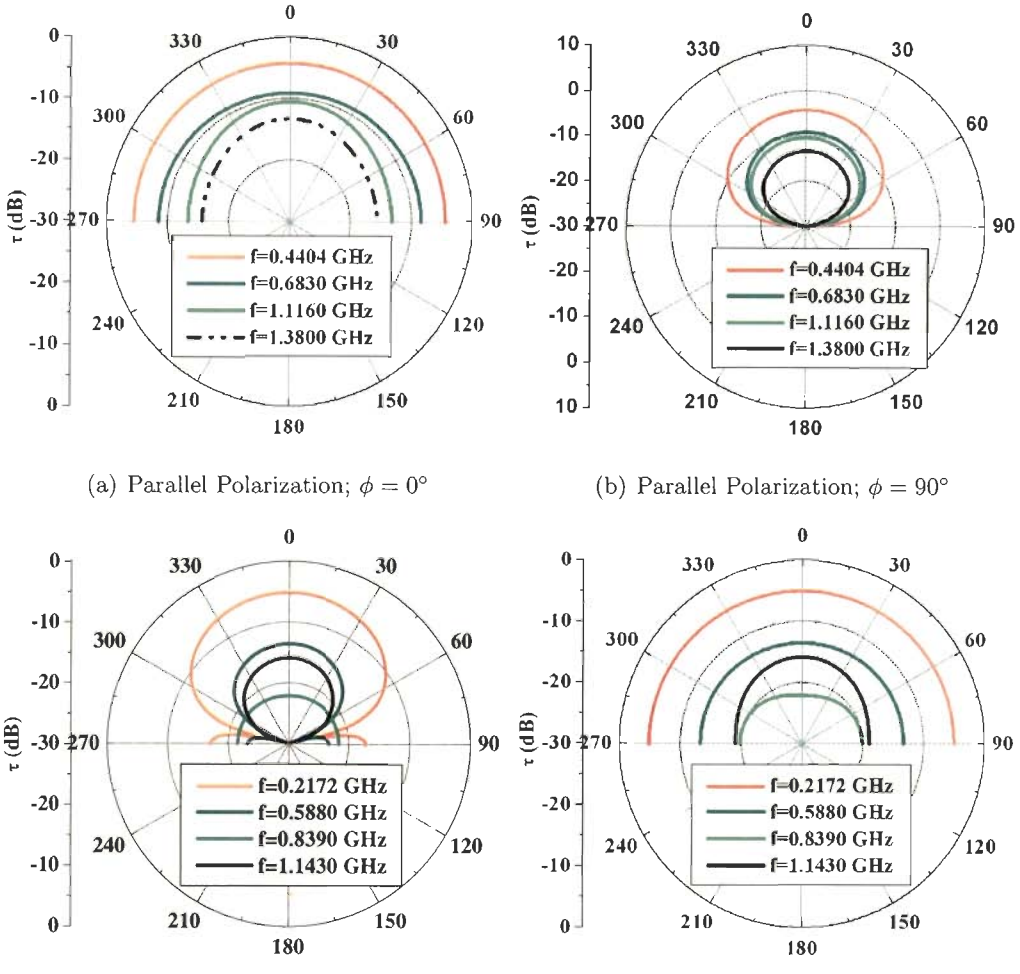

(a) Parallel Polarization; $\phi = 0°$

(b) Parallel Polarization; $\phi = 90°$

(c) Perpendicular Polarization; $\phi = 0°$

(d) Perpendicular Polarization; $\phi = 90°$

Figure 4.26: Transmission cross-section pattern of 4^{th} iteration Hilbert curve aperture at the first four resonant frequencies.

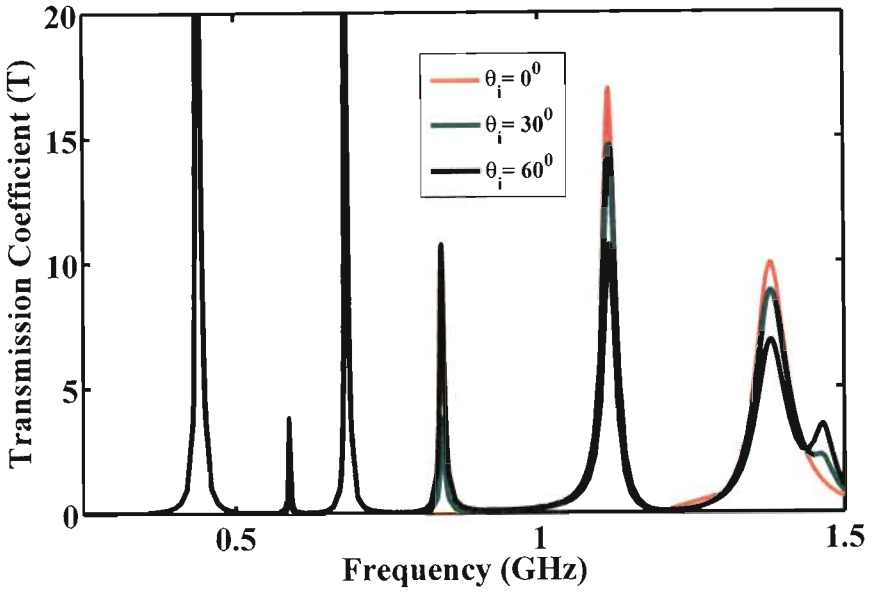

(a) Parallel Polarization

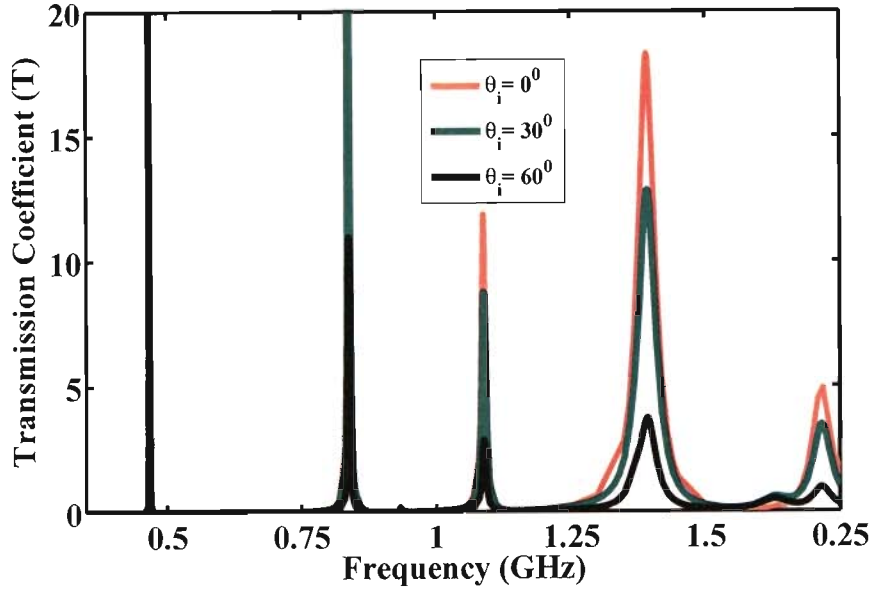

(b) Perpendicular Polarization

Figure 4.27: Transmission coefficient with different angles of incidence of 4^{th} iteration Hilbert slot.

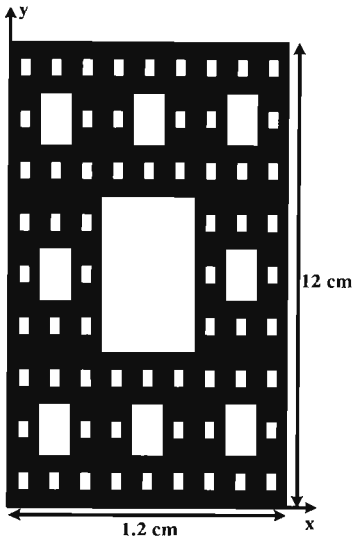

Figure 4.28: Sierpinski carpet aperture of 3rd iteration.

frequency decreases with an increase in the angle of incidence and the decrease is sharper in case of perpendicular polarization.

4.4.4 Sierpinski Carpet Aperture

Another fractal that can be used in multi-band antennas and FSS is Sierpinski carpet fractal [25]. The geometry of a third iteration Sierpinski carpet structure is shown in Fig. 4.28. The dimension used in the present analysis has an initial rectangular geometry of dimensions 1.2 cm $\times$ 12 cm. The transmission characteristics for different iterations of the fractal aperture for parallel polarization of incident wave at normal incidence are shown in Fig. 4.29. Again, it can be noted from the plots that the resonant frequency decreases as the order of iteration increases. Basically, the first iteration consists of a single aperture of dimension 0.4 cm $\times$ 4 cm with the larger dimension along y-direction. The first resonance occurs at a frequency of 3.30 GHz whose corresponding wavelength is twice the

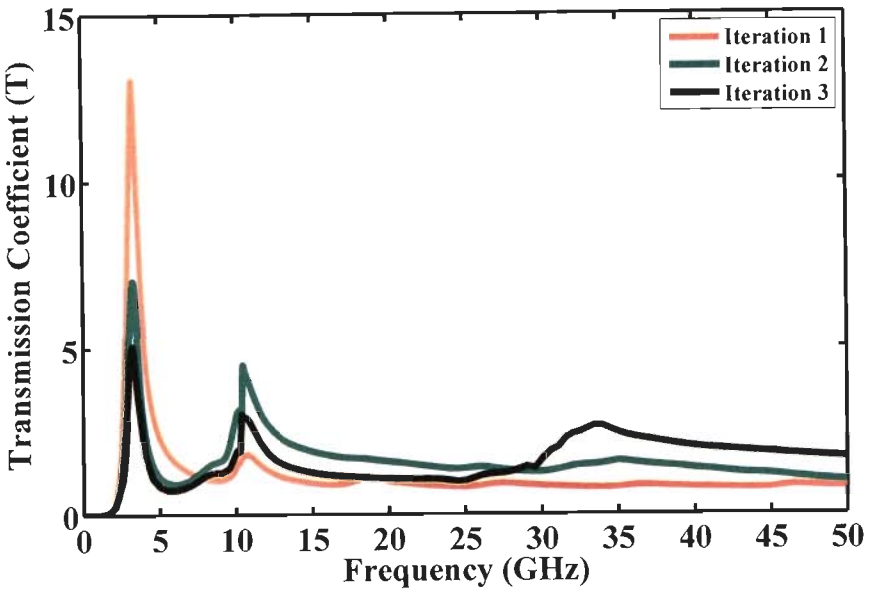

Figure 4.29: Transmission coefficient of Sierpinski carpet aperture with different iterations.

length of the slot in y-direction. In the next iteration, the aperture dimension gets reduced by a factor 3, and hence it is expected to have the second resonant frequency which is three times the first resonant frequency. Thus, the ratio between the successive resonant frequencies is approximately 3. For a 3^{rd} iteration Sierpinski carpet aperture the resonant frequencies occur at 3.3 GHz, 10.4 GHz and 33.7 GHz with frequency ratios as $f_2/f_1 = 3.15$ and $f_3/f_2 = 3.24$. Hence, the resonant frequencies are separated by a factor approximately equal to the theoretical value 3.

The transmission cross-section patterns of 3^{rd} iteration Sierpinski carpet fractal aperture for an incident wave with parallel polarization in two orthogonal planes are shown in Fig. 4.30. It can be seen from the plots that the maximum value of transmission cross section increases for higher order resonant frequencies

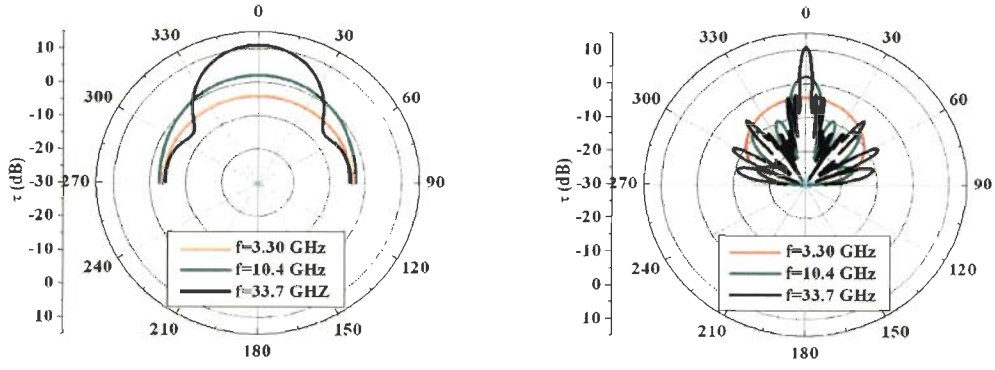

(a) $\phi = 0°$ (b) $\phi = 90°$

Figure 4.30: Transmission cross-section of 3rd iteration Sierpinski carpet aperture at first three resonant frequencies.

and the patterns become more directive. Also, for $\varphi = 90°$ plane, a large number of side lobes are generated for third resonant frequency.

The effect of variation of incidence angle for parallel polarization on the behavior of Sierpinski carpet aperture is shown in Fig. 4.31. It is found that as the incidence angle is increased, the third resonance peak gets distorted and some spurious peaks arise around 30 GHz.

4.4.5 Minkowski Fractal Aperture

Taking a line segment of length L, Minkowski operator divides the line into three equal segments with the middle section having a depth of aL [27]. The coefficient 'a' is known as "depression coefficient". The value of 'a' can be any value between 0 and 1/3 for a square initiator. The Minkowski fractal generator is shown in Fig. 4.32. In the first iteration, each line segment of the initial square is replaced by the generator curve. This process is successively applied to each line segment in the next iteration step. The Minkowski fractal geometry after second iteration

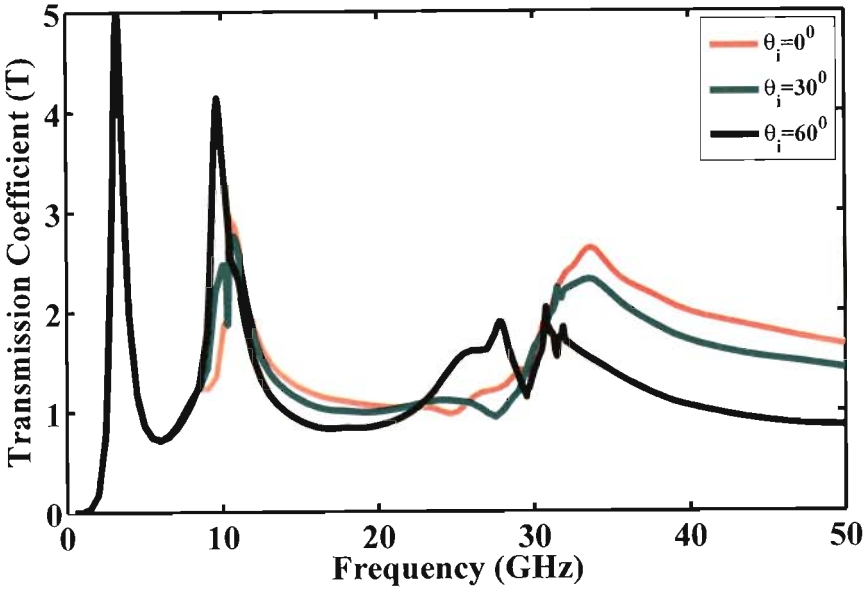

Figure 4.31: Transmission coefficient with different angles of incidence for 3rd iteration Sierpinski carpet aperture.

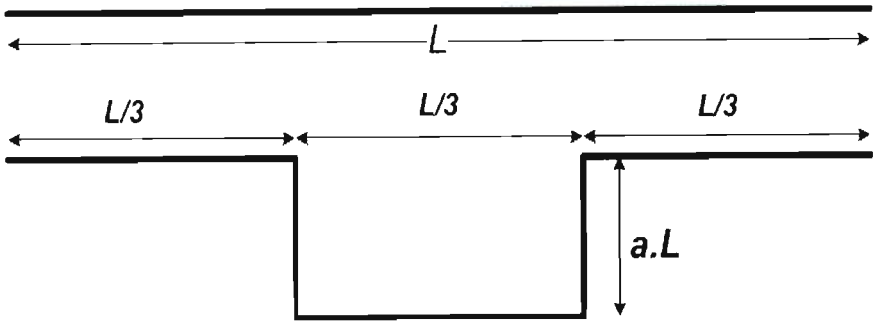

Figure 4.32: Minkowski fractal generator.

with different values of 'a' are shown in Fig. 4.33. The variation of transmission coefficient for different iterations of Minkowski fractal aperture with $a = 0.3$ for parallel polarization of incident wave at normal incidence is shown in Fig. 4.34. Since the geometry is symmetric along both x- and y-directions, the transmission characteristics are similar for both parallel and perpendicular polarizations of incident waves. For $a = 0.3$, the resonances occur at 0.92 GHz, 3.16 GHz and 12.1 GHz with the ratios between successive resonant frequencies of 3.43 and 3.83, although the third resonance peak is very small as compared to the first two resonant peaks. The variation of transmission coefficient of a 2^{nd} iteration Minkowski fractal aperture for different values of depression coefficients is shown in Fig. 4.35. As the value of depression coefficient decreases, the transmission coefficient at a particular resonant frequency decreases, and the higher-order resonant properties diminish. Also, it can be seen from the plot that, as the value of depression coefficient increases, the resonant frequency moves downwards, a behavior similar to that demonstrated in [27] for a Minkowski fractal patch antenna. Thus, it is evident that the fractal aperture shows a better multiband property for higher values of 'a'.

The transmission cross-section patterns of second iteration Minkowski fractal aperture for $a = 0.3$ with parallel polarization of incident wave are shown in Fig. 4.36. It can be seen that the value of transmission cross-section increases for higher resonant frequencies, but the number of side lobes also increases. Since the geometry is symmetric in x- and y- planes, the cross-section patterns are also symmetric.

The variation of transmission coefficient for different angles of incidence with $a = 0.3$ is shown in Fig. 4.37. The transmission coefficients at 1^{st} and 2^{nd} resonant frequencies get reduced with increase in the angle of incidence and for

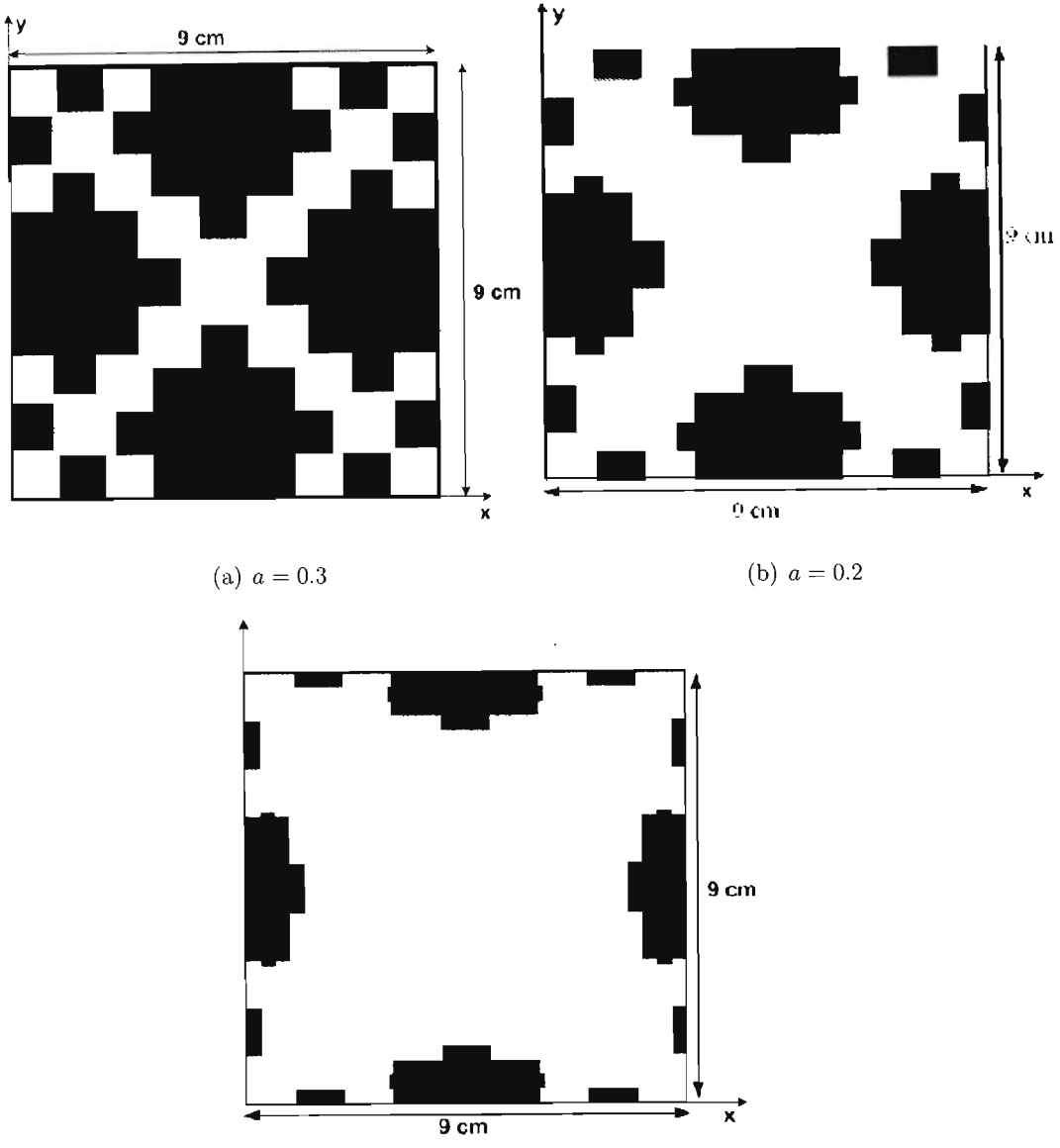

(a) $a = 0.3$

(b) $a = 0.2$

(c) $a = 0.1$

Figure 4.33: 2^{nd} iteration Minkowski fractal geometries for different values of depression coefficients.

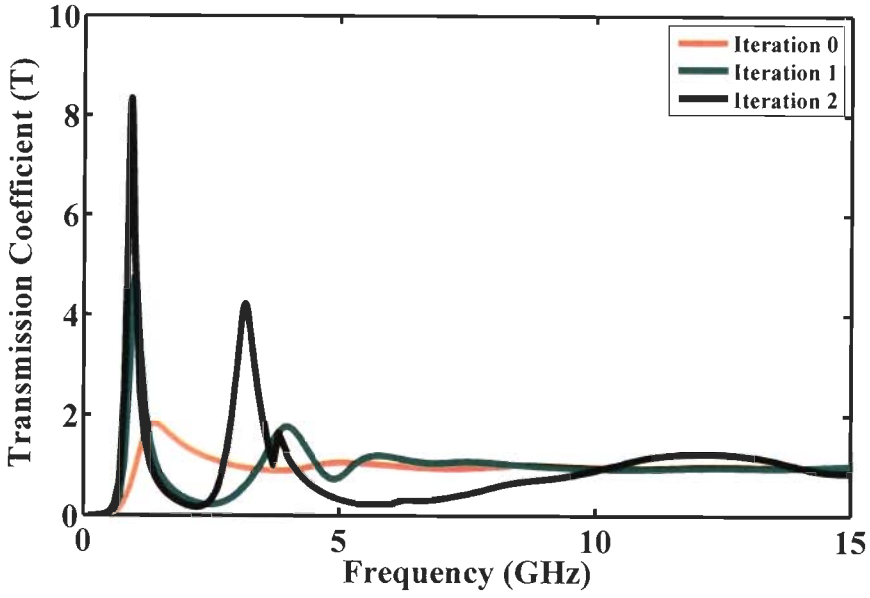

Figure 4.34: Transmission coefficient of Minkowski fractal aperture for different iterations with parallel polarization at normal incidence.

higher angles of incidence, the third resonances almost vanishes and hence, the multiband property of fractal is lost.

4.5 Summary

Numerical results for a number of fractal shaped apertures in an infinite conducting screen illuminated by a plane wave have been presented which show the existence of multiple passbands. For a Sierpinski fractal aperture, the bands are separated by a factor 2, which is similar to that obtained for a Sierpinski monopole antenna. As long as the initial triangle is equilateral, the transmission characteristics are similar for parallel and perpendicular polarizations of incident wave. Also, it has been found that the fractal property of the gasket aperture depends on the flare angle of the triangle as well as on the polarization of in-

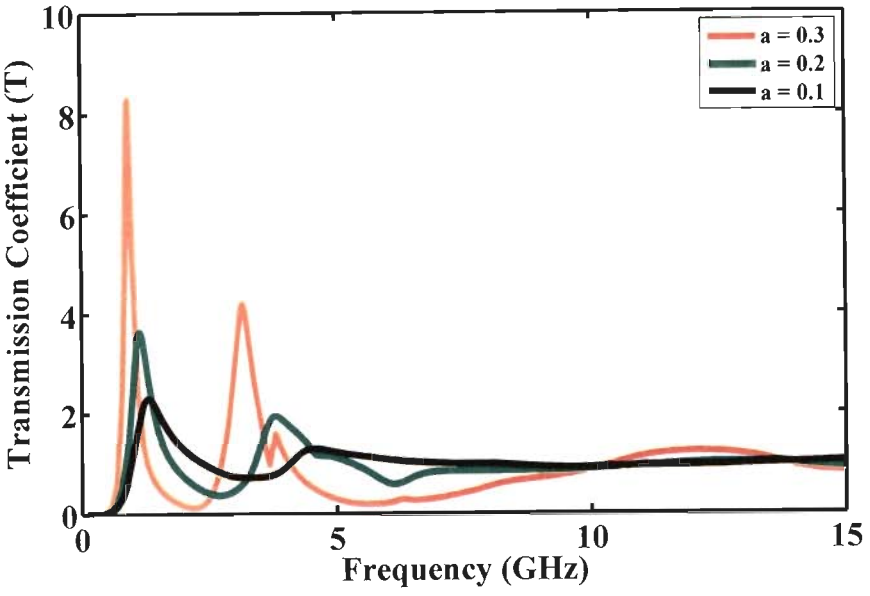

Figure 4.35: Transmission coefficient of 2nd iteration Minkowski fractal aperture for different values of depression coefficient.

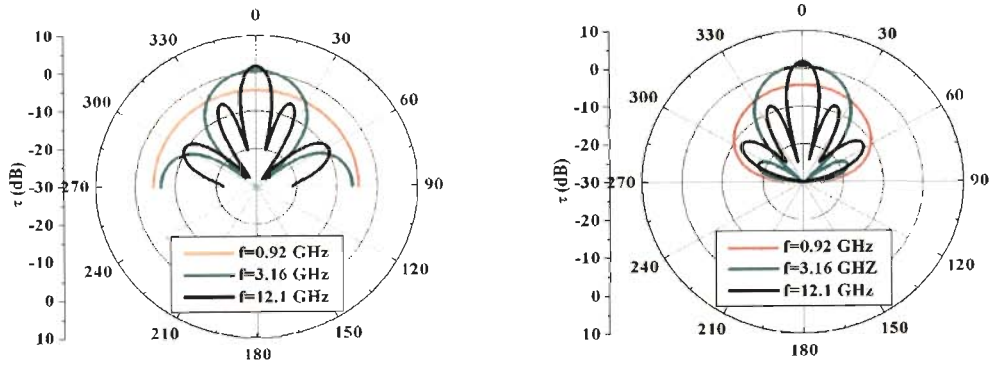

(a) $\phi = 0°$ (b) $\phi = 90°$

Figure 4.36: Transmission cross-section patterns of a 2nd iteration Minkowski fractal aperture at three resonant frequencies with $a = 0.3$ for parallel polarization at normal incidence.

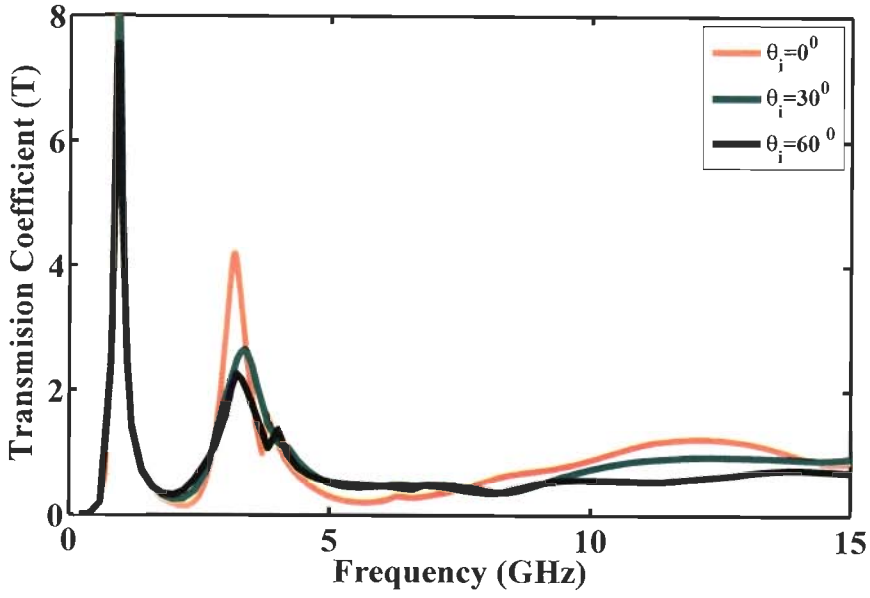

Figure 4.37: Transmission coefficient with different angle of incidence for 2^{nd} iteration Minkowski aperture with $a = 0.3$.

cident wave. The band separation also changes at oblique incidence due to the generation of some new passbands. Also, it is evident from the results that the number of passbands equals the number of iterations for Sierpinski carpet aperture. However, for Sierpinski gasket aperture, a transmission band is obtained for the initial triangular geometry and for any number of iterations, say k, the number of passbands are always $(k + 1)$, as is found in the case of fractal multiband antenna and FSS. Also, while it is true that for each fractal geometry, log periodic behavior can be achieved by using a large number of iterations, since here we are considering prefractal geometries the behavior is quasi log periodic.

Similar to a Koch fractal monopole antenna, the Koch fractal slot also possesses multiband characteristics and the location of different passbands can be changed by changing the indentation angle. Hilbert curve fractal slots are very

efficient for the reduction of resonant frequency, although the bandwidth of passbands decreases significantly for higher iterations. It has been found that some new passbands occur with the increase in angle of incidence for parallel polarization, whereas, the transmission coefficient at the resonant frequencies decreases significantly with increase in angle of incidence for perpendicular polarization. It may be noted that the Hilbert curve fractal geometry is not strictly self-similar as pointed out in [22], because additional line segments are required to connect the four scaled and rotated copies. However, the lengths of these additional line segments are small as compared to the overall length of the fractal, especially when the order of iteration is very large, which makes the geometry self-similar. For larger order iterations, the self-similarity dimension of the fractal approaches 2 which makes it a true space-filling curve. For lower order iterations, the self-similarity dimension of the fractal geometry can be much less than 2 [22].

The Sierpinski carpet fractal aperture also offers multiple passbands with the passbands separated by a factor of 3, equal to the self-similarity factor of the geometry. Also, it has been found that the variation of incidence angle does not change the transmission characteristics for lower frequencies, but the third resonance gets distorted. Lastly, it has been shown that the characteristics of Minkowski fractal depend upon the depression coefficient of the Minkowski operator. The transmission coefficient decreases with the increase in angle of incidence, although the ratios of successive bands remain same.

It must also be added here that that the fractals having space-filling properties give rise to enhanced subwavelength transmission as was seen in [86, 87, 88, 89]. For example, the lowest frequency of Hilbert curve aperture is 0.2171 GHz for a perpendicularly polarized incident wave, corresponding to a wavelength of 138.12 cm which is many times the lateral dimension of the square which it fills. Since

the geometry is not symmetric in both planes, the response of the aperture are different for different polarizations as was also seen in case of H shaped fractal slit [89]. The existence of subwavelength transmission can also be found in Koch curve due to their frequency reduction capability. Koch slot was found to have resonant frequencies of 0.484 GHz and 0.577 GHz for indentation angles of 80° and 60°, respectively. The corresponding wavelengths are 61.98 cm and 51.99 cm which are much larger than the Koch curve length. Since, the increase in indentation angle causes the resonant frequency to shift downward and also, the magnitude of transmission coefficient increases, it can be said that at higher indentation angle there is a more enhanced subwavelength transmission. For Minkowski fractal aperture, the lowest resonant frequency is 0.92 GHz for a 2^{nd} iteration fractal with $a = 0.3$, corresponding to a wavelength of 32.6 cm. Again the wavelength is much larger than the lateral dimension of fractal geometry.

On the other hand, self-similar structures like Sierpinski gasket and Sierpinski carpet do not exhibit subwavelength transmission, since for these structures the reduction in the first resonance frequency is very small for higher order iterations.

Chapter 5

RADIATION FROM RECTANGULAR WAVEGUIDE-FED FRACTAL APERTURE ANTENNAS

In this chapter, we investigate the characteristics of fractal apertures in an infinite conducting screen fed by a rectangular waveguide. The fractal geometries considered here are same as those investigated in chapter 3.

First, the operator equation (2.2) is specialized to the problem under consideration. The operator equation is then solved using the aperture admittance matrix and the excitation vector which have already been derived in chapter 2. A MATLAB code has been written based upon these equations and can be used to analyze different type of fractal apertures. The results obtained with this code have been validated through simulations on Ansoft's HFSS. The characteristics of the antennas are expressed in terms of input reflection coefficient and VSWR

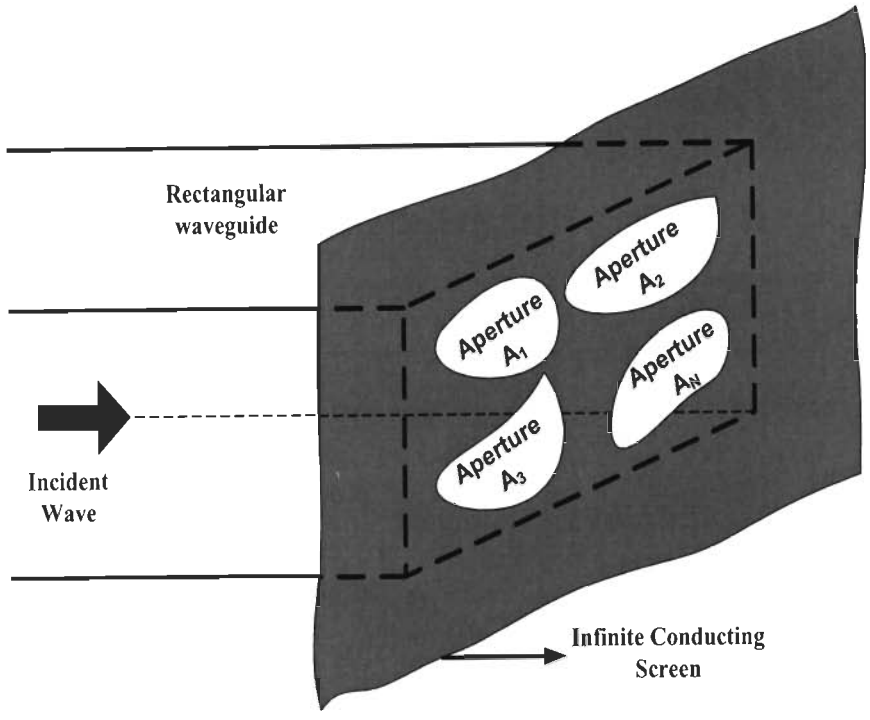

Figure 5.1: Multiple apertures in an infinite conducting screen fed by rectangular waveguide.

in the near-field region, and the far-field behavior is expressed in terms of gain pattern of the antenna.

5.1 Formulation of the Problem

Figure 5.1 shows the general problem geometry of radiation through multiple apertures in an infinite conducting screen fed by a rectangular waveguide. The apertures are located in $z = 0$ plane and can have any arbitrary shape. As described in chapter 2, the equivalence principle is used to decouple the original problem into two equivalent problems. Hence, region 'a' is now a semi-infinite rectangular waveguide short circuited at $z = 0$, in which the total field is the

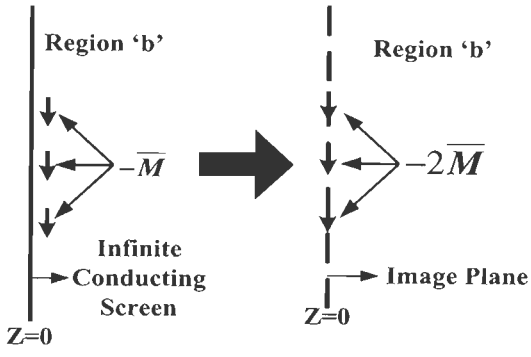

Figure 5.2: Equivalent model for the half space region.

superposition of the fields due to the incident wave and the equivalent surface magnetic current density $\overline{M}$ over the aperture regions. Region 'b' is a half-space in which the field is due to surface magnetic current $-\overline{M}$ radiating in presence of an infinite conducting plane. The equivalent problem for region 'b' can further be simplified by using the image theory as shown in Fig. 5.2, and hence, the field in region 'b' is due to the current $-2\overline{M}$ radiating in free space. The operator equation for the problem can be expressed as

$$\overline{H}_t^a(\overline{M}) + \overline{H}_t^b(\overline{M}) = -(H_t^{inc} + H_t^{ref}) \tag{5.1}$$

where $\overline{H}_t^{inc}$ is the magnetic field due to the incident wave and $\overline{H}_t^{ref}$ denotes the reflected magnetic field. Now, from image theory, the magnetic field in region 'b' can be expressed as

$$\overline{H}_t^b(\overline{M}) = \overline{H}_t^{hs}(\overline{M}) = \overline{H}_t^{fs}(2\overline{M}) \tag{5.2}$$

where $\overline{H}_t^{hs}$ denotes the magnetic field due to a current $\overline{M}$ radiating in the presence of complete conductor and $\overline{H}_t^{fs}$ denotes the magnetic field due to a current $2\overline{M}$ radiating in free space.

Using (5.2) and considering the perfect conductor at $z = 0$, the operator

equation in (5.1) can be expressed as

$$\overline{H}_t^{wg}(\overline{M}) + \overline{H}_t^{fs}(2\overline{M}) = -2\overline{H}_t^{inc} \tag{5.3}$$

Application of MoM results in the following matrix equation

$$\left[Y^{wg} + Y^{hs}\right] \overrightarrow{V} = \overrightarrow{I}^{i} \tag{5.4}$$

where the admittance matrices $[Y^{wg}]$ and $[Y^{hs}]$ can be calculated using (2.67) and (2.80) with the aperture surfaces modeled with the RWG functions. The excitation vector $\overrightarrow{I}^{i}$ is calculated using (2.94) as described in chapter 2 for a TE_{mn} incident mode.

5.2 Computation of Antenna Parameters

5.2.1 Input Reflection Coefficient

The input reflection coefficient can be expressed as given in (3.11), for a TE_{10} mode

$$S_{11} = -1 + \sum_{n=1}^{N} V_n A_{n0} \tag{5.5}$$

where the coefficients A_{n0} are given by

$$A_{n0} = \iint_{A_p} \overline{M}_n \cdot \hat{z} \times \bar{e}_{10}\, ds \tag{5.6}$$

The normalized input admittance can be expressed as

$$Y_{ap} = -\frac{2S_{11}}{1 + S_{11}} \tag{5.7}$$

5.2.2 Gain Pattern

Gain of an antenna is defined as the ratio of radiation intensity in a given direction to the radiation intensity which would exist if the total power were radiated

uniformly in half space. Thus

$$G(\theta,\varphi) = \frac{\psi(\theta,\varphi)}{\psi_{av}} \tag{5.8}$$

where, $\psi(\theta,\varphi)$ denotes the radiation intensity in a given direction and ψ_{av} is the average radiation intensity in half space. Radiation intensity in a given direction is given by

$$\psi(\theta,\varphi) = r_m^2 |\overline{H}_m|^2 \eta \tag{5.9}$$

Using (2.108), above equation can be expressed as

$$\psi(\theta,\varphi) = \frac{\eta\omega^2\varepsilon^2}{16\pi^2 r_m^2} \left| \widetilde{P}^m \overrightarrow{V} \right|^2 \tag{5.10}$$

The average radiated power is

$$\begin{aligned} U_{av} &= P_{rad}/4\pi \\ &= \frac{1}{2} Re \left(\iint\limits_{Apert} \overline{E} \times \overline{H}^* \,.\, \hat{n}\, ds \right) \\ &= \frac{1}{2} Re \left(\iint\limits_{Apert} \overline{M} \,.\, \overline{H}^* \, ds \right) \end{aligned}$$

Since, the power transmitted into region 'b' depends only on the tangential component of $\overline{H}$ at $z = 0$, and the application of image theory yields

$$\begin{aligned} U_{av} &= \frac{1}{2} Re \left(\iint\limits_{Apert} \overline{M} \,.\, \overline{H}_t^{b*}(-\overline{M})\, ds \right) \\ &= \frac{1}{2} Re \left(\iint\limits_{Apert} \overline{M} \,.\, \overline{H}_t^{fs*}(-2\overline{M})\, ds \right) \\ &= \frac{1}{2} Re \left(\sum_m \sum_n V_m V_n^* \iint\limits_{Apert} \overline{M}_m \,.\, \overline{H}_t^{fs*}(-2\overline{M}_n) \right) \, ds \end{aligned}$$

It is evident that the surface integral is same as the admittance matrix for the half-space region given in (2.69). Hence, it is written as

$$\begin{aligned} &= \frac{1}{2} Re\left(\sum_m \sum_n V_m V_n^* Y_{mn}^{hs*}\right) \\ &= \frac{1}{2} Re\left(\widetilde{V}[Y^{hs}]^* \overrightarrow{V}\right) \end{aligned} \tag{5.11}$$

Finally, the gain of the antenna can be expressed as

$$G = \frac{k_0^2}{8\pi\eta} \frac{|\widetilde{P}^m \overrightarrow{V}|}{Re(\widetilde{V}(Y^{hs})^* \overrightarrow{V}^*)} \tag{5.12}$$

5.3 Numerical Results

Based on the MoM formulation, a MATLAB code with the time critical routine coded in C has been developed to determine the characteristics of rectangular waveguide-fed fractal aperture antennas. In all the cases, a WR90 waveguide of dimensions a=22.86 mm and b=10.16 mm has been considered. The numerical results have been validated using the results obtained from the simulation on Ansoft's HFSS. In the following subsections, numerical results for various fractal shaped aperture antennas are presented and discussed.

5.3.1 Sierpinski Gasket Aperture Antenna

First, a 2^{nd} iteration self-affine Sierpinski gasket aperture, same as that used in chapter 3, is considered here (Fig. 5.3). In the first iteration, the length of the triangular aperture is $0.8a$ (18.29 mm). In the next iteration, the length of the apertures are $0.64a$ (14.63 mm) and $0.16a$ (3.66 mm). First, a convergence analysis on the number of basis functions and the waveguide modes is carried out. The magnitude of input reflection coefficient for a single triangular aperture of length 18.29 mm for different number of expansion functions is shown in

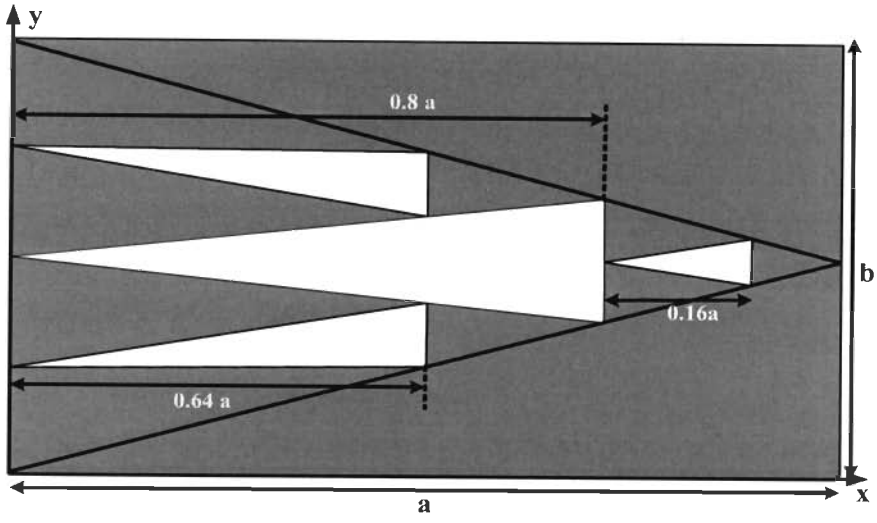

Figure 5.3: A 2nd iteration self-affine Sierpinski gasket aperture antenna.

Table 5.1. It is found that the magnitude of reflection coefficient converges as the maximum edge length becomes less than $0.1\lambda_g$, where λ_g is the guide wavelength. Based upon this observation, in the subsequent fractal aperture antennas, the mesh criterion is chosen such that the maximum edge length is less than $0.1\lambda_g$. The variation of return loss of a self-affine Sierpinski gasket aperture with a scale factor (s) equal to 0.8 is shown in Fig. 5.4 for two iterations. For the first iteration, $M = 10$ and $N = 15$ were used to yield a converged result, whereas, the values for the 2nd iteration were $M = 11$ and $N = 22$. Also shown in the figure are the results of simulation on Ansoft's HFSS, where a good agreement between the two can be seen. Various parameters obtained from the frequency response of the gasket aperture antenna are tabulated in Table 5.2. The aperture length to corresponding resonant wavelength ratio for the first and second iterations are 0.51 and 0.53. This is in line with the observations made in [111] for a rectangular aperture. It is seen that the first resonant frequency shifts downwards for the second iteration and also, the bandwidth for higher order resonant frequency is

Table 5.1: Convergence of reflection coefficient of waveguide-fed 1st iteration Sierpinski gasket aperture antenna. The frequency of operation is 12 GHz.

Sr. No.	No. of RWG functions	Max. Edge Length (mm)	Modal Indices M	Modal Indices N	$\|s_{11}\|$	% change
1	6	4.91	10	15	0.7583	
2	10	3.57	10	15	0.7859	3.64
3	14	2.98	10	15	0.7962	1.31
4	18	2.66	10	15	0.8012	0.63
5	22	2.47	10	15	0.8039	0.34

Table 5.2: Frequency response of waveguide-fed self-affine Sierpinski gasket aperture antenna.

Parameters	Iteration 1	Iteration 2	
Resonant Frequency (GHz)			
MoM	8.45	8.40	11.05
HFSS	8.44	8.39	11.05
Difference (%)	0.12	0.12	0.00
VSWR	1.29	1.26	1.03
Bandwidth (%)	11.83	10.12	13.58

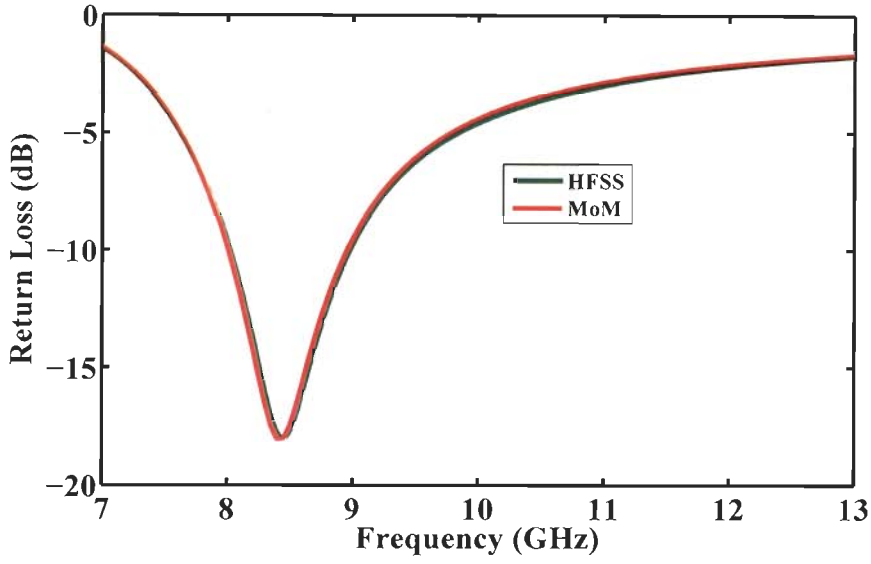

(a) 1st Iteration

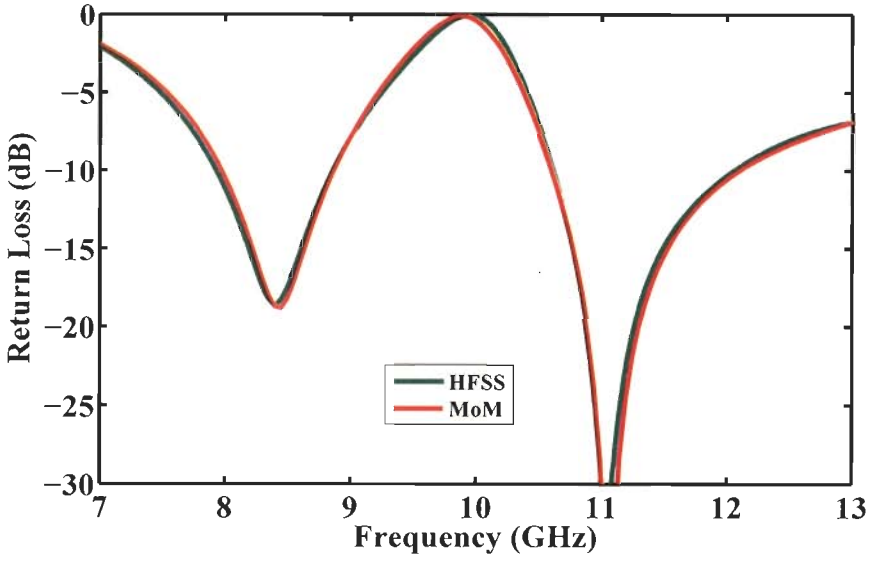

(b) 2nd Iteration

Figure 5.4: Return loss of a waveguide-fed self-affine Sierpinski gasket aperture antenna with $s = 0.8$ for two iterations.

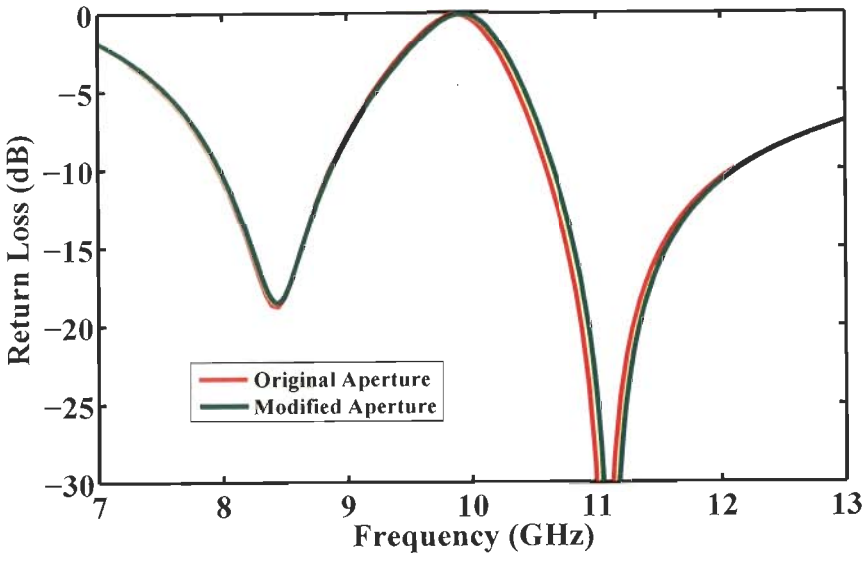

Figure 5.5: Return loss of a waveguide-fed 2nd iteration self-affine modified Sierpinski gasket aperture antenna with $s = 0.8$.

larger than that at the lower order resonance. The ratio between the successive resonant frequencies is 1.32 which is slightly greater than the ideal ratio of 1.25 for a scale factor of 0.8. Also, it is evident that a better impedance match is obtained at the second resonance of the antenna. The aperture of length 3.66 mm ($0.16a$) has no effect on the frequency band under consideration due to its small size and weak interaction with the electric field of TE_{10} mode, since it is located close to side wall of the waveguide. Fig. 5.5 shows the variation of return loss with the aperture of length 3.66 mm removed. It is evident from the figure that there is hardly any change in the frequency response.

In order to find out the effect of scale factor on the antenna performance, the scale factor of the self-affine gasket geometry was varied. The length of the first iteration triangle was kept constant and the dimension of the second iteration triangle was varied in the same way as described in chapter 3. In all the cases, the

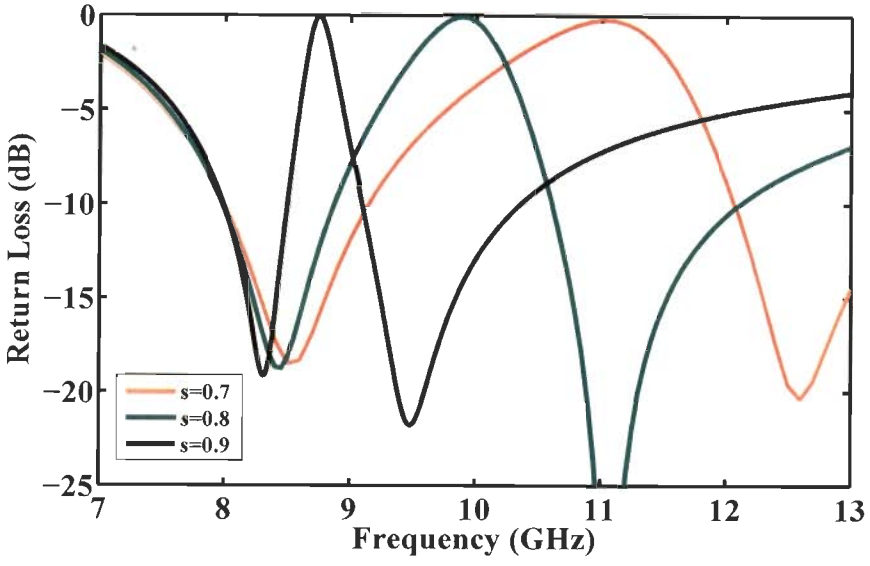

Figure 5.6: Return loss of a waveguide-fed 2nd iteration self-affine modified Sierpinski gasket aperture antenna with different scale factors.

second iteration triangle of length $0.16a$ was removed. The variation of return loss of the modified 2nd iteration Sierpinski gasket aperture for different scale factors is shown in Fig. 5.6. The effect of the scale factor on the frequency response of the antenna is summarized in Table 5.3. It may be noted that while 1st resonant frequency changes relatively little with the increase in scale factor, the bandwidth of the antenna decreases significantly with the increase in scale factor. On the other hand, the second resonant frequency undergoes a relatively large change while the bandwidth at this frequency remains more or less the same.

The gain patterns of a Sierpinski gasket aperture antenna of 2nd iteration, in $\varphi = 0°$ and $\varphi = 90°$ planes, are shown in Fig. 5.7 for the two resonant frequencies. It can be seen that the gain patterns remain the same at both frequencies, although a little ripple can be found in the pattern obtained from

Table 5.3: Frequency response of waveguide-fed self-affine Sierpinski gasket aperture antenna for different scale factors.

Scale factor (s)	Resonant frequencies		Ratio	Bandwidth (%)	
	f_1 (GHz)	f_2 (GHz)	$\frac{f_2}{f_1}$	f_1	f_2
0.7	8.50	12.50	1.47	13.52	13.76
0.8	8.40	11.05	1.32	10.12	13.58
0.9	8.31	9.48	1.14	6.26	13.40

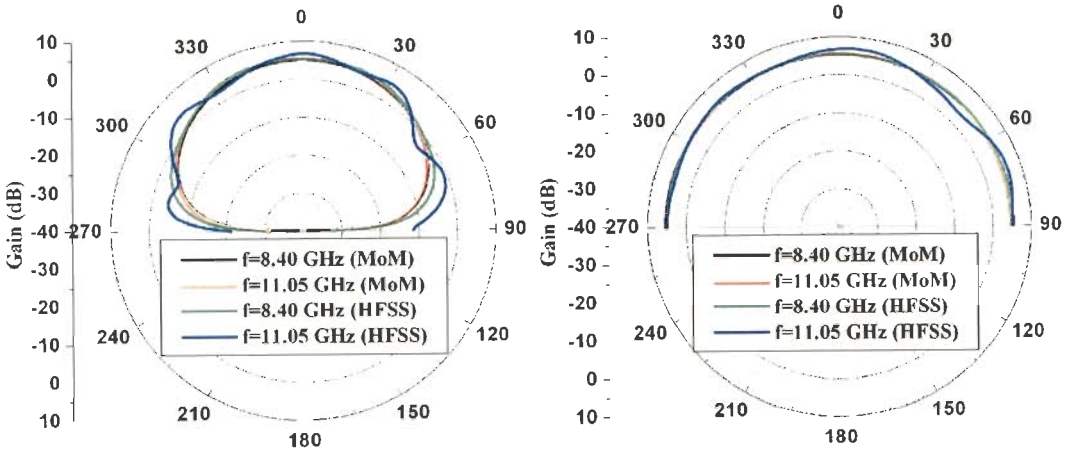

(a) $\varphi = 0°$ (b) $\varphi = 90°$

Figure 5.7: Gain pattern of waveguide-fed 2nd iteration Sierpinski gasket aperture antenna with $s = 0.8$.

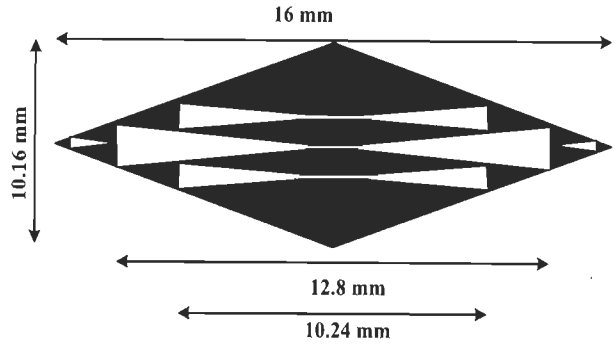

Figure 5.8: A self-affine modified Sierpinski gasket dipole aperture.

Table 5.4: Frequency response of waveguide-fed self-affine modified Sierpinski gasket dipole aperture antenna.

Parameters	Iteration 1	Iteration 2	
Resonant Frequency (GHz)			
MoM	8.96	8.40	11.80
HFSS	8.95	8.38	11.84
Difference (%)	0.11	0.24	0.34
VSWR	1.40	1.41	1.09
Bandwidth (%)	7.60	3.21	14.41

HFSS simulations for both planes. The maximum gain of the antenna is 5.14 dB. In the $\varphi = 90°$ plane, the antenna has a omnidirectional pattern at both resonant frequencies.

As in the case of waveguide diaphragms, next we considered the geometry obtained by a dipole arrangement of the original gasket geometry (Fig 5.8). The variation of return loss for two iterations of the dipole aperture antenna is shown in Fig. 5.9. Table 5.4 summarizes different parameters of the aperture antenna. The behavior of the aperture antenna is similar to that of the waveguide

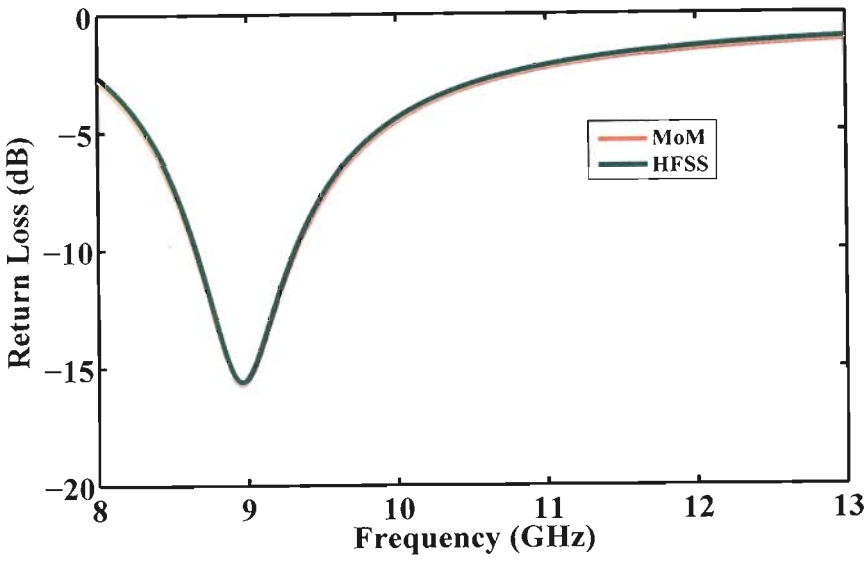

(a) 1st Iteration

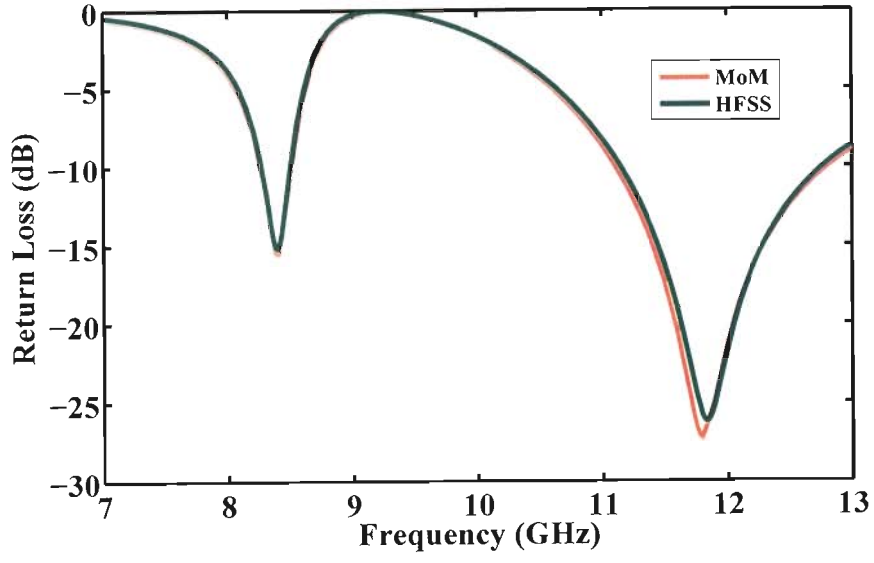

(b) 2nd Iteration

Figure 5.9: Return loss of waveguide-fed self-affine modified Sierpinski gasket dipole aperture antenna with $s = 0.8$ for two iterations.

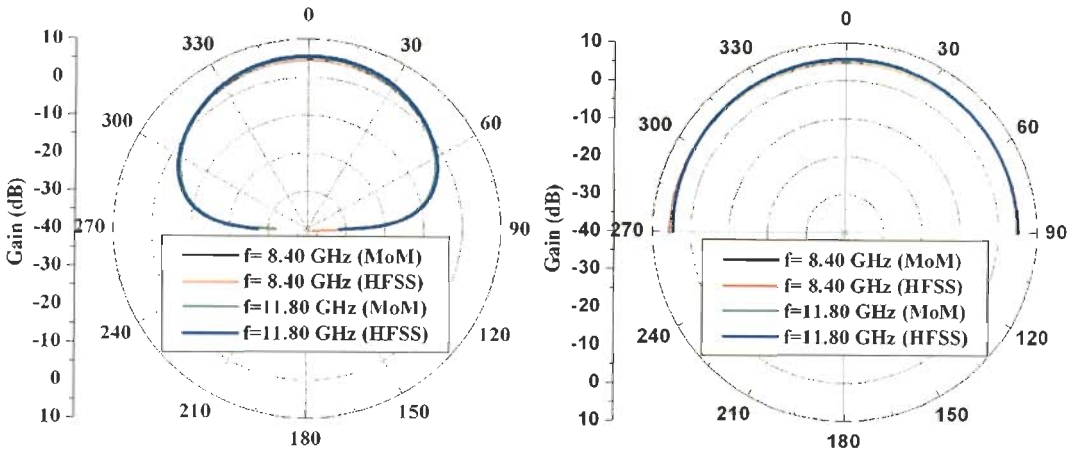

(a) $\varphi = 0°$ (b) $\varphi = 90°$

Figure 5.10: Gain pattern of waveguide-fed 2nd iteration modified Sierpinski gasket dipole aperture antenna with $s = 0.8$.

diaphragm. It can be seen that the first resonant frequency of the aperture antenna decreases by 6.25% as compared to 0.60% for the original self-affine gasket aperture antenna. The ratio between the successive resonant frequencies is 1.40 which is much larger than the theoretical value 1.25. This is due to the geometric modifications incorporated in the generation of gasket aperture.

The gain pattern of the 2nd iteration Sierpinski gasket dipole aperture antenna for both planes are shown in Fig. 5.10 for the two resonant frequencies. A good agreement with the HFSS results can be seen from the results. The gain pattern remains same for both the resonant frequencies. The maximum gain of the antenna is 5.00 dB and 5.31 dB for $\varphi = 0°$ and $\varphi = 90°$, respectively. The antenna pattern at $\varphi = 90°$ shows an omnidirectional pattern at both resonant frequencies.

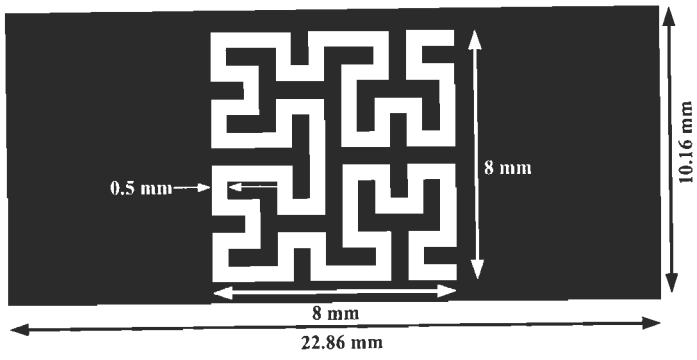

Figure 5.11: A 3rd iteration Hilbert curve aperture geometry.

5.3.2 Hilbert Curve Aperture Antenna

Hilbert curve fractal geometry has been widely used in the design of miniaturized antennas and electromagnetic bandgap structures. The geometry of a 2nd iteration Hilbert curve aperture antenna is shown in Fig. 5.11. The dimension of the square into which the curve can be fitted is chosen to be 8 mm×8 mm. The variation of return loss is shown in Fig. 5.12 for different iterations of Hilbert curve aperture antenna. From the plots, it is evident that the present MoM analysis agree well with the HFSS results, although there is a little difference in 1st resonant frequency for the third iteration. The various parameters of the Hilbert curve aperture antenna are tabulated in Table 5.5. It is evident that the first resonant frequency decreases as the order of iterations increase. The primary resonant frequency gets reduced by about 48.5% from 1st to 3rd iteration due to the increase in end-to-end length of the slot. The VSWR is minimum for 1st iteration and as the order of iteration increases, the impedance match degrades resulting in higher values of VSWR. The bandwidth of the antenna decreases significantly as the order of iteration is increased. The ratio between the successive resonant frequencies is 1.80 for second iteration and for the third

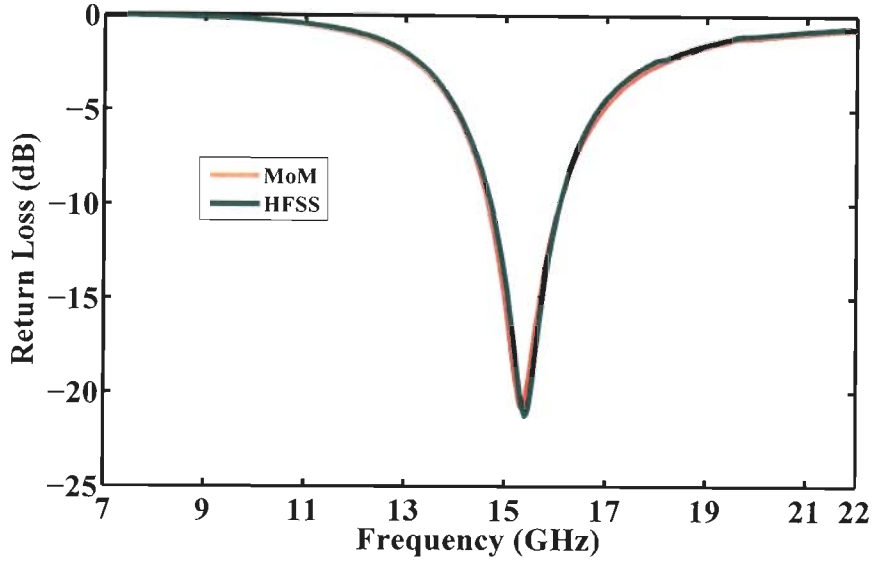

(a) 1st Iteration

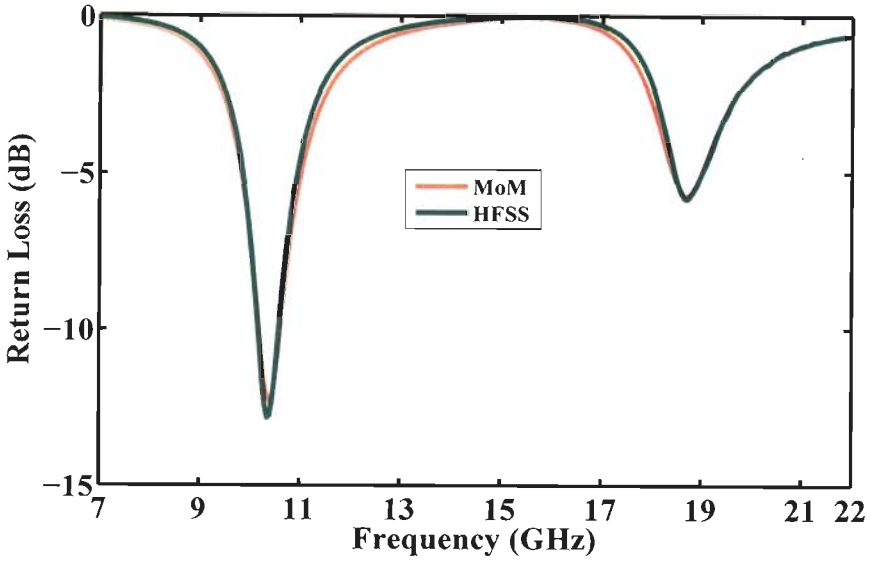

(b) 2nd Iteration

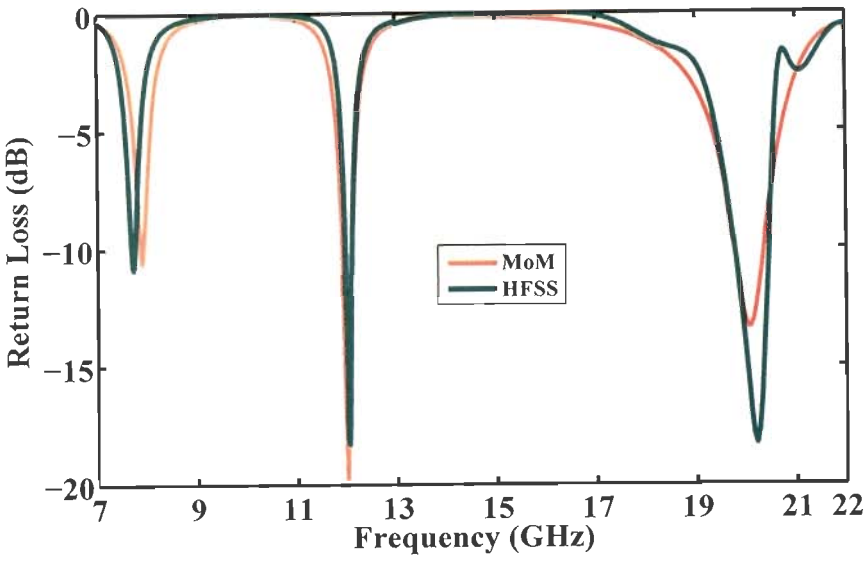

(c) 3rd Iteration

Figure 5.12: Return loss of waveguide-fed Hilbert curve aperture antenna for different iterations.

Table 5.5: Frequency response of waveguide-fed Hilbert curve aperture antenna.

Parameters	Iteration 1	Iteration 2		Iteration 3		
Resonant Frequency (GHz)						
MoM	15.34	10.40	18.70	7.90	12.00	20.05
HFSS	15.40	10.35	18.69	7.67	12.12	20.20
Difference (%)	0.39	0.48	0.05	2.91	1.00	0.75
VSWR	1.20	1.64	3.61	1.85	1.23	1.55
Bandwidth (%)	9.45	3.85	-	1.27	1.67	2.99

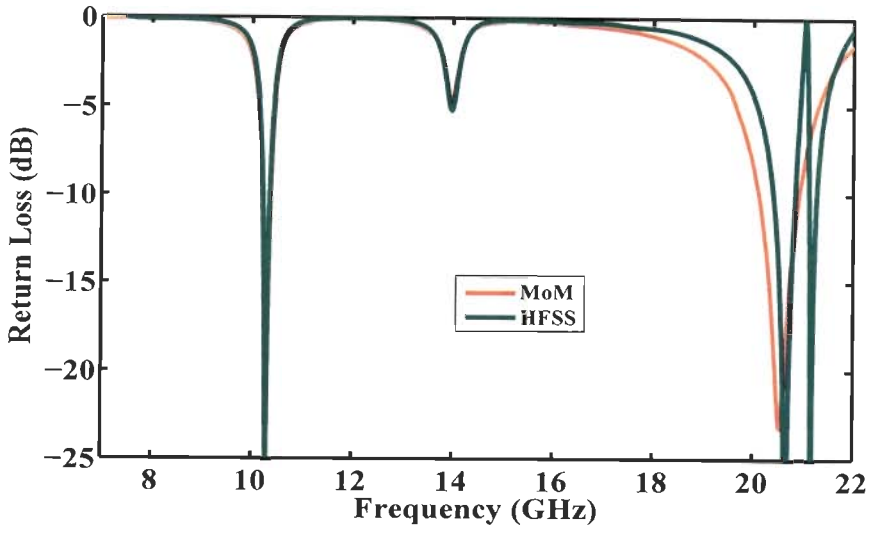

Figure 5.13: Return loss of waveguide-fed 3rd iteration rotated Hilbert curve aperture antenna.

iteration, the values are 1.52 and 1.71.

Similar to the Hilbert curve fractal diaphragm, the orientation of Hilbert curve aperture affects the characteristics of the antenna and also, the ratio between successive resonant frequencies can be changed as is evident from Fig. 5.13, where the variation of return loss of a 3rd iteration rotated Hilbert curve fractal aperture antenna is shown. The numerical results based on the MoM match very well in the low frequency regions and the result differs from the HFSS results beyond 18 GHz. A spurious resonance appears at 21.15 GHz in HFSS simulation and this is due to the convergence problem faced with HFSS simulation at these high frequencies. However, the resonant frequency at 20.56 GHz differs from HFSS result only by 0.53%. From the variation of return loss, it is seen that the resonant frequencies are at 10.3 GHz, 13.98 GHz and 20.56 GHz for a rotated third iteration Hilbert curve aperture antenna. The ratio between the successive resonant frequencies are 1.36 and 1.47, which differs from those for the origi-

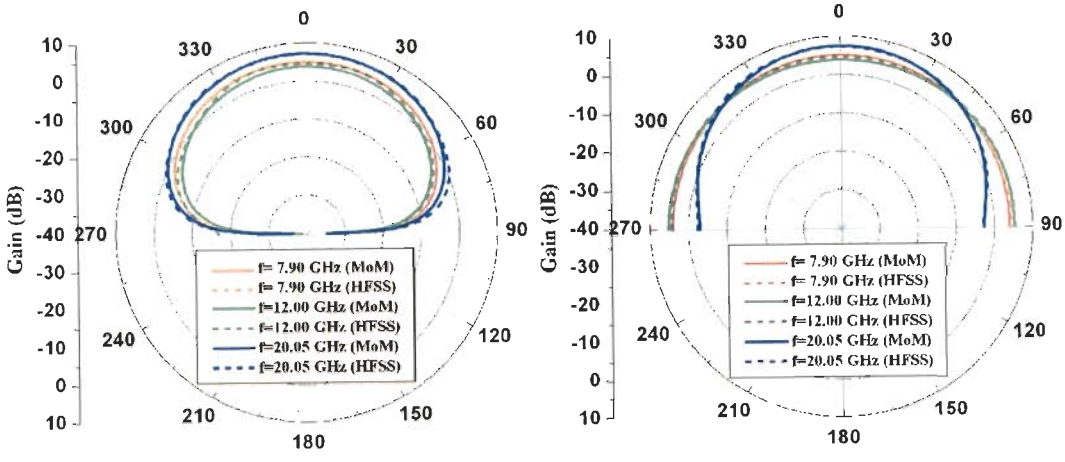

(a) $\varphi = 0°$ (b) $\varphi = 90°$

Figure 5.14: Gain pattern of waveguide-fed 3rd iteration Hilbert curve aperture antenna.

nal Hilbert aperture antenna. The impedance match at the second resonance is very poor and the impedance match at the 1st and 3rd resonant frequencies is significantly better than that for the original Hilbert curve aperture antenna.

The gain patterns of the original Hilbert aperture antenna in two principal planes are shown in Fig. 5.14 at three resonant frequencies. The nature of the gain patterns remains similar at all resonant frequencies and the maximum gain of the antenna is around 7.23 dB at the third resonance. Again, the pattern in $\varphi = 90°$ plane shows an omnidirectional pattern with a slight increase in the directivity at higher order resonant frequencies.

5.3.3 Plus Shape Fractal Aperture Antenna

Plus shape fractal geometries are used in the design of multiband frequency selective surface elements. Here, we have considered a self-affine plus shape fractal aperture. The initial plus shape has a length of 14 mm along x-axis

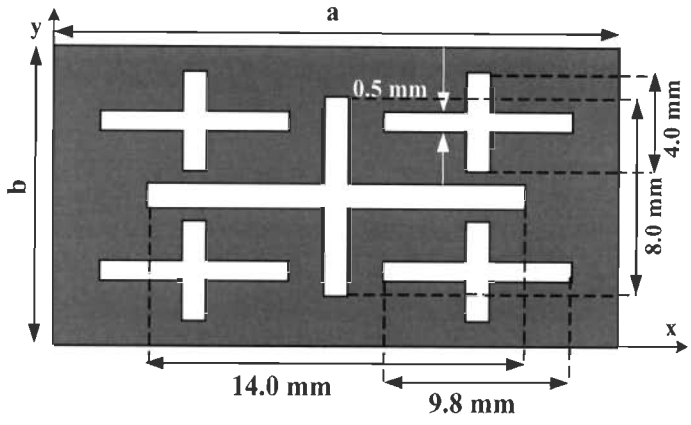

Figure 5.15: A self-affine plus shape fractal aperture antenna.

and 8 mm along y-axis and is placed at the center of waveguide cross-section. This initial geometry is scaled by a factor 0.7 in x-direction and by 0.5 in y-direction and four such copies are placed at (a/4,b/4), (3a/4,b/4), (3a/4,3b/4), and (a/4,3b/4), where $a \times b$ is the waveguide cross-section. The geometry of a 2^{nd} iteration plus shape fractal aperture is shown in Fig.5.15. The variation of return loss of the plus shape fractal aperture antenna is shown in Fig. 5.16 for two iterations. The antenna performance is tabulated in Table 5.6. It can be seen that the 1^{st} resonant frequency shifts downward by 6.25% in the second iteration. The ratio between the successive resonant frequencies is 1.63, which is larger than the theoretical value 1.43. In this case, the location of 1^{st} resonance is controlled by the length of initial plus shape along x-direction while, the 2^{nd} resonance, which is determined by the length of smaller plus, can be placed suitably by controlling the scale factor. Fig. 5.17 compares the return loss of the fractal of Fig. 5.15 with another second iteration plus fractal aperture with the length of initial plus as 18 mm and $s = 0.6$ along x-direction. In the later case, the two resonant frequencies are at 7.80 GHz and 14.74 GHz with a ratio of 1.88 as compared

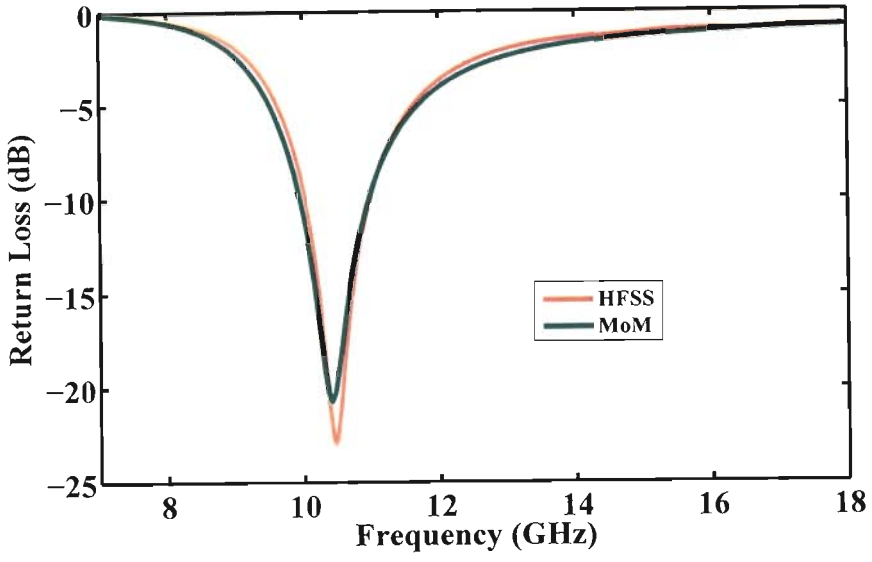

(a) 1st Iteration

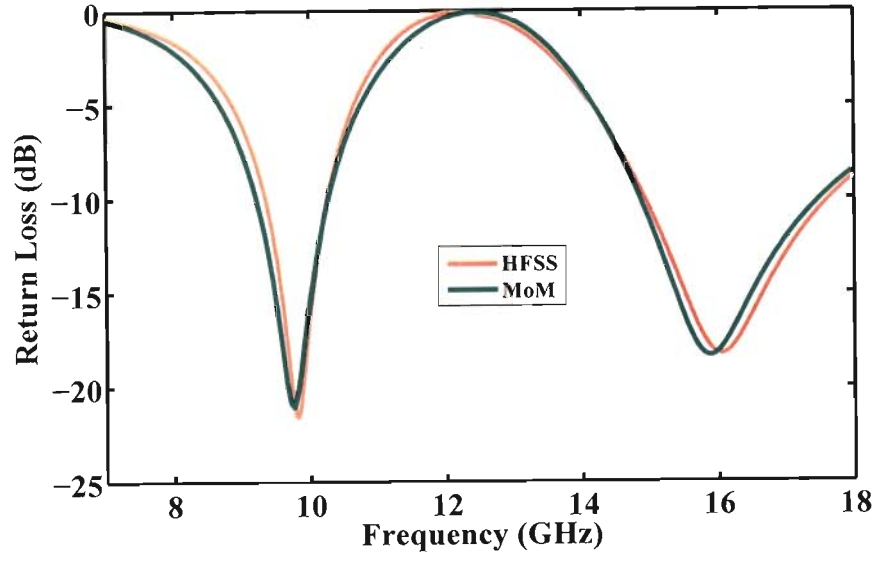

(b) 2nd Iteration

Figure 5.16: Return loss of waveguide-fed self-affine plus shape fractal aperture antenna for two iterations.

Table 5.6: Frequency response of waveguide-fed self-affine plus shape fractal aperture antenna.

Parameters	Iteration 1	Iteration 2	
Resonant Frequency (GHz)			
MoM	10.40	9.75	15.9
HFSS	10.46	9.81	16.05
Difference (%)	0.58	0.62	0.94
VSWR	1.20	1.19	1.28
Bandwidth (%)	9.62	10.81	16.67

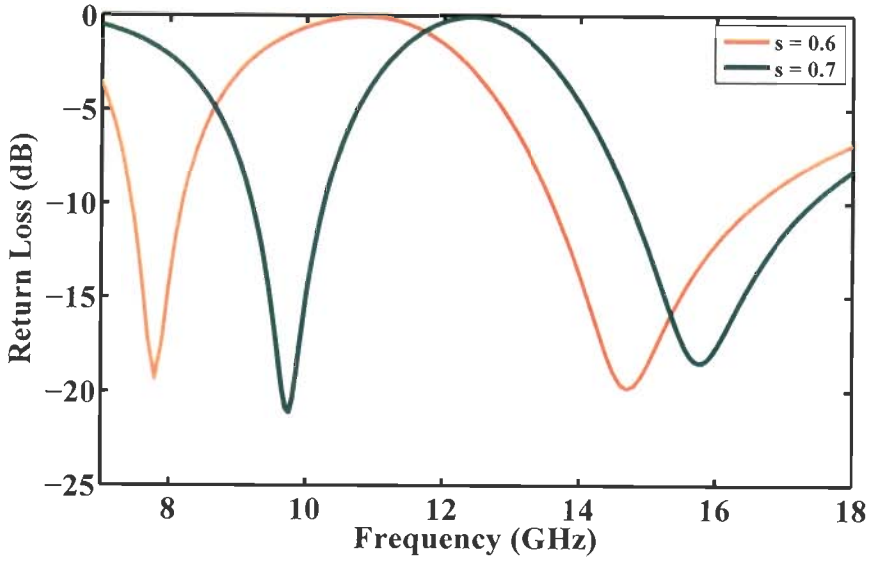

Figure 5.17: Return loss of a waveguide-fed 2nd iteration plus shape fractal aperture antenna with different scale factors.

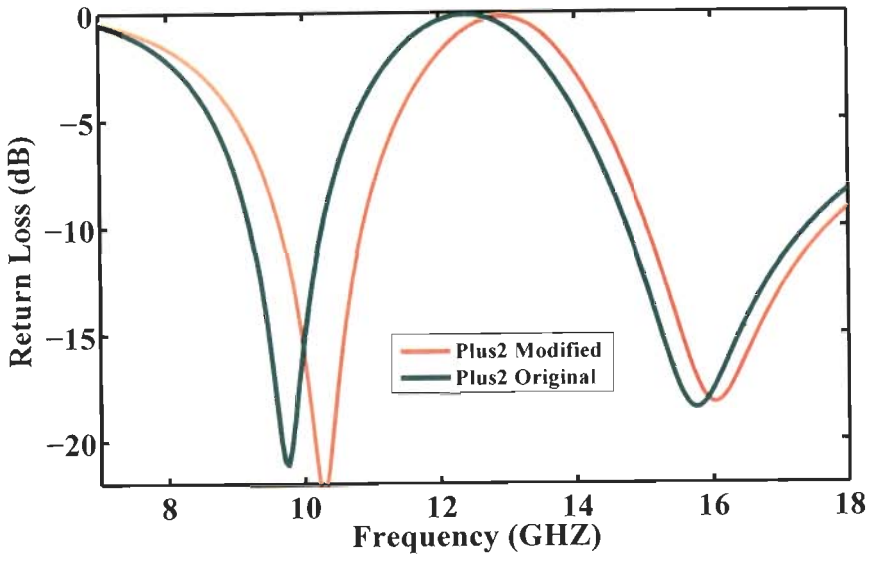

Figure 5.18: Return loss of a waveguide-fed 2nd iteration modified plus shape fractal aperture antenna.

to the desired value 1.63. Thus, the location of the resonant frequencies can be suitably chosen by properly selecting the dimension of the initial plus geometry and the scale factor. The effect of the size of vertical arm is also investigated and it was found that the reduction in the size of vertical arm of the initial plus geometry results in a slight increase in the resonant frequencies. This is shown in Fig. 5.18 for the case where the vertical arm length has been reduced to zero resulting in five rectangular apertures. Thus, an additional parameter is available to the designer for fine tuning the desired resonant frequencies.

The gain patterns of the 2nd iteration plus shape fractal aperture antenna with $s = 0.7$ at the two resonant frequencies are shown in Fig. 5.19 for the two principal planes. It is found that at the 2nd resonant frequency, the pattern becomes more directive and also, side lobes are generated. Again, an omnidirectional behavior was seen in $\varphi = 90°$ plane. The maximum gain for the aperture antenna is

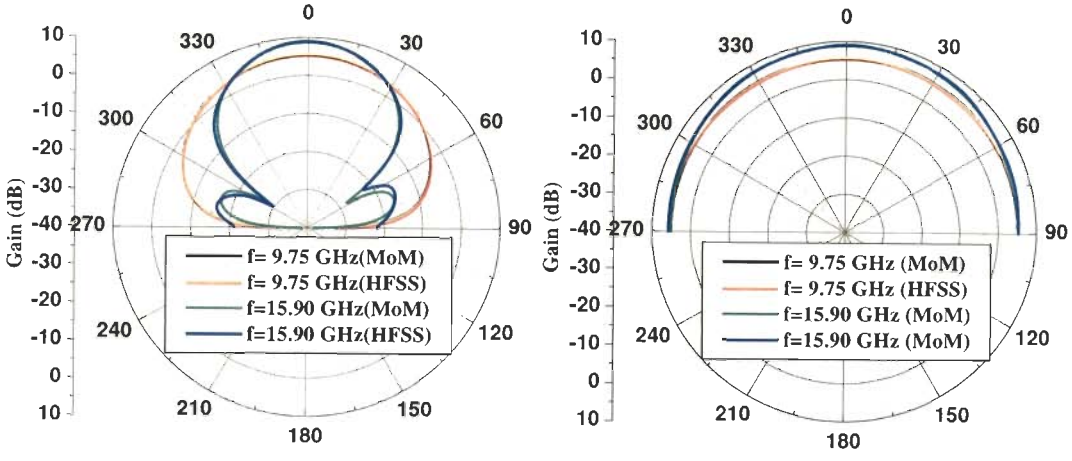

(a) $\varphi = 0°$ (b) $\varphi = 90°$

Figure 5.19: Gain pattern of waveguide-fed 2nd iteration plus shape aperture antenna with $s = 0.7$

8.90 dB. Also shown in Fig. 5.20 is the gain pattern of the modified plus shape fractal aperture antenna. It can be seen from the plots that there is hardly any change in the gain patterns of the aperture antenna. The maximum gain of the modified aperture antenna is 9.00 dB. In all the plots, a good agreement between the MoM results and HFSS can be observed.

5.3.4 Devil's Staircase Fractal Aperture Antenna

The generation steps of Devil's staircase fractal geometry have already been described in chapter 3. A 3rd iteration modified Devil's staircase fractal aperture is shown in Fig. 5.21. The variation of return loss for different iterations of modified Devil's staircase fractal aperture antenna is shown in Fig. 5.22. The performance of the fractal aperture antenna is summarized in Table 5.7. In the first iteration, the antenna resonates at 12.71 GHz which corresponds to a rectangular aperture of length 11.43 mm. The corresponding aperture length

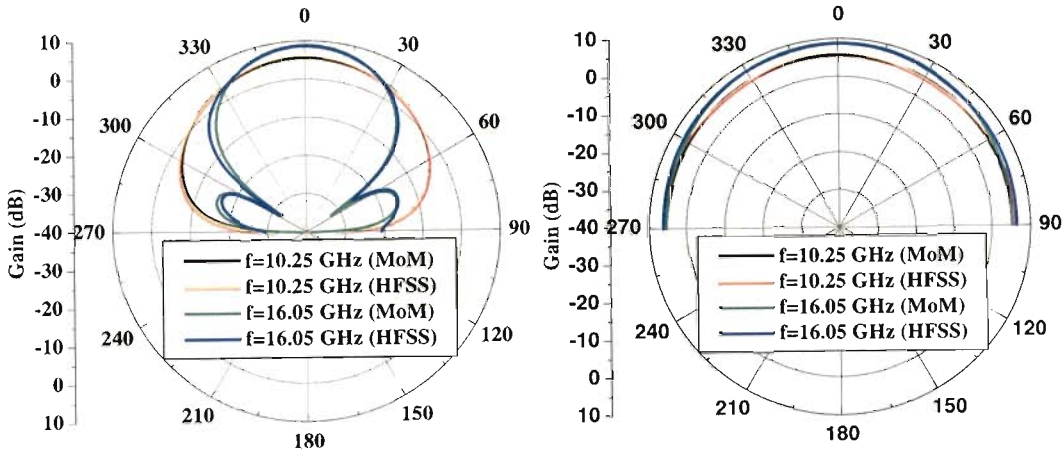

(a) $\varphi = 0°$ (b) $\varphi = 90°$

Figure 5.20: Gain pattern of waveguide-fed 2nd iteration modified plus shape aperture antenna with $s = 0.6$.

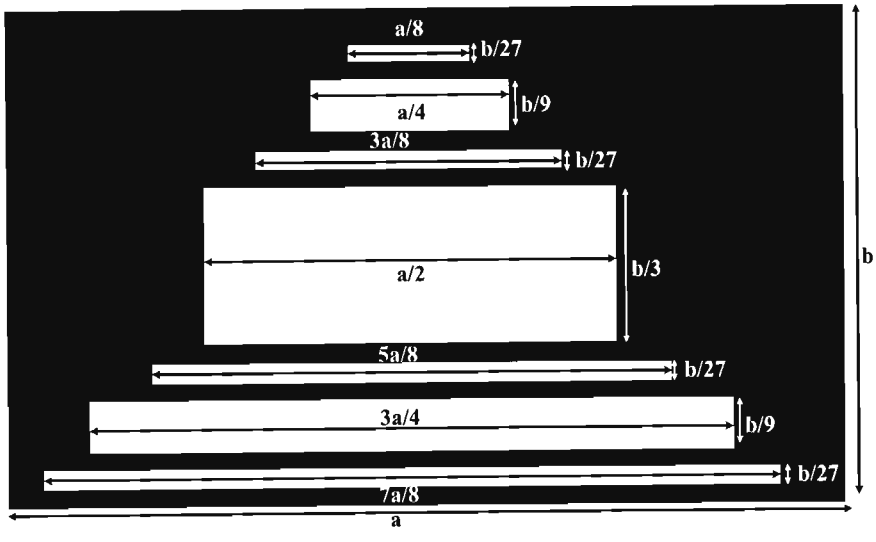

Figure 5.21: A 3rd iteration modified Devil's staircase fractal aperture (a=22.86 mm, b=10.16 mm).

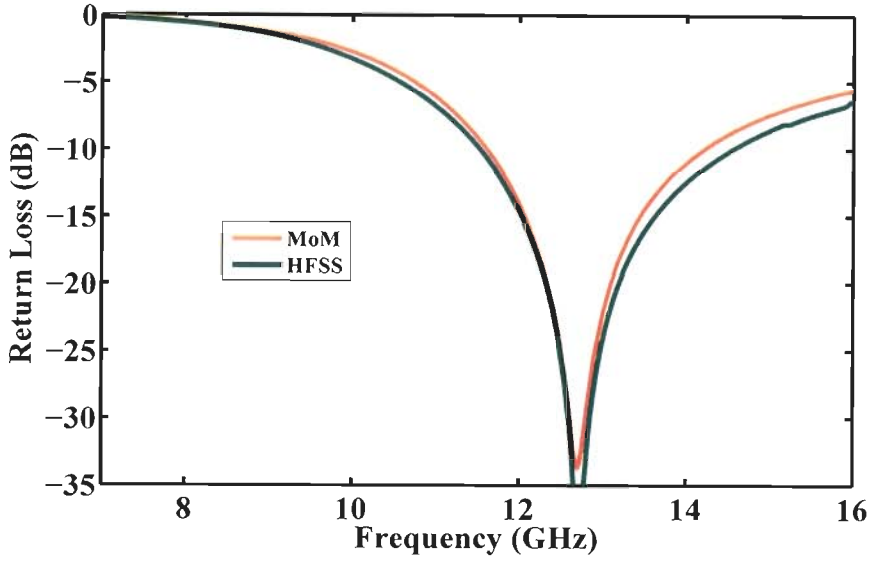

(a) 1st Iteration

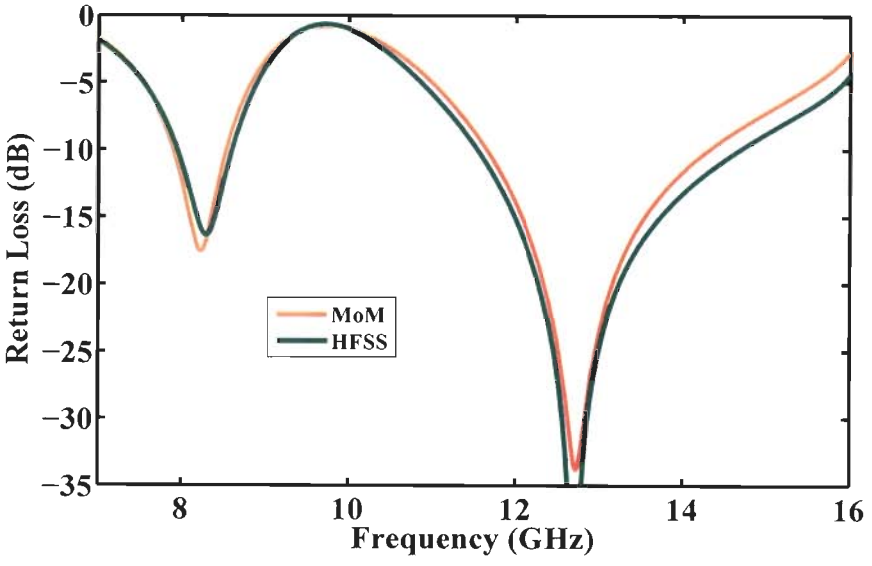

(b) 2nd Iteration

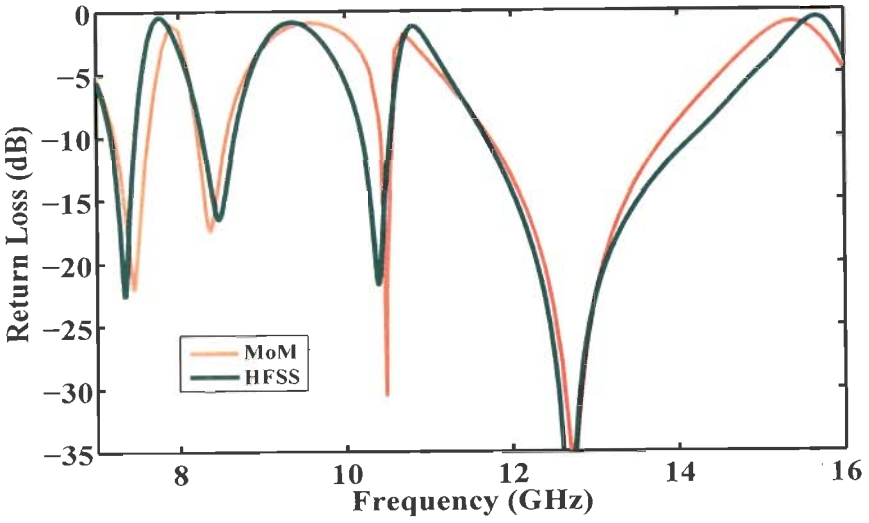

(c) 3rd Iteration

Figure 5.22: Return loss of waveguide-fed modified Devil's staircase fractal aperture antenna for different iterations.

Table 5.7: Frequency response of waveguide-fed modified Devil's staircase fractal aperture antenna.

Parameters	Iteration 1	Iteration 2		Iteration 3			
Resonant Frequency (GHz)							
MoM	12.71	8.23	12.73	7.46	8.37	10.49	12.73
HFSS	12.72	8.30	12.71	7.34	8.47	10.40	12.68
Difference (%)	0.08	0.85	0.16	1.61	1.19	0.86	0.39
VSWR	1.04	1.31	1.04	1.18	1.32	1.06	1.01
Bandwidth (%)	20.47	7.90	20.42	5.36	4.78	1.23	16.54

to resonant wavelength ratio is 0.48. In the second iteration, there are three apertures of different lengths and therefore, the antenna may have three different resonant frequencies. The two resonant frequencies namely 8.23 GHz and 12.73 GHz lie within the frequency band considered here, while the third resonant frequency arising due to the smallest aperture lies outside this band. Here, the first resonance is due to the aperture of length 17.145 mm and the second resonance is due to the aperture of length 11.43 mm of the first iteration. The ratio between the successive resonant frequencies is 1.53. The impedance match is better at the second resonance frequency. In the third iteration, we obtain four resonances in the frequency range 7 GHz–16 GHz. The resonance at 7.46 GHz and 10.49 GHz are due to the apertures of length 20 mm and 14.29 mm of 3^{rd} iteration, while the other two resonant frequencies corresponds to the apertures of previous iterations. There is a little difference with the results obtained from the simulation on HFSS and present MoM method. In all the cases, it is evident that the corresponding wavelength is twice the length of the aperture. The ratios between the successive resonant frequencies are 1.12, 1.25, and 1.21, which are close to the corresponding aperture length ratios 1.17, 1.20, and 1.25.

The gain patterns of the antenna at four resonant frequencies are shown in Fig. 5.23 in $\varphi = 0°$ and $\varphi = 90°$ planes. As seen from the plots, the pattern remains same at all the resonant frequencies and the maximum gain of the antenna is around 5.46 dB. The gain patterns in $\varphi = 90°$ plane are omnidirectional at all the resonant frequencies.

5.3.5 Koch Fractal Aperture Antenna

The advantage of using the Koch curve fractal is that the overall length of the curve increases with the increase of order of iteration, although the end-to-end

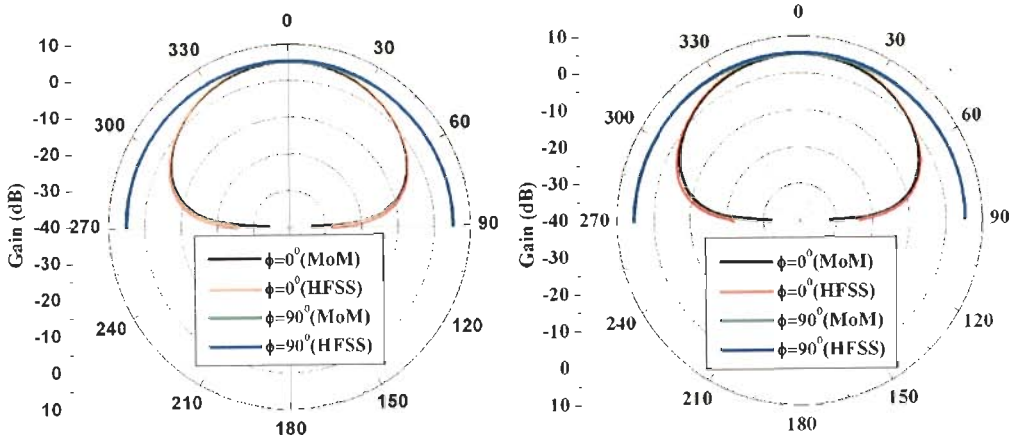

(a) 1st resonance

(b) 2nd resonance

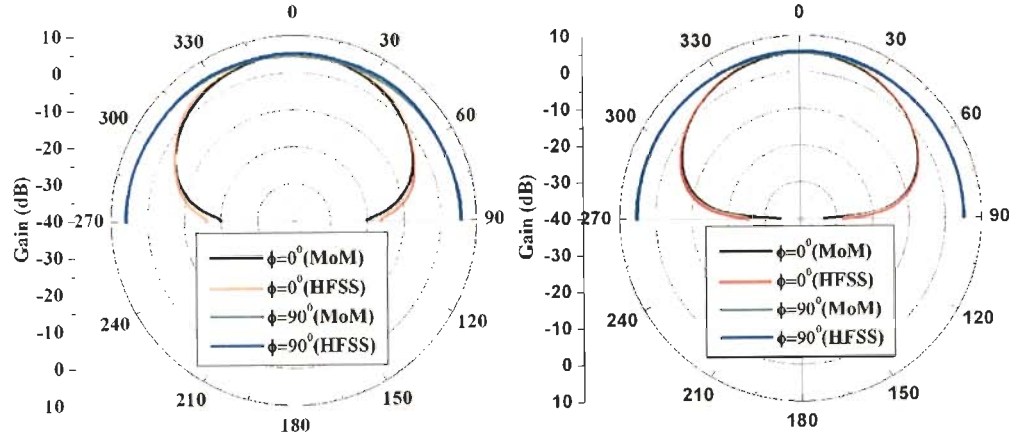

(c) 3rd resonance

(d) 4th resonance

Figure 5.23: Gain pattern of a waveguide-fed 3rd iteration modified Devil's staircase fractal aperture antenna at different resonant frequencies.

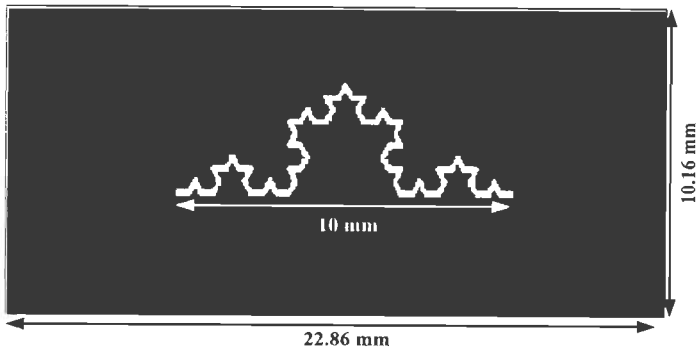

Figure 5.24: A 3rd iteration standard Koch curve aperture antenna.

Table 5.8: Frequency response of waveguide-fed Koch fractal slot antenna.

Parameters	Iteration 0	Iteration 1	Iteration 2	Iteration 3
Resonant Frequency (GHz)				
MoM	14.55	12.07	10.14	9.30
HFSS	14.51	11.94	10.05	9.20
Difference (%)	0.27	1.08	0.89	1.08
VSWR	1.29	1.04	1.33	1.44
Bandwidth (%)	5.15	4.14	2.47	2.15

length of the curve remains same. In this case, we have considered a Koch curve fractal aperture of length 10 mm along the larger dimension of the waveguide and width equal to 0.1 mm. Fig. 5.24 shows a 3rd iteration Koch curve aperture antenna and the variation of return loss with frequency is shown in Fig. 5.25 for different iterations. Table 5.8 summarizes the performance parameters of the Koch curve fractal aperture antenna. It can be seen that the present MoM analysis agrees well with the HFSS results with a difference of around 1%. For the zeroth iteration, the rectangular aperture of length 10 mm resonates corresponding to a wavelength twice the length of the aperture. The resonant

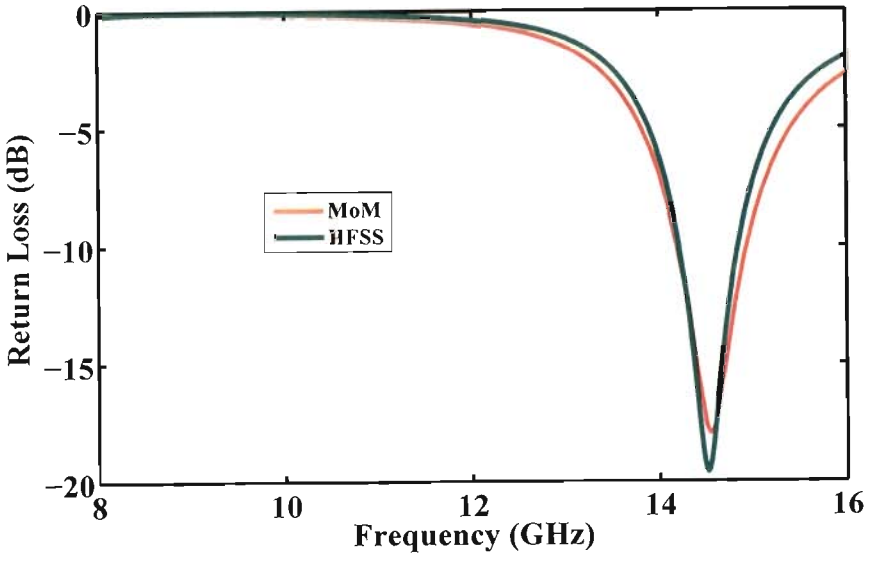

(a) 0^{th} Iteration

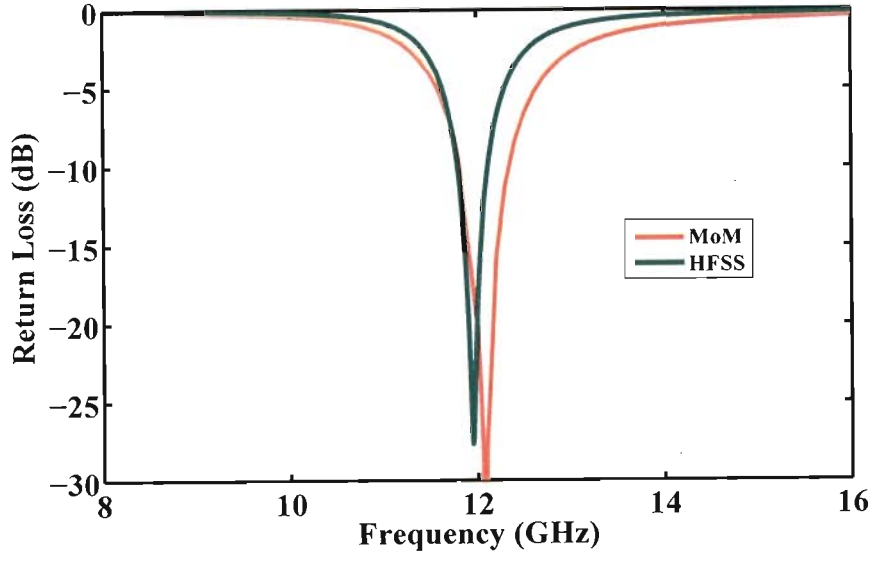

(b) 1^{st} Iteration

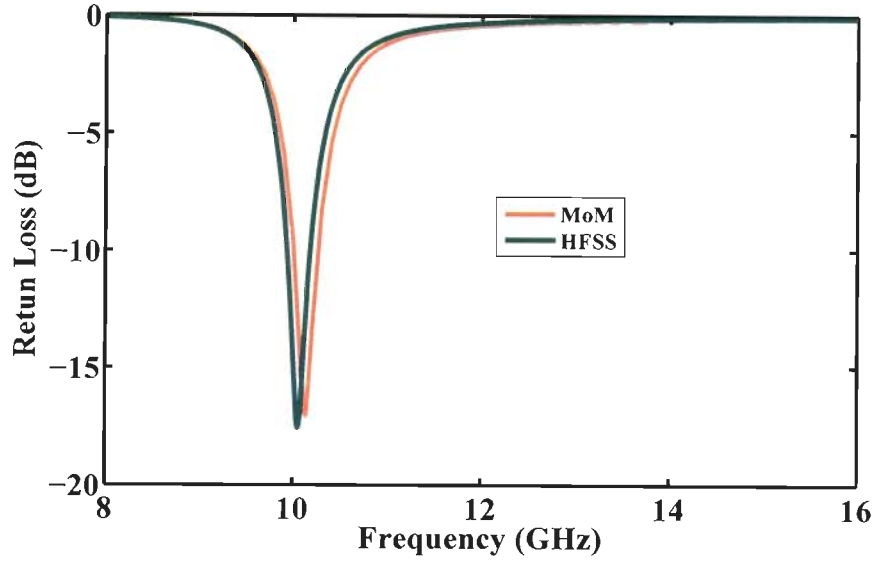

(c) 2nd Iteration

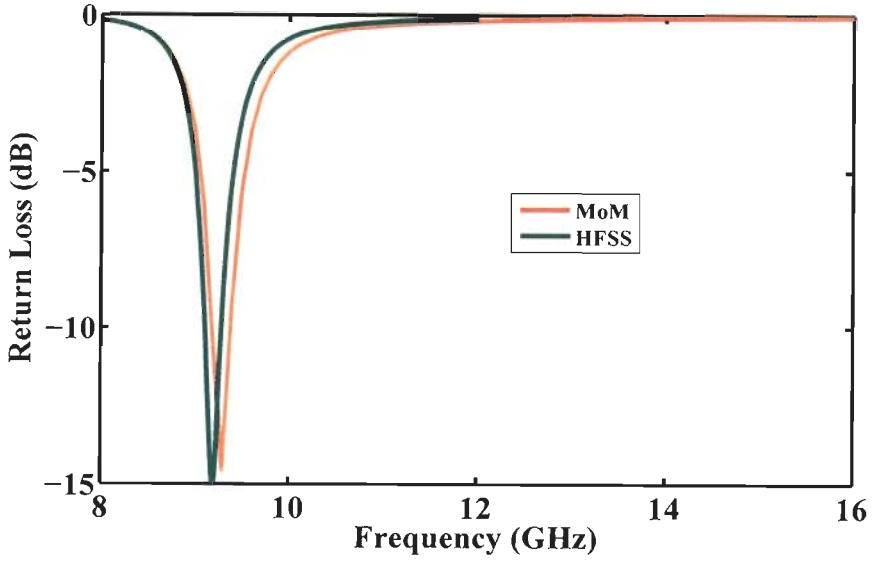

(d) 3rd Iteration

Figure 5.25: Return loss of waveguide-fed Koch curve aperture antenna for different iterations.

frequency of the antenna decreases by 36.08% from zeroth to third iteration and also, the bandwidth of the aperture antenna decreases significantly as the order of iteration increases. The location of resonant frequency can also be controlled by changing the indentation angle of the Koch fractal aperture.

The gain patterns of the antenna at the primary resonant frequencies for different iterations of Koch aperture are shown in Fig. 5.26. The gain of the antenna is around 5 dB for these iterations. However, the maximum gain of the antenna decreases slightly as the order of iteration increases. The numerical results agree very well with the results obtained from simulations with HFSS. The patterns are omnidirectional for all the iterations for $\varphi = 90°$ plane. For $\varphi = 0°$ plane, the pattern becomes more directive as the order of iteration increases.

5.3.6 Minkowski Fractal Aperture Antenna

The generation steps of the Minkowski fractal is described in chapter 3. This fractal geometry is also very popular in reducing the resonant frequency of the antenna. The geometry of a 2^{nd} iteration Minkowski fractal aperture is shown in Fig. 5.27. The variation of return loss of the aperture antenna is shown in Fig. 5.28 for different iterations. The performance parameters of the antenna is shown in Table 5.9. The HFSS results agrees well with the present MoM code. As can be seen, the resonant frequency of the square aperture is well beyond the frequency band considered here. The resonant frequency of the antenna shifts downward as the order of iteration increases with a significant decrease in the bandwidth of the antenna. Fig. 5.29 shows the gain pattern of the antenna for 1^{st} and 2^{nd} iterations. A very good agreement with the HFSS can be seen. Similar to the other waveguide-fed aperture antennas, the antenna shows an omnidirectional pattern for $\varphi = 90°$. The gain of the antenna is around 5 dB for

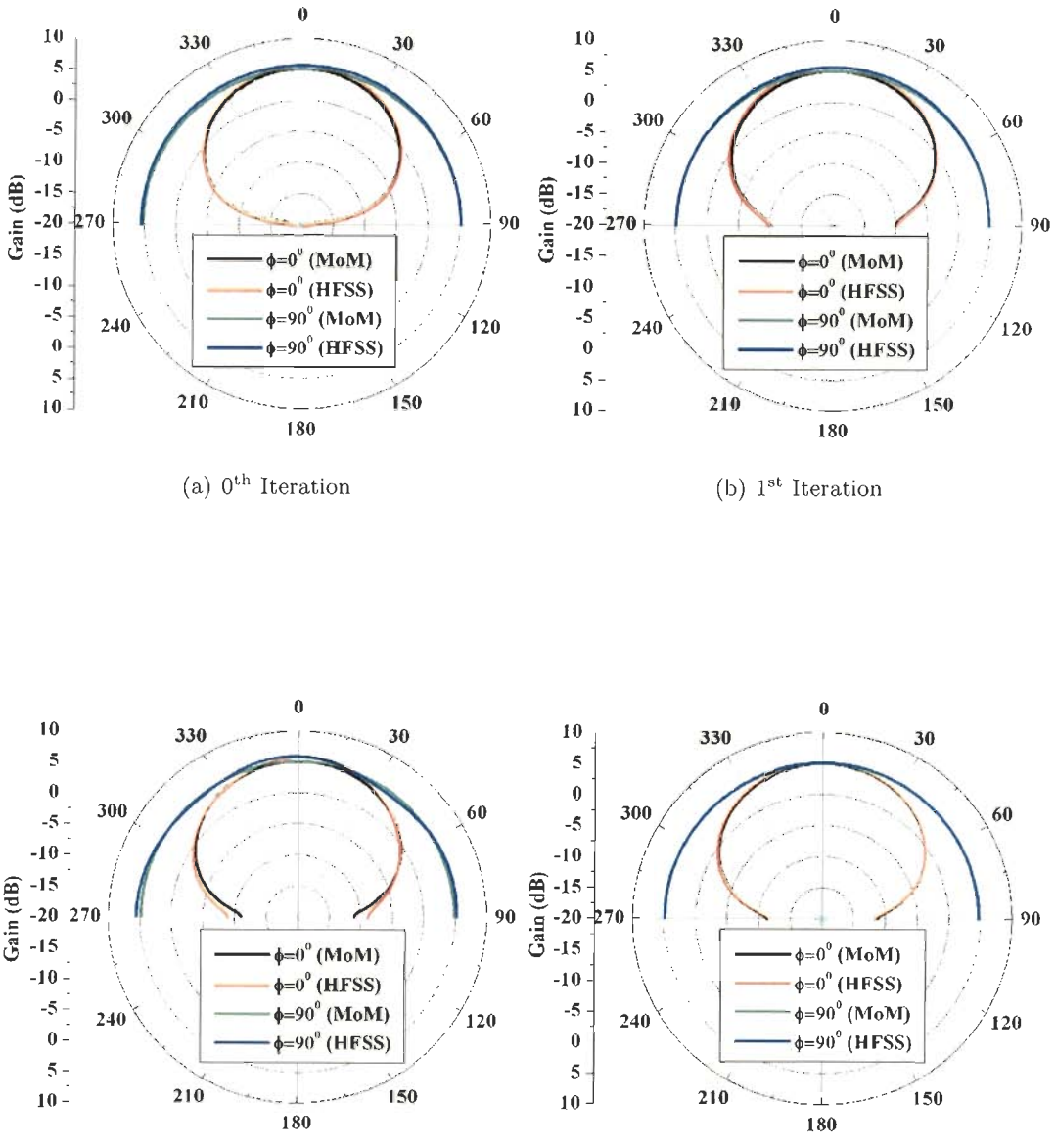

(a) 0^{th} Iteration

(b) 1^{st} Iteration

(c) 2^{nd} Iteration

(d) 3^{rd} Iteration

Figure 5.26: Gain pattern of a waveguide-fed Koch fractal aperture antenna for different iterations.

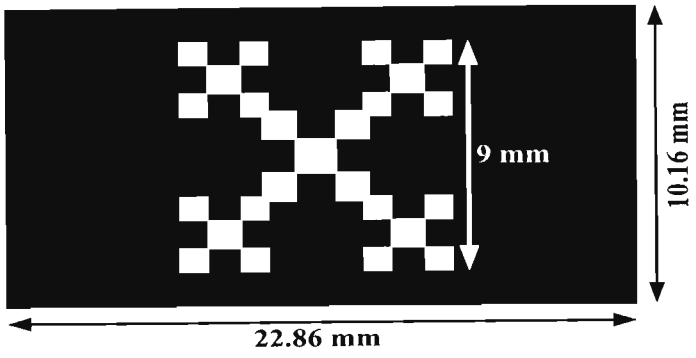

Figure 5.27: A 2nd iteration Minkowski aperture antenna.

Table 5.9: Frequency response of waveguide-fed Minkowski fractal slot antenna

Parameters	Iteration 1	Iteration 2
Resonant Frequency (GHz)		
MoM	11.70	9.60
HFSS	11.66	9.72
Difference (%)	0.34	1.25
VSWR	1.17	1.44
Bandwidth (%)	17.09	8.33

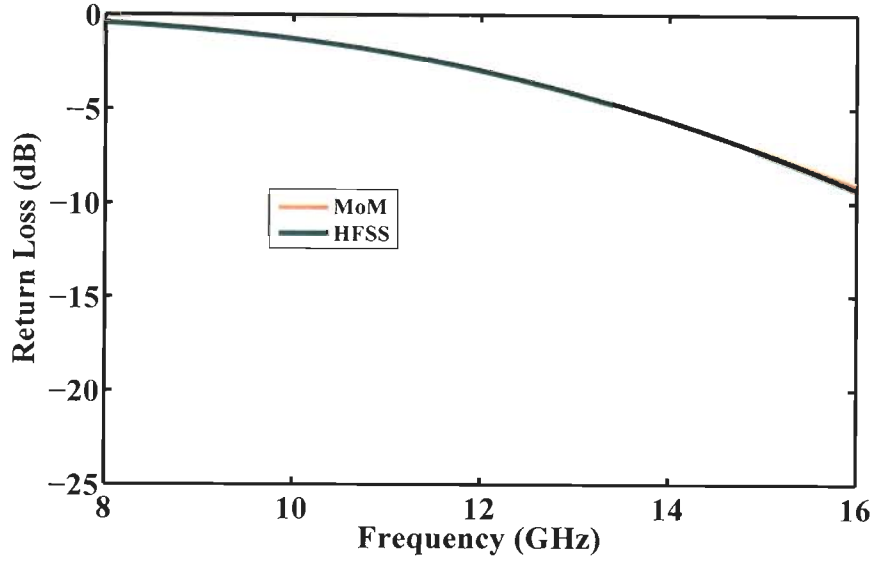

(a) 0^{th} Iteration

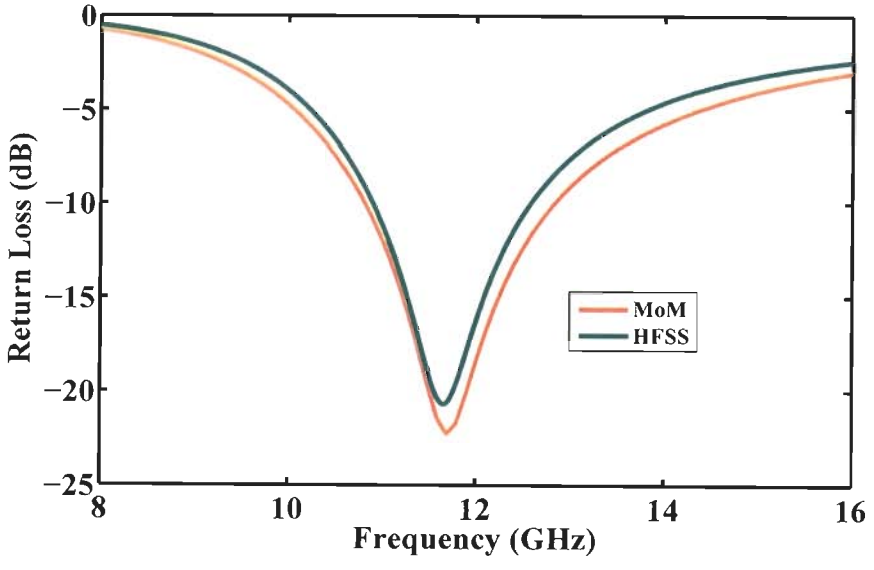

(b) 1^{st} Iteration

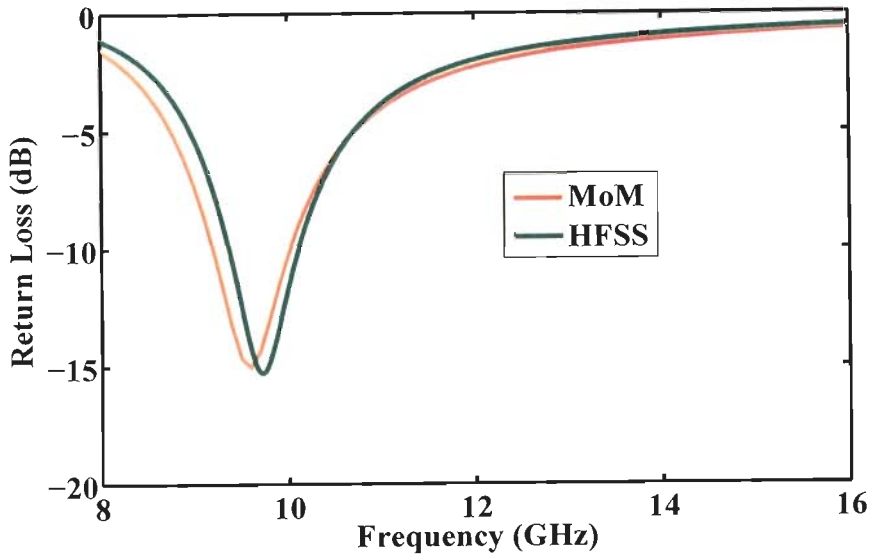

(c) 2nd Iteration

Figure 5.28: Return Loss of waveguide-fed Minkowski aperture antenna for different iterations.

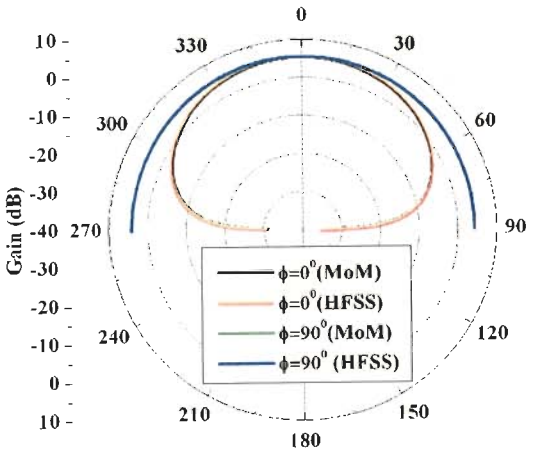

(a) 1st Iteration

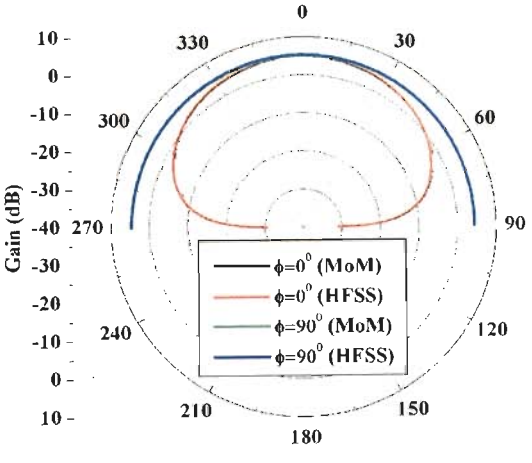

(b) 2nd Iteration

Figure 5.29: Gain pattern of waveguide-fed Minkowski aperture antenna for different iterations.

all the iterations.

5.4 Summary

The properties of fractal aperture antennas fed by a rectangular waveguide have been investigated. It has been found that using the fractal geometry, the input matching of the waveguide fed aperture antennas can be greatly improved. Also, it has been demonstrated that by changing the scale factor of the fractal apertures, the location of resonant frequencies can be controlled. The ratios of successive resonant frequencies are found to be larger than the ratios for ideal fractals, which is usual for fractal antennas with lower order of iterations. The gain patterns of the aperture antenna remain nearly the same at different resonant frequencies and for all the fractal apertures, the patterns are symmetric. Most of these aperture antennas offer a gain around 5 dB. The space-filling property of the Hilbert antenna can be efficient in reducing the antenna aperture dimension, although the input VSWR value increases with higher iterations. The antennas using Koch curve and Minkowski curve are capable of reducing the resonant frequency of the aperture antennas.

Chapter 6

INVESTIGATIONS ON CAVITY-BACKED FRACTAL APERTURE ANTENNAS

Cavity-backed aperture antennas are very popular in aerospace applications due to their conformal nature. As discussed in chapter 1, several cavity-backed aperture antennas and arrays have been investigated in the past. However, the behavior of fractal apertures backed by a cavity has not been explored so far. In this chapter, we investigate the characteristics of cavity-backed fractal aperture antennas. As pointed out in chapter 1, hybrid techniques have become more popular in the numerical analysis of such problems due to their ability to handle arbitrary shape of the cavity and complex material filling. The hybrid finite element-boundary integral (FE-BI) method is very efficient for the analysis of cavity-backed aperture antennas [154] and has been used here. In section 1, the problem of probe-fed cavity-backed aperture antenna has been analyzed using FE-BI method. The field inside the cavity is computed using the finite element

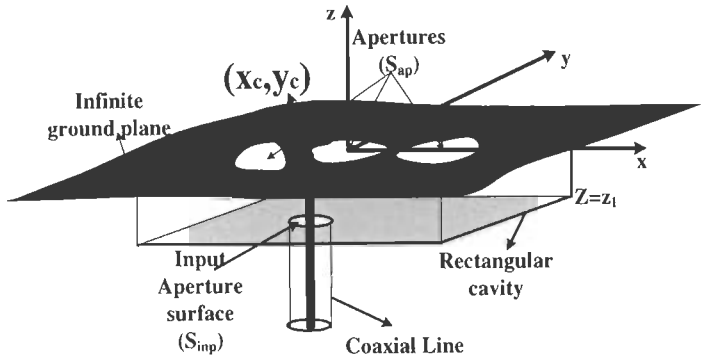

Figure 6.1: Geometry of a coaxial probe-fed cavity-backed aperture antenna.

method and MoM is used to calculate the field outside the cavity region. The method produces a partly sparse and partly dense matrix which is solved using direct solver to obtain the field on the aperture surface. Once the aperture field is obtained, the radiation pattern and the input characteristics of the antenna can readily be computed. In section 2, numerical results for several fractal aperture antennas are presented which give an insight into the behavior of fractal apertures.

6.1 Formulation of the Problem Using FE-BI Method

The geometry of the problem is shown in Fig. 6.1 where multiple apertures are placed on the cavity top surface and are assumed to located in $z = 0$ plane. The cavity, as well as the apertures, can have any shape and dimension. The equivalence principle is first applied to decouple the original problem into two equivalent problems, one for the cavity volume including the feed structure and other for the region above the infinite ground plane as was discussed in the

equivalent model in chapter 2 (Fig. 2.11).

For a linear isotropic and source free region, the electric field satisfies the vector wave equation given by

$$\nabla \times \left(\frac{1}{\mu_r} \nabla \times \overline{E} \right) - k_0^2 \varepsilon_r \overline{E} = 0 \tag{6.1}$$

where μ_r and ε_r denote the permeability and permittivity of the medium inside the cavity.

Multiplying (6.1) scalarly by a vector testing function $\overline{T}$ and integrating over the volume of the cavity, we get

$$\iiint_V \overline{T} \cdot \nabla \times \left(\frac{1}{\mu_r} \nabla \times \overline{E} \right) \, dv - k_0^2 \varepsilon_r \iiint_V \overline{T} \cdot \overline{E} \, dv = 0 \tag{6.2}$$

where V denotes the volume of the cavity.

Now,

$$\iiint_V \overline{T} \cdot \nabla \times \left(\frac{1}{\mu_r} \nabla \times \overline{E} \right) \, dv = \iiint_V \frac{1}{\mu_r} (\nabla \times \overline{T}) \cdot (\nabla \times \overline{E}) \, dv - j\omega\mu \oiint_S (\overline{T} \times \hat{n}) \cdot \overline{H} \, ds$$

Hence, (6.2) can be rewritten as

$$\iiint_V \frac{1}{\mu_r} (\nabla \times \overline{T}) \cdot (\nabla \times \overline{E}) \, dv - k_0^2 \varepsilon_r \iiint_V \overline{T} \cdot \overline{E} \, dv = j\omega\mu_0 \oiint_S (T \times \hat{n}) \cdot \overline{H} \, ds \tag{6.3}$$

where $\hat{n}$ is the unit outward normal to the cavity surface S.

The tangential component of the electric field is zero on the perfectly conducting walls of the cavity, except on the aperture surfaces. Thus, the surface integral on the right hand side of (6.3) is non zero only over the aperture surfaces (S_{ap}) on the infinite ground plane and on the input aperture surface S_{inp}.

Therefore, (6.3) can be rewritten as

$$\iiint_V \frac{1}{\mu_r}(\nabla \times \overline{T}) \cdot (\nabla \times \overline{E})\, dv - k_0^2 \varepsilon_r \iiint_V \overline{T} \cdot \overline{E}\, dv \qquad (6.4)$$
$$-j\omega\mu_0 \iint_{S_{ap}} (T \times \hat{n}) \cdot \overline{H}_{ap}\, ds = j\omega\mu_0 \iint_{S_{inp}} (T \times \hat{n}) \cdot \overline{H}_{inp}\, ds$$

where, $\overline{H}_{ap}$ denotes the magnetic field on the aperture surface and $\overline{H}_{inp}$ is the magnetic field on the input aperture surface.

Hence, the problem can be divided into three parts. The first part involves the computation of volume integrals inside the cavity volume. The second and third parts involve the evaluation of surface integrals over the apertures on the top surface of the cavity and the input aperture surface, respectively. In the following subsections, computation of these integrals is presented.

6.1.1 FEM Formulation in the Interior of the Cavity

In order to solve (6.4) for the unknown electric field inside the cavity and on the aperture surfaces, the entire cavity is divided into N_e number of small tetrahedral elements and within each volume element, the electric field is expressed as the linear sum of edge basis functions as

$$\overline{E}^e = \sum_{i=1}^{6} V_i^e \overline{E}_i^e \qquad (6.5)$$

where $\overline{E}_i^e$ are the basis functions associated with each edge of the tetrahedral element and V_i^e denotes the unknown coefficient associated with i$^{\text{th}}$ basis function. Referring to Fig. 6.2, let us assume that i_1 and i_2 are the vertices of the i$^{\text{th}}$ edge and the six edges of the tetrahedron are numbered according to the Table 6.1. The vector basis functions are defined as

$$\overline{E}_{7-i}^e(\bar{r}) = \begin{cases} \bar{f}_{7-i} + \bar{g}_{7-i} \times \bar{r}, & \bar{r} \text{ in } V_e \\ 0, & \text{Outside} \end{cases} \qquad (6.6)$$

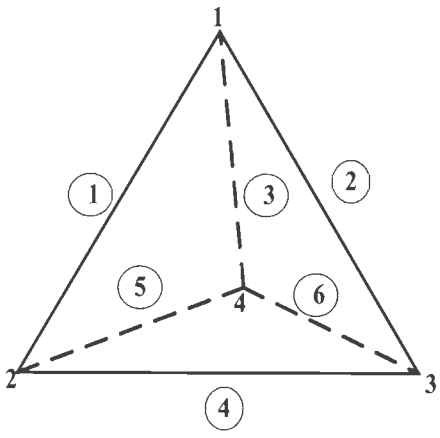

Figure 6.2: A tetrahedral volume element and associated edges.

Table 6.1: Tetrahedron edge definition.

Edge No.	i_1	i_2
1	1	2
2	1	3
3	1	4
4	2	3
5	4	2
6	3	4

where the vectors $\bar{f}$ and $\bar{g}$ are defined as

$$\bar{f}_{7-i} = \frac{l_{7-i}}{6V_e}\, \bar{r}_{i1} \times \bar{r}_{i2} \tag{6.7}$$

$$\bar{g}_{7-i} = \frac{l_i l_{7-i}}{6V_e}\, \bar{e}_i \tag{6.8}$$

$$\bar{e}_i = \frac{\bar{r}_{i2} - \bar{r}_{i1}}{l_i} \tag{6.9}$$

where $\bar{r}_{i1}$, $\bar{r}_{i2}$ are the position vectors of the vertices i_1 and i_2, l_i is the length of i^{th} edge, V_e is the volume of the tetrahedron element and $i = 1, 2, 3, ..., 6$.

From the definition of basis functions it is evident that the basis functions have the following properties

$$\nabla \cdot \overline{E}_i^e = 0 \tag{6.10}$$

$$\nabla \times \overline{E}_i^e = 2\bar{g}_i \tag{6.11}$$

$$\overline{E}_i^e(\bar{r}^j) \cdot \bar{e}_j = \delta_{ij} \tag{6.12}$$

where

$$\delta_{ij} = \begin{cases} 1, & i = j \\ 0, & i \neq j \end{cases}$$

and $\bar{r}^j$ has its tip on the edges of the tetrahedron. Hence, V_i^e is simply the amplitude of field at the i^{th} edge of the tetrahedral element.

Substituting (6.5) in (6.4), the volume integral over a tetrahedral element can be expressed as

$$I_{ev} = E_j^e \left[\frac{1}{\mu_r} \sum_{j=1}^{6} \iiint_{V_e} (\nabla \times \overline{T}_i) \cdot (\nabla \times \overline{E}_j)\, dv - k_0^2 \varepsilon_r \iiint \overline{T}_i \cdot \overline{E}_j^e\, dv \right] \tag{6.13}$$

Using (6.10), it can be written as

$$\iiint_{V_e} \frac{1}{\mu_r} (\nabla \times \overline{T}_i) \cdot (\nabla \times \overline{E}_j)\, dv = V_e \frac{4}{\mu_r} \bar{g}_i \cdot \bar{g}_j \tag{6.14}$$

Again,

$$\begin{aligned}\iiint_{V_e} \overline{E}_i^e \cdot \overline{E}_j^e \, dv &= \iiint_{V_e} (\bar{f}_i + \bar{g}_i \times \bar{r}) \cdot (\bar{f}_j + \bar{g}_j \times \bar{r}) \, dv \\ &= \iiint \bar{f}_i \cdot \bar{f}_j \, dv + \iiint_{V_e} \bar{r} \cdot \overline{D} \, dv \\ &\quad + \iiint_{V_e} (\bar{g}_i \times \bar{r}) \cdot (\bar{g}_j \times \bar{r}) \, dv \\ &= I_1 + I_2 + I_3 \end{aligned} \tag{6.15}$$

where

$$\overline{D} = (\bar{f}_i \times \bar{g}_j) + (\bar{f}_j \times \bar{g}_i) \tag{6.16}$$

$$I_1 = \iiint_{V_e} \overline{f}_i \cdot \overline{f}_j \, dv \tag{6.17}$$

$$I_2 = \iiint_{V_e} \bar{r} \cdot \overline{D} \, dv \tag{6.18}$$

$$I_3 = \iiint_{V_e} (\bar{g}_i \times \bar{r}) \cdot (\bar{g}_j \times \bar{r}) \, dv \tag{6.19}$$

Since $\bar{f}$ is a constant vector, I_1 can be expressed as

$$I_1 = \bar{f}_i \cdot \bar{f}_j V_e \tag{6.20}$$

In order to evaluate integral I_2, the coordinates are expressed as a linear sum of the shape functions over a tetrahedral element defined as

$$x = \sum_{i=1}^{4} L_i x_i$$

$$y = \sum_{i=1}^{4} L_i y_i$$

$$z = \sum_{i=1}^{4} L_i z_i$$

where L_i are the shape functions for the tetrahedral element and (x_i, y_i, z_i) with $i = 1, 2, 3, 4$ denote the vertices of the tetrahedral element. Using the standard

formulae of volume integration within the tetrahedral element, I_2 can be expressed as

$$I_2 = \frac{V_e}{4}\left[D_x \sum_{i=1}^{4} x_i + D_y \sum_{i=1}^{4} y_i + D_z \sum_{i=1}^{4} z_i\right] \tag{6.21}$$

where D_x, D_y, and D_y are the components of $\overline{D}$.

Next,

$$\begin{aligned} I_3 &= \bar{g}_i \cdot \bar{g}_j \iiint_{V_e} |r|^2 \, dv - \iiint_{V_e} (\bar{g}_i \cdot \bar{r})(\bar{g}_j \cdot \bar{r}) \, dv \\ &= (g_{iy}g_{jy} + g_{iz}g_{jz}) \iint_{V_e} x^2 \, dv + (g_{ix}g_{jx} + g_{iz}g_{jz}) \iint_{V_e} y^2 \, dv + \\ &\quad (g_{ix}g_{jx} + g_{iy}g_{jy}) \iint_{V_e} z^2 \, dv - (g_{ix}g_{jy} + g_{iy}g_{jx}) \iint_{V_e} xy \, dv - \\ &\quad (g_{ix}g_{jz} + g_{iz}g_{jx}) \iint_{V_e} zx \, dv - (g_{iy}g_{jz} + g_{iz}g_{jy}) \iint_{V_e} yz \, dv \end{aligned} \tag{6.22}$$

where g_{im} is the m$^{\text{th}}$ component of the vector $\bar{g}_i$.

The evaluation of above integrals takes the form

$$\iiint_{V_e} a_l a_m \, dv = \frac{V_e}{20}\left[\sum_{i=1}^{4} a_{li}a_{mi} + \sum_{i=1}^{4} a_{li} \sum_{i=1}^{4} a_{mi}\right] \tag{6.23}$$

where $l, m = 1, 2, 3$ and a_1, a_2 and a_3 represent the variables x, y and z, respectively.

6.1.2 Boundary-Integral Equation Formulation

The two surface integrals over the aperture surfaces S_{ap} and S_{inp} are evaluated using the boundary-integral formulation. The surface integral over the aperture surface at $z = 0$ is written as

$$I_{ap} = jk_0 Z_0 \iint_{Sap} (\overline{T} \times \hat{n}) \cdot \overline{H}_{ap}(\overline{M}) \, ds \tag{6.24}$$

where Z_0 is the intrinsic impedance of the space above the infinite ground plane and $\overline{H}_{ap}(\overline{M})$ is the magnetic field in the half-space region for a surface current $\overline{M}$

radiating in the presence of a complete conductor. Applying the image theory, the field in the region above the ground plane can be computed by considering an equivalent magnetic surface current $2\overline{M}$ radiating in free space. Hence, (6.24) can be written as

$$I_{ap} = jk_0 Z_0 \iint \overline{T}_s \, . \, \overline{H}_{ap}(2\overline{M}) \, ds \tag{6.25}$$

where $\overline{T}_s = \overline{T} \times \hat{n}$.

The integral over the aperture surface is same as that given in (2.69) except with a negative sign and hence, can be evaluated using (2.80).

Now, for any transmission line, the electric field can be expressed as a sum of incident and reflected field as

$$\overline{E} = \overline{E}_{inc} + \sum_m \left(a_m \bar{e}_m^{TEM/TE} + b_m \bar{e}_m^{TM} \right) e^{\gamma_m z} \tag{6.26}$$

where, $\overline{E}_{inc}$ is the incident electric field of unit amplitude, $\bar{e}_m^{TEM/TE}$, $\bar{e}_m^{TM}$ represent TEM/TE, TM modes, respectively, a_m, b_m are the reflection coefficients for TEM/TE and TM modes, respectively and γ_m is the propagation constant associated with m^{th} mode.

Using the orthogonality of modal vectors, the reflection coefficients a_m and b_m can be expressed as

$$a_m = e^{-\gamma_m z} \iint_{S_{inp}} (\overline{E} - \overline{E}_{inc}) \, . \, \bar{e}_m^{TEM/TE} \, dxdy \tag{6.27}$$

and

$$b_m = e^{-\gamma_m z} \iint_{S_{inp}} (\overline{E} - \overline{E}_{inc}) \, . \, \bar{e}_m^{TM} \, dxdy \tag{6.28}$$

Now for a coaxial input, only TEM mode exists and hence the reflection coefficient a_0 for a TEM incident mode can be expressed as

$$a_0 = e^{-\gamma_0 z} \iint_{S_{inp}} (\overline{E} - \overline{E}_{inc}) \, . \, \bar{e}_0^{TEM} \, dxdy \tag{6.29}$$

where

$$\overline{E}_{inc} = \bar{e}_{inc} e^{-\gamma_{inc} z} \tag{6.30}$$

Here, $\gamma_{inc} = jk_0\sqrt{\varepsilon_{rc}}$ and the modal vector for the incident wave is expressed as

$$\bar{e}_{inc} = \hat{\rho} \frac{1}{\sqrt{2\pi \ln\left(\frac{\rho_2}{\rho_1}\right)}} \frac{1}{\rho} \tag{6.31}$$

where ε_{rc} is the relative permittivity of the coaxial line and ρ_1 and ρ_2 denote the inner and outer radius of the coaxial line. Hence, substituting (6.31) in (6.29), the reflection coefficient can be expressed as

$$a_0 = \frac{e^{-jk_0\sqrt{\varepsilon_{rc}} z_1}}{\sqrt{2\pi \ln\left(\frac{\rho_2}{\rho_1}\right)}} \iint_{S_{inp}} \overline{E} \cdot \frac{\hat{\rho}}{\rho}\, ds - \exp\left(-2jk_0\sqrt{\varepsilon_{rc}} z_1\right) \tag{6.32}$$

Now, the surface integral over the input aperture surface is expressed as

$$\begin{aligned} I_{inp} &= j\omega\mu_0 \iint_{S_{inp}} (\overline{T} \times \hat{n}) \cdot \overline{H}_{inp}\, ds \\ &= -\iint_{S_{inp}} \overline{T} \cdot (\hat{n} \times \nabla \times \overline{E})\, ds \end{aligned} \tag{6.33}$$

Using (6.32) and after some vector calculations, the surface integral becomes

$$\begin{aligned} I_{inp} = &-\frac{jk_0\sqrt{\varepsilon_{rc}}}{2\pi \ln\left(\frac{\rho_2}{\rho_1}\right)} \left\{ \iint_{S_{inp}} (\overline{T} \cdot \frac{\hat{\rho}}{\rho})\, ds \iint_{S_{inp}} (\overline{E} \cdot \frac{\hat{\rho}}{\rho})\, ds \right\} \\ &+ \frac{2jk_0\sqrt{\varepsilon_{rc}}}{\sqrt{2\pi \ln\left(\frac{\rho_2}{\rho_1}\right)}} \exp(-jk_0\sqrt{\varepsilon}_{rc} z_1) \iint_{S_{inp}} \overline{T} \cdot \left(\frac{\hat{\rho}}{\rho}\right) ds \end{aligned} \tag{6.34}$$

Substituting (6.25) and (6.34) in (6.4), the system of equations for the combined

FEM/MoM technique can be expressed as

$$\begin{aligned}\iiint_V \frac{1}{\mu_r}(\nabla \times \overline{T}) \cdot (\nabla \times \overline{E})\, dv - k^2\varepsilon_r \iiint \overline{T} \cdot \overline{E}\, dv \\ +jk_0 Z_0 \iint_{S_{ap}} \overline{T}_s \cdot \overline{H}_{ap}(2\overline{M})\, ds \\ +\frac{jk_0\sqrt{\varepsilon_{rc}}}{2\pi \ln\left(\frac{\rho_2}{\rho_1}\right)} \left\{ \iint_{S_{inp}} (\overline{T} \cdot \frac{\hat{\rho}}{\rho})\, ds \iint_{S_{inp}} (\overline{E} \cdot \frac{\hat{\rho}}{\rho})\, ds \right\} \\ = \frac{2jk_0\sqrt{\varepsilon_{rc}}}{\sqrt{2\pi \ln\left(\frac{\rho_2}{\rho_1}\right)}} \exp(-jk_0\sqrt{\varepsilon_{rc}}z_1) \iint_{S_{inp}} \overline{T} \cdot \left(\frac{\hat{\rho}}{\rho}\right) ds \end{aligned} \tag{6.35}$$

The above system of equations can be expressed in matrix form as

$$A(k)e(k) = b(k) \tag{6.36}$$

where $b(k)$ denotes the excitation vector, $e(k)$ denotes the coefficient vector and $A(k)$ is a partly sparse and partly dense complex symmetric matrix given by

$$A(k) = A_1(k) + A_2(k) + A_3(k)$$

with

$$A_1(k) = \iiint_V \frac{1}{\mu_r}(\nabla \times \overline{T}) \cdot (\nabla \times \overline{E})\, dv - k^2\varepsilon_r \iiint \overline{T} \cdot \overline{E}\, dv \tag{6.37}$$

$$A_2(k) = jk_0 Z_0 \iint_{S_{ap}} \overline{T}_s \cdot \overline{H}_{ap}(2\overline{M})\, ds \tag{6.38}$$

$$A_3(k) = \frac{jk_0\sqrt{\varepsilon_{rc}}}{2\pi \ln\left(\frac{\rho_2}{\rho_1}\right)} \left\{ \iint_{S_{inp}} (\overline{T} \cdot \frac{\hat{\rho}}{\rho})\, ds \iint_{S_{inp}} (\overline{E} \cdot \frac{\hat{\rho}}{\rho})\, ds \right\} \tag{6.39}$$

$$b(k) = \frac{2jk_0\sqrt{\varepsilon_{rc}}}{\sqrt{2\pi \ln\left(\frac{\rho_2}{\rho_1}\right)}} \exp(-jk_0\sqrt{\varepsilon_{rc}}z_1) \iint_{S_{inp}} \overline{T} \cdot \left(\frac{\hat{\rho}}{\rho}\right) ds \tag{6.40}$$

Once the matrix equation in (6.36) is solved for the unknown coefficients, the field over the aperture surface can be calculated. Hence, the input reflection

coefficient can be expressed according to (6.32). Assuming the incident plane at $z_1 = 0$, the reflection coefficient is given by

$$\Gamma = a_0(z_1 = 0) = \frac{1}{\sqrt{2\pi \ln\left(\frac{r_2}{r_1}\right)}} \iint_{S_{inp}} \overline{E} \cdot \frac{\hat{\rho}}{\rho}\, ds - 1 \tag{6.41}$$

The magnetic field in the far-field region can be calculated as

$$\overline{H}(r,\theta,\varphi) = -\frac{jk_0}{\eta_0}\frac{e^{-jk_0 r}}{2\pi r} \iint_{S_{ap}} (\hat{\theta}\hat{\theta} + \hat{\varphi}\hat{\varphi}) \cdot \overline{M} e^{jk_0 \sin\theta(x\cos\varphi + y\sin\varphi)}\, dxdy \tag{6.42}$$

6.2 Numerical Results

Based on the formulation presented here, a MATLAB code has been developed to analyze the performance of a cavity-backed fractal aperture antenna. First, the characteristics of a cavity-backed rectangular aperture antenna have been investigated in order to get an insight into the properties of the aperture antenna. Next, several fractal aperture antennas are investigated and discussed.

6.2.1 Cavity-Backed Rectangular Aperture Antenna

A rectangular aperture of length L_s and width W_s has been considered which is backed by a rectangular cavity of dimensions 15 cm×15 cm×0.4 cm. The antenna is fed by a coaxial line of characteristic impedance 50 Ω. First, a parametric study on the probe location was carried out and the results are shown in Fig. 6.3. Here (x_c, y_c) denotes the location of probe as shown in the inset of Fig. 6.3. The length and width of the slot are taken to be 5 cm and 0.5 cm, respectively. It is found that the optimum probe location is $(x_c = 0, y_c = 6.5\ cm)$. The antenna resonates at 2.0 GHz with a ratio of aperture length to corresponding resonant wavelength equal to 0.33. The location of the probe parallel to the length of the slot is also varied and it is found that best impedance match is obtained when

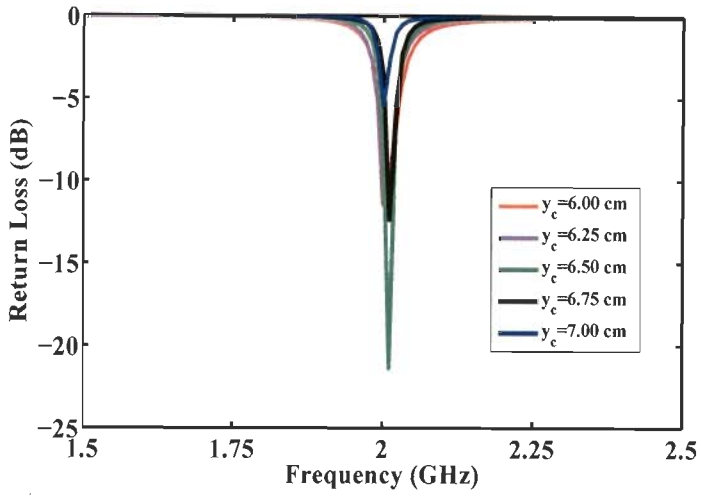

Figure 6.3: Return loss of a cavity-backed rectangular slot antenna for different probe positions.

the probe is on the y-axis. Next, the length of the slot is varied and for each slot length the optimum probe position is found. The effect of slot length on the resonant frequency of the antenna is depicted in Fig. 6.4. The width of the slot has been kept constant at 2.5 cm. Resonant frequencies of the aperture antenna for different slot lengths are tabulated in Table 6.2. It is seen that the resonant slot length approaches 0.5λ as the resonant frequency of the antenna approaches the fundamental resonant mode of the closed cavity. Similar variation of resonant frequencies of the slot antenna was reported in [156]. Also, the bandwidth of the antenna increases as the slot length increases.

6.2.2 Sierpinski Carpet Fractal Aperture

The generation of Sierpinski carpet fractal aperture is described in chapter 3. Here, a rectangle is taken as the initial geometry. The self-similarity factor for the Sierpinski carpet is 3 which causes a log-periodic behavior with a periodicity

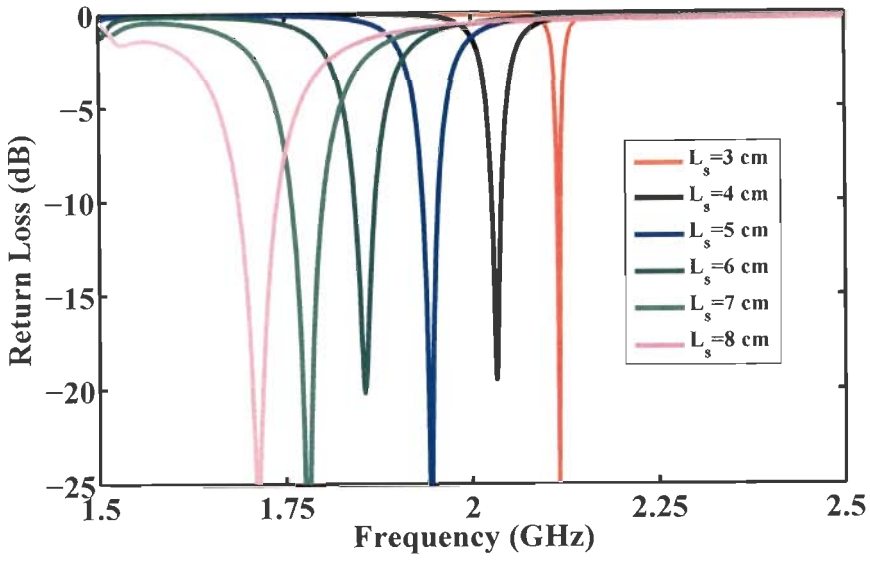

Figure 6.4: Return loss of a cavity-backed rectangular slot antenna for different slot lengths.

Table 6.2: Resonant frequencies of cavity-backed rectangular aperture antenna for different slot lengths.

Slot Length (L_s cm)	Probe Location (x_c, y_c)	Resonant Frequency (f_r) (GHz)	L_s/λ_r	Bandwidth (%)
3	(0,7)	2.12	0.21	0.24
4	(0,6.5)	2.03	0.27	0.64
5	(0,6.25)	1.94	0.32	1.08
6	(0,6.0)	1.86	0.37	1.51
7	(0,5.5)	1.78	0.42	2.36
8	(0,5.25)	1.71	0.46	2.98

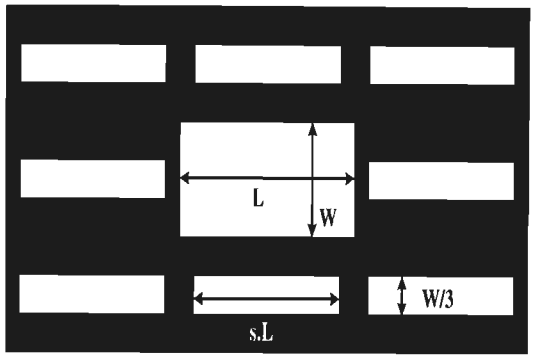

Figure 6.5: A 2nd iteration self-affine Sierpinski carpet aperture antenna.

of 3. To have a control over the location of resonant frequencies, the fractal geometry is modified as shown in Fig. 6.5. The length of the first iteration aperture is kept constant, whereas the length of the second iteration apertures is varied according to a scale factor (s). For the present analysis, the dimension of the initial rectangle is taken to be 15 cm×7.5 cm. Hence, in the first iteration, the antenna consists of a single aperture of length 5 cm and width 2.5 cm. In the next iteration, the dimension of the apertures are (4 cm×0.83 cm) with a scale factor (s) equal to 0.8.

For both the iterations, first a parametric study on the location of the probe is carried out. The variation of return loss for different probe locations is shown in Fig. 6.6 for two iterations. From the study, it is evident that the optimum positions of the probe are at (0, 6.0 cm) and (0, 5.4 cm) for 1st and 2nd iteration, respectively. The final frequency response of the antenna is shown in Fig. 6.7. A good agreement between the present method and HFSS can be seen from the plots. The discretization parameters and the resonant frequencies for the two iterations are given in Table 6.3. It is seen that the first resonant frequency shifts downwards as the order of iteration increases and the ratio between the resonant frequencies is 1.39 which is greater than the theoretical ratio

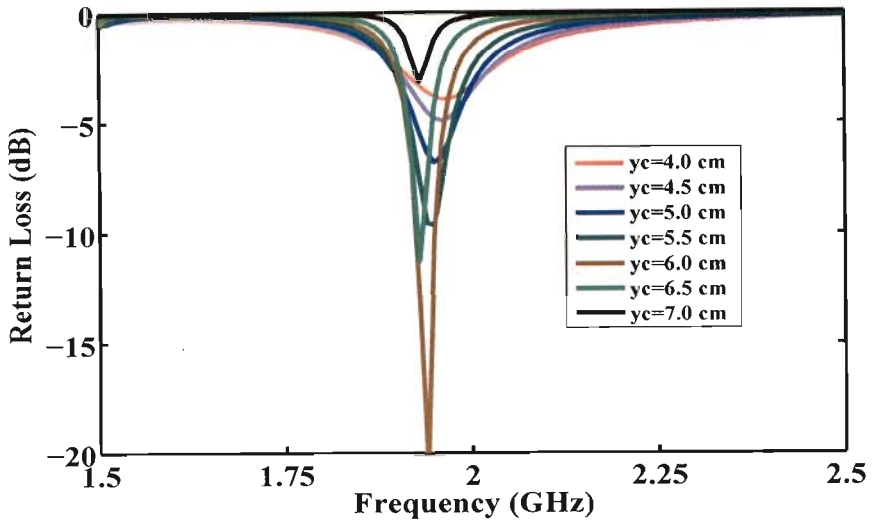

(a) 1st Iteration

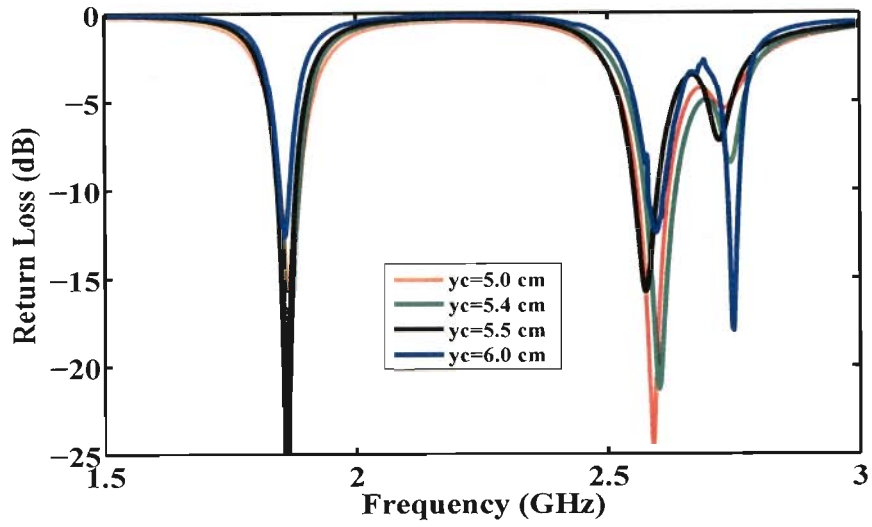

(b) 2nd Iteration

Figure 6.6: Parametric study on the probe position for the two iterations of cavity-backed Sierpinski carpet fractal antenna.

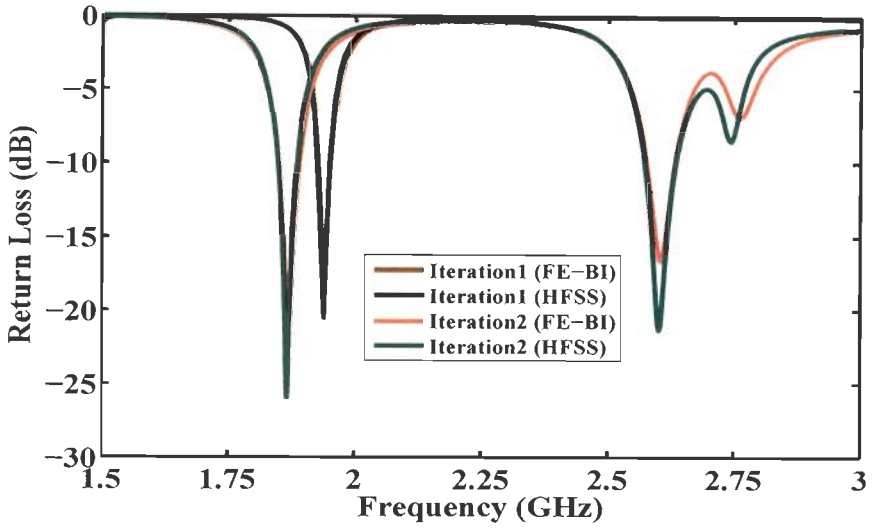

Figure 6.7: Return loss of a self-affine cavity-backed Sierpinski carpet fractal aperture antenna with s=0.8.

Table 6.3: Discretization parameters and resonant frequencies of cavity-backed Sierpinski carpet fractal aperture antenna.

Parameters	Iteration 1	Iteration 2	
Discretization			
No. of Tetrahedrals	2849	5620	
No. of Edges	4821	9501	
No. of Aperture Edges	24	379	
Resonant Frequency (GHz)			
FE-BI	1.94	1.87	2.60
HFSS	1.94	1.86	2.59
Difference (%)	0.00	0.54	0.38
VSWR	1.25	1.09	1.32
Bandwidth (%)	1.55	1.98	2.50

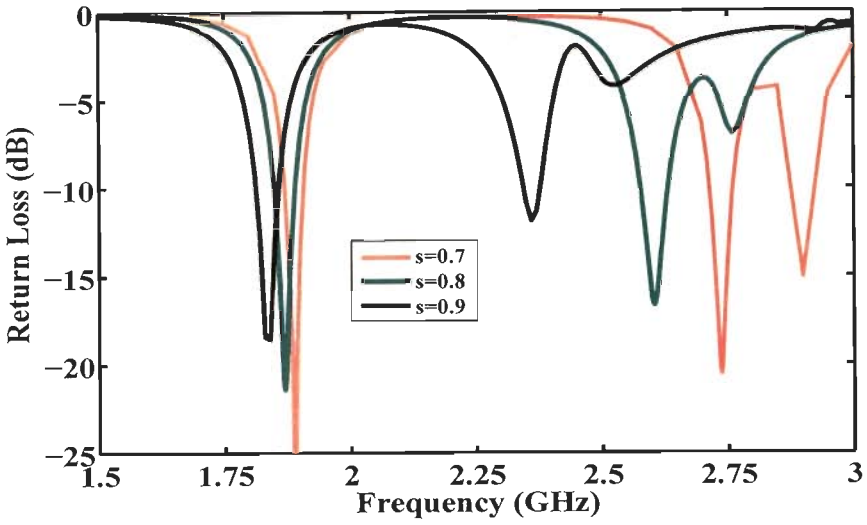

Figure 6.8: Return loss of 2nd iteration cavity-backed Sierpinski carpet aperture antenna for different scale factors.

of 1.25. The ratio between the successive resonant frequencies can be controlled by changing the scale factor (s). From the parametric study, it is found that the optimum probe position for s=0.7 and s=0.9 are (0, 5.7 cm) and (0, 5.0 cm), respectively. The variation of return loss of a 2nd iteration self-affine Sierpinski carpet fractal aperture antenna for different scale factors is shown in Fig. 6.8 and the results are summarized in Table 6.4. It is evident that while the first resonant frequency is relatively insensitive to the variation in scale factor, the second resonant frequency can be suitably located by selecting an appropriate scale factor. The frequency ratios are greater than the theoretical values, which is a characteristics of the pre-fractal geometries for lower order iterations. Also, the ratio between the successive resonant frequencies depends on the position of slot relative to the center of the cavity and the location of resonant frequencies can be fine tuned by varying the spacing between the apertures.

The normalized radiation pattern of a 2nd iteration Sierpinski carpet aperture

Table 6.4: Resonant frequencies of 2nd iteration cavity-backed Sierpinski carpet fractal aperture antenna for different scale factors.

Scale Factor	Resonant Frequencies		Ratio	Bandwidth (%)	
(s)	f_{r1}	f_{r2}	$\frac{f_{r2}}{f_{r1}}$	BW_1	BW_2
0.7	1.89	2.74	1.45	1.85	1.83
0.8	1.87	2.60	1.39	1.98	2.50
0.9	1.82	2.36	1.30	2.31	2.58

in the two principal planes is shown in Fig. 6.9 for s=0.8. The second resonant frequency of the cavity backed aperture antenna is above TM_{120} resonant mode of the cavity and hence, the second iteration apertures will be excited by the fields of opposite phase which causes a null along the z-axis.

6.2.3 Sierpinski Gasket Dipole Aperture Antenna

The generation steps for the self-affine Sierpinski gasket dipole geometry is described in chapter 3. The geometry of second iteration Sierpinski gasket dipole aperture antenna with a scale factor s=0.8 is shown in Fig. 6.10. The initial triangle has a height 3.75 cm and the base length is 7.5 cm. Fig 6.11 shows the frequency response of the self-affine gasket aperture for different probe locations. It is found that the optimum position of the probe is at (0, 5.25 cm) for both iterations. The variation of return loss of the Sierpinski gasket dipole aperture antenna with scale factor (s) equal to 0.8 is shown in Fig. 6.12. A good agreement with the present FE-BI code with the HFSS results can be found for both iterations. The discretization parameters and the resonant frequencies

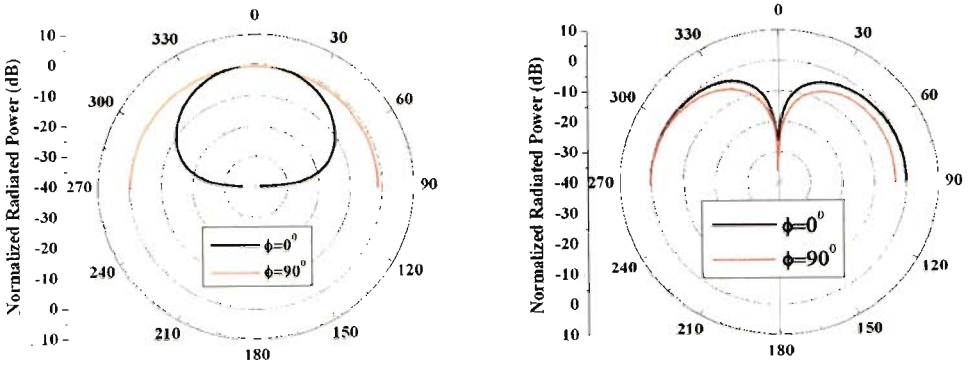

(a) 1st Resonance (b) 2nd Resonance

Figure 6.9: Normalized power pattern of a 2nd iteration cavity-backed Sierpinski carpet aperture antenna.

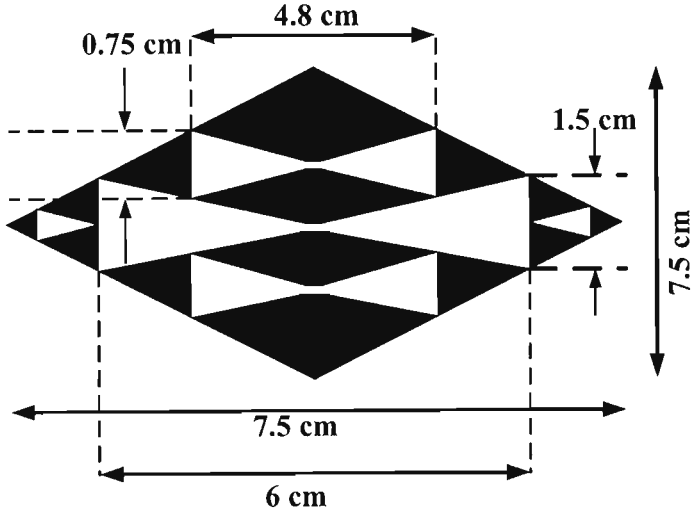

Figure 6.10: A 2nd iteration self-affine cavity-backed Sierpinski gasket dipole aperture antenna.

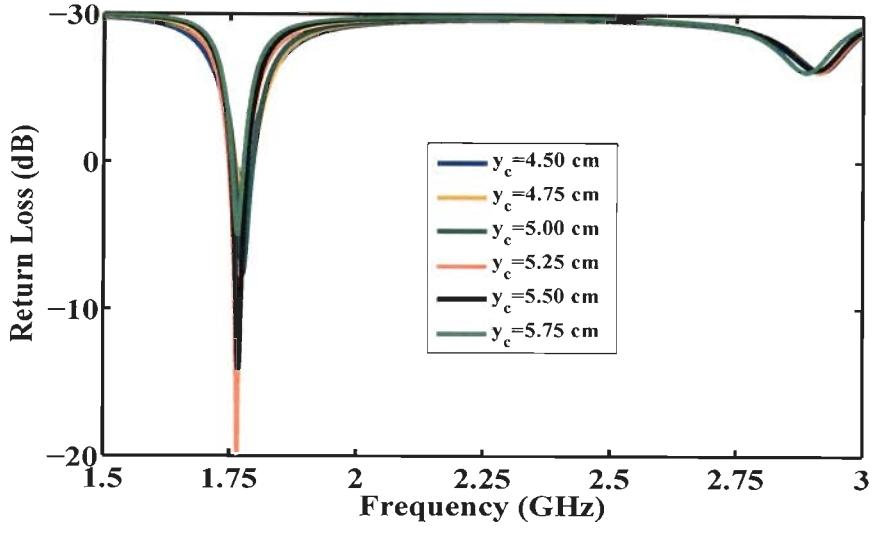

(a) 1st Iteration

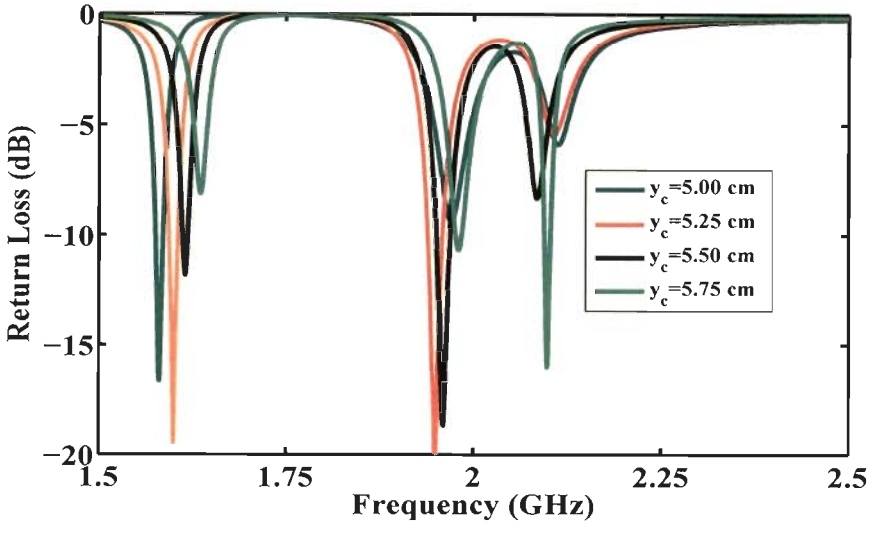

(b) 2nd Iteration

Figure 6.11: Parametric study on the location of probe for cavity-backed Sierpinski gasket dipole aperture antenna.

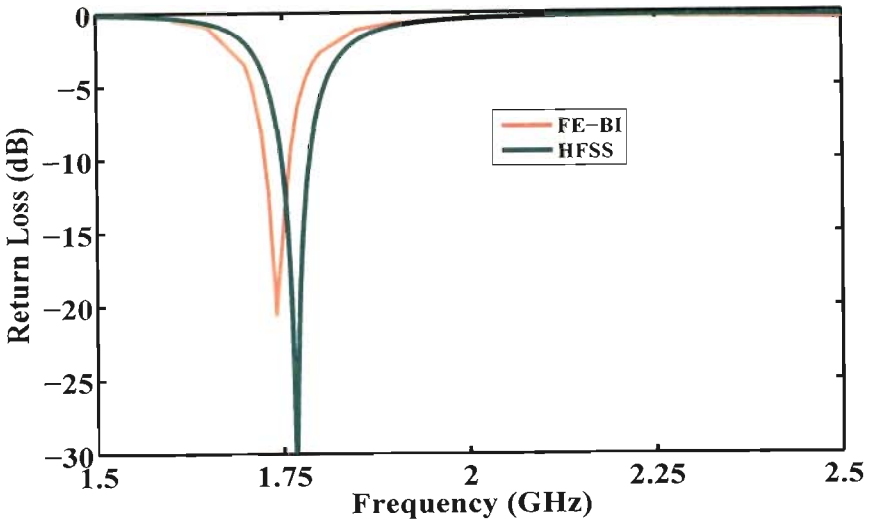

(a) 1st Iteration

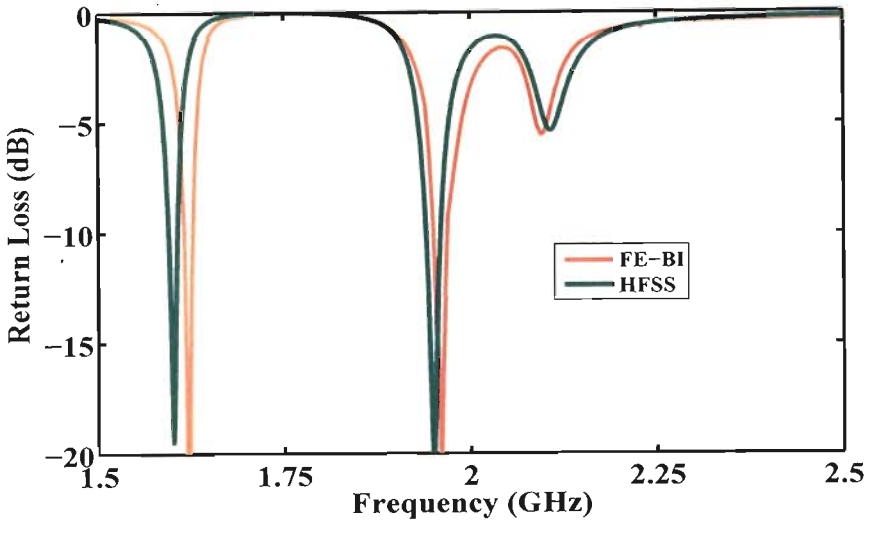

(b) 2nd Iteration

Figure 6.12: Return loss of cavity-backed Sierpinski gasket dipole aperture antenna for two iterations.

Table 6.5: Discretization parameters and resonant frequencies of cavity-backed Sierpinski gasket dipole aperture antenna.

Parameters	Iteration 1	Iteration 2	
Discretization			
No. of Tetrahedrals	2267	3564	
No. of Edges	3989	5956	
No. of Aperture Edges	355	408	
Resonant Frequency (GHz)			
FE-BI	1.74	1.60	1.95
HFSS	1.76	1.57	1.94
Difference (%)	1.15	1.88	0.52
VSWR	1.10	1.09	1.12
Bandwidth (%)	2.15	0.75	1.03

are summarized in Table 6.5. It can be seen that there is a 8.05% downward shift of first resonant frequency in the second iteration. The ratio between the successive resonant frequencies is 1.22, which is slightly less than the theoretical value 1.25. The bandwidth of the antenna decreases as the order of iteration increases. Although the input match is good in all the iterations, the bandwidth of the antenna is very small at both the resonant frequencies. In order to see the effect of scale factor on the response of the antenna, another gasket dipole aperture antenna with a scale factor 0.6 was investigated. The dimensions of the first iteration aperture are kept constant at 6 cm, so the length of the 2^{nd} iteration aperture is 3.6 cm. The variation of return loss of 2^{nd} iteration self-affine gasket dipole aperture antenna for different scale factors is shown in Fig. 6.13. It can be seen that there is a very little change in the first resonant frequency

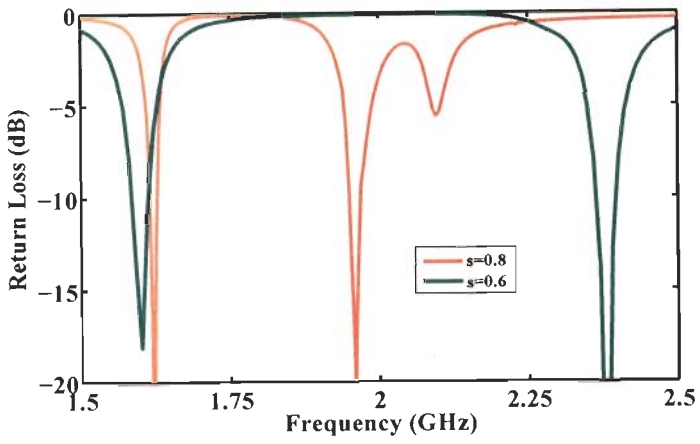

Figure 6.13: Return loss of 2nd iteration cavity-backed Sierpinski gasket dipole aperture antenna for different scale factors.

and the location of the 2nd resonance can be controlled by changing the scale factors. The resonant frequencies for $s = 0.6$ are 1.58 GHz and 2.38 GHz with a ratio of 1.49. This ratio is much less than the theoretical ratio of 1.67. This is due to the geometric modifications incorporated in the generation of fractal aperture. Also, it is found from the analysis of rectangular aperture antenna that the ratio between the aperture length and the resonant wavelength approaches 0.5λ as the resonant frequency of the antenna moves closer to the fundamental resonant mode of the closed cavity. However, as the resonant frequencies move away from fundamental resonant mode, the ratio decreases, which is another reason of smaller frequency ratio for $s = 0.6$.

The normalized radiation pattern of the 2nd iteration gasket dipole aperture antenna with $s = 0.8$ is shown in Fig. 6.14 in two principal planes and is similar at both resonant frequencies. The maximum gain of the aperture antenna at the resonant frequencies is around 4 dB. It is to be noted here that both the resonant frequencies for the dipole aperture antenna are within the fundamental resonant

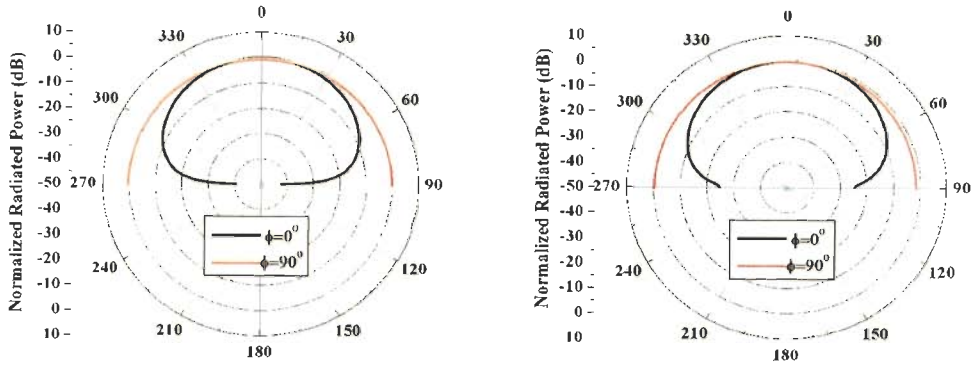

(a) 1st Resonance

(b) 2nd Resonance

Figure 6.14: Normalized power pattern of a 2nd iteration cavity-backed Sierpinski gasket dipole aperture antenna.

mode of the closed cavity, hence the pattern at both resonant frequencies remain same.

6.2.4 Plus Shape Fractal Aperture Antenna

The generation of the plus shape fractal aperture is described in chapter 3. The initial plus shape has a horizontal arm length L and vertical arm length W. The width of each arm is taken to be w_s. The initial geometry is scaled by a factor s in both directions and four such copies are placed with an offset $(\pm d_x, \pm d_y)$ as shown in Fig. 6.15. In the present analysis, the initial plus shape is assumed to have a length $L = W = 5$ cm. The width of each arm is 2 mm. The parametric study for the optimum probe location resulted in an optimum probe position of (0, 6.5 cm). The variation of return loss for first iteration is shown in Fig. 6.16. The initial plus aperture antenna resonates at 2.05 GHz with a bandwidth of 0.45%. Next, a 2nd iteration plus shape fractal aperture antenna is investigated for different offset parameter (d_x, d_y) with a scale factor s=0.8. Fig. 6.17 shows the variation of return loss for different offset values and

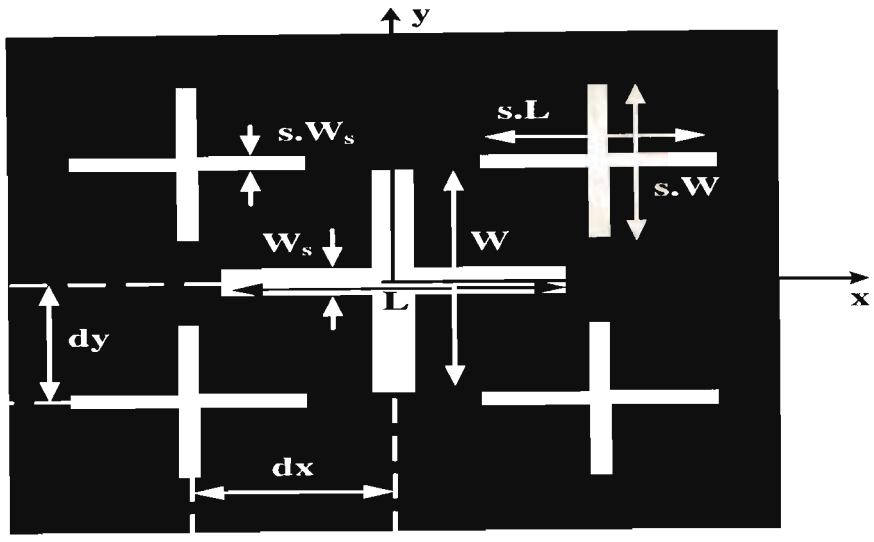

Figure 6.15: Geometry of a cavity-backed 2nd iteration plus shape fractal aperture.

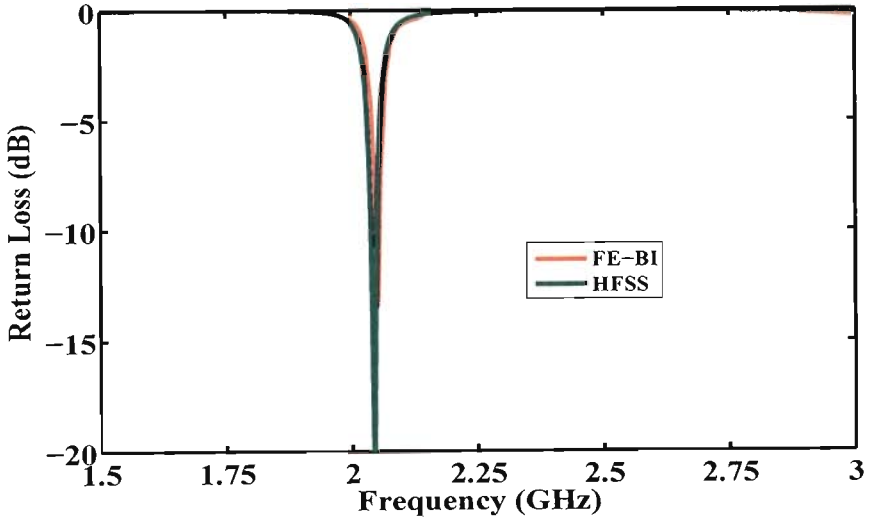

Figure 6.16: Return loss of 1st iteration cavity-backed plus shape fractal aperture antenna.

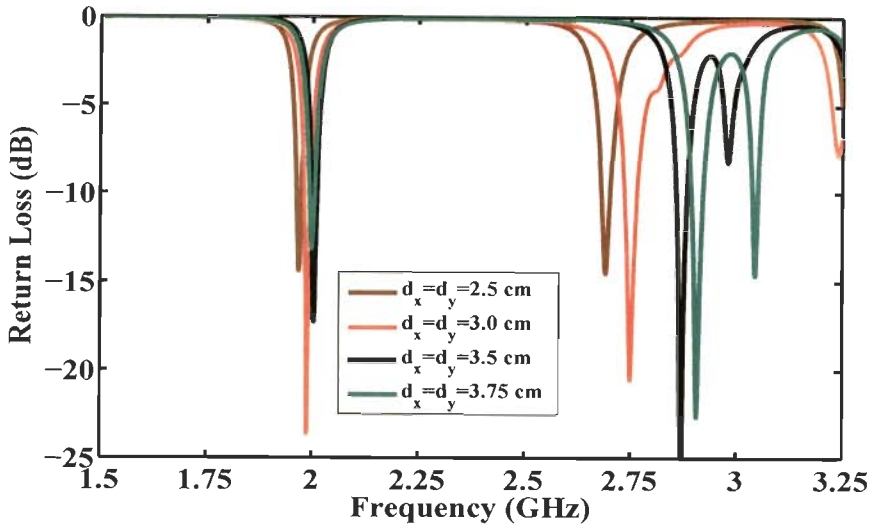

Figure 6.17: Return loss of 2nd iteration cavity-backed plus shape fractal aperture antenna for different offset values.

the results are summarized in Table 6.6. It is evident that the location of 2nd iteration apertures affects the location of 2nd resonant frequency and hence, the ratio of successive resonant frequencies. The variation of return loss for a 2nd iteration plus fractal aperture with $d_x = d_y = 2.5$ cm is shown in Fig. 6.18 and the results for two iterations are summarized in Table 6.7. It is seen that the first resonant frequency shifts downward and the ratio between the successive resonant frequencies is 1.36 as compared to the theoretical value 1.25. Two more fractal geometries with the scale factors s=0.7 and s=0.9 were investigated and Fig. 6.19 shows the frequency response of the aperture antenna for different scale factors. The value of offset is kept at 2.5 cm. From the figure, it is seen that the ratio between the successive resonant frequencies are 1.425, 1.37 and 1.31 for s=0.7, 0.8 and 0.9, respectively. Thus, the antenna resonant frequency can be controlled by changing the scale factor, which can be fine tuned with different offset values.

Table 6.6: Resonant frequencies of 2nd iteration cavity-backed plus shape fractal aperture for different offset values.

Offset	x_c	y_c	Resonant Frequencies		Ratio
$(d_x = d_y)$	(cm)	(cm)	f_1 (GHz)	f_2 (GHz)	f_2/f_1
2.50	0	6.6	1.97	2.69	1.37
3.00	0	6.4	1.99	2.75	1.38
3.50	0	6.4	2.00	2.87	1.44
3.75	0	6.25	2.00	2.91	1.455

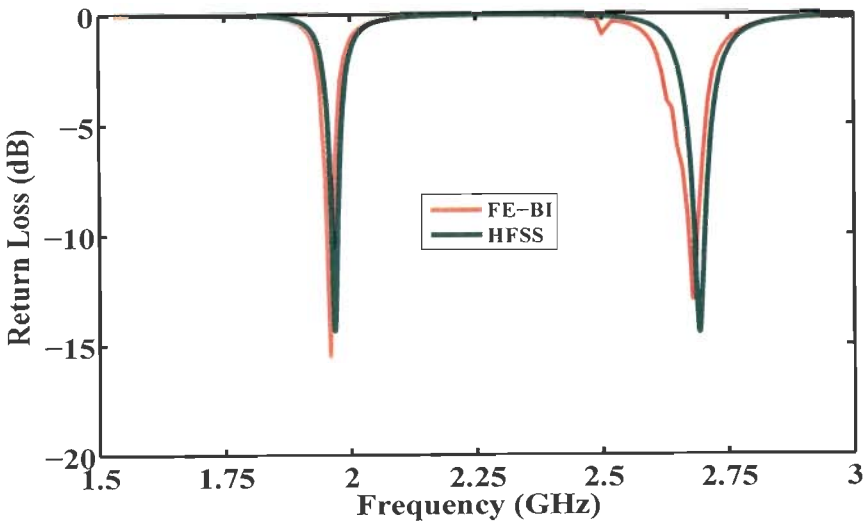

Figure 6.18: Return loss of 2nd iteration cavity-backed plus shape fractal aperture antenna with s=0.8 and d_x=d_y=2.5.

Table 6.7: Discretization parameters and resonant frequencies of cavity-backed plus shape fractal aperture antenna.

Parameters	Iteration 1	Iteration 2	
Discretization			
No. of Tetrahedrals	4296	5020	
No. of Edges	6914	8251	
No. of Aperture Edges	43	175	
Resonant Frequency (GHz)			
FE-BI	2.04	1.96	2.68
HFSS	2.05	1.97	2.69
Difference (%)	0.49	0.51	0.37
VSWR	1.25	1.09	1.32
Bandwidth (%)	0.45	0.56	0.74

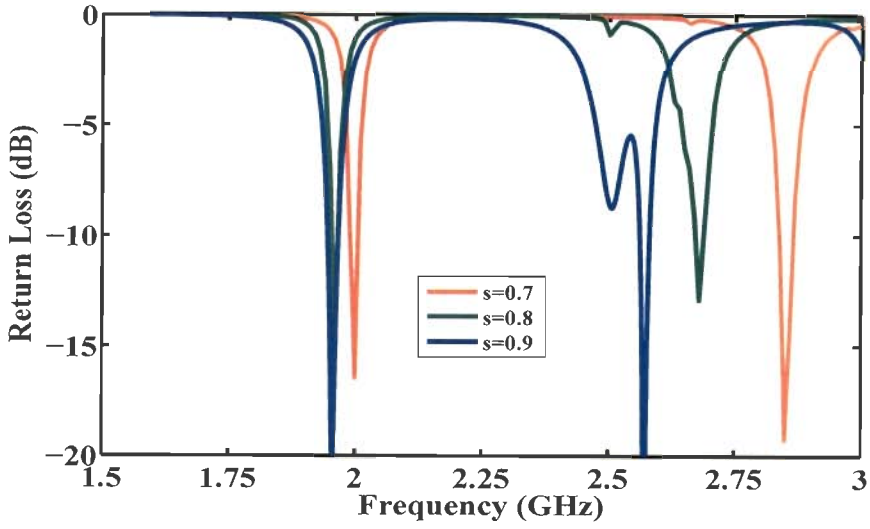

Figure 6.19: Return loss of 2nd iteration cavity-backed plus shape fractal aperture antenna for different scale factors.

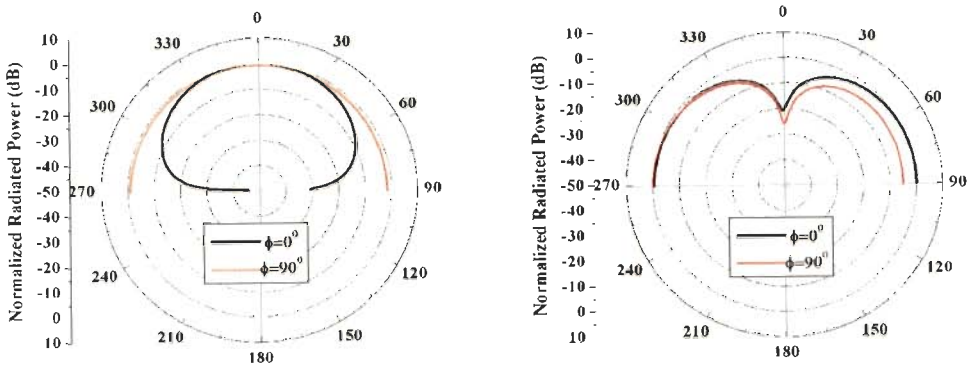

(a) 1st Resonance (b) 2nd Resonance

Figure 6.20: Normalized power pattern of a 2nd iteration cavity-backed plus shape fractal aperture antenna.

The radiation pattern of the 2nd iteration plus shape fractal aperture antenna is shown in Fig. 6.20. The pattern shows a similar behavior as that of carpet antenna which shows a null along z-axis.

6.2.5 Minkowski Fractal Aperture Antenna

Minkowski fractal geometries are widely used in the miniaturization of antenna and frequency selective surface design. Here, we have considered a second iteration Minkowski aperture antenna as shown in Fig. 6.21. The dimension of the initial square is taken to be 3 cm×3 cm and the dimension of the cavity is 10 cm×10 cm×0.4 cm. The variation of return loss of the Minkowski aperture antenna for different iterations are shown in Fig. 6.22 and the results are summarized in Table 6.8. It should be noted here that the optimum probe locations are (0, 4.25 cm), (0, 3.80 cm) and (0, 3.60 cm) for 0th, 1st and 2nd iterations, respectively. It is found that the resonant frequency of the antenna decreases by 12.66% as the order of iterations increases from 0 to 2. The ratio of the square aperture length to the resonant wavelength is 0.31, a behavior similar to that

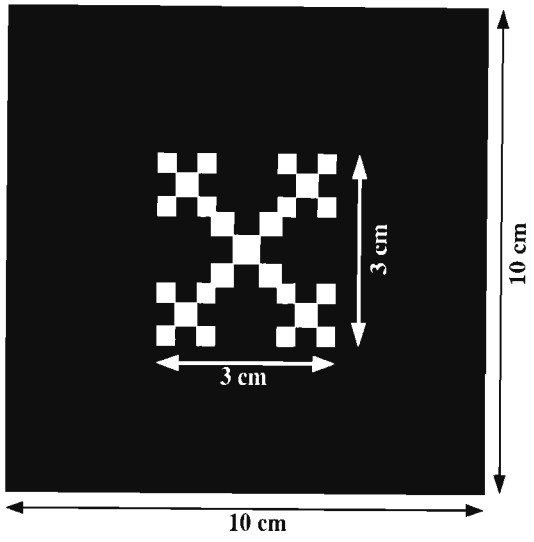

Figure 6.21: Geometry of a 2nd iteration Minkowski aperture antenna.

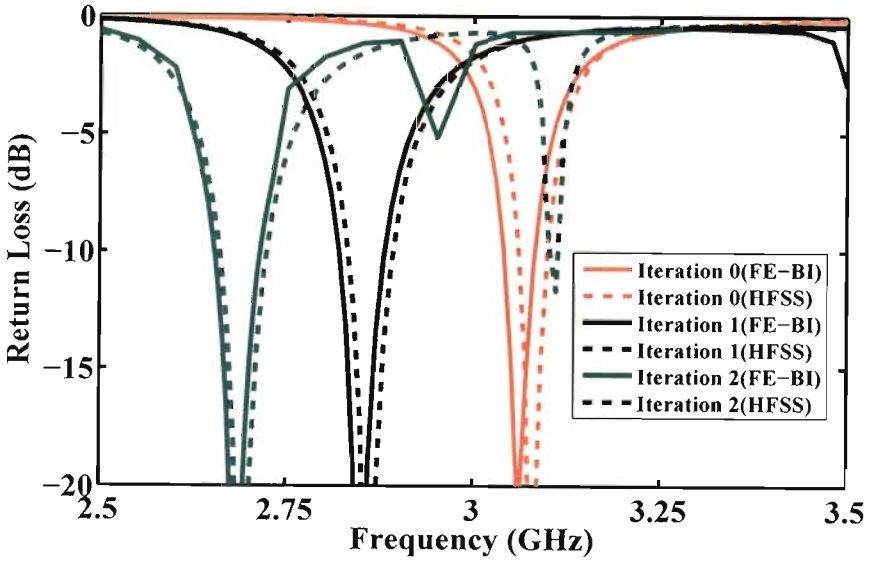

Figure 6.22: Return loss of cavity-backed Minkowski aperture antenna for different iterations.

Table 6.8: Discretization parameters and resonant frequencies of cavity-backed Minkowski fractal aperture antenna.

Iteration	No. of Tetrahedrals	No. of Edges	Aperture Edges	Resonant frequency (GHz)	Bandwidth (%)	VSWR
0	1326	2247	193	3.08	1.30	1.10
1	3053	5103	405	2.86	2.45	1.29
2	12132	16649	902	2.69	2.60	1.05

obtained for rectangular aperture. Generally, it is found that the antenna bandwidth decreases with the miniaturization of the antenna structure. However, in this case, the antenna bandwidth increases as the order of iteration increases. This behavior of the aperture antenna is similar to antenna presented in [27]. The impedance match for all the iterations are very good.

The normalized radiated power patterns of the antenna at the resonant frequency of the Minkowski antenna for different iterations are shown in Fig. 6.23 where M0 to M2 denote the iterations of the Minkowski aperture antenna. The normalized power pattern of the antenna remains same for all the iterations. However, it is found that the maximum gain of the antenna decreases as the order of iterations increases. The gain of the antenna for different iterations are 6.76 dB, 5.88 dB and 5.40 dB.

6.3 Summary

A hybrid FE-BI analysis for the cavity backed aperture antenna with a coaxial feed is presented. Some dual-band cavity-backed antenna based upon the self-affine fractal geometries such as Sierpinski gasket, Sierpinski carpet, plus shape

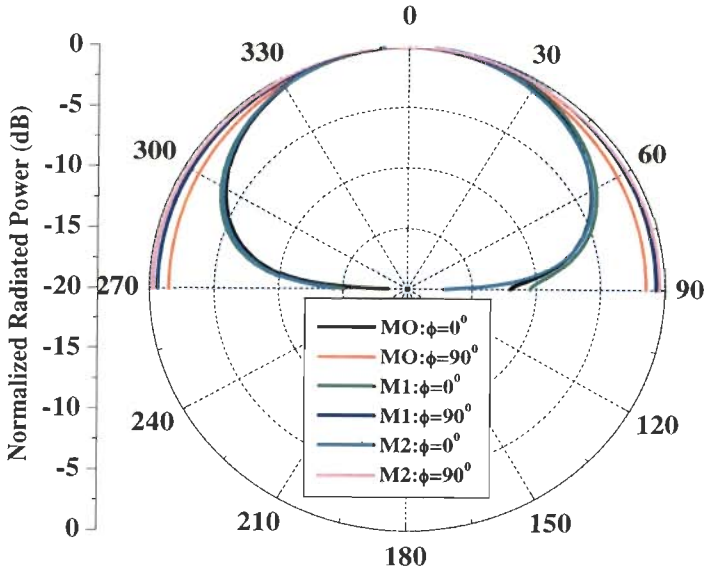

Figure 6.23: Normalized power pattern of cavity-backed Minkowski aperture antenna for different iterations.

fractals are investigated and discussed. The scale factor of the fractal apertures are used to suitably locate the resonant frequencies of the antenna. Also, it is found that the location of the aperture relative to the center of the cavity changes the frequency response of the antenna. One of the main drawback of the cavity backed antenna is that they have a small bandwidth due to the cavity resonances. The normalized radiation pattern of the antenna remains same for Sierpinski gasket dipole aperture antenna, but it is found that a null appears along z-axis for aperture antennas like Sierpinski carpet and plus shape fractal antennas. From the results presented here, it can be concluded that the radiation pattern of the antenna can be kept same if the antenna is operated within a single mode. A self-similar antenna based on the Minkowski fractal is also analyzed and it is found that this fractal geometry can be useful to minimize the dimension of the aperture.

Chapter 7

CONCLUSIONS AND FUTURE WORK

Fractal electromagnetics has thrown open a wide vista of opportunities in front of electromagnetic engineers. What makes fractal geometries attractive, is their self-similarity which leads to multi-band properties. Thus, fractals have resulted in the design of novel miniaturized and multi-band antennas, frequency selective surfaces, and electromagnetic bandgap structures.

The present research was motivated by the realization that fractal apertures can also be a useful tool in the design of multi-band waveguide components and antennas, as well as, frequency selective surfaces and EBG structures.

The work presented in this dissertation has amply demonstrated that fractal apertures indeed offer several interesting properties which can be exploited in the design of a new class of waveguide components and antennas. Some of main conclusions of the research are summarized below:

- Fundamental properties of some self-affine and self-similar fractal apertures in the transverse cross-section of a rectangular waveguide have been

investigated numerically. The fractal apertures offer a multiple frequency selective property and the frequency response of the fractal diaphragms is directly related to scale factor of the geometry. It has been found that the ratio between the successive resonant frequencies of the fractal diaphragm varies with the scale factor. However, the ratio is a little higher than the theoretical value due to the lower order of iterations used. Typical applications of the fractal diaphragms in the design of waveguide based passive elements have also been investigated. A simple dual-band waveguide filter design has been presented which offers a good out-of-band rejection. Also, an electromagnetic band gap structure based on self-affine Sierpinski gasket aperture was found to exhibit a wide bandgap with good roll-of factor outside the stopband.

- Electromagnetic transmission through some typical self-similar fractal apertures illuminated by a plane wave of arbitrary polarization is investigated which shows the existence of multiple passbands and stopbands. Equivalent magnetic current distributions on the aperture surface have been used to get an insight into the behavior of fractal apertures. It is found that the current is distributed over the entire aperture surface for primary resonant frequency and for higher order iterations, the current is concentrated over the scaled copies of the fractal geometry. The frequency response of the fractal apertures is found to be dependent on the polarization as well as the incidence angle. Some new passbands are generated for inclined incidence. It is found that the fractal apertures support subwavelength transmission of electromagnetic waves, and this property is more pronounced in case of space-filling fractals. The behavior of the fractal apertures has been found to be similar to the fractal multi-band monopole and dipole antennas.

- Fractal apertures in an infinite conducting screen fed by a rectangular waveguide offer multiple resonant bands. Some self-affine fractal apertures have been proposed which offer dual-band radiation characteristics and it is found that the scale factor of the fractal apertures can be used as a design parameter for locating the resonant bands at desired locations. The space-filling fractal apertures are efficient in reducing the aperture geometry. The waveguide-fed fractal aperture antennas exhibit wide bandwidth with moderate gain.

- Some dual-band cavity-backed aperture antennas have been proposed based on some self-affine fractal apertures. The antenna characteristics can be controlled by varying the scale factor of the fractal apertures. The characteristics of these antennas have been found to depend on the location of apertures over the cavity surface, because of the nature of field distribution in the cavity. A good impedance match is obtained for the resonant bands of the antenna. However, the cavity-backed antennas have inherently a narrow bandwidth.

7.1 Future Work

The present research work has opened up a number of possibilities for further investigation on fractal apertures. Some areas that need to be investigated are:

- In the present work, the apertures are assumed to be located in a thin conducting screen. From practical point of view, the screen may have some finite thickness. It is expected that the finite thickness of the screen will have a significant effect on the transmission properties of the apertures. Hence, it is important to include the thickness of the screen and the analysis

should be extended to include the finite thickness of the screen.

- The fabrication of thin fractal diaphragms is difficult and these may be efficiently fabricated only with a dielectric support. Also, the design of waveguide based metamaterial structures requires proper dielectric backing. So, the fractal apertures have to be backed by a dielectric layer which can be efficiently analyzed using the generalized scattering matrix (GSM) approach. The study can be further extended to analyze the dual of the present problem which consists of fractal screens instead of the fractal apertures in the transverse cross-section of the rectangular waveguide.

- In the present study, it has been demonstrated that fractal diaphragms can be used in the design of multiband filters and EBG structures. However, considerable effort needs to be directed in developing a design procedure for specific applications. Further research is also required in exploring the possibility of designing multiband waveguide power dividers, directional couplers, and tee junctions.

- Recently, soft computing techniques like Particle Swam Optimization (PSO), Artificial Neural Networks (ANNs) and Genetic Algorithms (GAs) have emerged as powerful tools in design, modeling, and optimization of complex electromagnetic problems. It is envisaged that these techniques would prove to be useful in the design of fractal-aperture based structures and need to be investigated.

- The electromagnetic transmission through fractal apertures shows a polarization dependency. So, the fractal geometry can be optimized to obtain a polarization independent frequency response. The analysis can be further extended to study the characteristics of conducting screen perforated

with fractal apertures sandwiched between two dielectric layers, which is of importance in the design of bandpass radoms. In the present work, the analysis is limited to the radiation from apertures fed by a single waveguide. This analysis can be extended to investigate the properties of fractal aperture antenna arrays. Also, the gain of the aperture antennas are found to be around 5 dB, which can be improved by using electromagnetic bandgap layers.

- The major issue in the analysis of cavity-backed aperture antennas is the computational efficiency. The efficiency of the present analysis can be enhanced by using asymptotic waveform evaluation (AWE) technique. The present analysis is limited to single cavity which can be further extended to study the cavity-backed aperture antenna arrays. For this case, the adaptive integral method (AIM) can be used to analyze the problem efficiently. In the present analysis, the cavity is assumed to be empty. The characteristics of inhomogeneous cavity filling should also be investigated.

Appendix A

Calculation of Integrals over Triangular Domains

The area coordinates associated with a triangle are shown in Fig. A.1. The area coordinates are defined in terms of cartesian coordinates as

$$\begin{aligned} x &= x_1\mathcal{L}_1 + x_2\mathcal{L}_2 + x_3\mathcal{L}_3 \\ y &= y_1\mathcal{L}_1 + y_2\mathcal{L}_2 + y_3\mathcal{L}_3 \\ 1 &= \mathcal{L}_1 + \mathcal{L}_2 + \mathcal{L}_3 \end{aligned} \tag{A.1}$$

Thus, these coordinates are not independent, rather are related by 3^{rd} equation. For every set of $\mathcal{L}_1$, $\mathcal{L}_2$, and $\mathcal{L}_3$, there is a unique set of cartesian coordinates. At

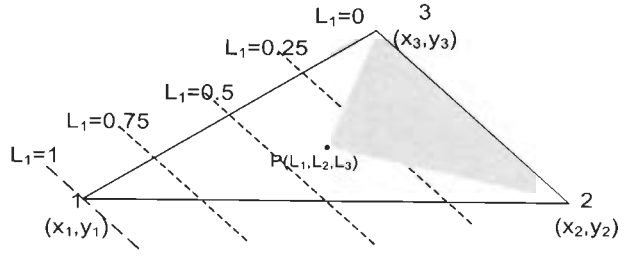

Figure A.1: Area Coordinates.

point j, $\mathcal{L}_j = 1$ and $\mathcal{L}_j = 0$ at any other vertex. The linear relationship between the area coordinates and cartesian coordinates implies that the contours of $\mathcal{L}_j$ are equally spaced straight lines parallel to the side on which $\mathcal{L}_j = 0$.

The area coordinate $\mathcal{L}_j$ at a point P can alternatively be defined as the ratio of area of triangle formed by P and vertices other than j^{th} vertex to the total area of the triangle. Thus

$$L_1 = \frac{\text{Area of } \triangle P23}{\text{Area of } \triangle 123}$$

The integrals I_1 and I_2 can be transformed into the integrals over the area coordinates by using the formula

$$\begin{aligned} I &= \iint_{Triangle} f(x,y)dxdy \\ &= A_T \int_0^1 \int_0^{1-\mathcal{L}_2} f(\mathcal{L}_2, \mathcal{L}_3)\, d\mathcal{L}_2\, d\mathcal{L}_3 \end{aligned}$$

where A_T denotes the area of the triangle.

Using the Gauss-Legendre quadrature formula, the above integral can be expressed as

$$I = A_T \sum_{k=1}^{K_N} W(k) f(\mathcal{L}_{2k}\mathcal{L}_{3k}) \tag{A.2}$$

where weights W_k and coefficients $\mathcal{L}_{1k}$, $\mathcal{L}_{2k}$, and $\mathcal{L}_{3k}$ can be obtained from [161] for different values of K_N. Hence using (A.2), I_1 and I_2 can be expressed as

$$\begin{aligned} I_1 &= A_T \sum_{k=1}^{K_N} (x_k - x_i) \sin\left(\frac{m\pi x_k}{a}\right) \cos\left(\frac{n\pi y_k}{b}\right) \\ I_2 &= A_T \sum_{k=1}^{K_N} (y_k - y_i) \cos\left(\frac{m\pi x_k}{a}\right) \sin\left(\frac{n\pi y_k}{b}\right) \end{aligned} \tag{A.3}$$

where,

$$x_k = x_1 + (x_2 - x_1)\mathcal{L}_{2k} + (x_3 - x_1)\mathcal{L}_{3k}$$

$$y_k = y_1 + (y_2 - y_1)\mathcal{L}_{2k} + (y_3 - y_1)\mathcal{L}_{3k}$$

Appendix B

Computation of Singular Integrals

It is well known that potential integrals involving free space Green's function suffer from singularity, which occurs when the source and observation points coincide. A number of authors have reported the evaluation of these integrals based on singularity subtraction approach [164, 165, 166, 167]. In the singularity subtraction approach, the term having the asymptotic behavior at singularity is first subtracted from the integrand, and the resulting regular integral is computed numerically. The subtracted singular term is calculated using analytical methods and the result is added back to the numerically integrated term to obtain the final result. The approach can be summarized as

$$\iint_T \mathbf{M}(\mathbf{r}) G(r|r')ds' = \underbrace{\iint_T \mathbf{M}(\mathbf{r})\left[G(r|r') - G^{asym}(r|r')\right]ds'}_{\text{Numerical Integration}} + \underbrace{\iint_T \mathbf{M}(\mathbf{r}) G^{asym}(r|r')ds'}_{\text{Analytical Integration}}$$

where, $\mathbf{M(r)}$ is a scalar or vector basis function. Although, the singularity subtraction approach is extensively used in the computation of singular integrals, this methods suffers from some limitations. The difference term after subtraction of the asymptotic term cannot be well approximated in the neighborhood of the singularity because of the existence of higher order derivatives. The complexity of the problem increases for complex geometries and higher order basis functions. Also, the analytical evaluation of singular term becomes complicated for complex geometries and basis functions.

Due to these limitations, a more efficient method has been proposed in [168], which is based on the singularity cancellation method. The fundamental advantage of this method is that, the singular integral can be evaluated by purely numerical quadrature approach. Here, we have followed the singularity cancelation method for the evaluation of singular integrals.

The integral to be calculated is of the form

$$I = \iint_T \mathbf{M}(\bar{r}') \frac{e^{-jkR}}{4\pi R} ds' \tag{B.1}$$

where, $R = |\bar{r} - \bar{r}'|$ is the distance between the source and observation point. The geometry of the triangle over which the integration has to be performed is shown in Fig. B.1. Here, $\bar{r}_1$, $\bar{r}_2$ and $\bar{r}_3$ are the position vectors of the vertices of triangle and $\bar{r}_0$ denotes the observation point. The original triangle is subdivided into three subtriangles by connecting the vertices of the original triangle with the observation point as shown in Fig. B.1. The contribution of the integral defined in (B.1) is calculated for each subtriangle and then added back to obtain the final result.

The geometrical quantities for subtriangle 1 (see Fig. B.2) are

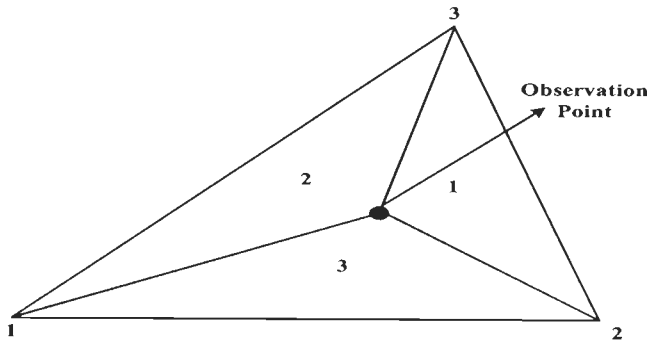

Figure B.1: Subdivision of original triangle.

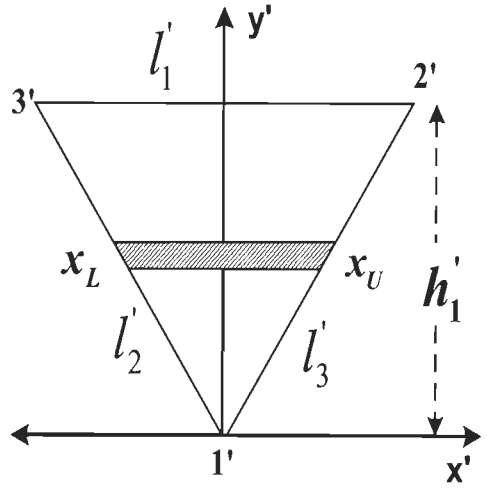

Figure B.2: Local coordinate system for subtriangle 1.

$$
\begin{aligned}
\bar{r}'_1 &= \bar{r}_0 & \bar{l}'_1 &= \bar{r}'_3 - \bar{r}'_2 \\
\bar{r}'_2 &= \bar{r}_2 \rightarrow \bar{r}_3 \rightarrow \bar{r}_1 & \bar{l}'_2 &= \bar{r}'_1 - \bar{r}'_3 \\
\bar{r}'_3 &= \bar{r}_3 \rightarrow \bar{r}_1 \rightarrow \bar{r}_2 & \bar{l}'_3 &= \bar{r}'_2 - \bar{r}'_1 \\
\hat{n}' &= \frac{\bar{l}'_1 \times \bar{l}'_2}{|\bar{l}'_1 \times \bar{l}'_2|} \\
\bar{h}_1 &= \frac{2A'}{|\bar{l}'_1|^2}\bar{l}'_1 \times \hat{n}' \\
A' &= \frac{\hat{n}'.\bar{l}'_1 \times \bar{l}'_2}{2}
\end{aligned}
\tag{B.2}
$$

Here, the arrows indicate the parameters for subtriangles 1 to 3 as one goes from subtriangle 1 to subtriangle 3. The primed and unprimed parameters denote the quantities for the original triangle and subtriangle, respectively.

The integral over the subtriangle 1 can now be expressed as

$$
I_1 = \int_0^{h1'} \int_{x_L}^{x_U} \mathbf{M}(r') \frac{e^{-jkR}}{4\pi R} dx' dy' \tag{B.3}
$$

where, $R = (\sqrt{(x')^2 + (y')^2})$, is the distance between the source and observation point. The limits of the integration can be expressed in terms of normalized area coordinate $\mathcal{L}'_1$ at node 1'. $\mathcal{L}'_1$ is unity at $y' = 0$ and zero at $y' = h'_1$. Hence

$$
y' = (1 - \mathcal{L}'_1)h'_1 \tag{B.4}
$$

$$
x_L = \hat{n}' \; . \; (\hat{h}'_1 \times \bar{l}'_2)(1 - \mathcal{L}'_1) \tag{B.5}
$$

$$
x_U = -\hat{n}' \; . \; (\hat{h}'_1 \times \bar{l}'_3)(1 - \mathcal{L}'_1) \tag{B.6}
$$

Now, as the source and observation points coincide, the term $\frac{1}{R}$ becomes singular. To remove this singularity, we make the substitution

$$
du = \frac{dx'}{R} = \frac{dx'}{\sqrt{x'^2 + y'^2}} \tag{B.7}
$$

Integrating (B.7) with respect to x', we obtain

$$
u(x') = \sinh^{-1}\left(\frac{x'}{y'}\right) \tag{B.8}
$$

Hence, (B.3) can be expressed as

$$I_1 = \frac{1}{4\pi} \int_0^{h1'} \int_{u_L}^{u_U} \mathbf{M}(r') e^{-jkR} du dy' \tag{B.9}$$

where, $R = y' \cosh u$.

From the above equation it is clear that the integrand is analytic in u and y' and the integral can be evaluated using repeated Gauss-Legendre quadrature method with weights w_i and coefficients $\mathcal{L}_i$ in the normalized interval (0,1) as given in [169]. Using this approach

$$I_1 = \frac{1}{4\pi} \sum_{i=1}^{K} \sum_{j=1}^{N} w_i w_j h_1' (u_U^{(j)} - u_L^{(j)}) \mathbf{M}(r') e^{-jkR^{i,j}} \tag{B.10}$$

where, the superscripts (i) or (j) denotes the i$^{\text{th}}$ or j$^{\text{th}}$ sampled values of corresponding variable and $R^{(i,j)} = y_j^{\prime(j)} \cosh u_i^{(i)}$.

The sampled values in the (u, y) domain can be expressed in terms of the area coordinates of the original triangle as follows:

1. y' samples are calculated from $(B.4)$ as

$$y'^{(j)} = h_1'(1 - \mathcal{L}_j) \tag{B.11}$$

2. x_l and x_U are calculated using (B.5) and (B.6).

3. Once these are calculated, we can use (B.8) to calculate u_L and u_U.

4. $u^{(i,j)}$ can be calculated using

$$u^{(i,j)} = u_l^{(j)}(1 - \mathcal{L}_i) + u_U^{(j)} \mathcal{L}_i \tag{B.12}$$

5. Once the u samples are calculated, corresponding x samples can be obtained from (B.8) as

$$x'^{(i,j)} = y'^{(j)} \sinh u^{(i,j)} \tag{B.13}$$

6. Next, we can calculate the remaining area coordinates as

$$\mathcal{L}_3^{\prime(i,j)} = \frac{\hat{n}' \cdot \vec{l}_3 \times (\hat{h}_1' y^{\prime(j)} - \hat{l}_1 x^{\prime(i,j)})}{2A'} \tag{B.14}$$

$$\mathcal{L}_2^{\prime(i,j)} = 1 - \mathcal{L}_3^{\prime(i,j)} - \mathcal{L}_1^{\prime(i,j)} \tag{B.15}$$

7. Finally, the area coordinates of the subtriangles are transformed to that of original triangle as

$$\begin{bmatrix} \mathcal{L}_1^{(j)} \\ \mathcal{L}_2^{(j)} \\ \mathcal{L}_3^{(j)} \end{bmatrix} = [T] \begin{bmatrix} \mathcal{L}_1^{\prime(j)} \\ \mathcal{L}_2^{\prime(j)} \\ \mathcal{L}_3^{\prime(j)} \end{bmatrix} \tag{B.16}$$

where,

$$[T] = \begin{bmatrix} \mathcal{L}_1^0 & 0 & 0 \\ \mathcal{L}_2^0 & 1 & 0 \\ \mathcal{L}_3^0 & 0 & 1 \end{bmatrix} \rightarrow \begin{bmatrix} \mathcal{L}_1^0 & 0 & 1 \\ \mathcal{L}_2^0 & 0 & 0 \\ \mathcal{L}_3^0 & 1 & 0 \end{bmatrix} \rightarrow \begin{bmatrix} \mathcal{L}_1^0 & 1 & 0 \\ \mathcal{L}_2^0 & 0 & 1 \\ \mathcal{L}_3^0 & 0 & 0 \end{bmatrix} \tag{B.17}$$

where, $(\mathcal{L}_1^0, \mathcal{L}_2^0, \mathcal{L}_3^0)$ denote the area coordinates at the observation point. The arrow indicates the value of matrix as we go from subtriangle 1 to subtriangle 3.

Thus, the integral can finally be expressed as a sum of contribution of three subtriangles as

$$I \approx 2A \sum_k W_k \mathbf{M}(\bar{r}') \frac{e^{-jkR^{(k)}}}{4\pi R^{(k)}} \tag{B.18}$$

where, W_k are the weights corresponding to the sample points of area coordinates of original triangle of area A. From (B.10), we can write

$$W_k = (\hat{n}'.\hat{n}) \frac{w_i w_j h_1' (u_U^{(j)} - u_L^{(j)}) R^{(i,j)}}{2A} \tag{B.19}$$

Bibliography

[1] B. B. Mandelbrot, *The Fractal Geometry of Nature.* New York: W. H. Freeman, 1982.

[2] H. O. Peitgen, H. Jurgens, and D. Saupe, *Chaos and Fractals: New Frontiers of Science.* New York: Springer-Verlag, 1992.

[3] J. F. Gouyet, *Physics and Fractal structures.* New York: Springer-Verlag, 1996.

[4] D. H. Werner and R. Mittra, *Frontiers in Electromagnetics.* New York: IEEE Press, 2000.

[5] D. H. Werner and S. Ganguly, "An overview of fractal antenna engineering research," *IEEE Antennas Propag. Mag.*, vol. 45, no. 1, pp. 38–57, Feb. 2003.

[6] C. Puente, J. Romeu, R. Pous, X. Garcia, and F. Benitez, "Fractal multiband antenna based on the Sierpinski gasket," *Electron. Lett.*, vol. 32, no. 1, pp. 1–2, Jan. 1996.

[7] C. Puente, J. Romeu, R. Pous, and A. Cardama, "On the behavior of the Sierpinski multiband fractal antenna," *IEEE Trans. Antennas Propag.*, vol. 46, no. 4, pp. 517–524, Apr. 1998.

[8] C. Borja, C. Puente, and A. Medina, "Iterative network model to predict the behavior of a Sierpinski fractal network," *Electron. Lett.*, vol. 34, no. 15, pp. 1443–1445, Jul. 1998.

[9] C. Puente, C. Borja, M. Navarro, and J. Romeu, "An iterative model for fractal antennas: Application to the Sierpinski gasket antenna," *IEEE Trans. Antennas Propag.*, vol. 48, no. 5, pp. 713–719, May 2000.

[10] C. Puente, J. Romeu, R. Bartoleme, and R. Pous, "Perturbation of the Sierpinski antenna to allocate operating bands," *Electron. Lett.*, vol. 32, no. 24, pp. 2186–2188, Nov. 1996.

[11] C. Puente, M. Navarro, J. Romeu, and R. Pous, "Variations on the fractal Sierpinski antenna flare angle," in *Proc. IEEE Int. Symp. Antennas Propag.*, vol. 4, Atlanta, GA, USA, Jun. 1998, pp. 2340–2343.

[12] S. R. Best, "On the significance of self-similar fractal geometry in determining the multiband behavior of the Sierpinski gasket antenna," *IEEE Antennas Wireless Propag. Lett.*, vol. 1, pp. 22–25, 2002.

[13] ——, "Operating band comparison of the perturbed Sierpinski and modified Parany gasket antennas," *IEEE Antennas Wireless Propag. Lett.*, vol. 1, pp. 35–38, 2002.

[14] ——, "On the radiation pattern characteristics of the Sierpinski and modified Parany gasket antennas," *IEEE Antennas Wireless Propag. Lett.*, vol. 1, pp. 39–42, 2002.

[15] R. K. Mishra, R. Ghatak, and D. R. Poddar, "Design formula for Sierpinski gasket pre-fractal planar monopole antennas," *IEEE Antennas Propag. Mag.*, vol. 50, no. 3, pp. 104–107, Jun. 2008.

[16] C. Puente, J. Romeu, R. Pous, J. Ramis, and A. Hijazo, "Small but long Koch fractal monopole," *Electron. Lett.*, vol. 34, no. 1, pp. 9–10, Jan. 1998.

[17] C. Puente, J. Romeu, and A. Cardama, "The Koch monopole: A small fractal antenna," *IEEE Trans. Antennas Propag.*, vol. 48, no. 11, pp. 1773–1781, Nov. 2000.

[18] S. R. Best, "A discusson on the significance of geometry in determining the resonant behavior of fractal and other non-Euclidean wire antennas," *IEEE Antennas Propagat. Mag.*, vol. 45, no. 3, pp. 9–28, Jun. 2003.

[19] ——, "On the performance properties of the Koch fractal and other bent wire monopoles," *IEEE Trans. Antennas Propag.*, vol. 51, no. 6, pp. 1292–1300, Jun. 2003.

[20] K. J. Vinoy, K. A. Jose, and V. K. Varadan, "On the relationship between fractal dimension and the performance of multi-resonant dipole antennas using Koch curves," *IEEE Trans. Antennas Propag.*, vol. 51, no. 9, pp. 2296–2303, Sep. 2003.

[21] K. J. Vinoy, K. A. Jose, V. K. Varadan, and V. V. Varadan, "Resonant frequency of Hilbert curve fractal antennas," in *Proc. IEEE Int. Symp. Antennas and Propag.*, Boston, USA, Jul. 2001, pp. 648–651.

[22] ——, "Hilbert curve fractal antenna: A small resonant antenna for VHF/UHF applications," *Microw. Opt. Technol. Lett.*, vol. 29, no. 4, pp. 215–219, Apr. 2001.

[23] ——, "Hilbert curve antenna with reconfigurable characteristics," in *Proc. IEEE MTT-S Int. Microw. Symp. Dig.*, Phoenix, USA, May 2001, pp. 381–384.

[24] J. P. Gianvittorio, "Fractal Antennas: Design, Characterization and Applications," Master's thesis, Deptt. Electrical Engg., University of California, Los Angeles, Mar. 2000.

[25] J. P. Gianvittorio and Y. Rahmat-Samii, "Fractal antennas: A novel antenna miniaturization technique, and applications," *IEEE Antennas Propag. Mag.*, vol. 44, no. 1, pp. 20–36, Feb. 2002.

[26] F. Arazm, R. K. Baee, C. Ghobadi, and J. Nourinia, "Square loop antenna miniaturization using new fractal geometry," in *Proc. 6th Int. Conf. Advanced Communication Tech.*, 2004, pp. 164–169.

[27] R. Ataeiseresht, C. Ghobadi, and J. Nourinia, "A novel analysis of Minkowski fractal microstrip patch antenna," *Journal of Electromagnetic Waves and Applications*, vol. 20, no. 8, pp. 1115–1127, 2006.

[28] A. R. Harish, A. Agarwal, N. Kuchhal, and V. Jain, "Compact loop antennas and arrays," in *Proc. Int. Conf. on Antenna Technologies (ICAT-2005)*, 2005, pp. 531–534.

[29] R. K. Joshi and A. R. Harish, "Parasitically loaded Vivaldi antenna," in *Proc. Int. Conf. on Antenna Technologies (ICAT-2005)*, 2005, pp. 525–529.

[30] ——, "Broadband concentric rings fractal slot antenna," in *28th General Assembly of URSI*, New Delhi, Oct. 2005.

[31] A. R. Harish and R. K. Joshi, "Studies on application of fractal based geometries in printed antenna structures," in *IEEE Applied Electromagnetics Conference (AEMC-2007)*, Kolkata, Dec. 2007, pp. 1–4.

[32] W. Chen, G. Wang, and C. Zhang, "Small size microstrip patch antennas combining Koch and Sierpinski fractal shapes," *IEEE Antennas Wireless Propag. Lett.*, vol. 7, pp. 738–741, 2008.

[33] J. Anguera, E. Martinez, C. Puente, C. Borja, and J. Soler, "Broadband dual-frequency microstrip patch antenna with modified Sierpinski fractal geometry," *IEEE Trans. Antennas Propag.*, vol. 52, no. 1, pp. 66–73, Jan. 2004.

[34] ——, "Broadband tripple-frequency microstrip patch radiator combining a dual-band modified Sierpinski fractal and a monoband antenna," *IEEE Trans. Antennas Propag.*, vol. 54, no. 11, pp. 3367–3373, Nov. 2006.

[35] J. Romeu, C. Borja, and S. Blanch, "High directivity modes in the Koch island fractal patch antenna," in *Proc. IEEE Int. Symp. Antennas Propag.*, vol. 3, Salt Lake City, USA, Jul. 2000, pp. 1696–1699.

[36] C. Borja, G. Font, S. Blanch, and J. Romeu, "High directivity fractal boundary microstrip patch antenna," *Electron. Lett.*, vol. 36, no. 9, pp. 778–779, Apr. 2000.

[37] J. Anguera, C. Puente, C. Borja, and J. Soler, "Dual-frequency broadband-stacked microstrip antenna using a reactive loading and a fractal-shaped radiating edge," *IEEE Antennas Wireless Propag. Lett.*, vol. 6, pp. 309–312, 2007.

[38] K. Zhang, C. Chen, C. Guo, and J. Xu, "On the behavior of conformal Sierpinski fractal microstrip antenna," in *Proc. Int. Conf. Microw. Millimeter Wave Tech.*, Apr. 2008, pp. 1073–1076.

[39] K. Zhang, Q. Zhang, C. Guo, and J. Xu, "Analysis of conformal Sierpinski fractal microstrip antenna," in *Proc. Int. Conf. Microw. Millimeter Wave Tech.*, Apr. 2008, pp. 1106–1109.

[40] D. E. Anagnostou, J. Papapolymerou, M. M. Tentzeris, and C. G. Christodoulou, "A printed log-periodic Koch-dipole array (LPKDA)," *IEEE Antennas Wireless Propag. Lett.*, vol. 7, pp. 456–460, 2008.

[41] R. H. Patnam, "Broadband CPW-fed planar Koch fractal loop antenna," *IEEE Antennas Wireless Propag. Lett.*, vol. 7, pp. 429–431, 2008.

[42] D. D. Krishna, M. Gopikrishna, C. K. Anandan, P. Mohanan, and K. Vasudevan, "CPW-fed Koch fractal slot antenna for WLAN/WiMAX applications," *IEEE Antennas Wireless Propag. Lett.*, vol. 7, pp. 389–392, 2008.

[43] D. Chang, B. Zeng, and J. Liu, "CPW-fed circular fractal slot antenna design for dual-band applications," *IEEE Trans. Antennas Propag.*, vol. 56, no. 12, pp. 3630–3636, Dec. 2008.

[44] R. Ghatak, R. K. Mishra, and D. R. Poddar, "Perturbed Sierpinski carpet antenna with CPW feed for IEEE 802.11 a/b WLAN application," *IEEE Antennas Wireless Propag. Lett.*, vol. 7, pp. 742–744, 2008.

[45] J. Romeu and Y. Rahmat-Samii, "A fractal based FSS with dual band characteristics," in *Proc. IEEE Int. Symp. Antennas Propag.*, Florida, USA, Aug. 1999, pp. 1734–1737.

[46] ——, "Dual band FSS with fractal elements," *Electron. Lett.*, vol. 35, no. 9, pp. 702–703, Apr. 1999.

[47] ——, "Fractal FSS: A novel dual-band frequency selective surface," *IEEE Trans. Antennas Propag.*, vol. 48, no. 7, pp. 1097–1105, Jul. 2000.

[48] D. H. Werner and D. Lee, "Design of dual-polarized multiband frequency selective surfaces using fractal elements," *Electron. Lett.*, vol. 36, no. 6, pp. 487–488, Mar. 2000.

[49] ——, "A design approach for dual-polarized multiband frequency selective surfaces using fractal elements," in *Proc. IEEE Int. Symp. Antennas Propag.*, Salt Lake City, USA, Jul 2000, pp. 1692–1695.

[50] J. P. Gianvittorio, J. Romeu, S. Blanch, and Y. Rahmat-Samii, "Self-similar prefractal frequency selective surfaces for multiband and dual-polarized applications," *IEEE Trans. Antennas Propag.*, vol. 51, no. 11, pp. 3088–3096, Nov. 2003.

[51] R. Holakouei, J. Nourinia, and C. Ghobadi, "A design approach for a dual-polarized, dual-band-reject frequency selective surface using a new fractal element," *International Journal of Electronics and Communications*, vol. 61, no. 9, pp. 568–579, Oct. 2007.

[52] M. Weng, D. Lee, R. Yang, H. Wu, and C. Liu, "A Sierpinski fractal based dual-mode bandpass filter," *Microw. Opt. Technol. Lett.*, vol. 50, no. 9, pp. 2287–2289, Sep. 2008.

[53] J. Xiao, H. Huang, and W. Ji, "Wideband microstrip bandpass filter using single patch resonator," in *Proc. Int. Conf. Microw. Millimeter Wave Tech.*, Apr. 2008, pp. 1470–1473.

[54] W. Chen, G. Wang, and Y. Qi, "Fractal shaped Hi-Lo microstrip low-pass filters with high passband performance," *Microw. Opt. Technol. Lett.*, vol. 49, no. 10, pp. 2577–2579, Oct. 2007.

[55] F. Frezza, L. Pajewski, and G. Schettini, "Fractal two dimensional electromagnetic bandgap structures," *IEEE Trans. Microw. Theory Tech.*, vol. 52, no. 1, pp. 220–227, Jan. 2004.

[56] X. L. Bao, G. Ruvio, M. J. Ammann, and M. John, "A novel GPS patch antenna on a fractal hi-impedance surface substrate," *IEEE Antennas Wireless Propag. Lett.*, vol. 5, pp. 323–326, 2006.

[57] J. McVay, N. Engheta, and A. Hoorfar, "High impedance metamaterial surfaces using Hilbert-curve inclusions," *IEEE Microw. Wireless Compon. Lett.*, vol. 14, no. 3, pp. 130–132, Mar. 2004.

[58] J. McVay, A. Hoorfar, and N. Engheta, "Thin absorbers using space-filling-curve high-impedance surfaces," in *Proc. IEEE Int. Symp. Antennas Propag.*, vol. 2A, Jul. 2005, pp. 22–25.

[59] D. J. Kern, D. H. Werner, A. Monorchio, L. Lanuzza, and M. J. Wilhelm, "The design synthesis of multiband artificial magnetic conductors using high impedance frequency selective surfaces," *IEEE Trans. Antennas Propag.*, vol. 53, no. 1, pp. 8–17, Jan. 2005.

[60] D. Yunfeng, L. Shaobin, and W. Yong, "A novel dual-band compact electromagnetic bandgap (EBG) structure and its application," in *Proc. Int. Conf. Microw. Millimeter Wave Tech.*, Apr. 2008, pp. 51–53.

[61] G. L. Matthaei, L. Young, and E. M. T. Jones, *Microwave Filters, Impedance Matching Networks and Coupling Structures.* NewYork:McGraw-Hill, 1964.

[62] K. Chang and P. J. Khan, "Coupling between narrow transverse inductive strips in waveguide," *IEEE Trans. Microw. Theory Tech.*, vol. 24, no. 2, pp. 101–105, Feb. 1976.

[63] H. Auda and R. F. Harrington, "Inductive posts and diaphragms of arbitrary shape and number in a rectangular waveguide," *IEEE Trans. Microw. Theory Tech.*, vol. 32, no. 6, pp. 606–613, Jun. 1984.

[64] R. Safavi-Naini and R. H. MacPhie, "Scattering at rectangular-to-rectangular waveguide junctions," *IEEE Trans. Microw. Theory Tech.*, vol. 30, no. 11, pp. 2060–2063, Nov. 1982.

[65] J. D. Wade and R. H. MacPhie, "Scattering at circular-to-rectangular waveguide junctions," *IEEE Trans. Microw. Theory Tech.*, vol. 34, no. 11, pp. 1085–1091, Nov. 1986.

[66] M. Piloni, E. Ravenelli, and M. Guglielmi, "Resonant aperture filters in rectangular waveguide," in *Proc. IEEE MTT-S Int. Microw. Symp. Dig.*, vol. 3, Anaheim, CA, USA, Jun. 1999, pp. 911–914.

[67] M. Capurso, M. Piloni, and M. Guglielmi, "Resonant aperture filters: Improved out-of-band rejection and size reduction," in *Proc. 31st European Microw. Conf.*, London, England, Oct. 2001, pp. 1–4.

[68] N. G. Paterson and I. Anderson, "Bandstop iris for rectangular waveguide," *Electron. Lett.*, vol. 12, no. 22, pp. 592–594, Oct. 1976.

[69] A. A. Kirilenko and L. P. Mospan, "Reflection resonances and natural oscillations of two-aperture iris in rectangular waveguide," *IEEE Trans. Microw. Theory Tech.*, vol. 48, no. 8, pp. 1419–1421, Aug. 2000.

[70] ——, "Two- and three-slot irises as bandstop filter sections," *Microw. Opt. Technol. Lett.*, vol. 28, no. 4, pp. 282–284, Feb. 2001.

[71] R. Yang and A. S. Omar, "Investigation of multiple rectangular aperture irises in rectangular waveguide using TE^{x}_{mn}-modes," *IEEE Trans. Microw. Theory Tech.*, vol. 41, no. 8, pp. 1369–1374, Aug. 1993.

[72] M. Ohira, H. Deguchi, M. Tsuji, and H. Shigesawa, "A new dual-behavior FSS resonator for waveguide filter with multiple attenuation poles," in *Proc. 35th European Microw. Conf.*, Paris, Oct. 2005, pp. 189–192.

[73] R. D. Seager, J. C. Vardaxoglou, and D. S. Lockyer, "Close coupled resonant aperture inserts for waveguide filtering applications," *IEEE Microw. Wireless Compon. Lett.*, vol. 11, no. 3, pp. 112–114, Mar. 2001.

[74] T. VuKhac, "Solutions for some waveguide discontinuities by the method of moments," *IEEE Trans. Microw. Theory Tech.*, vol. 20, no. 6, pp. 416–418, Jun. 1972.

[75] H. Auda and R. F. Harrington, "A moment solution for waveguide junction problems," *IEEE Trans. Microw. Theory Tech.*, vol. 31, no. 7, pp. 515–520, Jul. 1983.

[76] S. N. Sinha, "Analysis of multiple-strip discontinuity in a rectangular waveguide," *IEEE Trans. Microw. Theory Tech.*, vol. 34, no. 6, pp. 696–700, Jun. 1986.

[77] A. Datta, B. N. Das, and A. Chakraborty, "Moment method formulation of thick diaphragms in a rectangular waveguide," *IEEE Trans. Microw. Theory Tech.*, vol. 40, no. 3, pp. 592–595, Mar. 1992.

[78] B. N. Das, G. S. N. Raju, and A. Chakraborty, "Analysis of coplanar E-H plane T junction using dissimilar rectangular waveguides," *IEEE Trans. Microw. Theory Tech.*, vol. 36, no. 3, pp. 604–606, Mar. 1988.

[79] A. I. Khalil, A. B. Yakovlev, and M. B. Steer, "Efficient method-of-moments formulation for the modeling of planar conductive layers in a shielded guided-wave structure," *IEEE Trans. Microw. Theory Tech.*, vol. 47, no. 9, pp. 1730–1736, Sep. 1999.

[80] A. I. Khalil and M. B. Steer, "A generalized scattering matrix method using the method of moments for electromagnetic analysis of multilayered structures in waveguide," *IEEE Trans. Microw. Theory Tech.*, vol. 47, no. 11, pp. 2151–2157, Nov. 1999.

[81] S. W. Lee, W. R. Jones, and J. J. Campbell, "Convergence of numerical solutions of iris-type discontinuity problems," *IEEE Trans. Microw. Theory Tech.*, vol. 19, no. 6, pp. 528–536, Jun. 1971.

[82] R. Mittra, T. Itoh, and T. Li, "Analytical and numerical studies of the relative convergence phenomenon arising in the solution of an integral equation by the moment method," *IEEE Trans. Microw. Theory Tech.*, vol. 20, no. 2, pp. 96–104, Feb. 1972.

[83] M. I. Aksun and R. Mittra, "Choices of expansion and testing functions for the method of moments applied to a class of electromagnetic problems," *IEEE Trans. Microw. Theory Tech.*, vol. 41, no. 3, pp. 503–509, Mar. 1993.

[84] C. C. Chen, "Transmission of microwave through perforated flat plates of finite thickness," *IEEE Trans. Microw. Theory Tech.*, vol. 21, no. 1, pp. 1–6, Jan. 1973.

[85] L. P. Mospan and O. V. Chistyakova, "Rejection frequency selective surface with two different apertures over the period," in *Proc. 5th Int. Kharkov Symp. MSMW' 04*, vol. 1, Kharkov, Ukrain, June. 2004, pp. 269–271.

[86] W. Wen, L. Zhou, J. Li, W. Ge, C. T. Chan, and P. Sheng, "Subwavelength photonic band gaps from planar fractals," *Phys. Rev. Lett.*, vol. 89, no. 22, pp. 223 901(1–4), Nov. 2002.

[87] L. Zhou, C. T. Chan, and P. Sheng, "Theoritical studies on the transmission and reflection properties of metallic planar fractals," *Journal of Physics D: Applied Physics*, vol. 37, pp. 368–373, Nov. 2004.

[88] B. Hou, G. Xu, and W. Wen, "Tunable band gap properties of planar metallic fractals," *J. Appl. Phys.*, vol. 95, no. 6, pp. 3231–3233, Mar. 2004.

[89] W. Wen, L. Zhou, B. Hou, C. T. Chan, and P. Sheng, "Resonant transmission of microwaves through subwavelength fractal slits in a metallic plate," *Phys. Rev. B*, vol. 72, no. 15, pp. 153 406(1–4), 2005.

[90] R. F. Harrington and J. R. Mautz, "A generalized network formulation for aperture problems," *IEEE Trans. Antennas Propag.*, vol. 24, no. 6, pp. 870–873, Nov. 1976.

[91] J. R. Mautz and R. F. Harrington, "Electromagnetic transmission through a rectangular aperture in a perfectly conducting screen," Deptt. of Electrical and Computer Engg., Syracuse University, New York, 13210, Tech. Rep. TR-76-1, 1976.

[92] R. F. Harrington and D. T. Auckland, "Electromagnetic transmission through narrow slots in thick conducting screens," *IEEE Trans. Antennas Propag.*, vol. 28, no. 5, pp. 616–622, Sep. 1980.

[93] I. Chih-Lin and R. F. Harrington, "Electromagnetic transmission through an aperture of arbitrary shape in a conducting screen," Syracuse University, Tech. Report Contract No 0014-76-0225, 1982.

[94] S. M. Rao, D. R. Wilton, and A. W. Glisson, "Electromagnetic scattering by surfaces of arbitrary shape," *IEEE Trans. Antennas Propag.*, vol. 30, no. 3, pp. 409– 418, May 1982.

[95] J. Lin, W. L. Curtis, and M. C. Vincent, "On the field distribution of an aperture," *IEEE Trans. Antennas Propag.*, vol. 22, no. 3, pp. 467–471, May 1974.

[96] R. L. Gluckstern, R. Li, and R. K. Cooper, "Electric polarizability and magnetic susceptibility of small holes in a thin screen," *IEEE Trans. Microw. Theory Tech.*, vol. 38, no. 2, pp. 186–192, Feb. 1990.

[97] W. T. Cathey, "Approximate expressions for field penetration through circular apertures," *IEEE Trans. Electromagn. Compatibility*, vol. 25, no. 3, pp. 339–345, Aug. 1983.

[98] S. V. Savov, "Mutual coupling between two small circular apertures in a conducting screen," *IEEE Trans. Microw. Theory Tech.*, vol. 41, no. 1, pp. 143–146, Jan. 1993.

[99] A. E. Hajj and K. Y. Kabalan, "Characteristic modes of a rectangular aperture in a perfectly conducting plane," *IEEE Trans. Antennas Propag.*, vol. 42, no. 10, pp. 1447–1450, Oct. 1994.

[100] Y. S. Kim and H. J. Eom, "Fourier-transform analysis of electrostatic potential distribution through a thick slit," *IEEE Trans. Electromagn. Compatibility*, vol. 38, no. 1, pp. 77–79, Feb. 1996.

[101] R. Luebbers and C. Penney, "Scattering from apertures in infinite ground planes using FDTD," *IEEE Trans. Antennas Propag.*, vol. 42, no. 5, pp. 731–736, May 1994.

[102] T. K. Sarkar, M. F. Costa, C. Lin, and R. F. Harrington, "Electromagnetic transmission through mesh covered apertures and arrays of apertures in a conducting screen," *IEEE Trans. Antennas Propag.*, vol. 32, no. 9, pp. 908–913, Sep. 1984.

[103] W. L. Ko and R. Mittra, "Scattering by a truncated periodic array," *IEEE Trans. Antennas Propag.*, vol. 36, no. 4, pp. 496–503, Apr. 1988.

[104] T. Cwik and R. Mittra, "The effects of the truncation and curvature of periodic surfaces: A strip grating," *IEEE Trans. Antennas Propag.*, vol. 36, no. 5, pp. 612–622, May 1988.

[105] R. Kastner and R. Mittra, "Iterative analysis of finite-sized planar frequency selective surfaces with rectangular patches or perforations," *IEEE Trans. Antennas Propag.*, vol. 35, no. 4, pp. 372–377, Apr. 1987.

[106] L. Gurel and W. C. Chew, "Recursive algorithms for calculating the scattering from N strips or patches," *IEEE Trans. Antennas Propag.*, vol. 38, no. 4, pp. 507–515, Apr. 1990.

[107] H. H. Park and H. J. Eom, "Electromagnetic scattering from multiple rectangular apertures in a thick conducting screen," *IEEE Trans. Antennas Propag.*, vol. 47, no. 6, pp. 1056–1060, Jun. 1999.

[108] Y. B. Park and H. J. Eom, "Electromagnetic transmission through multiple circular apertures in a thick conducting plane," *IEEE Trans. Antennas Propag.*, vol. 52, no. 4, pp. 1049–1055, Apr. 2004.

[109] T. Andersson, "Moment method calculations on apertures using basis singular functions," *IEEE Trans. Antennas Propag.*, vol. 41, no. 12, pp. 1709–1716, Dec. 1993.

[110] S. Gupta, A. Bhattacharya, and A. Chakraborty, "Analysis of an open-ended waveguide radiator with dielectric plug." *IEE Proc. Microw., Antennas Propagat.*, vol. 144, no. 2, pp. 126–130, Apr. 1997.

[111] S. Gupta, A. Chakraborty, and B. N. Das, "Admittance of waveguide fed slot radiators," in *Proc. IEEE Int. Symp. Antennas Propag.*, vol. 2, San Jose, CA, USA, Jun. 1989, pp. 968–971.

[112] M. H. Cohen, T. H. Crowley, and C. A. Levis, "The aperture admittance of a rectangular waveguide radiating into half-space," Antenna Lab, Ohio State University, Columbus, Tech. Rep. 339-22, 1951.

[113] B. N. Das, "Admittance of rectangular apertures," *J. Institution of Electronics and Telecommunication Engineers (India)*, vol. 22, pp. 133–137, Mar. 1976.

[114] A. R. Jamieson and T. E. Rozzi, "Rigorous analysis of cross-polarisation in flange-mounted rectangular waveguide radiators," *Electron. Lett.*, vol. 13, no. 24, pp. 742–744, Nov. 1977.

[115] R. H. MacPhie and A. I. Zaghloul, "Radiation from a rectangular waveguide with infinite flang–Exact solution by the correlation matrix method," *IEEE Trans. Antennas Propag.*, vol. 28, no. 4, pp. 497–503, Jul. 1980.

[116] H. Baudrand, J. W. Tao, and J. Atechian, "Study of radiating properties of open-ended rectangular waveguides," *IEEE Trans. Antennas Propag.*, vol. 36, no. 8, pp. 1071–1077, Aug. 1988.

[117] M. Mongiardo and T. Rozzi, "Singular integral equation analysis of flange-mounted rectangular waveguide radiators," *IEEE Trans. Antennas Propag.*, vol. 41, no. 5, pp. 556–565, May 1993.

[118] Z. Shen and R. H. MacPhie, "A simple method for calculating the reflection coefficient of open-ended waveguides," *IEEE Trans. Microw. Theory Tech.*, vol. 45, no. 4, pp. 546–548, Apr. 1997.

[119] J. R. Mautz and R. F. Harrington, "Transmission from rectangular waveguide in half-space through rectangular aperure," Airforce Cambridge Research Lab., USA, Tech. Rep. TR-76-5, 1976.

[120] J. Luzwick and R. F. Harrington, "Mutual coupling analysis in a finite planar rectangular waveguide antenna array," *Electromagn.*, vol. 2, no. 1, pp. 25–42, 1982.

[121] A. J. Fenn, G. A. Thiele, and B. A. Munk, "Moment method analysis of finite rectangular waveguide phased arrays," *IEEE Trans. Antennas Propag.*, vol. 30, no. 4, pp. 554–564, Jul. 1982.

[122] J. Luzwick and R. F. Harrington, "A reactively loaded aperture antenna array," *IEEE Trans. Antennas Propag.*, vol. 26, no. 4, pp. 543–547, Jul. 1978.

[123] F. Arndt, K. H. Wolff, L. Brunjes, R. Heyen, and F. Siefken, "Generalized moment method analysis of planar reactively loaded rectangular waveguide arrays," *IEEE Trans. Antennas Propag.*, vol. 37, no. 3, pp. 329–338, Mar. 1989.

[124] R. Garg, P. Bhartia, I. Bahl, and A. Ittipiboon, *Microstrip Antenna Design Handbook.* London, U. K.: Artech House, 2001.

[125] A. Hadidi and M. Hamid, "Aperture field and circuit parameters of cavity-backed slot radiator," *IEE Proc. Microw., Antennas Propag., Pt. H.*, vol. 136, no. 2, pp. 139–146, Apr. 1989.

[126] T. Kotani, K. Hirasawa, S. Shi, and Y. Chang, "A rectangular cavity-backed slot antenna with parasitic slots," in *Proc. IEEE Int. Symp. Antennas Propag.*, vol. 3, Jul. 2001, pp. 166–169.

[127] T. Kotani, K. Hirasawa, and S. Song, "A rectangular cavity backed S-type slot antenna," in *Proc. IEEE Int. Symp. Antennas Propag.*, vol. 4, Jun. 2003, pp. 22–27.

[128] T. Takahashi and K. Hirasawa, "A broadband rectangular-cavity-backed meandering slot antenna," in *Proc. IEEE Int. Workshop Antenna Technology: Small Antennas and Novel Metamaterials*, Mar. 2005, pp. 21 – 24.

[129] S. Shi, K. Hirasawa, and Z. N. Chen, "Circularly polarized rectangularly bent slot antennas backed by a rectangular cavity," *IEEE Trans. Antennas Propag.*, vol. 49, no. 11, pp. 1517–1524, Nov. 2001.

[130] T. Takahashi, T. Kotani, K. Hirasawa, and S. Shi, "A rectangular cavity-backed cross-loop slot antenna," in *Proc. IEEE Int. Symp. Antennas Propag.*, vol. 2, Mar. 2002, pp. 448 – 451.

[131] R. Azadegan and K. Sarabandi, "A compact planar folded-dipole antenna for wireless applications," in *Proc. IEEE Int. Symp. Antennas Propag.*, vol. 1, Jun. 2003, pp. 439–442.

[132] W. Hong, N. Behdad, and K. Sarabandi, "Size reduction of cavity backed slot antenna," *IEEE Trans. Antennas Propag.*, vol. 54, no. 5, pp. 1461–1466, May 2006.

[133] Y. Liu, Z. Shen, H. C. Chin, and W. L. Lim, "A single-feed wide-and dual band cavity-backed slot antenna," *Microw. Opt. Technol. Lett.*, vol. 49, no. 7, pp. 1570–1572, Jul. 2007.

[134] J. Galejs, "Admittance of a rectangular slot which is backed by a rectangular cavity," *IEEE Trans. Antennas Propag.*, vol. 11, no. 2, pp. 119–126, Mar. 1963.

[135] A. T. Adams, "Flush mounted rectangular cavity slot antennas: Theory and design," *IEEE Trans. Antennas Propag.*, vol. 15, no. 3, pp. 342–351, May 1967.

[136] C. R. Cockrell, "The input admittance of the rectangular cavity-backed slot antenna," *IEEE Trans. Antennas Propag.*, vol. 24, no. 3, pp. 288–294, May 1976.

[137] J. Hirokawa, H. Arai, and N. Goto, "Cavity-backed wide slot antenna," *IEE Proc. Microw., Antennas Propag., Pt. H.*, vol. 136, no. 1, pp. 29–33, Feb. 1989.

[138] T. Lertwiriyaprapa, C. Phongcharoenpanich, and M. Krairiksh, "Characterization of the input impedance of a probe excited rectangular cavity-backed slot antenna," in *Proc. 5th Int. Symp. Antennas Propag. and EM Theory*, Aug. 2000, pp. 654–657.

[139] T. Lertwiriyaprapa, C. Phongcharoenpanich, S. Kosulvit, and M. Krairiksh, "Analysis of impedance characteristics of a probe fed

rectangular cavity-backed slot antenna," in *Proc. IEEE Int. Symp. Antennas Propag.*, vol. 1, Jul. 2001, pp. 576–579.

[140] T. Lertwiriyaprapa, C. Phongcharoenpanich, and M. Krairiksh, "Analysis of radiation characteristics of a probe fed rectangular cavity backed slot antenna with finite-size ground plane," in *Proc. IEEE Int. Symp. Antennas Propag.*, vol. 2, Jul. 2000, pp. 714–717.

[141] J. Y. Lee, T. S. Horng, and N. G. Alexopoulos, "Analysis of cavity-backed aperture antenas with a dielectric overlay," *IEEE Trans. Antennas Propag.*, vol. 42, no. 11, pp. 1556–1562, Nov. 1994.

[142] E. M. Biebl and G. L. Friedsam, "Cavity-backed aperture antennas with dielectric and magnetic overlay," *IEEE Trans. Antennas Propag.*, vol. 43, no. 11, pp. 1226–1232, Nov. 1995.

[143] H. Moheb, L. Shafai, and J. Shaker, "Numerical solution of radiation from single and multiple arbitrary apertures backed by a cavity," in *Proc. IEEE Int. Symp. Antennas Propag.*, Chicago, USA, Jul. 1992, pp. 61–64.

[144] M. D. Deshpande and C. J. Reddy, "Electromagnetic scattering from a rectangular cavity recessed in a 3D conducting surface," NASA, Hampton, Verginia, Contractor Report 4697, Oct. 1995.

[145] M. Omiya, T. Hikage, N. Ohno, K. Horiguchi, and K. Itoh, "Design of cavity-backed slot antennas using the finite-difference time-domain technique," *IEEE Trans. Antennas Propag.*, vol. 46, no. 12, pp. 1853–1858, Dec. 1998.

[146] T. Hikage, M. Omiya, and K. Itoh, "Considerations on performance evaluation of cavity-backed slot antenna using the FDTD technique," *IEEE Trans. Antennas Propag.*, vol. 49, no. 12, pp. 1712–1717, Dec. 2001.

[147] S. M. Rao, G. K. Gothard, and D. R. Wilton, "Application of finite-integral technique to electromagnetic scattering by two-dimensional cavity-backed aperture in a ground plane," *IEEE Trans. Antennas Propag.*, vol. 46, no. 5, pp. 679–685, May 1998.

[148] G. Marrocco, S. Fari, and F. Bardati, "A hybrid FDTD-MoM procedure for the modeling of electromagnetic radiation from the cavity-backed apertures," in *Proc. IEEE Int. Symp. Antennas Propag.*, vol. 4, Boston, USA, 2001, pp. 302–305.

[149] S. V. Georgakopoulos, A. C. Polycarpou, C. A. Balanis, and C. Birtcher, "Analysis of coupling between cavity-backed slot antennas: FDTD, FEM and measurements," in *Proc. IEEE Int. Symp. Antennas Propag.*, vol. 1, Orlando, USA, Aug. 1999, pp. 582–585.

[150] J. M. Jin and J. L. Volakis, "A finite element-boundary integral formulation for scattering by three-dimensional cavity-backed apertures," *IEEE Trans. Antennas Propag.*, vol. 39, no. 1, pp. 97–104, Jan. 1991.

[151] ——, "A hybrid finite element method for scattering and radiation by microstrip patch antennas and arrays residing in a cavity," *IEEE Trans. Antennas Propag.*, vol. 39, no. 11, pp. 1598–1604, Nov. 1991.

[152] J. Gong, J. L. Volakis, A. C. Woo, and H. T. G. Wang, "A hybrid finite element-boundary integral method for the analysis of cavity-backed anten-

nas of arbitrary shape," *IEEE Trans. Antennas Propag.*, vol. 42, no. 9, pp. 1233–1242, Sep. 1994.

[153] S. Baudou, P. Borderies, P. Combes, and R. Mittra, "Analysis of a conformal cavity-backed patch antenna using a hybrid MoM/FEM technique," in *Proc. IEEE Int. Symp. Antennas Propag.*, vol. 2, Boston, USA, Aug. 2001, pp. 354–357.

[154] C. J. Reddy, M. D. Deshpande, C. R. Cockrell, and F. B. Beck, "Analysis of three-dimensional cavity-backed aperture antennas using a combined Finite Element Method/ Method of Moments/ Geometrical Theory of Diffraction technique," NASA, Hampton, Verginia 23681–0001, Technical Paper 3548, Nov. 1995.

[155] ——, "Radiation characteristics of cavity-backed aperture antennas in finite ground plane using hybrid FEM/MoM technique and geometrical theory of diffraction," *IEEE Trans. Antennas Propag.*, vol. 44, no. 10, pp. 1327–1333, Oct. 1996.

[156] T. N. Chang, L. C. Kuo, and M. L. Chuang, "Coaxial-fed cavity-backed slot antenna," *Microw. Opt. Technol. Lett.*, vol. 14, no. 5, pp. 291 – 294, Apr. 1997.

[157] R. Azaro, S. Caorsi, M. Donelli, and G. L. Gragnani, "A circuital approach to evaluating the electromagnetic field on rectangular apertures backed by rectangular cavities," *IEEE Trans. Microw. Theory Tech.*, vol. 50, no. 10, pp. 2259–2266, Oct. 2002.

[158] "Ansoft corporation. (2004) products," [Online]. Available: http://www.ansoft.com/products/.

[159] D. R. Wilton, "Review of current status and trends in the use of integral equations in computational electromagnetics," *Electromagn.*, vol. 12, pp. 287–341, Jul. 1992.

[160] S. K. Verma, "A moment solution for thick dielectric-filled windows in a waveguide," Master's thesis, Deptt. of Electronics and Computer Engg., University of Roorkee, Roorkee, India, Sep. 1987.

[161] O. C. Zienkiewicz, R. L. Taylor, and J. Z. Zhu, *The Finite Element Method : Its Basis and Fundamentals*, 6th ed. Elsevier Butterworth-Heinemann, 2005.

[162] R. S. Kshetrimayum and L. Zhu, "Guided-wave characteristics of waveguide based periodic structures loaded with various FSS strip layers," *IEEE Trans. Antennas Propag.*, vol. 53, no. 1, pp. 120–124, Jan. 2005.

[163] ——, "EBG design using FSS elements in rectangular waveguide," *Applied Computational Electromagnetics Society Journal*, vol. 21, no. 2, pp. 149–154, 2006.

[164] D. R. Wilton, S. M. Rao, A. W. Glisson, D. H. Schaubert, O. M. Al-Bundak, and C. M. Butler, "Potential integrals for uniform and linear source distributions on polygonal and polyhedral domains," *IEEE Trans. Antennas Propag.*, vol. 32, no. 3, pp. 276–281, Mar. 1984.

[165] R. D. Graglia, "On the numerical integration of the linear shape functions times the 3D Green's function or its gradient on a plane triangle," *IEEE Trans. Antennas Propag.*, vol. 41, no. 10, pp. 1448–1455, Oct. 1993.

[166] T. F. Eibert and V. Hansen, "On the calculation of poltential integrals for linear source distributions on triangular domains," *IEEE Trans. Antennas Propag.*, vol. 43, no. 12, pp. 1499–1502, Dec. 1995.

[167] L. Rossi and P. J. Cullen, "On the fully numerical evaluation of the linear shape function times 3D Green's function on a plane triangle," *IEEE Trans. Microw. Theory Tech.*, vol. 47, no. 4, pp. 398–402, Apr. 1999.

[168] M. A. Khayat and D. R. Wilton, "Numerical evaluation of singular and near-singular potential integrals," *IEEE Trans. Antennas Propag.*, vol. 53, no. 10, pp. 3180–3190, Oct. 2005.

[169] M. Abramowitz and I. A. Stegun, *Handbook of Mathematical Functions.* New York: Dover Publications, Inc., 1970.

Author's Publications

International Journals (published)

1. B. Ghosh, S. N. Sinha, M. V. Kartikeyan, "Electromagnetic Transmission Through Fractal Apertures in Infinite Conducting Screen," *Progress in Electromagnetic Research B*, vol. 12, pp. 105-138, 2009.

International and National Conferences

1. Basudeb Ghosh, Sachendra N. Sinha, M. V. Kartikeyan, "Fractal Apertures in Waveguides and Conducting Screen," in *Proc. TENCON 2008*, Hyderabad, India, November 18-21, 2008.

2. B. Ghosh, Sachendra N. Sinha, M. V. Kartikeyan, "Investigations on a Fractal Shaped Aperture in a Rectangular waveguide," in *Proc. National Symposium on Antennas and Propagation (APSYM 06)*, Kochi, India, pp. 131-134.

International Journals (under communication)

1. Basudeb Ghosh, Sachendra N. Sinha, M. V. Kartikeyan, "Radiation From Rectangular Waveguide-Fed Fractal Apertures," *IEEE Trans. Antennas and Propag.*, 2008.